COUPLED MICROWAVE RESONATORS FOR DISTANT SENSING APPLICATIONS

by

ZAHRA ABBASI

A thesis submitted in partial fulfillment of the requirements for the degree of

Doctor of Philosophy

in

Microsystems and Nanodevices

Department of Electrical and Computer Engineering
University of Alberta

Abstract

For the past two decades, planar microwave resonators have been used for sensing and monitoring applications due to their unique characteristics such as non-contact and real-time sensing capability, simple and low-cost fabrication process, which make them a high performance alternative to traditional bulky waveguide sensors. However, the limitation of electronic readout circuitry in harsh environment sensing, low-sensitivity, and distance limited sensing performance are the important challenges and limitations for their successful implementation into a wireless sensing system and the Internet of Thing (IoT) ecosystem. The work presented in this thesis focuses on distance and resolution enhancement of coupled split-ring resonator (SRR) based structures, and several highly sensitive distant sensing systems and their applications are presented.

To address the distance limited sensing performance in the conventional SRR-based sensors, a reader-tag structure based on coupled SRR structures is designed. The presence of the second resonator, the tag, enhances the design's sensitivity significantly and enables the sample under the test to be placed at further distances from the reader. Applications of the proposed technology in non-contact real-time hazardous gas sensing, humidity percentage monitoring, and non-invasive glucose concentration sensing is investigated.

In the second step, sensing distance in the reader-tag structure is enhanced using a locally strong coupled microwave resonator. Backed with theory, simulations, optimization, and experimental results, this concept demonstrates the ability to significantly increase the distance between the tag and the reader. The flexible ultra-thin tag resonator empowers the proposed design to perform real-time noncontact sensing using an inexpensive sensing element that could be easily mounted on any material container.

The design applications in high-temperature bitumen sensing, humidity monitoring, and disposable microfluidic biomedical sensors are explored.

Furthermore, to enhance the resolution of the sensing, an active feedback loop has been added to the conventional SRR-based planar structure to compensate for different sources of loss and create a sharp high-Q response, capable of high-resolution sensing performance. The application of high-resolution active sensors is investigated for pH level sensing in biomedical and pipeline integrity.

Finally, in order to enable microwave sensing systems to be capable of high-resolution measurement and protect them is harsh environment applications, the active feedback loop and the tag-reader coupled structure are combined in one structure and a flexible low-cost, RF chipless tag-reader sensor is developed, capable of ultra high-quality factor performance. The chipless RF tag is a great candidate for harsh environment sensing applications since the main sensing element in the design is a passive structure. The high level of sensitivity offered by design, empowers it for concentration measurement in nano-liter samples. The presented technique provides a practical solution for highly sensitive, non-invasive, and real-time sensing applications.

Preface

This thesis is an original work by Zahra Abbasi submitted in partial fulfillment of the requirements for the degree of doctor of philosophy in electromagnetics and microwaves. The subject mainly includes microwave sensor design and applications. In all the subjects presented in this thesis, Zahra Abbasi is the main student contributor. The work is performed individually or in collaboration in paper-based format with the details as follows:

Portions of Chapters 3 has been published as Z. Abbasi, P. Shariaty, M. Nosrati, Z. Hashisho, and M. Daneshmand, "Dual-Band Microwave Circuits for Selective Binary Gas Sensing System," *IEEE Trans. Microw. Theory Tech*., vol. 67, no. 10, 2019, Z. Abbasi, M. H. Zarifi, P. Shariati, Z. Hashisho, and M. Daneshmand, "Flexible coupled microwave ring resonators for contactless microbead assisted volatile organic compound detection," in *Microwave Symposium (IMS), 2017 IEEE MTT-S Internationa*l, 2017, pp. 1228–1231, Z. Abbasi, P. Shariaty, Z. Hashisho, and M. Daneshmand, "SilicaGel-Integrated Chipless RF Tag for Humidity Sensing," *in 2018 18th International Symposium on Antenna Technology and Applied Electromagnetics (ANTEM)*, 2018, pp. 1–2, and Baghelani, Masoud, Zahra Abbasi, Mojgan Daneshmand, and Peter E. Light. "Non-invasive continuous-time glucose monitoring system using a chipless printable sensor based on split ring microwave resonators." Scientific Reports 10, no. 1 (2020): 1-15.

A portion of Chapter 4 has been published as and Z. Abbasi, M. Baghelani, M. Nosrati, A. Sanati-Nezhad, and M. Daneshmand, "Real-Time Non-Contact Integrated Chipless RF Sensor for Disposable Microfluidic Applications," *IEEE J. Electromagn. RF Microwaves Med. Biol.*, 2019, M. Baghelani, Z. Abbasi, and M. Daneshmand, "Noncontact high

sensitivity chipless tag microwave resonator for bitumen concentration measurement at high temperatures," *Fuel*, vol. 265, p. 116916, 2020, M. Nosrati, Z. Abbasi, M. Baghelani, S. Bhadra, and M. Daneshmand, "Locally Strong-Coupled Microwave Resonator Using PEMC Boundary for Distant Sensing Applications," *IEEE Trans. Microw. Theory Tech*., 2019, and Abbasi, Zahra, Masoud Baghelani, and Mojgan Daneshmand. " Highly Reliable Real-time Microwave Tire Tread Monitoring Sensor" *Under Review in Mechanical Systems and Signal Processing (2020)*.

Chapter 5 has been published as Abbasi, Zahra, Hamid Niazi, Mohammad Abdolrazzaghi, Weixing Chen, and Mojgan Daneshmand. "Monitoring pH Level Using High-Resolution Microwave Sensor for Mitigation of Stress Corrosion Cracking in Steel Pipelines." IEEE Sensors Journal 20, no. 13 (2020): 7033-7043 and Abbasi, Zahra, and Mojgan Daneshmand. "Contactless pH measurement based on high resolution enhanced Q microwave resonator." In 2018 IEEE/MTT-S International Microwave Symposium-IMS, pp. 1156-1159. IEEE, 2018.

Chapter 6 has been accepted, as Z. Abbasi, M. Baghelani, and M. Daneshmand, **"** High-Resolution Chipless Tag RF Sensor," IEEE Transactions on Microwave Theory and Techniques 68.11 (2020): 4855-4864.

In all the publications where Zahra Abbasi is the first author, she is responsible for the design, fabrication, sensing tests, data collections, and analysis. Zahra Abbasi is the sole student author of the publications, where she is the second author and extensively involved in the design, fabrication, sensing tests, data collections, and analysis. Dr. Mojgan Daneshmand was the supervisory author and involved in concept formation and manuscript composition.

To the Memory of

Mojgan Daneshmand, Pedram Mousavi, Daria, Dorina

and

all the 176 passengers of flight PS752

Acknowledgments

First, I would like to express my sincere appreciation and gratefulness to my late supervisor Professor Mojgan Daneshmand. I cannot dedicate this work to her because she is the owner of all the work. This PhD work shows a small part of her passion for science and proves how unbelievably genius she was in creating a significant project based on a simple idea. She was the best mentor that I could have, and I was lucky to learn from her how to be a good researcher and, more importantly, how to balance life and work. She trusted me and gave me a chance to work with her, and I cannot explain how lucky and privileged I feel, and it is my honor to be her student. In a field like Electrical Engineering with women in the minority, she never let me feel isolated and always pushed me to overcome stereotypes. She always told me, "you can get anything you want, just you need to work harder." She made me believed that hard work pays off by being the best example of it. I did not lose my supervisor; I lost my best friend, the only family I had far from family, and the most substantial source of encouragement and support. I am incredibly grateful for her sense of humor, patience, guidance, and mentorship. I have been in tears since January 7th and it is still unbelievable that she was in flight PS572. We will never forget; we will never forgive.

A special thanks to my mentor, friend, and advisor, Dr. Masoud Baghelani, for his unconditional support. Without him, this PhD could not be here. I will never forget his caring and continually pushing me forward for the better. He is truly a legacy Mojgan wanted to leave behind.

I would like to thank Professor Raafat Mansour for supporting me by being involved in my work in my most challenging time. His support is greatly appreciated. I would also like to thank Professor Greg Bridges, Professor Edmond Lou, Professor Vien Van, Professor Douglas Barlage, Professor Masum Hossain, and Professor Yindi Jing for serving on my committee and for their constructive criticisms and suggestions in the preparation of the final report.

Many thanks to M2M group members for their invaluable support and help, especially during the last year of my study. I am really indebted to Dr. Mehdi Nosrati, who was there for me when I needed to learn, to Dr. Sameir Deif, who always help me calm down when I was the most stressed, to Dr. Thomas Jones, who always gave me the best advice when I was confused, to Dr. Mohammad Zarifi who first taught me about microwave sensors, to Mohammad Abdolrazzaghi whose expertise never let me be worried about knowing how to use the lab equipment. I will deeply miss our long discussions. A big thanks goes to my friends Ghazaleh, Peyman, Nazli, Prof. Pedram Mousavi, Rezvan, Asal, Maryam, Ali, Elham, Negeen, Amirhossein, Mahtaab, Haniyeh, Mahsa, Brent, Navid, Sabreen, Nahid, and Hamid for the support and joy they brought to my life.

Last but certainly, the most important thank goes to my husband, Sina, for being beside me in all the sweet and bitter moments. He is truly the best thing that happened to me, and I cannot thank him enough for his kindness and teaching me to enjoy life. Without his hopeful vision on the down days of my research and encouragements on the up days, this work would be far from completion. Extended thanks go to my Mom and Dad, Mitra and Mohammad, for their support, patience, and sacrifice during my education life. My Mom was my first teacher, who taught me to be curious and not give up. I will never forget their

endless support and kindness. I want to thank my little brother, Ali, who cheered me up every single day and believing in me more than myself. I would like to thank all my family and friends for their support and kindness throughout my PhD program.

Table of Contents

Table of Figures

List of Tables

Abbreviations and Acronyms

CW	Continuous-Wave
EAC	Environmentally Assisted Cracking
EM	Electromagnetic
FID	Flame Ionization Detector
GCTL	Gap-Coupled Transmission Line
HpHSCC	High Ph Stress Corrosion Cracking
IoT	Internet Of Thing
ISF	Interstitial Fluid
LoD	Limit Of Detection
MEK	Methyl Ethyl Ketone
MFC	Mass Flow Controller
MUT	Material Under Test
NDT	Non-Destructive Testing
NIRS	Near Infra-Red Spectroscopy
NNpHSCC	Near-Neutral Ph Stress Corrosion Cracking
RFID	Radio-Frequency Identification
SAGD	Steam-Assisted Gravity Drainage
SCC	Stress Corrosion Cracking
SRR	Split Ring Resonator
UWB	Ultra-Wideband
VOC	Volatile Organic Compound

Chapter 1 Introduction

1.1 Motivation

The recent advancements in wireless sensing demands for a distant monitoring/sensing platform, which is the most compatible approach in expanding the Internet of Thing (IoT) ecosystem. Massive sensor deployment and real-time data acquisition for control, optimization, and data-driven predictions in various applications are current, and near-future IoT demands. Moreover, remote sensing is the best solution for harsh environments and inaccessible real-time monitoring, bio-implants inside the human body, drug delivery, air-quality monitoring, and pipeline integrity (high temperature and pressure media) are all among the most important applications that have been looking for non-contact real-time sensing solutions. However, more innovative approaches are needed to perform long-term and highly reliable noncontact and non-invasive sensing in out-of-access environments with different variables.

Planar microwave resonators and split ring resonators (SRRs) have been among the main configuration that achieved great deals of interest in the past two decades due to their simple fabrication process, easy integration with CMOS, lab-on-chip compatibility and flexibility in design [1]. They have been utilized for a wide range of highly sensitive measurements such as concentration study [2], biological interaction monitoring [3], [4], pH sensing [5], [6], Volatile Organic Compound (VOC) sensing [7], and chemical solutions sensing [8], [9]. The important and exciting capability of microwave sensing is their non-contact sensing ability due to the interaction of the electromagnetic (EM) field with the sensing material in the surrounding environment [7].

However, the conventional microwave sensors suffer from two major deficiencies: 1) limited sensitivity and resolution, and 2) distance-limited sensing performance. This thesis's main goal is to focus on empowering microwave sensors for highly sensitive measurements in harsh environmental conditions such as high temperature, high pressure, and/or with materials with limited accessibility at their ambient (i.e., explosive, corrosive, and toxic materials). To keep the readout circuit electronics safe in harsh environment sensing applications, the distance sensing capability has to be added to the conventional structure while enhancing the sensing resolution and sensitivity of the proposed design.

1.2 Objectives

The main objective of this thesis is to develop a new microwave sensing platform in order to enable high-resolution sensing while the material under test (MUT) is placed far enough from the readout circuitry providing proper immunity for sensing applications in harsh environmental conditions. The path to the proposed design can be divided into four different stages, as shown in Fig. 1.1:

- Taking advantage of the electromagnetic coupling between the resonators to maximize the distance between the sample and the readout circuit compared to the passive sensor. The second passive resonator that we call “chipless tag” can solve many experimental challenges such as high-temperature sensing, toxic gas sensing without being contaminated, and removing the impact of humidity.
- Combine the coupling benefits between the resonators and the ground engineered structures into a coupled reader-tag sensor to develop a distant sensing platform.

- Improving the quality factor is the other main focus of this thesis as well as being an asset for the sensor to detect ultra-small variation with the minimum error.
- Finally, by preserving the benefits of high-resolution microwave sensors and including the advantages of chipless structure, a new type of high-resolution microwave sensors is proposed based on the coupled ring resonators enabling the long distant sensing using a passive flexible SRR.

The designed sensor in this thesis offers a solution for the applications requiring distant high resolution sensing and could be a start point for a new generation of harsh environment sensing devices.

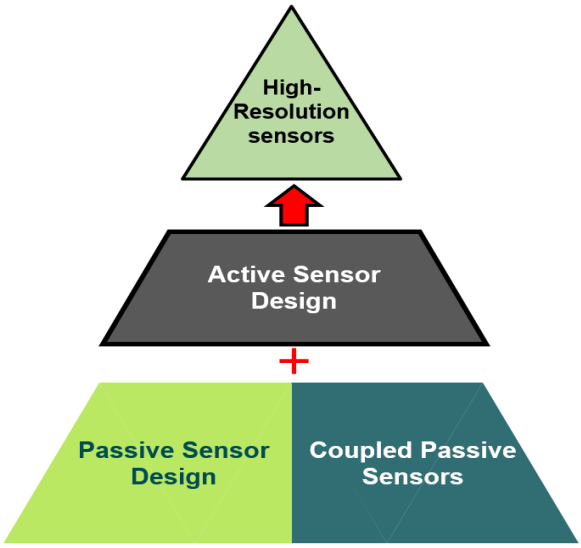

Fig. 1.1. The proposed steps for approaching high-resolution noncontact sensing.

1.3 Structure of the Thesis

This thesis has been written in a paper-based format. The entire dissertation is presented in seven chapters.

In Chapter 1, the motivations and research objectives of the thesis are introduced.

Chapter 2 presents a literature survey on the topics related to the research, focusing on the techniques for noncontact distant sensing and the capability of sensing provided by each of them and their challenges. It is followed by a brief review of the literature on ultra-high-Q active resonator designing and the theoretical analysis of their loss compensation mechanism.

Chapter 3 highlights the primary goal of this thesis and presents the coupled microwave SRR-based sensor, which enables non-contact real-time sensing. In this chapter, the benefits of SRR-based microwave planar sensors in real-time noncontact sensing are combined with a second chipless sensing element, the tag, to improve the sensing capabilities significantly while the material under test (MUT) is placed in further distance from the readout circuitry. It is shown that the proposed reader-tag pair sensor detects not only very small variations in the permittivity of the ambient, but also the implementation of the tag on a flexible substrate empowers the sensor to operate with near-zero electric power in harsh and inaccessible environments and simplifies reshaping and bending of the sensor to be mechanically adaptable with various surfaces. The proposed designs are applied to different applications that be described later in the chapter.

In Chapter 4, new coupled structures have been investigated to achieve longer distances in planar microwave sensors. It is shown that there is a positive correlation between the gap size in a pair of gap-coupled transmission lines (GCTLs) and the effective distance of the reader and sensing resonators in a planar microwave sensor. On the other hand, the coupling strength in a pair of GCTLs is negatively correlated to the gap size between the two lines, where the larger gap sizes result in weaker coupling strength or vice versa. This technique enables a sensor designer to increase the gap size in a pair of GCTLs and subsequently, the

distance between the reader and sensing resonators of the sensor. Strong electromagnetic coupling is locally demonstrated between a pair of GCTLs using a new artificial perfect electromagnetic conductor (PEMC) boundary. The proposed structure with strong localization of EM coupling is successfully utilized to design a flexible distant microwave gap-coupled resonator for humidity, Bitumen, and glycerol concentration sensing applications. The design has demonstrated the ability to sense in harsh environmental conditions by improving the distance of the flexible sensing resonator to as high as 60 mm from the readout circuitry.

Chapter 5 is devoted to the quality factor enhancement in the sensor to utilize microwave resonator armed with an active feedback loop to compensate for the sample loss and enable high-resolution microwave sensing. A passive microwave planar resonator is utilized and combined with an active feedback loop to enhance the quality factor for orders of magnitude and enable high-resolution measurements. The proposed design has been applied to pH level sensing by relating ε' and ε'' to pH values base on equations. The introduced pH sensor enabled non-invasive pH sensing using microwave sensors for the first time and by modification in design, it has been applied for early-stage pH variation monitoring to prevent steel pipeline corrosion.

In Chapter 6, the benefit of the high-resolution sensing using active feedback loop and distant sensing enabled by EM coupling between the reader and the tag are combined. The reason that makes this combination distinguishable among all the chipless tags, is the fact that the proposed sensor is capable of high-resolution distant sensing initiated by the coupling between resonators enabling sensing in a lossy environment. Designing the sensing

tag as a chipless structure minimizes the susceptibility of the design to the environmental parameters, i.e., temperature.

In Chapter 7, the significant results of this thesis work will be summarized, and some of the possible future work directions are outlined.

Chapter 2 Background

This chapter presents a literature survey on different sensing systems that have been presented in order to perform non-contact sensing. Passive microwave planar sensors will be described in Section 2.1. Section 2.2 focuses on the presented sensing platforms in the literature with the capability of distant sensing and highlights the high power consumption and low sensing resolution they offer. Chipless RFID sensors are presented in Section 2.3 as a competing technique, and finally, active resonator design for sensing applications is presented in Section 2.4.

2.1 Passive Microwave Planar Sensors

Microwave sensors can be used to evaluate the changes of the MUTs close to them, such as soil moisture sensing, and this proximity to the MUT controls its sensitivity. Microwave sensors were developed in various industries, including remote sensing, medicine, and material sensing [3], [10]–[16], studying nanotube structures [17]–[19] to compensate for the lack of enough sensitivity provided by other technologies.

Since resonance-based sensors offer high resolution sensing performance, they achieve great deals on interest in the sensors research community. Planar microwave sensors are privileged of small size, ease of fabrication, low-cost, and lightweight properties compared to different microwave cavity resonators and micro-cantilever-based sensors. Open-ended half-wavelength resonators are modified as SRR and widely used as sensing elements due to their high-quality (Q) factor and small size.

These resonators are integrated into many microwave circuits such as filters or oscillators. The resonant microstrip section of these sensors is the open-/short-ended quarter-/half-/full

wavelength in size. Multiple harmonics of the fundamental frequency of resonance can also be found in the transmission response of the sensors due to their accommodation in the same ring/split-ring. The half-wavelength sized sensors are governed by the following expression for their resonance frequency:

$$l = \frac{nc}{2f\sqrt{\varepsilon_{eff}}} \qquad (2\text{-}1)$$

where c is the speed of light, f is the frequency and ε_{eff} is the effective permittivity of the substrate and the surrounding medium.

Using the planar micro-strip design, one can perform the measurements in a non-invasive manner using the propagation of the electromagnetic waves into free space and its interaction with the MUT around it. Material-assisted techniques can improve the sensitivity and resolution of the microwave sensors. Fig. 2. 1(a) shows the simplest structure for an SRR that has been used as a gas sensor. A simple SRR at 5.5 GHz is shown to provide a highly sensitive region exploited in detecting different concentrations of VOC in the air stream (Fig. 2. 1(b)) [10]. Using an adsorbent as a sensing medium signifies the effect of permittivity variation. The permittivity of adsorbent changes due to its interaction (i.e., adsorption) with the target compound. This permittivity variation, however, depends on the concentration of the mixture in the gas stream. Therefore, the concentration of a specific adsorbate in the gas stream can be measured using the microwave sensor by correlating the variations in permittivity to the adsorbate concentration. In another reported design for VOC sensing, the microwave sensor has been coated with a thin layer of polydimethylsiloxane (PDMS) which acts as an adsorbent layer that signifies the resonance frequency variation (Fig. 2. 1(c)). Stronger localized E-fields around the material under the test (MUT) using

circuit design techniques, empowers the sensor to demonstrate more variations observed at the output and leads to sensitivity enhancement and error cancellation of the microwave sensors. An excellent example of modifying the microwave sensor to cancel temperature and humidity effects while increasing the sensitivity is presented in Fig. 2. 1(d). In this structure, using doubled SRR on each side, the sensor's hotspot area is increased. Since the two resonators on each side of the microstrip line are isolated, one can be used as the reference for sensing, which helps in canceling unwanted effects [20].

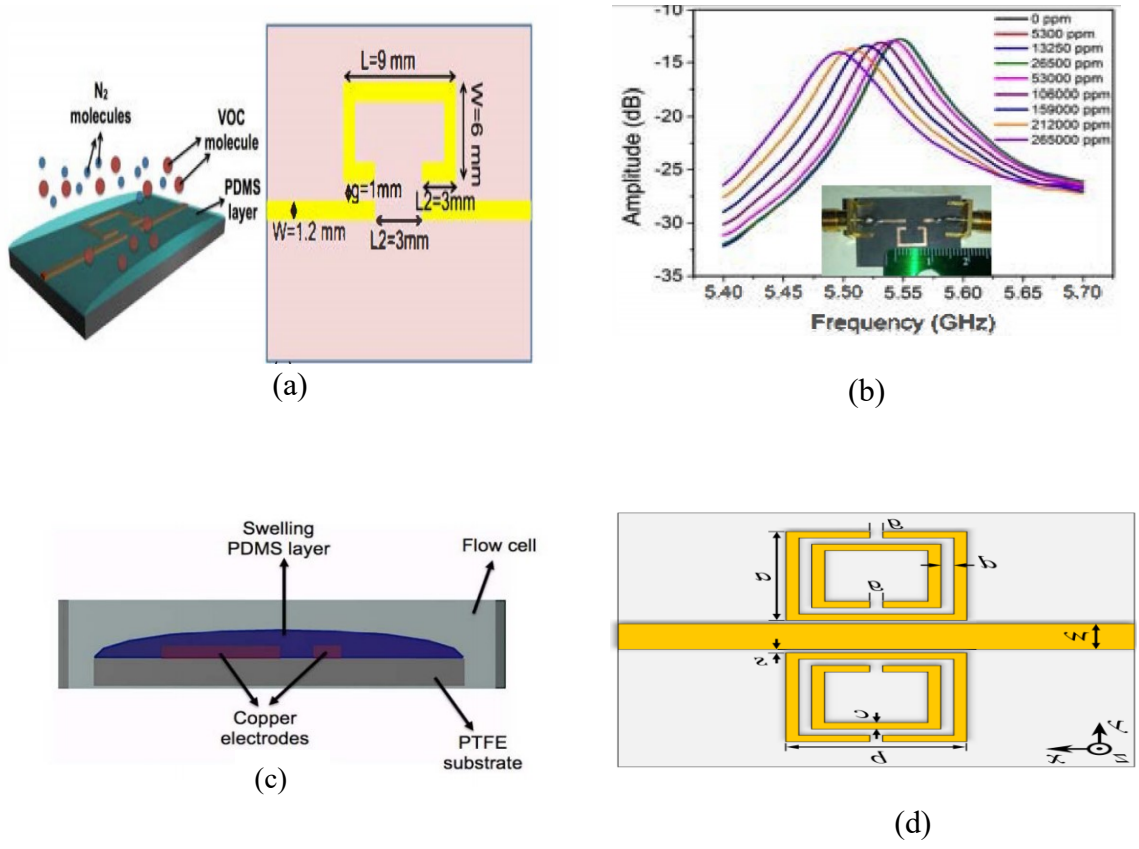

Fig. 2.1 (a) The proposed PDMS-covered microwave ring resonator alongside its critical dimensions [10] (b) measured results for various VOC concentrations. The inset shows the actual device used in this study. [10] (c) Contact mode gas exposure method. [21](d) the layout of the SRR-based sensor yellow areas indicating the metallization and gray showing the dielectric substrate [20].

Passive microwave resonators can be coupled to increase the dynamic range for sensing as proposed in [22]. The sensing platform consists of two capacitive or inductive coupled

planar SRR, as shown in Fig 3(a). The SRRs are magnetically coupled to the input and output signal line, while the two rings are electrically coupled to each other. For the inductive coupling structure, the two rings are magnetically coupled to each other, while a capacitive coupling establishes a link to the signal input/output lines. These rings are highly coupled in both capacitive and inductive coupled structures. This can create a coupled-resonator with two resonant frequencies in its frequency profile. The distance between two resonant frequencies in each coupled resonator's resonance profile is adjustable by changing the structural parameters that control the coupling factor between the rings. Simulation results in Fig. 2.2 (b) present the effect of varying the coupling gap (gr) between the rings on the resonant profiles of the presented structures in Fig. 3(a) [23].

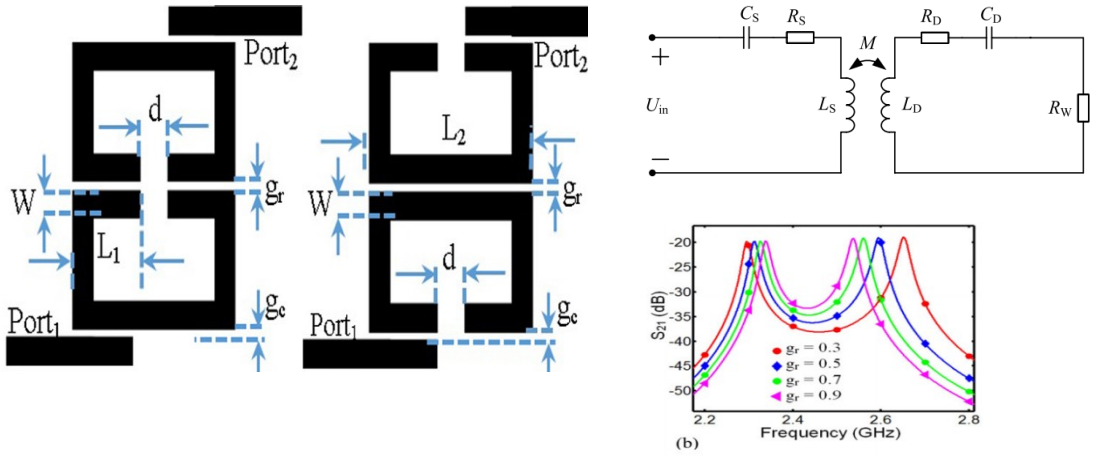

(a) (b)

Fig. 2.2 (a) Planar coupled-resonator sensor structure for capacitive coupling (right) and inductive coupling (left). (b) The equivalent circuit model, including the mutual coupling and inductively coupled resonators as the coupling, varies [22].

2.2 Non-contact Sensing Based on Scattering and Reflection

Researchers have demonstrated the feasibility of radar-based sensing systems for detecting or monitoring various parameters in many applications such as diagnostic tools in the biomedical field [24], respiratory-rate measurement, rescue tools for finding survivors

buried under snow cover [25], security devices [26], agricultural systems, and environmental applications. Several radar systems have been proposed in the literature for detecting vital signs, e.g., Continuous-Wave (CW) and Ultra-Wideband (UWB) radars. As reported in the literature, the performance of these radar-based systems is strongly dependent to the performance of the antennas. In this sensing method, the goal is to find some guidelines in choosing the antennas for such systems for improving the accuracy and decreasing the dependency to the environmental factors. One of the recent applications of this sensing method is respiratory-rate measurement. Different types of antennas with different radiation properties such as antenna directivity, gain, and cross-polarization levels have been used in the literature, and three of them have been tested in [27], [28] to show the capability of this sensing technique for respiratory-rate measurement (Fig. 2.3(a)). Mimicking the chest wall movement (by imitating human respiration) has been stimulated by the moving plate shown in Fig. 2.3(b). In this sensing system, the mechanical setup was programmed to perform a simple back-and-forth motion toward the fixed position radar. At this stage, the main goal was to compare and quantify the antenna performance and its effect on system accuracy. The controlled moving unit was placed in front of the antennas attached to the radar.

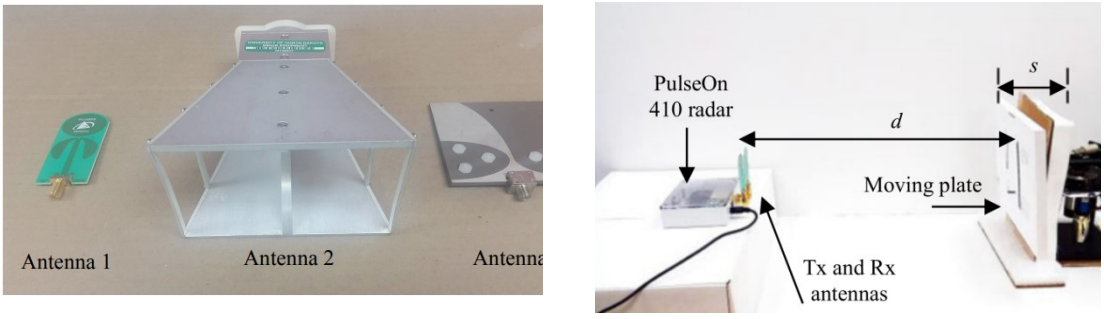

Fig. 2.3 (a) three different antennas used for the radio link of the system (b) Experimental setup for measuring the movement of a controlled mechanical-based moving unit.

This system provides the ability of long-distance sensing with very high precision. Besides the benefit of far-field sensing in this category of sensors, there are some challenges that should be mentioned. One of the major problems in this structure is the huge field of view for sensing, which makes detection of very small variation difficult as well as being vulnerable to the unwanted environmental variation. This system is also not capable of being integrated and being used as a wearable device. Additionally, since the sensing is occurring based on the doppler effect and not the coupling, the high-resolution sensing could not take place.

2.3 Chipless RFID Sensors

Conventional RFID system interrogates RFID tag with a silicon integrated circuit (IC) to identify objectives, where a microprocessor and a memory are included in silicon IC so that a large amount of data can be read (Fig. 2.4 [29]). However, the use of silicon IC in an RFID tag may restrict the versatility of RFID. The main reasons are some economic factors (e.g. the tag cost) and the fact that RFID tags are not able to be applied to harsh environment applications since the electronic circuit of them adds limitations to the design. Eliminating the IC in RFID tag leads to a chipless RFID tag [30]. Contrary to a conventional RFID tag, a chipless tag needs neither a chip integrated circuit (IC), nor self or remote power supply and the manufacturing process becomes very compatible with printing techniques, which means that chipless tags can be directly printed results in very low costs (Fig. 2.5a)) [31], [32]. Moreover, the chipless RFID tag retains the advantage of a large read range in a non-line-of-sight circumstance that the traditional RFID designs have. Also, chipless RFID systems may find exciting applications, such as identifying objects in the harsh environment [31], [33], [34] e.g., pipeline coating integrity [35]. As we can see in Fig. 2.5(b), the flexible

chipless tag contains transmit/receive antennas that communicate the environment's variation around the tag to the reader antennas.

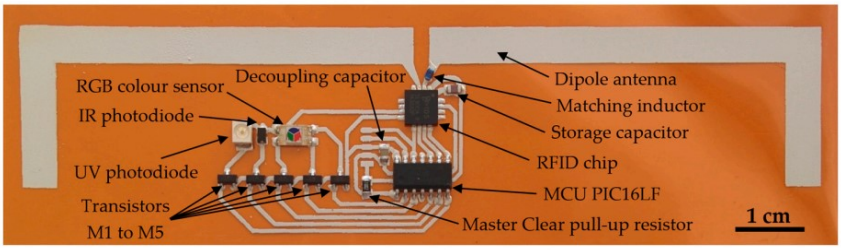

Fig. 2.4. A sample circuit is representing an RFID tag, including the active circuit.

As the concentration of the salt in the water around the pipeline changes, results the variation of permittivity and conductivity, which can be detected by the tag and can be transmitted to the receiver antennas [35]. Chipless RFID sensors can be designed to measure minimal variations while having the great capability of non-contact sensing. Chipless RFID sensors consist of reader antennas, chipless tag, as the sensing element, and tag antennas. The sensing is performed based on the transmission and receiving any variation around the passive tag using antennas and not the electromagnetic coupling. This work aims to design a high-resolution sensing platform, which enhances the distance sensing potential based on the coupling between the resonators. However, chipless RFID structures are not suitable for being integrated to perform high resolution since there is no coupling between the reader and the sensing element, and the communication between the reader and the chipless RFID tag requires antennas.

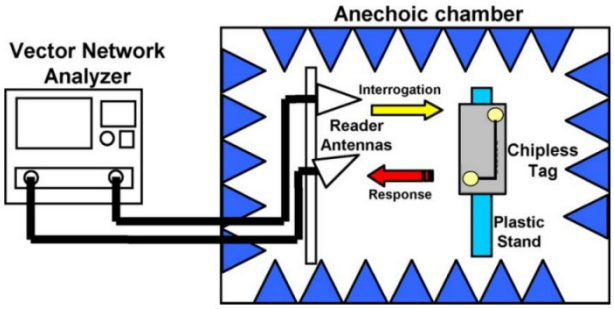

(a)

(b)

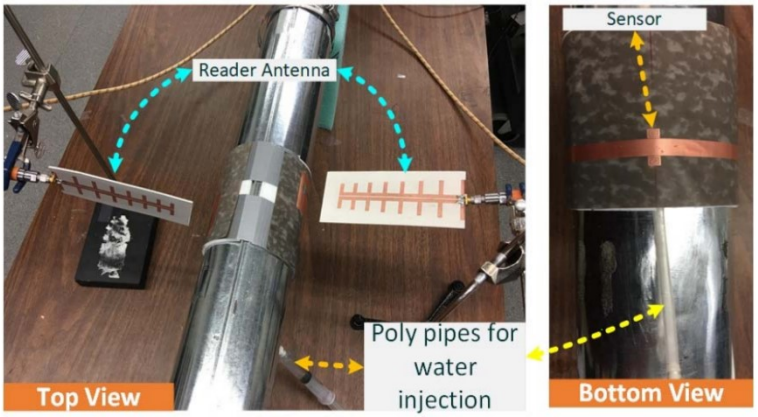

(c)

Fig. 2.5. (a) Block diagram chipless RFID tag experimental setup [31] (b) Integrated system including a sensor and receives antennas [35] (c) In-lab measurement setup shows the passive tag attached to the pipe structure [35].

2.4 Active Microwave Sensors

In this section, a literature review of active sensors will be presented. Initially, active resonators and the Q-factor improvement methods are explained, and then their application in designing high-resolution sensors are reviewed.

2.4.1 Active Resonators and Basics of Loss Compensation Mechanism

An important parameter that can be used as an indicator of a resonator's performance is the Q-factor. The Q-factor is defined as the ratio of the resonant frequency to the bandwidth of the resonator and plays a critical role in the determination of sensing resolution and Limit of Detection (LoD) of a sensing platform [11], [36]–[39]. Although planar microstrip resonators have demonstrated outstanding potential in sensing liquid materials, they suffer from low resolution and quality factor. A microwave device with a high-quality factor can lead to a sensing platform with higher resolution than its conventional counterparts, as shown in Fig. 2.6 [38]. Since the highest level of Q-factor is desired, a technique should be used to minimize the loss in the circuit and to provide a sharp resonance. The loss compensation mechanism employed in this work is embedding a positive feedback amplifying loop around the resonator, which demonstrates promising results for increasing the quality factor.

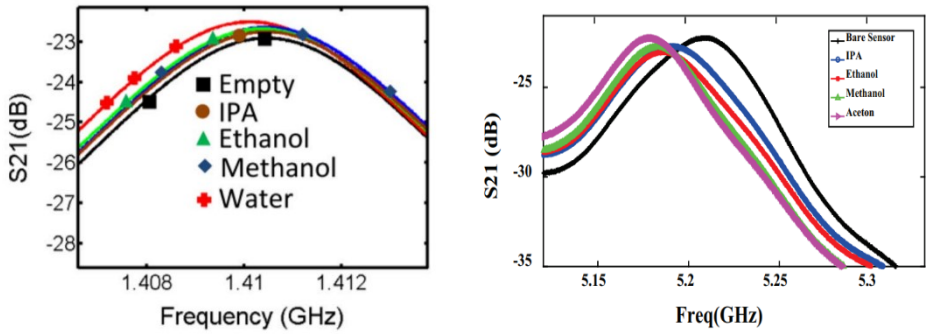

Fig. 2.6. Lack of enough resolution and sensitivity in a passive sensor leads to unsuccessful liquid sensing [38].

Using an amplifier circuit as an active feedback loop can compensate for the loss in microwave resonator. The transmission response will be very high-Q compared to the passive resonator (Fig. 2.7(a)). The structures consisting of

passive microwave resonators combined with active circuitry to enhance their Performance has been previously studied for communication applications, as shown in Fig. 2.7(b). The voltage gain of the amplifier is denoted with A_0, and the gain of the feedback path presented with β. Elementary feedback theory suggests that the regenerative-amplifier gain is:

$$A = \frac{A_0}{1-A_0\beta} \qquad (2\text{-}2)$$

The regenerative amplifier's maximum gain occurs when the denominator of the (2-2) is small. Additionally, the condition $A_0\beta > 0$ means that the feedback is positive, whereas $A_0\beta < 1$ is necessary to keep the loop gain below the oscillation threshold since the oscillation occurs at the frequency point the closed-loop gain is unity.

2.4.2 A Short Review of Active Microwave Sensors

There has been effort toward this generation of resonators for sensing and proving its capability as microwave sensors. High-quality factors, a translation of low electromagnetic losses, can increase the resolution of the microstrip resonator sensor and relax the requirement for a close physical distance of the medium and the sensor, therefore, enabling contactless measurements. This becomes more important in chemical sensing, noting that MUT usually generates a considerable amount of loss that should be compensated in the sensor.

With assistance from the positive feedback loop coupled with the SRR-based sensor, as it is shown in Fig. 92.8(a), the sensor’s quality factor can be retrieved and regenerated while applying to microwave sensing applications (Fig. 2.8(b)) [5].

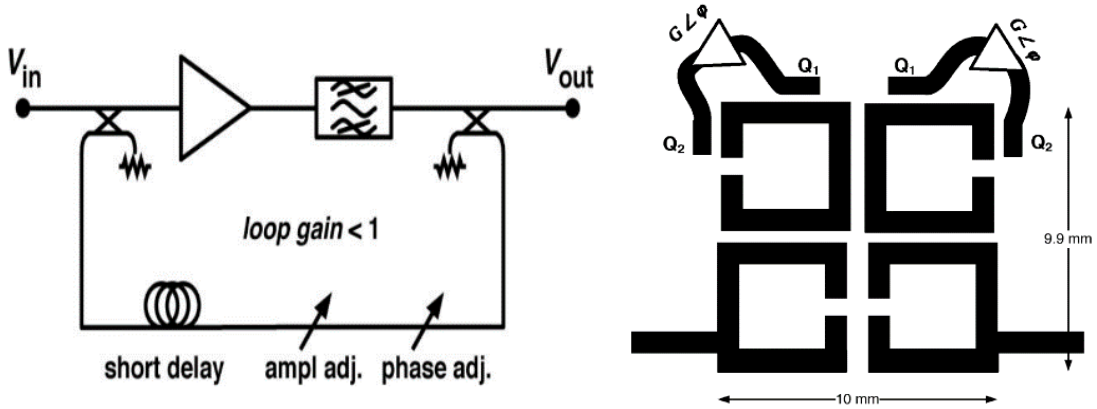

(a) (b)

Fig. 2.7. (a) regenerative (positive-feedback) amplifier [40]. (b) Active four-pole elliptic-response bandpass filter designed for low phase-noise oscillator applications. Only the two middle resonators are loss compensated [41].

In [38], a high-resolution liquid sensor was developed using active feedback. The sensor architecture consists of a planar ring resonator microwave microstrip resonator, and the length of the micro-strip line determines the resonance frequency of this resonator. This passive structure has a moderate quality factor (220 in measurement, 240 in simulation). An active feedback loop with an active device (BJT-Transistor) is added to the passive resonator, and this regenerative feedback loop creates a 180-degree phase shift on its output, and another 180-degree phase shift is introduced by the passive resonator. Therefore a constructive (positive) feedback is created around the passive resonator, which compensates for the power loss and increases the quality factor. The fluid flow path will go through the gap designed to coincide with areas of high field intensity to maximize interaction with the microwaves (Fig. 2.9(a)). Fig. 2.9 (b) shows the resonator schematic with a transistor amplifier in feedback to compensate for the loss.

Another application for active microwave sensors was presented in [42] for asphaltene nano-particle deposition sensing, where very small variation is important to be detected to have more cost-effective oil and gas production to refining stages. As shown in Fig. 2.10,

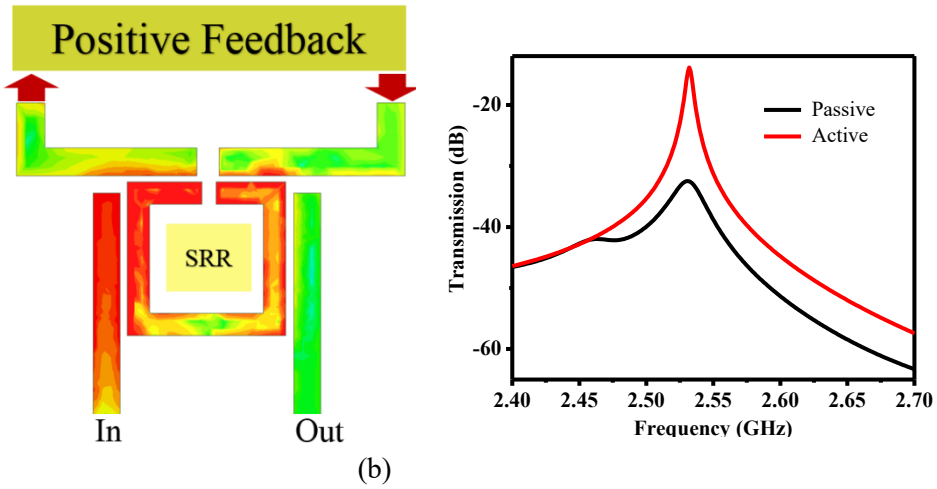

Fig. 2.8. (a) Conceptual Active Resonator with loss compensation schematic (b) Quality-factor improvement in the active resonator

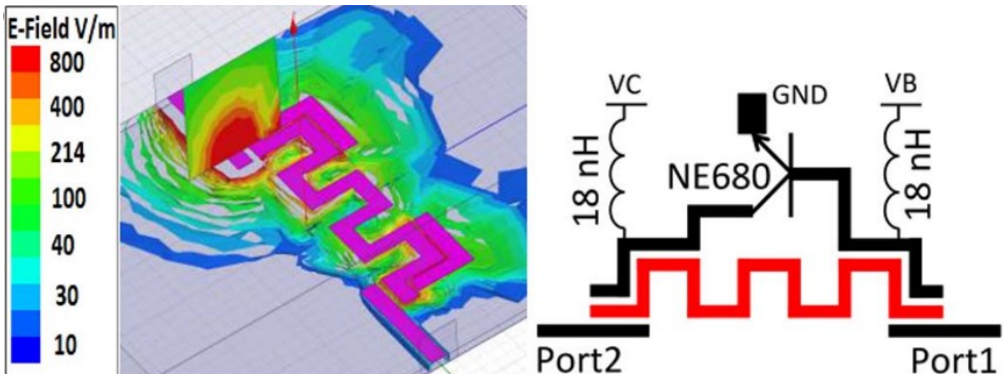

Fig. 2.9. (a) Field distribution in the active sensor's hotspot and (b) active microwave senor schematic including the transistor amplifier [38].

dual active resonator with two hotspots is designed and experimented with monitoring deposition rate is shown. The tube is extended enough after the first SRR to provide a reasonable distance in time for the resonators to identify two considerably different profiles due to deposition. When the liquid's flow rate is slow enough inside the tube, particle deposition occurs, and the variation of each resonance would be different from each other.

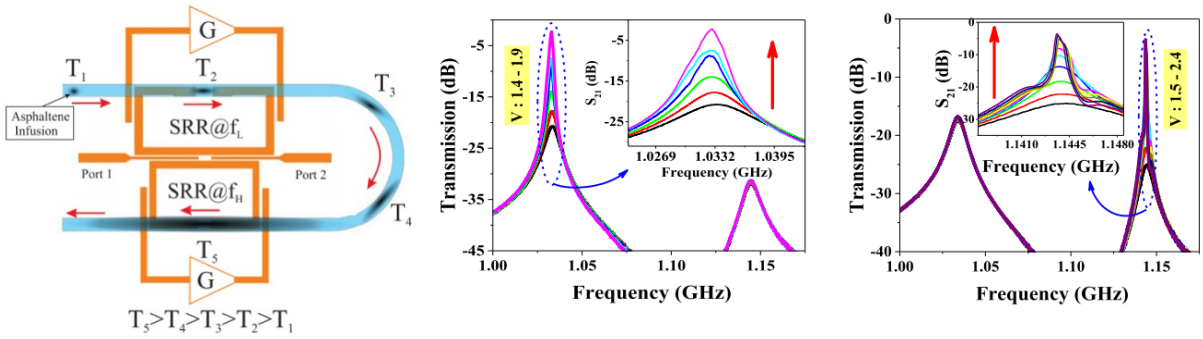

Fig. 2.10. (a) Schematic of the test setup for dispersion characterization, (b) Quality factor improvement in lower and (c) higher resonance frequency.

Chapter 3
Coupled microwave Split Ring Resonators

Besides all the numerous applications of the conventional SRR-based sensors presented in Chapter 2, they suffer from problems such as distance-limited sensing performance and low sensing resolution [43]. Different approaches and structures have been reported to enhance the performance of the conventional planar microwave structures as a sensing device; however, there is a need for a simple, inexpensive structure to increase the sensing distance and sensitivity.

In this section, we are presenting coupled microwave SRR-based sensors that enabling non-contact real-time sensing. This thesis's primary goal is to develop a new type of microwave sensing platform that enables sensing while improving the sensitivity and minimum detectable level significantly. In this chapter, the benefit of SRR-based microwave sensors in real-time noncontact sensing is combined with a second chipless sensing element, the tag. The tag resonator's presence produces significant improvement in sensing while the under test material is placed in further distance from the readout circuit electronics. It is shown that the proposed reader-tag pair sensor not only detects very small variation in the permittivity of the ambient but also the implementation of the tag on flexible substrate makes the design user-friendly and empowers the sensor to operate with near-zero electric power in harsh and inaccessible environments.

The organization of the chapter is as follows. Section 3.1 begins with introducing the proposed single tag structure following by the theoretical investigation and circuit model

of the proposed coupled tag-reader design, including the detailed discussion on the impact of circuit elements of the developed model in Section 3.2. The design, simulation, and measurement results of a coupled sensing structure are provided in Section 3.3, along with a detailed study to examine the sensing capability of the design is performed to illustrate the impact of distance between the tag and the reader resonators, permittivity variation of the MUT, and misalignment between the reader and the tag. In Section 3.4, some of the applications enabled by the reader-tag coupled sensors are described in detail. The proposed structure shows promising results in gas concentration monitoring and non-invasive glucose sensing.

3.1 Proposed Tag-Reader Structure at a Glance

The simple form for the conceptual sensor schematic is shown in Fig. 3.1. The sensing tag's flexibility enables it to be easily mounted on various shape chemical and environmental reactors. Simultaneously, the reader ring resonator establishes a wireless connection between the tag and the readout circuitry. The proposed robust microwave sensor can detect very small variation in the electrical property of the medium around the chipless tag. The proposed sensor's main sensing element is a ring-shaped copper trace designed for a specific frequency range based on the application. Since the sensor is constructed of two resonators, there are two peaks and notches in the spectrum. As shown in Fig. 3.2, the sensor contemplates the medium's variations to the tag depending on the sensor mounting location. Variations in the material's permittivity in the regions are subjected to higher concentration electromagnetic fields and have more contribution to frequency shift.

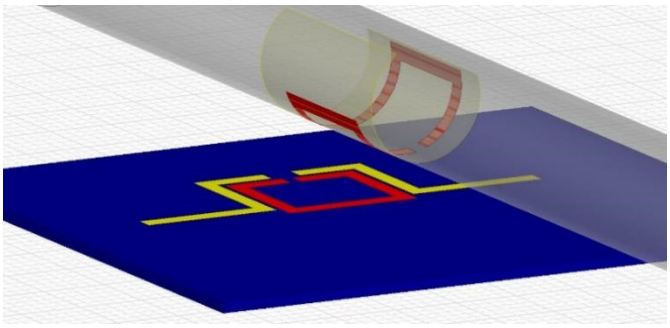

Fig. 3.1. Conceptual sensor with a reader resonator and chipless tag resonator.

Fig. 3.2 presents the perspective view of the field concentrations of the chipless microwave sensor. As shown in Fig. 3.2 (a), in the traditional microwave ring resonator, the field is concentrated between the resonator and its ground-plane. Therefore, the substrate plays the most important role in determining the resonance frequency. Also, the field concentration on top of the sensor, which usually considered as the sensing area

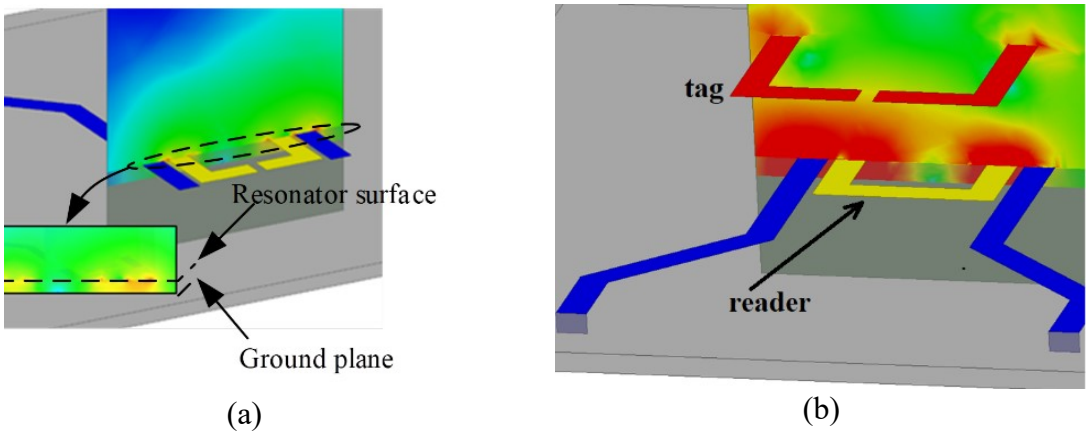

Fig. 3.2. (a) The field concentration of a traditional microwave ring resonator; (b) perspective view and field concentration of the resonator, it could be seen that the fields around the tag is almost constantly distributed in both on top (where material-under the test is placed) and underneath (where could be considered as its substrate). Therefore, one could expect a higher frequency dependency of the tag to the MUT, which could be translated to higher sensitivity compared to traditional microwave resonator sensors.

is smaller which limits the sensitivity of microwave resonator-based sensors. On the other hand, the presence of the secondary tag resonator coupled to the reader modifies the field distribution around the circuit and increases the field intensity in further distances from the reader resonator circuit. This relatively small, but high impact, increasing the distance

between the reader and the tag makes the proposed design a great candidate for wearable and harsh environment sensor structure.

3.2 Theoretical analysis and circuit Model

The basic element for the proposed work is a split ring resonator, which has the advantages of a low profile and compact size design. The conventional SRR integrated with two gap-coupled micro-strip lines is used as the readout circuit (Fig. 3.3(a)). The *LC* circuit modeling is found to be very useful in analyzing and control the behavior of the EM structure for the final sensing system. Considering the SRR coupled to micro-strip lines as the readout circuit, the structure is designed on a 0.79 mm thick substrate with a dielectric constant of 2.2. Fig. 3.3(a) shows the lumped element equivalent circuit of the readout circuit. The input and output microstrip transmission lines are modeled by two Π C_{μ}-L_{μ}-C_{μ} circuits with a capacitive coupling of $C_{c\mu}$ in between [44]. On the other hand, the SRR is modeled by two cascaded Π C_r-L_r-C_r circuits at λ/2 and the capacitive coupling of C_{cr} standing for the coupling at the two ends of the resonator [44]. Including the loss, the resonator and micro-strip lines are coupled through two capacitors and resistors ($R_{c\mu r}$ and $C_{c\mu r}$). Equations given in [13] are utilized to calculate initial values for C and L and slightly fine-tuned to match the simulations. Fig. 3.3(b) compares the EM and LC performances of the resonator over a wide frequency band including the transmission pole and zero of the structure. The quantities of all the components after fine tuning resulted in a good agreement between the two EM (HFSS, finite element method) and *LC* (ADS Agilent) performances. The readout circuit demonstrates a transmission pole at f_0=4.86 GHz.

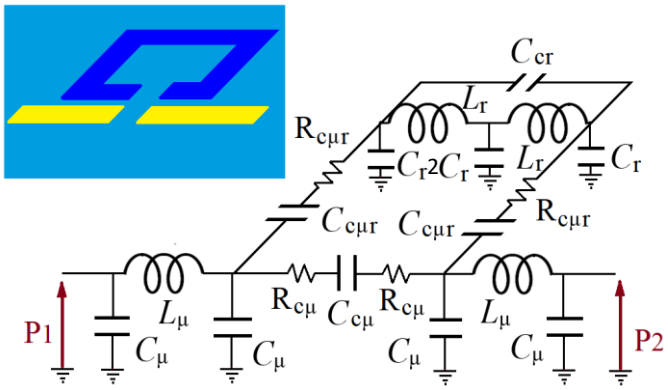

(a)

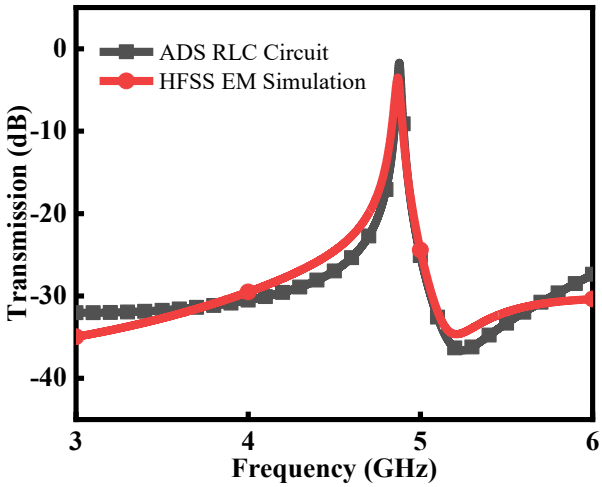

(b)

Fig. 3.3 (a) Distributed- and lumped-element circuits of the coupled reader-only resonator and microstrip lines (b) Wide-band EM (HFSS) and LC (ADS) performances of the structure.

Equations given in [44] are utilized to calculate C and L's initial values and slightly fine-tuned to match the simulations. Fig. 3.3(b) compares the resonator's EM and LC performances over a wide frequency band, including the transmission pole and zero of the structure. The quantities of all the components after fine-tuning are shown in Table 3.1, which results in a good agreement between the two EM (HFSS, finite element method) and LC (ADS Agilent) performances. The readout circuit demonstrates a transmission pole at f_0=4.86 GHz.

Table 3.1 Simulated Lumped Model Parameters For Split Ring Resonator in ADS

Parameter		PARAMETER	
Ccr (pF)	0.135	Lμ (nH)	0.198
Lr (nH)	0.706	Ccμ (pF)	0.7
Cr (pF)	0.722	Cμ (pF)	4.35
Ccμr (pF)	0.525	Rcμ (Ω)	10
Rcμr (Ω)	0.28		

For our desired coupled tag to be created, the structure is integrated with another passive SRR (tag) through EM coupling to sense and detect a material. The EM behavior of the integrated readout and tag resonators is similarly modeled using lumped element equivalent circuit. Fig. 3.4(a) schematically shows the tag resonator coupled to the reader resonator. The tag resonator is arranged in such a way to realize a mixed EM coupling between the two resonators. The EM waves through the inductors of tag resonators are coupled to the capacitors of the reader resonator to realize the mixed EM coupling (Fig. 3.4(b)). Fig. 3. 4(a) shows the lumped element equivalent circuit of the integrated structure. The SRR in the tag is similarly modeled with two cascaded Π C_t-L_t-C_t circuits at λ/2 and the capacitive coupling of C_{ct} standing for the coupling at the two ends of the resonator [21]. As shown in the circuit, the mutual coupling between the tag and the reader resonators is modeled with three C_{crt} capacitors, the mutual coupling between the inductors (L_t and L_r) with the coupling coefficient of k=0.12, and the loss (R_{crt}). Both electric and magnetic field distribution between the two resonators are shown in Fig. 3.4(b). It offers a vertical view of the magnetic field when there is a 5 mm distance between the sensing tag and the reader resonator. Fig. 3.4(c) shows a vertical view of the magnetic field when there is 5 mm distance between the sensing tag and the reader resonator.

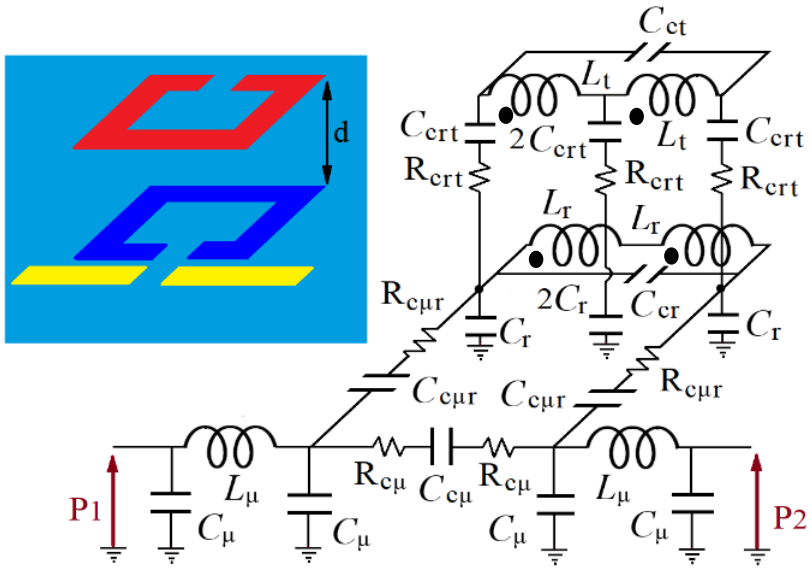

(a)

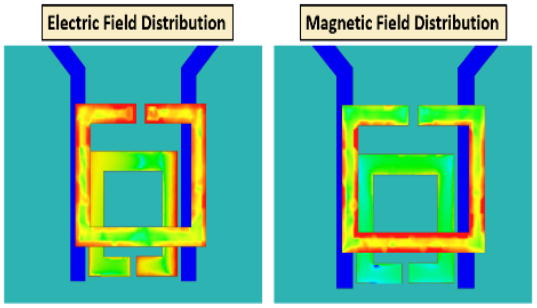

(b)

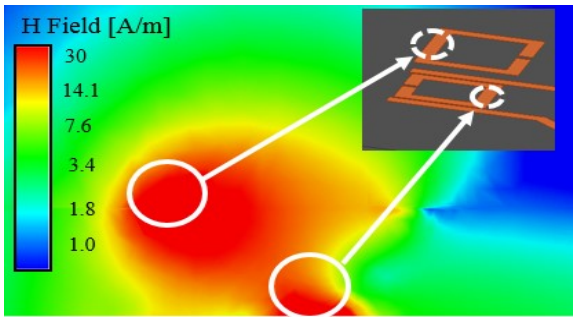

(c)

Fig. 3.4. (a) Distributed- and lumped- element circuits of the coupled tag-reader resonators. (b) Top view EM field distribution between the two resonators. (c) HFSS simulation, studying magnetic field distribution around the sensor. Inductive coupled areas demonstrate higher field intensity than the others.

Fig. 3.5(a) compares the EM and LC performances of the integrated tag-reader resonators over a wide frequency band. A good agreement is observed between the two EM (HFSS) and LC (ADS Agilent) performances. Adding Material Under Test (MUT) over the tag reader affects the quantity of C_{ct} and as a result, the frequency shift appears in the transmission response (Fig. 3.5(b)). The readout circuit demonstrates two transmission poles at f_0=4.86 GHz and f_{r1}=4.02. The parameters for the circuit model after fine tuning are presented in Table 3.2.

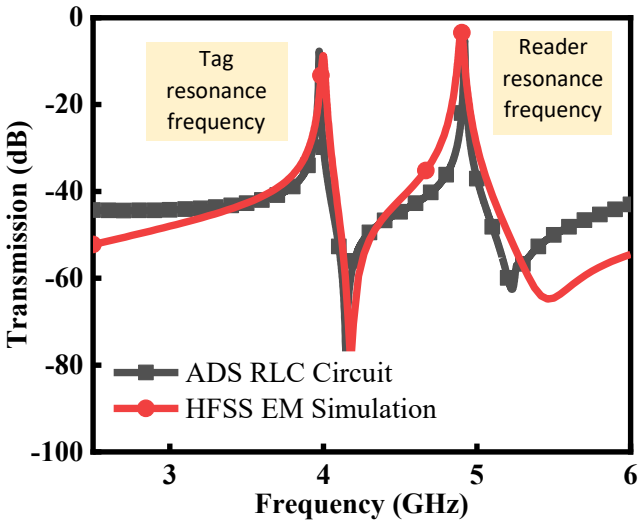

(a)

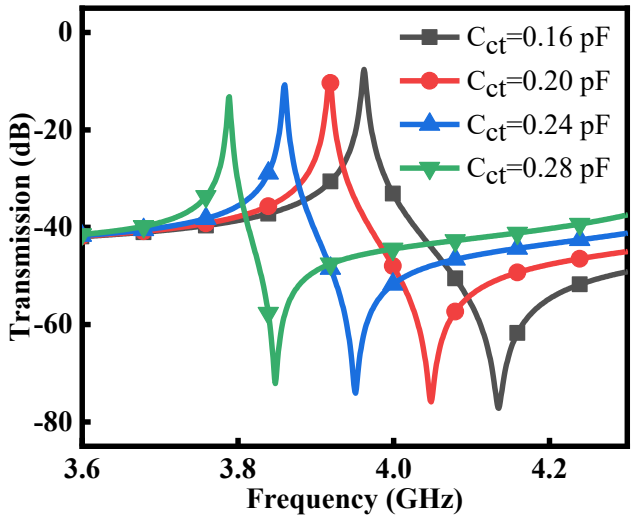

(b)

Fig. 3.5(a) EM (HFSS) and LC (ADS) performances of the coupled structure. (b) Sensing simulation results when the permittivity of MUT changes (which affects C_{ct} to be changed).

The strong electromagnetic (EM) coupling between the two SRRs on each pair of tag-reader resonators enables the expansion of this structure to two-stage design, including two reader resonators and two tags, which will be explained in the next section. Although the sensors are generally calibrated before the operation to their initial state, understanding the impact of the position (i.e., distance, alignment, tilt) on the sensor's sensing results and performance are important.

Table 3.2 Simulated Lumped Model Parameters For Coupled Reader and Tag Resonators in ADS

Parameter		PARAMETER	
Ccr (pF)	1.018	Ccμ (pF)	0.7
Lr (nH)	0.465	Cμ (pF)	6.02
Cr (pF)	0.1175	Rcμ (Ω)	10
Ccμr (pF)	0.525	Cct (pF)	0.16
Rcμr (Ω)	0.05	Lt (nH)	1.53
Lμ (nH)	0.141	Ccrt (pF)	0.51
		Rcrt (Ω)	0.23

EM simulation results for the effect of the distance between the reader and the tag resonators is presented in Fig. 3.6(a). As it is shown, by increasing the distance between the tag and the reader from 5 mm to 12 mm, the peak amplitude drops. Although the resonant frequency is detectable even up to 12 mm distance; however, the quality factor reduces by distance. Additionally, the *LC* simulation illustrates similar behavior while the distance changes since the distance is reversely proportional to the coupling between the tag and the reader, which is modeled in the circuit by C_{crt} capacitors.

The lower-Q response of the system could also be used for non-contact sensing applications. However, for the applications requiring a high sensitivity level, it is recommended to place the tag in 3 mm to 10 mm distance. Fig. 3.6(b) demonstrates the resonance profile variation if the tag and the reader, which are place in the vertical distance of 5 mm (d = 5 mm), experience misalignment in x or y direction. The longest dimension of the tag is 10 mm, and for misalignment analysis, 30% of the 10 mm, which is 3 mm movement in x or y direction, is considered. As shown in Fig. 3.6(b), the results show a negligible impact on the sensor reference point. Tilting the tag while the reader is fixed in 5 mm vertical distance from the reader is another important simulation that has been done to confirms the sensor's sustainability, which is presented in Fig. 3.6(c).

It is worth noting that the sensors are generally calibrated to their initial state and therefore, a slight change of parameters at their reference point does not impact their time-based measurements such as the ones presented here.

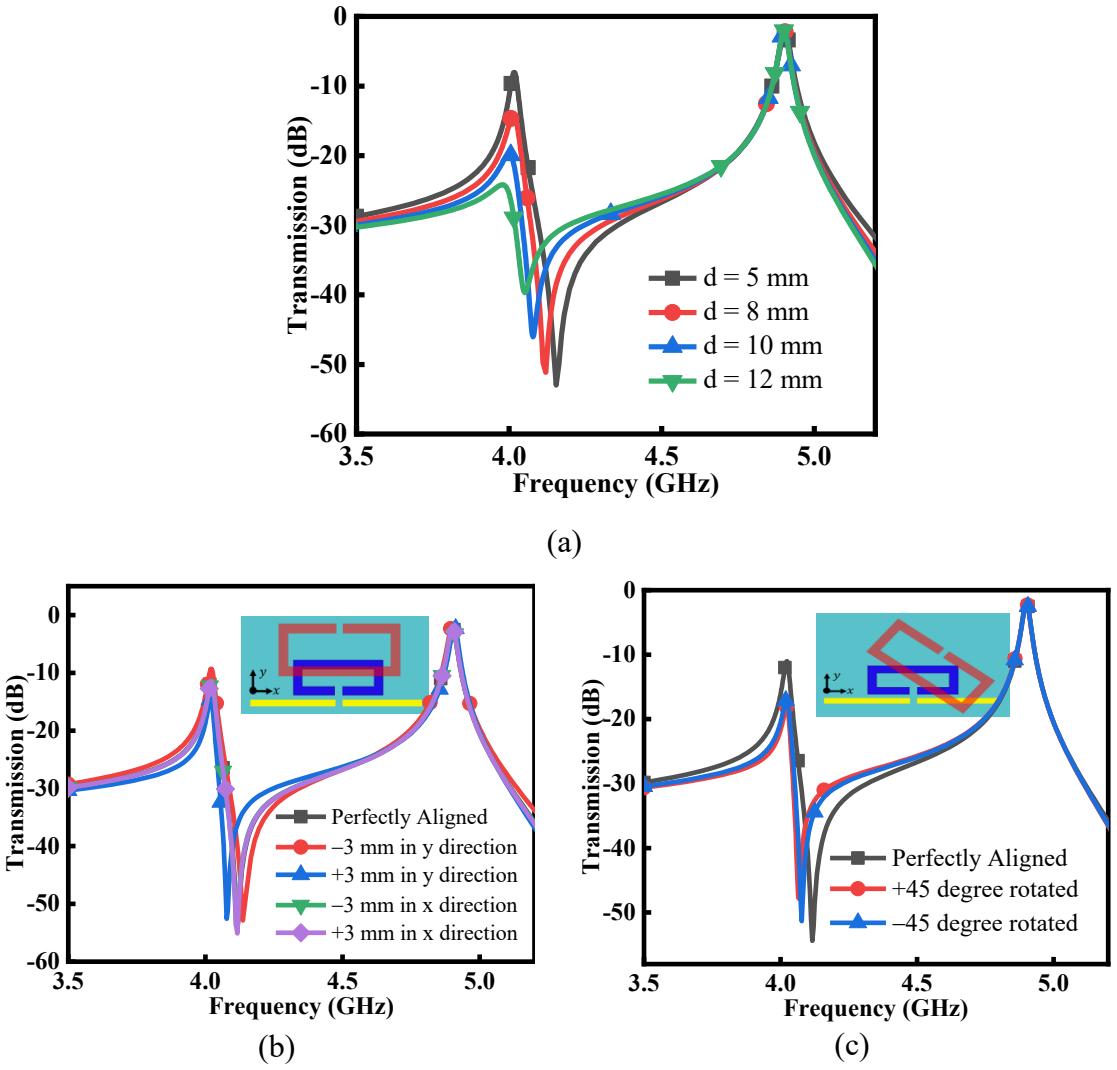

Fig. 3.6. Simulation results illustrating the sensor behavior when (a) the tag and the reader distance changes from d = 5 mm to 12 mm, (b) the tag is miss-aligned and, (c) tag is rotated ± 45 degrees (the top view of the tag-reader pair is included).

3.3 Simulation of Sensing Enhancement in Coupled Resonator Structure

Considering frequency shift as the main output parameter for the sensor, sensitivity could be defined as the frequency shift versus permittivity variations of MUT for a certain volume.

Since each research uses arbitrary container volume and shape for having a meaningful understanding of sensitivity improvement in the proposed sensor, a comparison between traditional microwave resonators and the current introduced sensor designed at the same frequency is presented here. As illustrated in Fig. 3.7., a superficial material with specific volume and shape covering the whole area of both resonators with $\varepsilon_r = 4$ is introduced as MUT. The frequency shift resulted from relative permittivity variation to 10 for the proposed sensor is 700 MHz, which is more than 3.5 times higher than the frequency shift for the traditional resonator. Limited sensitivity of the traditional resonator is as the result of confined electromagnetic fields between the resonator and its ground plane (see Fig. 3.2 (a)). In conventional resonators, because of this phenomenon, the substrate has a more important role in defining the resonance frequency rather than MUT. Because of removing the substrate for the tag in the presented work, the main variable parameter defining the resonance frequency of the tag is the MUT permittivity. For studying this concept, another simulation has been accomplished for both conventional and presented resonators. As depicted in Fig. 3.8, different substrate permittivity has been used with different permittivity for MUT for both traditional and the proposed sensors. It could be seen that, for traditional resonator sensors, substrate permittivity is the dominant parameter in determining the resonant frequency of the structure while the impact of substrate permittivity variations on the proposed sensor is very small and even negligible.

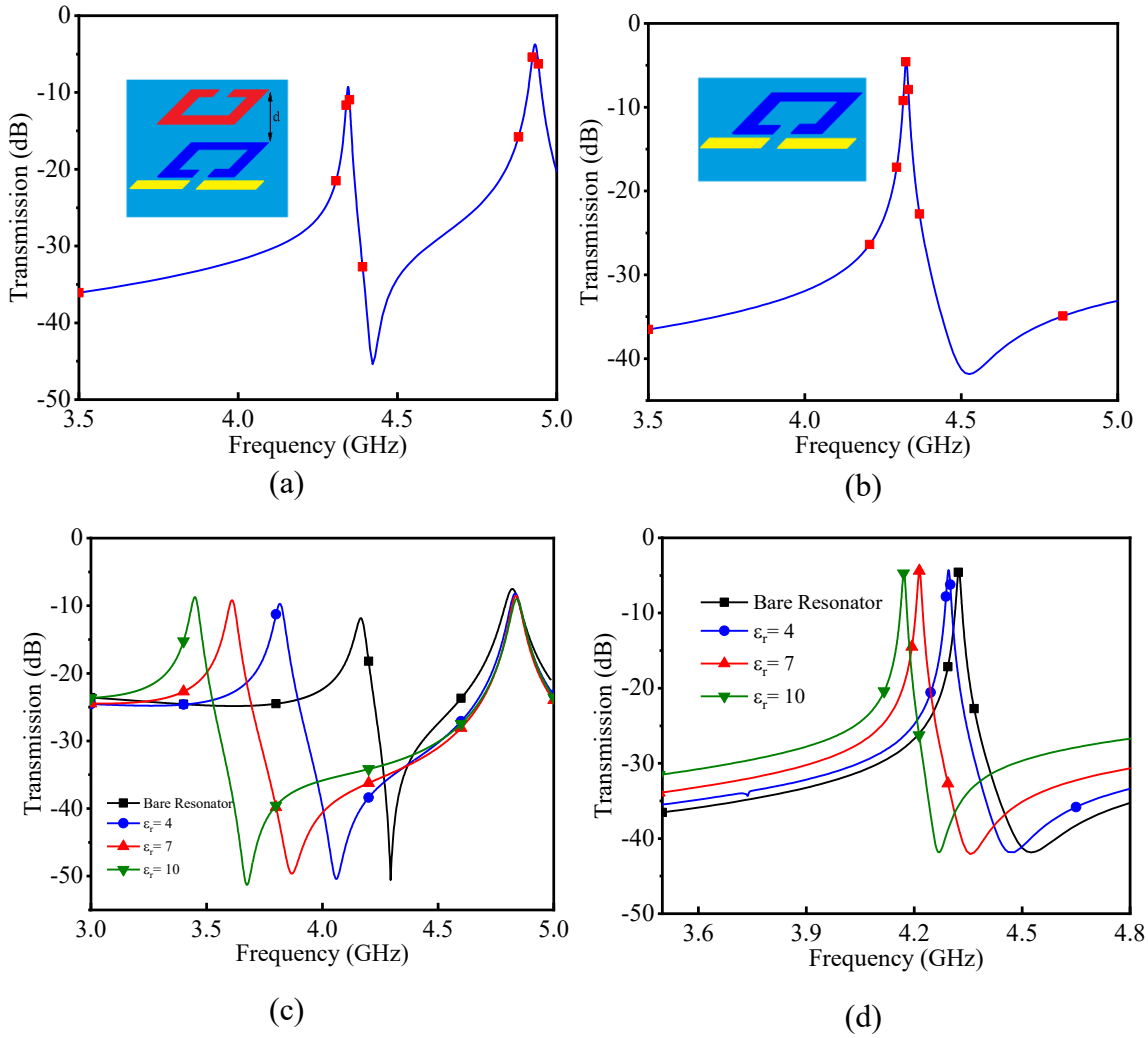

Fig. 3.7. Sensitivity comparison between the presented sensor and traditional microwave resonator sensors. (a) proposed sensor sensitivity test setup with a superficial material with the relative permittivity between 1 (bare resonator) and 10. (b) traditional microwave resonator sensor with the same volume and permittivity. (c) and (d) The spectrum of both setups from sections (a) and (b) respectively as well as their resulted spectrums from MUT relative permittivity variations from $\varepsilon_r = 1$ (bare resonator) to $\varepsilon_r = 10$. It could be seen that, frequency shift related to the proposed sensor is 700 MHz (c) in comparison with 200 MHz for the traditional sensor (d) under the same condition.

3.4 Applications of Coupled Microwave SRR-Based Sensor

After illustrating the superiority of the proposed reader-tag microwave sensor and proving their strong capability for sensing applications, in this section, some of the most important applications that have been enabled by this design are selected to be mentioned in more detail. The applications cover a variety of different fields, from air quality monitoring to medical sensing, which supports the versatility of the design.

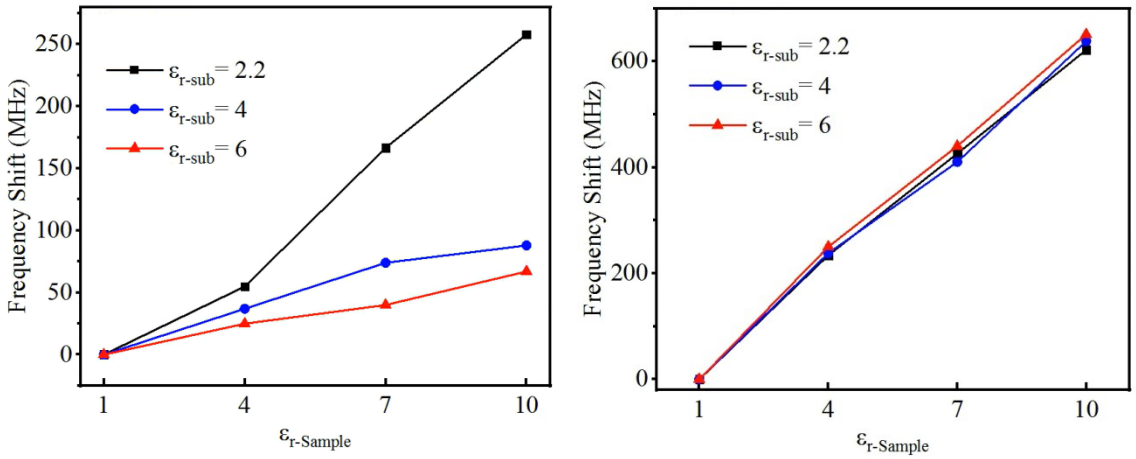

(a) (b)

Fig. 3.8. Comparison between the impact of the substrate in determining the resonance frequency of the traditional and proposed sensors. Frequency shift versus MUT permittivity for different permittivity values for the substrate for (a) traditional sensors, (b) proposed sensors; it could be seen that the effect of substrate permittivity in traditional resonator sensors is dominant while its impact is negligible for the proposed sensor. This is the reason for higher achieved sensitivity of this design in comparison with the traditional sensors.

3.4.1 Application of Coupled Microwave Coupled Sensor in VOC and Humidity Sensing

VOCs emission in the gaseous streams should be monitored and controlled due to their potential health and environmental impacts. VOCs, depending on the type, can be toxic (causing damages to the liver, central nervous system, lungs, etc.) [45]–[47] and carcinogenic [48]. They are also known as a reason for stratospheric ozone layer depletion [49], [50], and precursors for the formation of tropospheric ozone (ground-level ozone) [51]. Common sources of VOCs emission are organic solvents, glues, adhesives, agricultural operations, gasoline leakage during loading, fuel combustion, petroleum refineries [47], [52], [53], and painting processes [54]. An effective method to improve selectivity and sensitivity of the microwave sensor is using the adsorbent material in the vicinity of the resonator [55], [56]. Previously, adsorbent assisted coupled microwave sensor has enabled real-time single compound VOC monitoring [57].

The schematic of our first coupled SRR based sensor has been applied to humidity/VOC sensing is shown in Fig. 3.9. The flexibility of the sensing tag enables its adaptability to various shape chemical and environmental reactors, while the reader ring resonator establishes a wireless connection between the tag and the readout circuitry. The proposed robust microwave sensor is able to detect various concentrations of Methyl Ethyl Ketone (MEK), Cyclohexane, and percentage of humidity in an airstream at room temperature (23℃). It has been demonstrated in a simulation that, having the sensing tag enhances the sensitivity of the sensor in comparison to a single resonator structure.

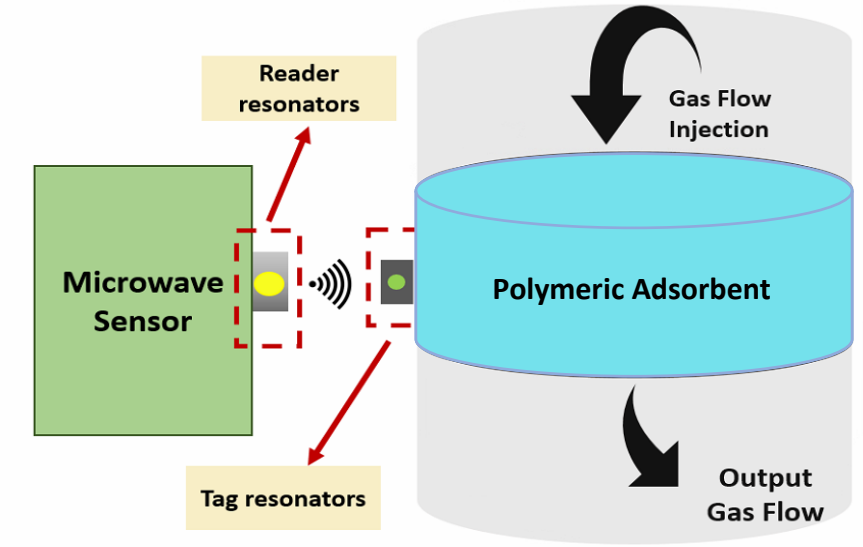

Fig. 3.9. Conceptual sensor with a reader, chipless tag, and polymeric adsorbent, as the Material Under test (MUT).

In principle, microwave sensors are sensitive to permittivity variation of the sensing media, which alters the electric field distribution around the sensor, and enables sensing operation. When an adsorbent is used as a sensing medium, its permittivity will change due to its interaction (i.e. adsorption) with target compound (e.g. VOCs). This permittivity change, however, depends on the concentration of the compound in the gas stream. The compound (i.e. adsorbate) concentration in the gas, therefore, can be measured using the

sensor by correlating the variations in permittivity and compound concentration. This correlation can be described as follow:

During adsorption, the target compound will be adsorbed onto the adsorbent pores causing a change in the permittivity within the pore volume. Pore permittivity during adsorption (ε_{pore}) can be described using the Maxwell-Garnett equation (Eq. (3-1)):

$$\varepsilon_{pore} = \varepsilon_{Air} + 3f\varepsilon_{Air}\frac{\varepsilon_{adsorbate}-\varepsilon_{Air}}{2\varepsilon_{Air}+\varepsilon_{adsorbate}-f(\varepsilon_{adsorbate}-\varepsilon_{Air})} \quad (3\text{-}1)$$

$$f = V_{adsorbate}/V_{Air} \quad (3\text{-}2)$$

Where, ε_{Air} is permittivity of air, $\varepsilon_{adsorbate}$ is the permittivity of adsorbate, f is filling factor, $V_{adsorbate}$ is volume of adsorbate on the adsorbent, and V_{Air} is adsorbent pore volume, respectively.

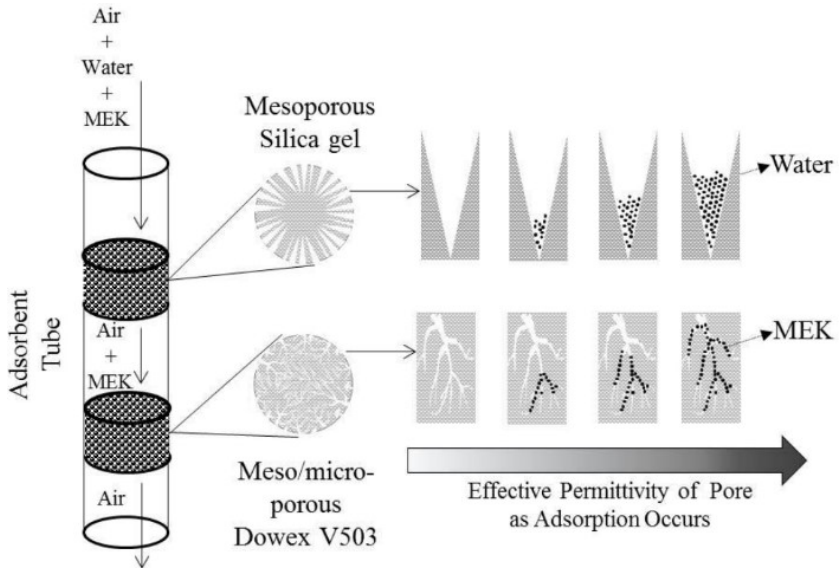

Fig. 3.10. Schematic of the adsorption process.

Additionally, different adsorbents have different affinities towards compounds. Several parameters define adsorbents affinity such as, microporousity, pore size distribution, surface activity, etc. In this work, silica gel (as an industrial desiccant) and micro/meso-porous polymeric adsorbent (Dowex Optipore V503) were selected for water and VOCs

adsorptions, respectively. Silica gel is a hydrophilic adsorbent and has a high affinity towards water, while it has a poor performance on adsorbing VOCs due to its mesoporous structure. V503, however, is a hydrophobic adsorbent (i.e. no affinity towards the water) and has a high affinity towards VOCs. Therefore, in the binary adsorbent tube, silica gel selectively adsorb water, while V503 selectively adsorb VOCs. Furthermore, Methyl Ethyl Ketone (MEK) was selected as a surrogate VOCs due to its high polarity, which could boldly show the permittivity change when adsorbed on low permittivity adsorbent (V503). Fig. 3.10 schematically describes the adsorption process used in this work [58], [59].

The schematic and experimental setup of the VOC sensor is presented in Fig. 3.11. The gas detection set up includes a quartz tube reactor containing polymeric (V503) VOC adsorbent, a ring resonator on the flexible tag, a reader resonator, mass flow controller (MFC), VOC injection pump, a Vector Network Analyzer (VNA), and a data acquisition system which is performed using LabVIEW software. Data is sampled every 10 seconds and the VOC concentration at the reactor outlet is monitored by a flame ionization detector (FID). The implemented resonators are shown in Fig. 3.11 (b), where the tag is placed inside the reactor tube. Adsorption of VOC on V503 inside the sensing medium affects the effective permittivity of the adsorbent bed (V503) during the adsorption process [60]. The permittivity and conductivity change on the bed are transferred to circuit parameters variation on the tag, which is wirelessly coupled to reader circuit. The height of adsorbent in the reactor is 1cm and the reader has placed 5 mm away from the reactor (Fig. 3.11 (c)). The proposed platform is used to detect two different types of VOC gases; Methyl Ethyl Ketone (MEK) as polar VOC and Cyclohexane as a nonpolar VOC. Dry air is applied as VOC carrier gas. Change of the VOC concentration causes different VOC/V503 interaction

during adsorption resulted in a varied effective permittivity of the bed. The resonant frequency and resonant amplitude variation as direct results of permittivity change in bed are monitored during the adsorption process (Fig. 3.12). The sensor could distinguish between different VOCs concentrations in both cases. However, the changes in resonant frequency are more significant in the case of polar VOC (MEK) due to higher permittivity change during adsorption. This distinctive change in resonance frequency could be used as an effective method for detection of the VOC concentration level.

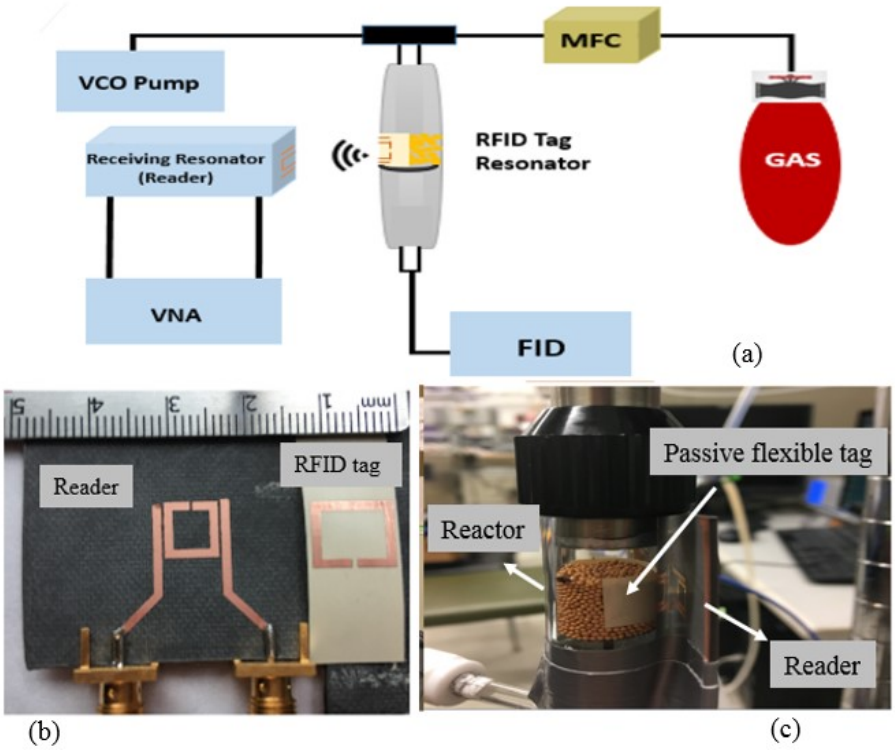

Fig. 3.11. VOC detection set-up: (a) schematics. (b)The implemented reader and sensing tag. (c) actual test set-up with details of the reactor and the sensing tag inside it.

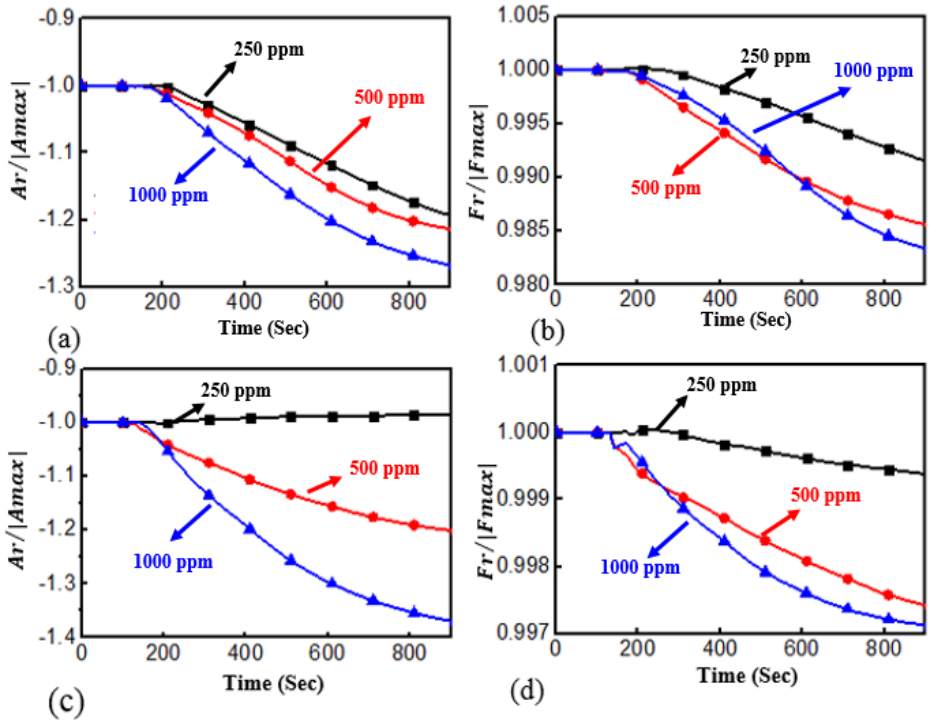

Fig. 3.12 (a) resonant amplitude variation for 3 different concentrations of MEK (polar molecule) VOC gas, (b) resonant frequency response for the same concentrations of MEK, (c) resonant amplitude variation versus time for 3 different concentrations of Cyclohexane (nonpolar molecule) VOC gas, (d) resonant frequency shift for the same concentrations of Cyclohexane.

Additionally, different VOCs and their concentration change the loss constant of the adsorbent and this loss causes an amplitude reduction of the peak frequency. The variation of resonance frequency and amplitude of this frequency is clearly recognizable between the VOC different concentrations. It should be noted that the capacity of the adsorbent is limited and as a result of that the slope of the variation gradually goes to zero, and the shift saturates. However, depending on what type of gas (comparing Fig. 3.12 (b) and (d)), the observed frequency shift is different. This phenomenon can be utilized for selective monitoring of different VOCs.

Another application that has been enabled through coupled microwave resonators is distant humidity sensing. Humidity sensing has gathered attention in both industrial and academic research due to their usefulness and a wide range of applications in various fields

such as environmental science, agriculture, medicine, and industrial processing. To meet industrial demands, the humidity sensors must satisfy high-performance requirements, such as high accuracy, good repeatability, easy fabrication process, the ability of real-time sensing, and low production cost [61]–[63]. The integration of the passive chipless tag with Industrial Silica Gel has been applied to humidity sensing applications. It is shown that assisting fixable passive tag and humidity adsorbent beads increase the sensitivity of the sensor and enable measurement of the lower percentage of humidity in the dry air stream. It has been demonstrated in a simulation that having the sensing tag enhances the sensitivity of the sensor in comparison to a single resonator structure.

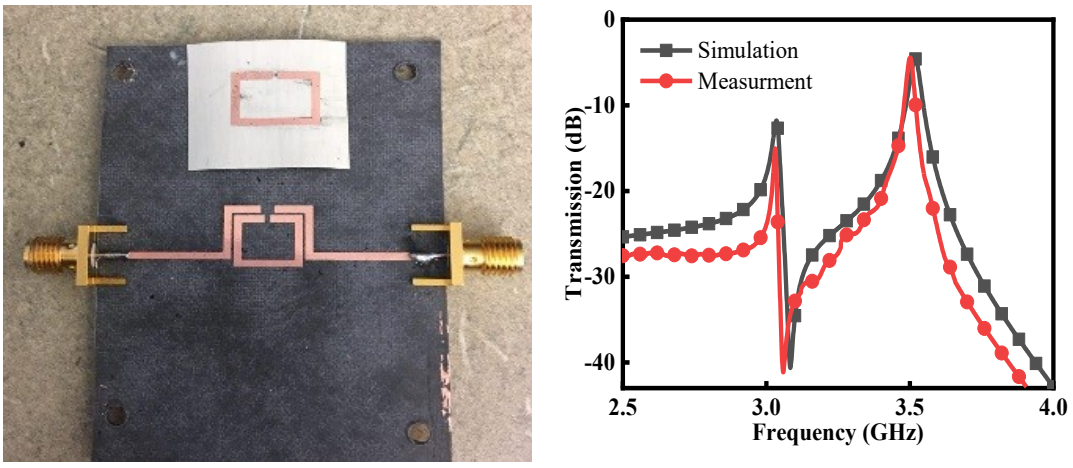

(a) (b)

Fig. 3.13. (a) Comparison between transmission response of the simulated and fabricated humidity sensor. (b) The implemented reader and flexible sensing tag.

The proposed microwave humidity sensor is shown in Fig. 3.13(a). The simulated transmission response and measured results of the fabricated sensor are presented in Fig. 3.13(b). The experimental setup for humidity sensing is presented in Fig. 3.14(a). The reactor is filled with 2 grams of silica gel for all the measurements, and the passive flexible tag is placed over the reader resonator with 5 mm distance. The proposed platform is used to detect different permittivity of the bed. The resonant frequency and resonant amplitude

changes are the direct results of complex permittivity variations in the adsorbent beads. The commercial silica gel adsorbent beads have specific capacity to adsorb moisture and the beads will be saturated after some time. The more the percentage of moisture, the sooner is the saturation time and the slope of the resonant frequency variation is sharper as shown in Fig. 3.14(b). The slope of the variation gradually goes to zero and the shift saturates. The proposed sensor is very powerful sensor for real-time humidity measurements and significant resonant frequency shift in the less that 50 seconds for all the humidity percentage from 20 to 100 percent.

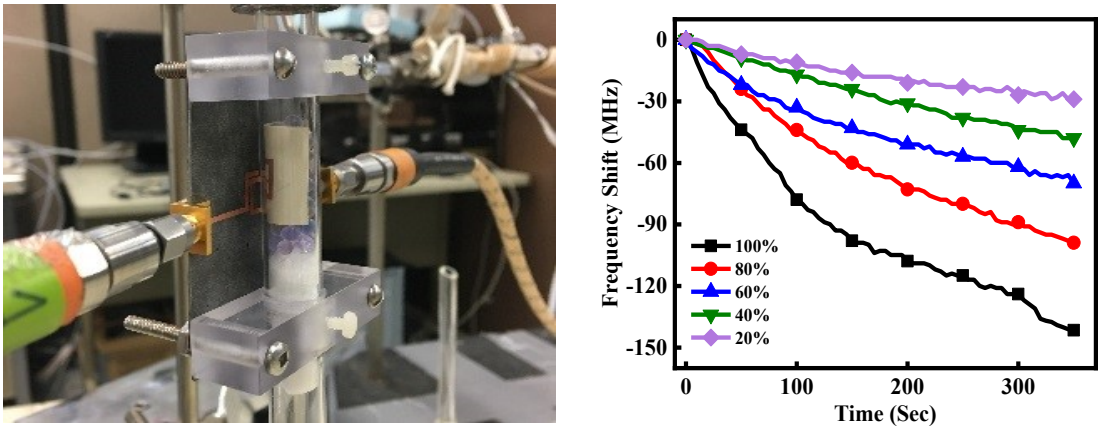

(a) (b)

Fig. 3.14. (a) Humidity detection set-up is containing the implemented reader, chipless tag, and silica gel as the humidity adsorbent. (b) Time based resonant frequency variation for different percentage of humidity in dry air.

3.4.2 Design, Fabrication, and Measurement of Microwave Coupled SRR Sensor for Selective Binary Gas Detection System

An effective method to improve the selectivity and sensitivity of the microwave sensor is using adsorbent material in the vicinity of the resonator [55], [56]. Previously, adsorbent assisted coupled microwave sensor has enabled real-time single compound VOC monitoring.[57]. However, in most realistic gas sensing applications, water vapour is

present with the VOC [64], which could result in poor sensing quality and detection limit. Generally, any unwanted compound such as humidity or another type of VOC that could interact with the sensing media could affect the detection accuracy [65].

One of the most challenging issues for the realization of an effective VOC sensor is achieving selectivity with high sensitivity. In real-world scenarios where high humidity conditions and availability of unwanted VOC/gas are an inseparable part of a gas stream, lack of such capability limits performing real-time selective VOC sensing ([66], [67]).

Herein, we propose to utilize a new technique for tracking two mixed species with a specific focus on VOCs and humidity. It's worthy to mention that any two different types of VOC could also be monitored and detected independently based on the same technique. The proposed solution as illustrated in Fig. 3.15(a), utilizes two flexible microwave tags at the vicinity of selective adsorbent beads tube coupled to the microwave reader. The reader portion of the sensing system consists of two identical SSRs integrated with two power divider and a combiner. The tags are integrated with polymeric adsorbent (non-conductive) beads (Dowex Optipore V503) as a sensing media and silica gel as a desiccant. Besides the benefit of having two pairs of tags in the elimination of unwanted effects, the proposed structure could also be implemented for real-time binary-mixture sensing. Chipless passive tag empowers the sensor to operate with near-zero electric power in harsh and inaccessible environments. The lumped element equivalent circuit is employed to rigorously model the EM behavior of the structure. It is shown that the proposed solution enables accurate selective real-time monitoring of VOC and humidity concentration and more importantly, it demonstrates contactless gas sensing potential.

The proposed solution as illustrated in Fig. 3.15(a), utilizes two flexible microwave tags at the vicinity of selective adsorbent beads tube coupled to the microwave reader. The reader portion of the sensing system consists of two identical SSRs integrated with two power divider and a combiner. The tags are integrated with polymeric adsorbent (non-conductive) beads (Dowex Optipore V503) as a sensing media and silica gel as a desiccant. Besides the benefit of having two pairs of tags in the elimination of unwanted effects, the proposed structure could also be implemented for real-time binary-mixture sensing. Chipless passive tag empowers the sensor to operate with near-zero electric power in harsh and inaccessible environments. It is shown that the proposed solution enables accurate selective real-time monitoring of VOC and humidity concentration and more importantly, it demonstrates contactless gas sensing potential.

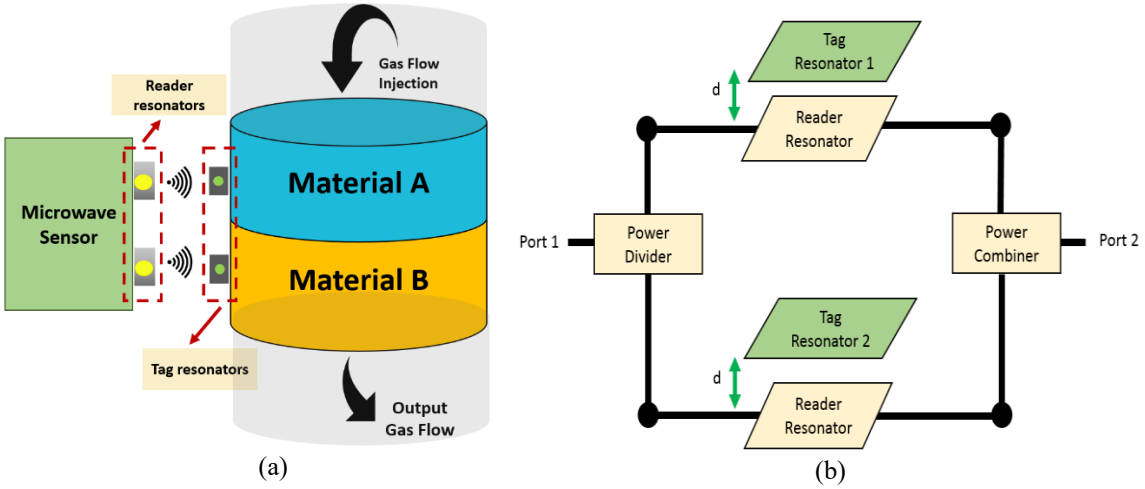

Fig. 3.15. (a) Schematic of a non-invasive, non-contact gas sensor based on microwave ring resonators. (b) Block diagram of the microwave gas sensing system.

A distributed-element structure is developed to independently sense and detect two materials (e.g., sensing humidity and monitoring the VOC concentration variations). As schematically shown in Fig. 3.16(a), the structure of the reader consists of two balanced power divider and combiner devices integrated with two SRRs.

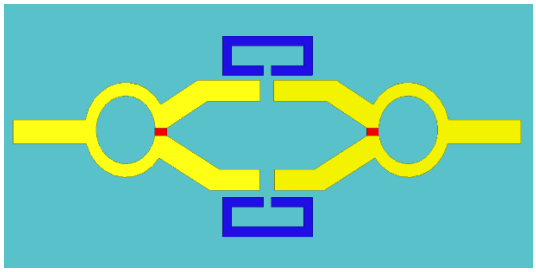

(a)

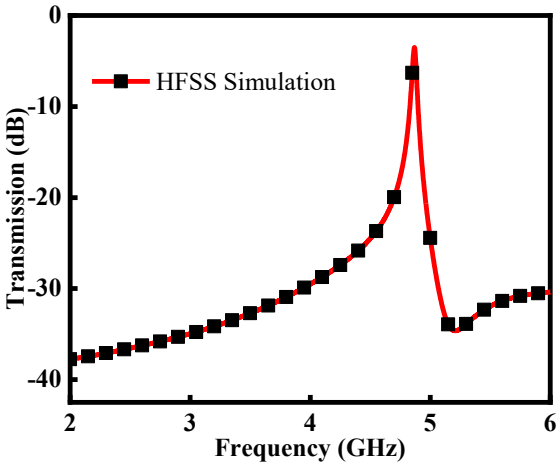

(b)

Fig. 3.16. (a) Integrated SRRs with power divider/combiner structure as a reader. (b) HFSS simulation results for the reader structure.

Integration of the design with two identical power divider/combiner passes the power through the two SRRs with the same resonance frequencies resulting in a single transmission pole realization. The length and angle of the two output ports of the power divider are designed in order to minimize the interference between the two resonators by providing port isolation and removing loading effects [43]. The HFSS simulation result for the transmission response of the structure is shown in Fig. 3.16(b), and since the resonators are designed to be identical, there is only one resonance in the response.

To utilize the proposed sensing module in integration with adsorbent beads, the tag is required to be placed inside the quartz tube where the beads will be interacting with the gas streams. The reader circuit is placed outside of the tube at a 5 mm distance. This structure

enables both tags to couple through the glass tube to the reader and transfers the information to the reader as shown in Fig. 3.17(a). The resonance profile of the simulated sensor including the reader and the tags are presented in Fig. 3.17(b). As demonstrated in Fig. 3.17(b) three different resonance occurs at the transmission profile: f_r is created by the reader, f_{t1} depends on tag 1, and f_{t2} is associated with the tag 2.

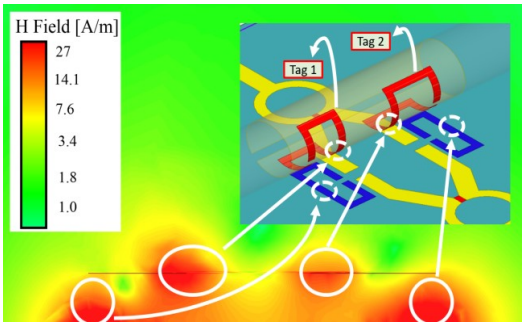

(a)

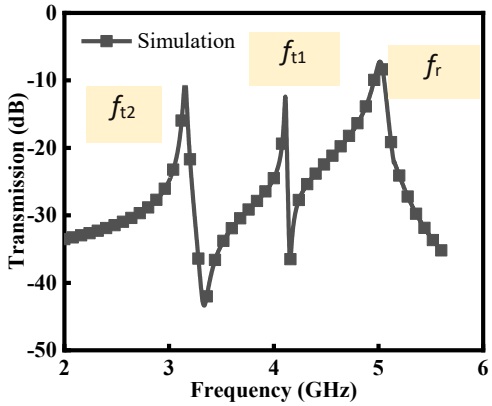

(b)

Fig. 3.17. (a) HFSS simulation, studying magnetic field distribution around the sensor. Inductive coupled areas demonstrate higher field intensity than the others. (b) Transmission response of the simulated sensor including reader resonance frequency (f_r), tag 1 resonance frequency (f_{t1}), and tag 2 resonance frequency (f_{t2}).

The binary sensing capability of the structure is verified for both chipless tags independently. To describe more details about the sensitivity simulations in HFSS, it is important to mention that both the flexible clipless tags are wrapped around the quartz tube and the tube is placed in 5 mm vertical distance from the reader resonators (Fig. 3.17). This 5 mm distance between the reader and the tags provides noteworthy flexibility to the system

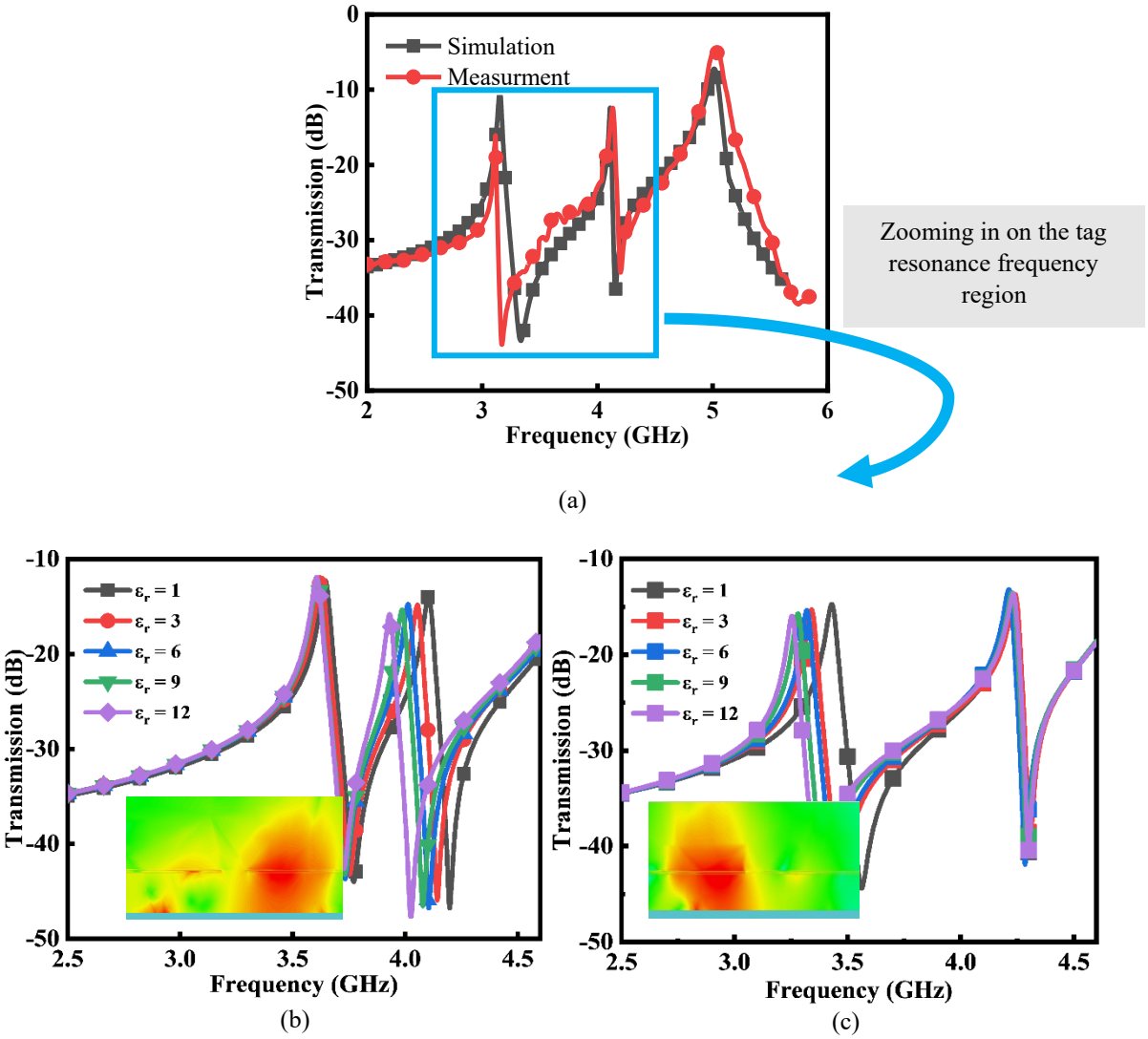

Fig. 3.18. (a) Comparison between transmission response (from lower to higher frequency: tag 2 resonance, tag 1 resonance, and reader resonance) of the simulated and fabricated sensor. Simulation of sensing and field distribution for tag 1 and tag 2 using MUT with different permittivity values (εr=1 to εr=12) when only (b) tag 1 (c) tag 2 demonstrate sensing capability (The reader resonance is not included).

such as the opportunity of high-temperature sensing and hazardous gas monitoring without having electronics in contact with the MUT. The tag, which could only be a copper layer, can be placed inside the high-temperature container while the reader, including the cables, active parts, and batteries is protected from being in the vicinity of high temperature and hazardous gas.

The results presented in Fig. 3.18 illustrate the independence of the resonant structure and highlights the potential of the proposed microwave system for two independent reading. For the independency analysis, a MUT box with the dimensions of 2x2x2 mm in placed inside the quartz tube and over the gap area of one of the chipless tags while there is no permittivity variation in the vicinity of the second tag. S_{21} parameter is extracted for different permittivities (ε_r = 1-12) of the MUT. The comparison between simulation and measured transmission response of the sensor are nicely matched and presented in Fig. 3.18(a). As expected, three resonant peaks are observed at f_{t1}=4.13 GHz, f_{t2}=3.11 GHz, and f_r=5.02 GHz. f_{t1} and f_{t2} are associated with tag 1 and tag 2 and f_r is created by the reader resonator. Since both resonators of the readers are designed with the same length, their resonance frequency occurs at the same frequency of f_r. By zooming in the tag resonance frequency, the sensitivity potential of the structure has been verified. The resonance frequency of the two tags are shown in Fig. 3.18(b) and Fig. 3.18(b). When the MUT is placed over the smaller sensing tag, which is tag 1, the sensor depicts significant sensitivity to the different level of permittivity (ε_r=1 to ε_r=12) of the MUT while the large sensing tag, which is tag 2, demonstrates negligible frequency variation (Fig. 3.18(a)). If the MUT with variable permittivity be placed over tag 2 while there is no permittivity variation around tag 1, the lower resonance frequency demonstrates frequency shift as the permittivity of the MUT changes while the resonance frequency related to tag 1 stays constant. As a result, the tags demonstrate independent sensing potential which makes the sensor applicable to selective gas and VOC sensing applications. These specifications along with two separate adsorbents, develops the base for selective sensing of the proposed sensing system.

The fabricated binary gas sensor is presented in Fig. 3.19. One important point to note is that to increase the dynamic range of sensing, it is required for the tag resonator frequency to be distant from the reader resonant frequency. This enables an extended dynamic range before the frequencies interfere. In order to do so, the passive chipless tags are designed with different length in order to have enough distance between resonance frequencies. The large frequency gap between the two provides a large dynamic range such that even at the maximum concentrations of the humidity and VOC tested in this experiment, frequency peaks never overlap.

After illustrating the details of the sensor design, the proposed structure is utilized to conduct VOC and humidity sensing in both single and binary compounds scenarios. The tag with the lower resonance frequency (tag 2 in Fig. 3.19) has been chosen for humidity sensing (humidity peak) since this peak sweep higher frequency range as the humidity of the adsorbent changes from 0 to 100%.

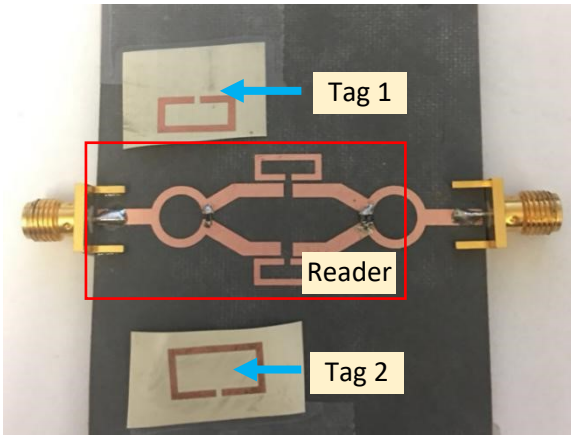

Fig. 3.19. Fabricated binary gas sensor including Double resonator passive reader, flexible passive tag 1, and flexible passive tag 2.

The higher resonance frequency (tag 1 in Fig. 3.19) represents VOC monitoring. The schematic and experimental setup of the VOC sensor are presented in Fig. 3.20(a) and Fig. 3.20(b). The gas detection set-up includes mass flow controllers (MFC), VOC injection

pump, a Vector Network Analyzer (VNA), and a data acquisition system which is performed using LabVIEW software recording the signals every 10 seconds. The output of one of the MFCs is humidified to saturation (100% relative humidity) and the other one is dry air. By mixing the two streams with different flow rates, the desired humidity level could be generated which is injected inside the quartz tower, including the adsorbent and the tags. The tag is placed in 5 mm vertical distance from the readout circuitry. This specific distance is the result of the compromise between the proposed quality factor of the sensor and minimizing the limitation induced to the sensing system. For all the experiments, 1.5g of V503 adsorbent and 4g of Industrial Silica gel adsorbent is used. The samples are heated in an oven at 120°C overnight before testing to remove impurities such as moisture. The post-processing analysis was performed in MATLAB.

Resonant frequencies of the sensor change when the effective permittivity of the environment (V503 or Silica Gel) changes. Each passive tag resonator represents exclusive behavior with respect to near-by ambient change. The following will explain the steps and experiments for independent binary gas sensing.

- *Humidity Sensing Using Binary Gas Sensor:*

The environment near-by the chipless tag with the higher resonance frequency, which is responsible for VOC detection, is filled with V503 while the other chipless tag interacts with silica Gel as a humidity adsorbent. The syringe pump is out of the system and only input is the 30% humid air. The sensor monitors as the permittivity undergoes significant change due to the adsorption of water vapor onto the beads. Blue Silica Gel beads start to change their color to pink after 2 minutes of being purged by humid air which is an additional indication of adsorbed humidity. Fig. 3.21(a) presents transmission response of

the sensor at the start time and after an hour of having the humid air flowing through the quartz tube.

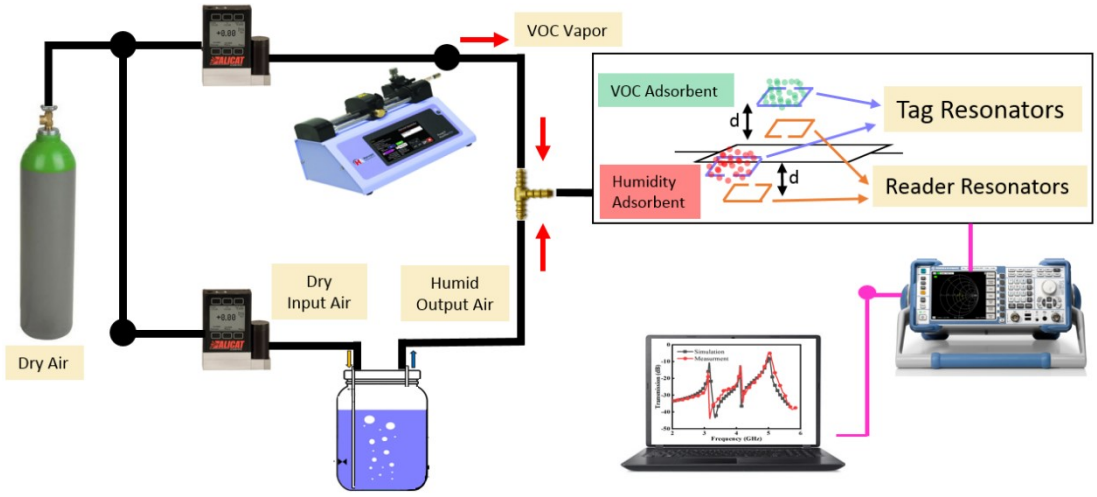

(a)

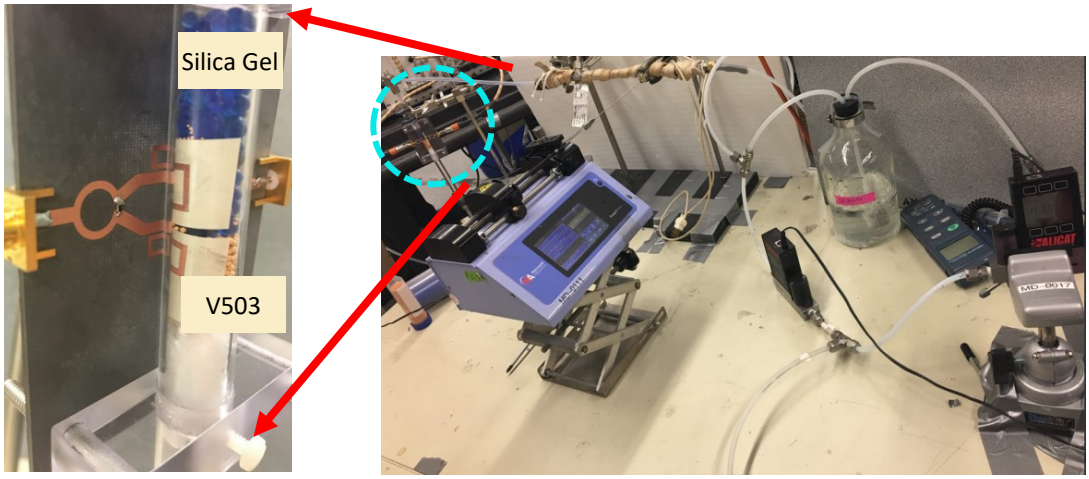

(b) (c)

Fig. 3.20. (a)Schematic illustration of the instrumentation and experimental setup for studying the effect of injecting a mixture of humidity and VOC vapour on the passive binary microwave double resonator sensor. (b) VOC and humidity binary detection set-up containing the implemented reader, chipless tags, and adsorbents.

The upper peak has stayed at the same frequency during the experiments since not compound interacted with V503 (no permittivity change) while the humidity peak has 100MHz shift after one hour. The humidity sensing experiments were performed in three different humidity concentration and the frequency shift of the lower resonance is shown in

Fig. 3.21(b). It should be noted that in all the experiments, the resonant frequency stayed the same which is an indication of the fact that the beads can adsorb selectively, and the microwave resonant structure tags monitor independently.

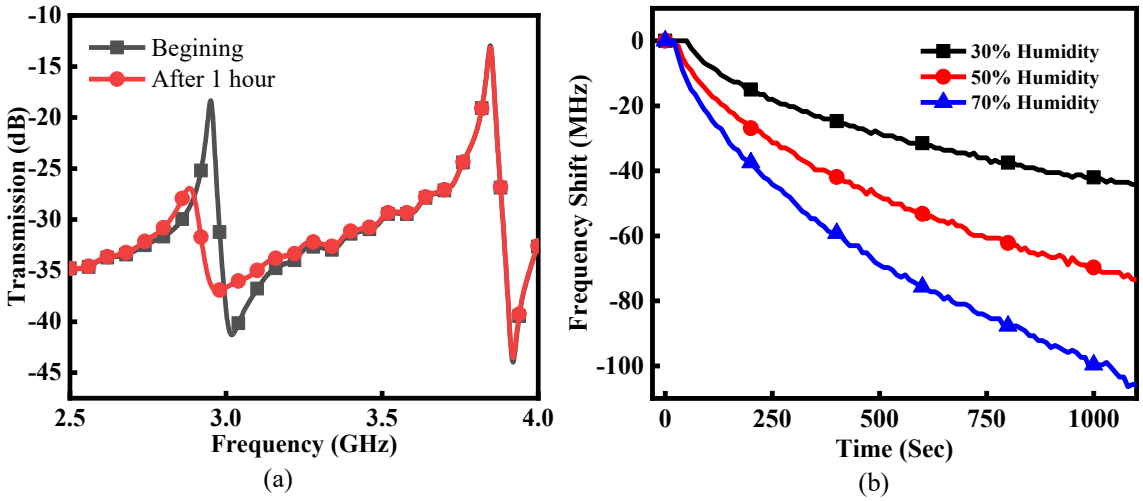

Fig. 3.21. (a)Transmission response of the sensor at the beginning and when only humidity has been injected into the tube for an hour (b)Time-base measurements of the resonance frequency of different concentration of humid air.

- *VOC Sensing Using Binary Gas Sensor:*

Here, the microwave sensor is used for VOC real-time sensing and detection. MEK is injected with a specific rate to create different MEK concentrations within 50-500 ppm range using the vapor generation system consisted of a syringe pump. Fig. 3.22(a) shows the transmission response of the VOC and humidity peaks for 5000 seconds. The higher resonance used for humidity sensing illustrates frequency shift during the time since the adsorption causes permittivity variation in the V503 beads. Simultaneously, since humidity is not injected inside the quartz reactor and due to the incapability of silica gel beads in MEK adsorption, the resonance frequency for humidity peak shift is negligible (<1%) when only VOC injection happens (Fig. 3.22(b)).

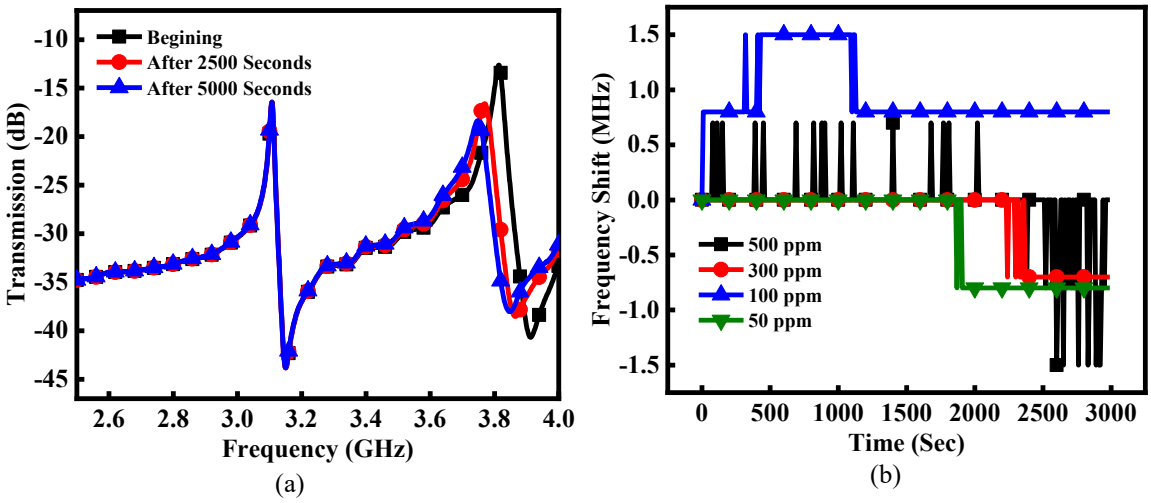

Fig. 3.22. MEK only injection: (a) Transmission response of VOC and humidity peak in 5000 seconds. (b) humidity peak frequency variation during the first 3000 second of experiment.

However, variation of resonance frequency is clearly recognizable even for low concentrations of VOC as shown in Fig. 3.23. Higher concentration of VOC inside the tube increases the overall permittivity and loss constant in the bed quicker and settles in a larger frequency shift. It should be noted that the capacity of the adsorbent is limited and as a result

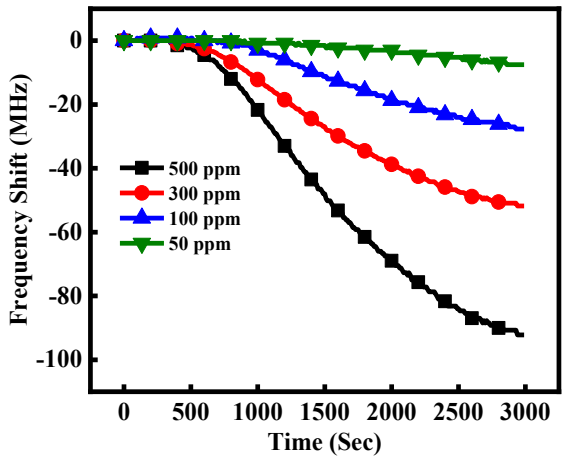

Fig. 3.23. VOC peak variation for different concentrations of MEK vapor (500ppm, 300ppm, 100ppm, and 50ppm).

of that the slope of the variation gradually goes to zero and the shift saturates. However, depending on what type of gas, the observed frequency shift would be different in both

direction of the shift and quantity of resonance frequency variation. This phenomenon can be utilized for selective monitoring of different VOCs.

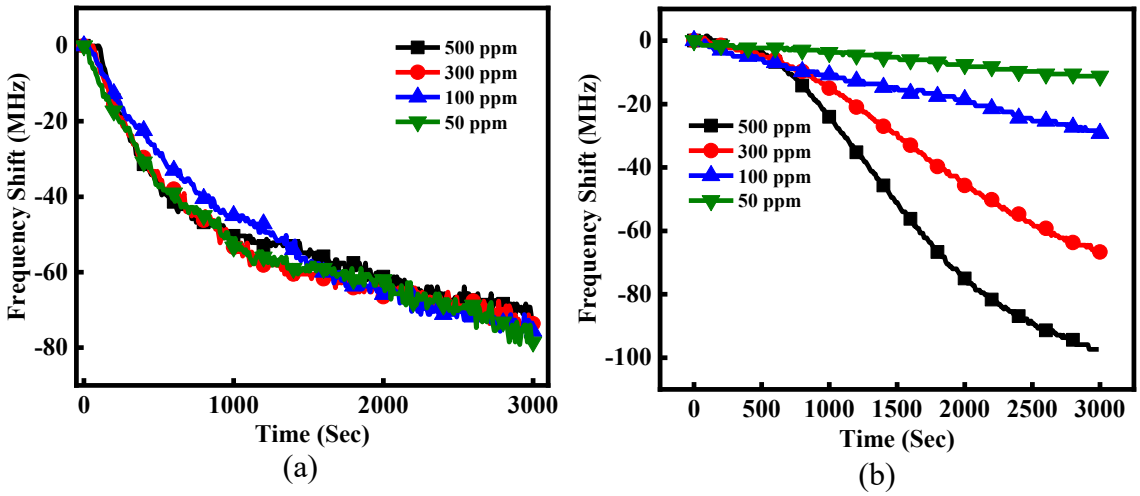

Fig. 3.24. MEK and 30% humid air injection: (a) humidity peak frequency variation (b) VOC peak variation for different concentrations of MEK vapor (500ppm,300ppm,100ppm, and50ppm).

- *Simultaneous VOC and Humidity Binary Sensing:*

Both VOC vapour and humid air are injected into the quartz tube at the same time. Since each of the adsorbent available in the system is able to interact with either MEK or humidity, maximum shifts for both humidity and VOC peak are expected. Fig. 3.24(a) presents the humidity peak variations when 30% humidity is injected constantly during all the experiments for different concentration of MEK. Humidity peak frequency variation is almost the same for all the experiments with different MEK concentration which is a confirmation for decoupled sensing of humidity and MEK.

Fig. 3.25 presents transmission response of the sensor at the start time and after an hour of having 30% humidity in the air flow inside the quartz tube as well as 300 ppm of VOC and it verifies the frequency shift during the time for both humidity and VOC peaks. The comparison between the final frequency shift in VOC sensing and VOC and humidity binary sensing (Fig. 23 and Fig. 24 (b)) is shown in Fig. 3.26. The final frequency in both cases are

very close with less than 5 percent error which confirms independent sensing of humidity and VOC.

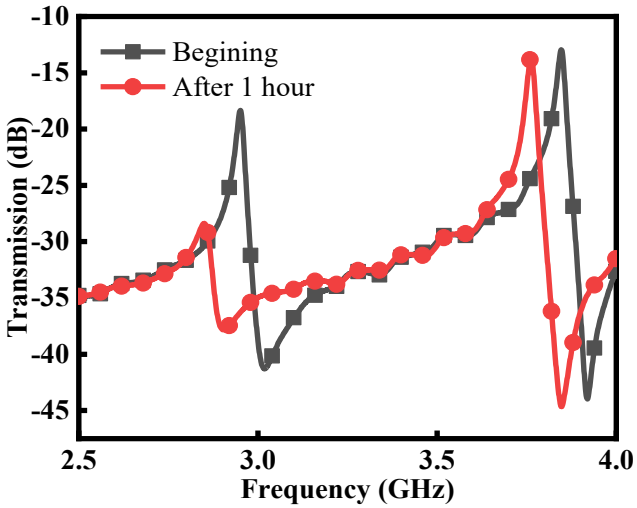

Fig. 3.25. (a)Transmission response of the sensor at the beginning and when a mixture of humidity (30%) and VOC (300 ppm) has been injected into the quartz tube for an hour.

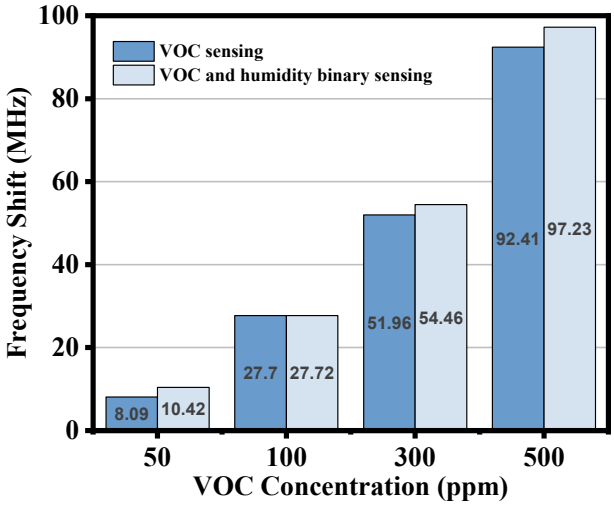

Fig. 3.26. Final VOC peak frequency shift in VOC sensing and VOC and humidity binary sensing.

The results demonstrate the capability of the proposed system for selective sensing of a VOC in the presence of humidity in a gas stream. The microwave system here, presents a prototype that can be used with different types of adsorbent beads for mixed gas sensing.

This system is also expected to be expandable to a larger number of adsorbent-gas/vapour detection simply by adding the power combiner and number of the adsorbents in the tower.

Table 3.3 summarizes the performance of the developed chipless microwave wireless VOC sensor compares the proposed sensing platform to some of the most recent available gas sensors in the literature. However, each of them suffers from at least one important aspect comparing to the novel binary gas sensing technique proposed in this paper.

Simultaneous selective sensing capability, minimum detectable concentration, temperature compatibility, and the technology are the main figures of merit that have been compared in Table 3.3. Chromatography is one of the very popular technologies which has shown potential in selective VOC sensing in [11] and [12]. This technology also provides highly sensitive structures with a resolution of 1 ppm. Besides the necessity of using customized nanocomposites and nanoparticles in this technique to signify the effect of gas presence, this method requires complicated setup with lots of elements, making this approach to require specialized skills and devices for method development, operation, and maintenance.

In [13], a UHF-RFID sensor has been presented which utilized active RFID combined with nanomaterial. Although they have claimed this technique could be utilized for selective sensing, it has not been demonstrated. In addition, the presence of active elements adds to the complexity of the devices such as the unreliability of the results due to the temperature sensitivity and limited readout life time. It worth mentioning that assisting material available in [13] is carboxylated polypyrrole (C-PPy) nanoparticles, bonded to the sensitive area of the tag. This material fabrication procedure is an expensive, complicated, with the timely process while our proposed V503 and Industrial Silica Gel is commercially available at low

cost. Other types of microwave sensors have been applied to wireless sensing. Some of them, like [42], use an active feedback loop to be able to detect low concentrations of VOC (35 ppm). This structure is extensively dependent on temperature and they are also not flexible, which makes them hard to utilize in harsh environments. Besides, they have not presented any selective or multi-material gas sensing.

Having all the above in mind highlights the superiority of this work and introduces the first selective chipless microwave VOC sensor presented in the literature. The coupling between the reader and the chipless tag allows the sensor to have more freedom to use at the site. Because of strong coupling, the tag can be placed up to 10 mm away from the reader while detecting the VOC concentration variation in real-time. The distance between the reader and the tag secures the capability of the structure to be able to perform in high temperature and hazardous sensing applications. While the tag, which could only be a copper layer, is placed inside a high VOC container, the reader, including the cables, active parts and the potential battery is safe from being in the vicinity of the harsh sensing environment.

Table 3.3 Comparison of Different Techniques For VOC Sensor

Ref.	Binary sensing tested	Technology	Assisting material	Flexibility	Temperature compatibility	Selectivity sensing potential	Minimum detectable concentration	Δf
[68]	Yes	chromatography	NA	No	No	Yes	1ppm	NA
[69]	Yes	chromatography	Nanocomposite	No	No	Yes	1 ppm	NA
[70]	No	UHF-RFID	Nanoparticle	yes	No, very dependent	Yes	0.1 ppm	NA
[57]	No	Microwave Sensing	Industrial adsorbent	Yes	Yes	No	250 ppm	~10MHz
[71]	No	Nanomaterial	Nanomaterial	No	Yes	No	400 ppm	NA
[72]	No	RF Resonant Cavity	Customized P25DMA	No	No	No	625ppm	NA
[73]	No	Microwave Sensing	Industrial adsorbent	No	No	No	35 ppm	~160kHz
[56]	No	Microwave Sensing	PDMS	No	No	No	0.265ppt	≤5MHz
This work	Yes	Microwave Sensing	Industrial adsorbent	Yes	Yes	Yes	50ppm	~10MHz

3.4.3 Non-invasive glucose sensing using chipless printable sensor

The World Health Organization estimates that there are >500M people worldwide who have diabetes. Diabetes is primarily characterized by poorly controlled blood glucose concentrations that, if allowed to remain chronically high (hyperglycemia), result in the development of serious and life-threatening diseases such as stroke, heart attack, heart failure, kidney failure, adult blindness and amputation. Moreover, many patients also experience episodes of very low blood glucose (hypoglycemia) that can rapidly lead to coma and death. The most common glucose-sensing technology in use today are finger-prick based glucose strips, although this requires sampling many times per day and the continual purchase of the consumable once-use strips. As such, patient compliance to regular glucose monitoring is often not possible. Moreover, real-time continuous glucose monitoring offers a much more accurate assessment of the large fluctuations in blood glucose that can occur in patients with diabetes. In this regard, newer glucose-sensing technologies include the placement of a thin needle-like sensor under the skin to measure glucose levels within interstitial fluid that closely tracks with blood glucose levels. Although this technology removes the need for finger-prick blood sampling and can sample glucose levels every few minutes, the sensor is consumable, is expensive, and requires the insertion of a new sensor every 10-14 days. Therefore, many patients cannot take advantage of this technology. What is really required is a non-invasive, reliable and cost-effective technology that measures glucose in real-time [74]–[81].

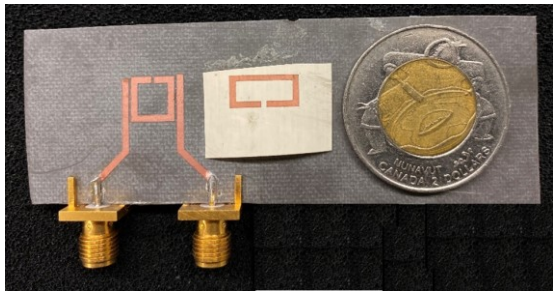

(a)

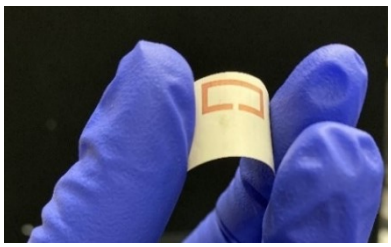

(b)

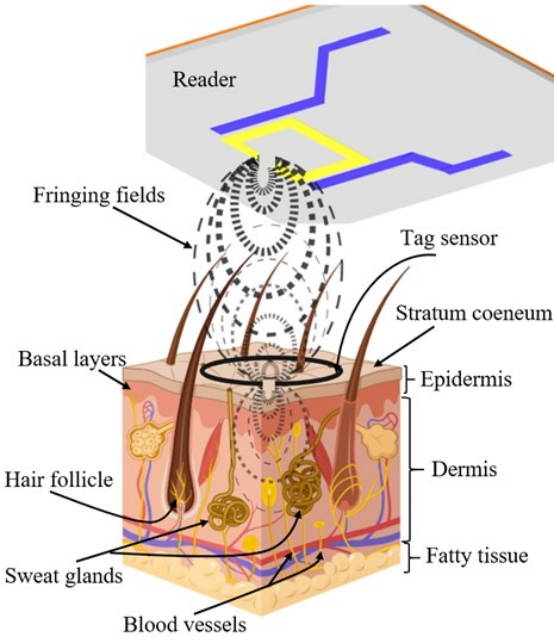

(c)

(d)

Fig. 3.27. Conceptual representation of the operation of the proposed glucose monitoring system. (a) Fabricated sensor system including the reader and the tag, (b) sensing tag flexibility (c) detailed exaggerated presentation with irrelevant scaling. It could be seen that the field concentration inside the body is decaying by increasing the distance from the sensor. The immediate layer in contact with the sensor, Stratum Corneum, contains no ISF and hence doesn't contribute to the glucose monitoring response (i.e. frequency variation). The next epidermal layer, basal layers, contains around 40% of ISF and according to its low distance from the sensor, it is the dominant layer determining the sensor response. Besides ISF, this layer contains cells and cell water without blood vessels or lymph fluid. Considering the cells as static variables, which is a reasonable assumption because of their very slow dynamics, the most important variables in this layer that could interfere with the response of the propose sensor are dehydration and saline variation. These topics are experimentally studied throughout the paper to have negligible impact on the sensor response. The overall epidermal thickness is about 100µm varies depending to the location. The next layer is dermis containing around 40% of ISF, less cells, very small percentage of lymph fluid and about 8% of blood plasma. Again, the main possible interfering parameters in this layer are the same as epidermis. Since the average dermal thickness is about 2mm, the layers after dermis have negligible impact on the sensor response because the field strength at those layers is very low. In addition, this figure conceptually presents the communication between the tag sensor and the reader which is mostly accomplished through fringing fields, (d) general conceptual presentation of the whole system as a non-invasive microwave glucose monitoring system.

To date, there has been much interest in developing novel glucose-sensors and a variety of sensor technologies have been tested. One of the most promising therapeutic systems for diabetes patients is the artificial pancreas, whereby an automated insulin delivery system is coupled to a real-time glucose sensing devise. Such technology promises much tighter control of blood glucose levels. However, the main drawback associated with the artificial pancreas is the real-time and continuous glucose monitoring system. Indeed, a great deal of research has focused on the development of optimal real-time non-invasive glucose-sensing [82]–[88], that optical, transdermal and infra-red techniques. The majority of techniques are based on near infra-red spectroscopy (NIRS) and impedance spectroscopy [89], [90].While, other optical techniques have also been tested that include Raman spectroscopy [91], tomography [92] and photoacoustic methods [93]. Optical methods suffer from absorption by other materials, low signal to noise ratio (SNR), thermal noise, calibration drift, environmental susceptibility, power consumption and cost. Transdermal glucose monitoring systems are based on glucose extraction from interstitial fluid (ISF) using reverse iontophoresis techniques [94], [95] followed by a chemical sensor for glucose concentration measurement. Although they claim to be non-invasive, they actually inject electrical current through the skin. Furthermore, the sensors degrade over time and the technology is expensive. The thermal emission infra-red thermography technique which uses the body temperature for gaining an understanding about blood glucose levels [96] is expensive and inaccurate with respect to glucose monitoring. Other techniques such as saliva, breath, sweat and tear analysis are being developed but all have inherent problems and limitations [96]–[101].

Due to their high-quality factor, low cost, and non-invasive nature, microwave resonator-based sensors have garnered a great deal of interest in the last decade. Their potential applications have now expanded from the oil and gas industry to microfluidic and biomedical applications [7], [17], [102]–[107] that include glucose-sensing [8], [108]–[114]. Since blood glucose is tightly regulated, even the largest variations that occur in diabetes are within a relatively small range (2-25 mM/lit). To date, much research has been published that report non-physiological values for glucose sensing in the 1000 mM/lit, emphasizing low sensitivity as the major problem associated with existing microwave-based resonator sensor technology. Sensitivity for this kind of sensors is defined as the resonance frequency variation versus the change in the permittivity of the MUT.

Fig. 3.27 presents the fabricated glucose sensing system including the reader and the tag as well as the conceptual structure of the sensor and its application as a glucose monitoring system. The sensor is constructed of a substrate-less split ring resonator tag operating as the sensing element that is electromagnetically coupled with a traditional split ring resonator designed at a different frequency as the reader. Since the sensing part is without substrate, huge improvement in sensitivity is achieved. This sensitivity achievable is much greater than the values for glucose reported in the literature to date. The structure enables the integration of the reader and the required circuitry within a smartwatch, cell phone or an application-specific device for distance measurement capabilities. The sensing element itself is just a metallic trace that could be simply taped on the patient's skin and is replaceable at an extremely low cost. In addition, since the power is coupled from the reader to the sensor through fringing fields, the tag itself consumes zero power negating the requirement for a power supply on the sensor itself. The proposed sensor can measure

glucose concentration in the range of 0-200 mM/lit with the precision of ~1mM/lit which should provide sufficient sensitivity for the accurate real-time measurement of interstitial fluid glucose levels from patients with diabetes. Our results demonstrate that microwave bio-sensing technology can be optimized to reproducibly detect glucose concentrations ranging from 2-25 mM/lit in physiological solutions designed to mimic interstitial fluid. Importantly, this range is the same as the blood glucose levels seen during hypoglycaemia and hyperglycemia in diabetes patients. Furthermore, the current design is also compatible with the development of wearable electronics applications.

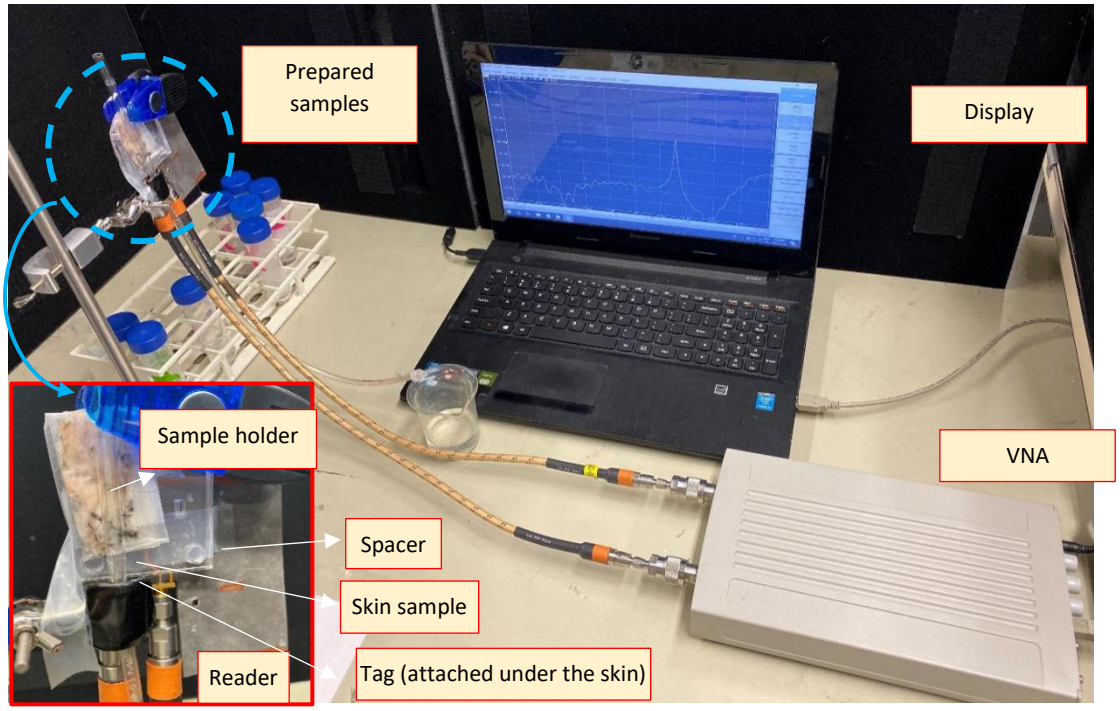

Fig. 3.28. experimental setup including sensor structure, skin sample, holder and fixture, VNA and interfacing software.

Various measurements have been accomplished verifying the performance of the proposed non-invasive glucose measurement sensor. All the microwave measurements (Fig. 3.28) have been accomplished using S5085 2-port vector network analyzer (VNA) from Copper Mountain Technologies Inc. The liquid samples were also tested inside a

borosilicate tube with ε_r=4.3 and tan(δ)=0.0047 and wall thickness of 1 mm. The total exposed volume of liquid was 200 µlit. Simulations have also been carried out using High Frequency Spectrum Simulator (HFSS®).

First of all, glucose concentration measurement in deionized (DI) water is carried out. For studying consistency and stability of the sensor as well as setup a return-to-zero test is accomplished with as high concentrations of glucose as 200 mM/lit (Fig. 3.29). Although this value is unrealistically high, but it will provide invaluable insight through consistency of the sensor performance by introducing DI water with zero glucose concentration and DI water with 200mM/lit glucose concentration alternatively to the sensor. Fig. 3.29(d) sketches the resonance frequency notch amplitude of S_{21} response of the sensor. It could be seen that, sensor response is both stable and repeatable. Also, the high sensitivity characteristic of the sensor is noticeable. To the best of our knowledge, the achieved sensitivity of this work, 60 kHz/1mM/lit of glucose concentration, which is far beyond the best results reported in literature regardless of shape and volume of MUT. This means the response of the sensor is less susceptible to environmental noises than its conventional counterparts.

From now on each experiment is accomplished with one step toward more realistic liquid similar to ISF. For the next step samples are prepared with 10 volumetric percent of horse

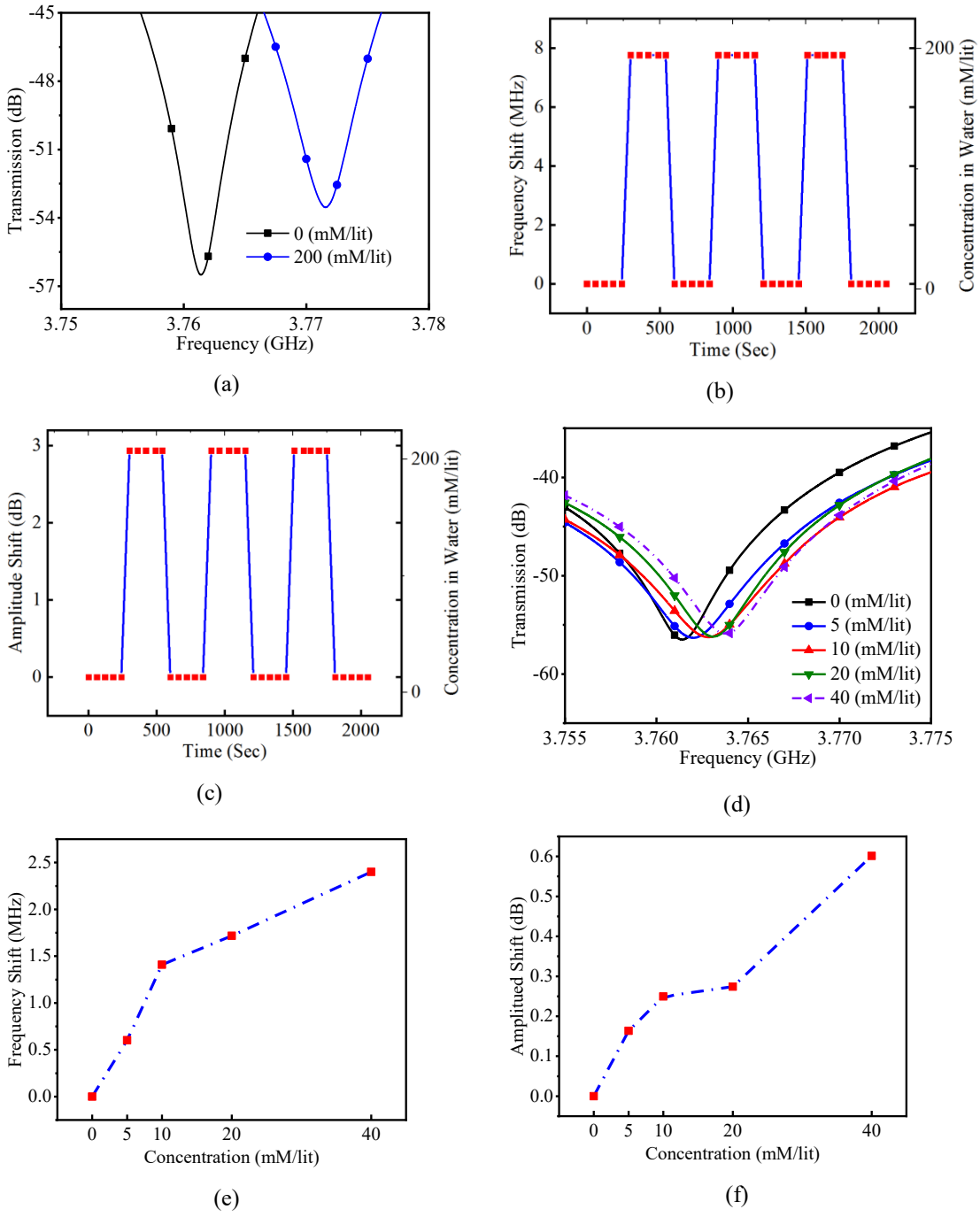

Fig. 3.29. (a) S21 experimental response of the sensor for extreme case of introducing samples with 0 mM/lit and 200 mM/lit of glucose concentration for the sensor. (b) Frequency shift versus glucose concentration for the extreme case of 0 and 200 mM/lit glucose concentration in DI water. It could be seen that the response of the sensor is very consistent and repeatable. (c) Amplitude shift versus glucose concentration for the extreme case of 0 and 200 mM/lit glucose concentration in DI water. (d) S21 response of the sensor for small variations of glucose concentration in DI water from 0 to 40mM/lit. (e) Frequency shift versus glucose concentration for concentration variations from 0 to 40mM/lit. It could be seen that great results have been achieved with very high average sensitivity of 60 KHz/1mM/lit of glucose concentration. (f) Amplitude shift versus glucose concentration for concentration variations from 0 to 40mM/lit.

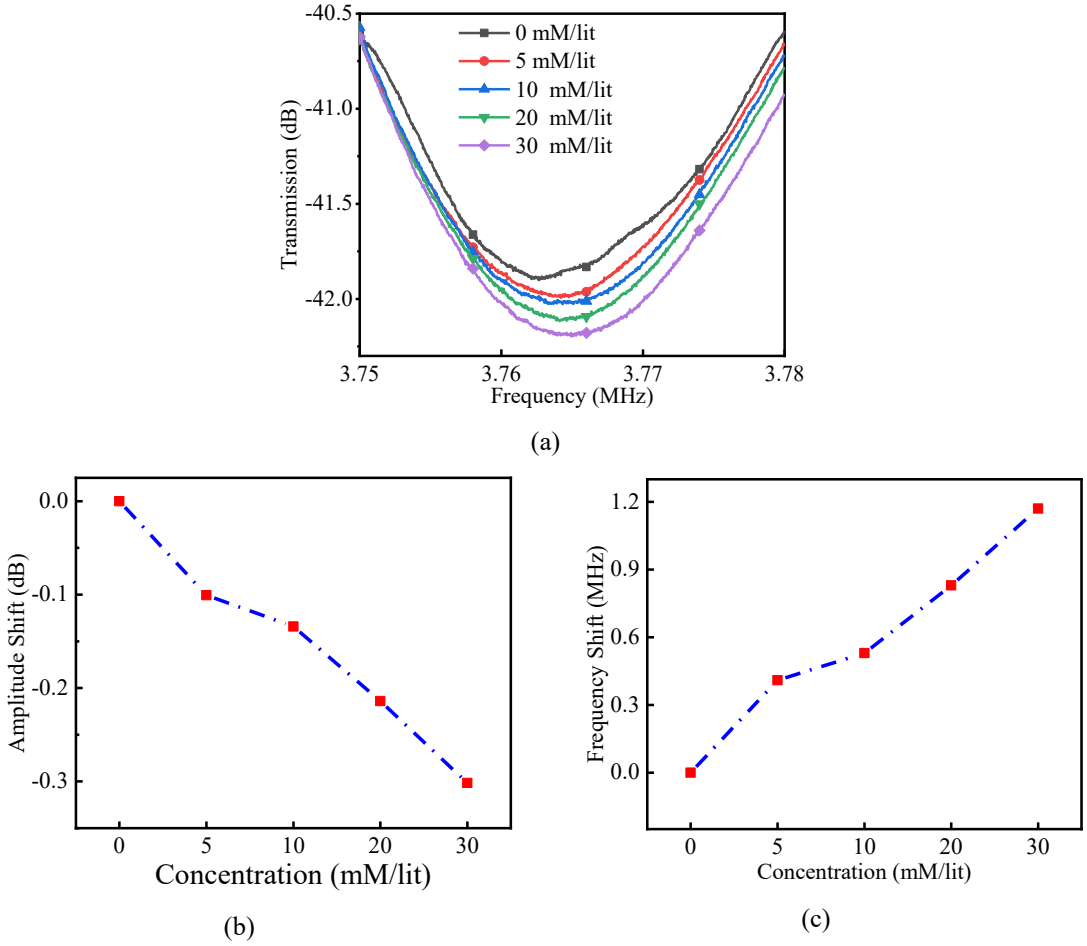

Fig. 3.30. Experimental results of samples with glucose concentration in DI water with 10% of horse serum content. (a) S21 response of the sensor for glucose concentrations from 0 to 30mM/lit. (b) Amplitude variations versus glucose concentration from the same experiment. (c) Frequency shift versus glucose concentration. It could be seen that, according to lower permittivity of serum in comparison with water, the total permittivity of water-serum solution is reduced and therefore the impact of the glucose variation on the overall permittivity of the solution is reduced as well which results in a lower sensitivity of 43 kHz/1mM/lit of glucose concentration. (if we had return to zero results, we could integrate them with this fig as well)

serum for modeling ISF. Both return-to-zero and small variations of glucose concentration samples have been tested with promising results achieved as sketched in Fig. 3.30.

The last accomplished experiment of the sensor for even more realistic conditions is glucose concentration monitoring in serum and saline samples over a biological skin layer. In this experiment, saline is included in the sample with electrolytes and ionic concentrations described in section 3. According to the conductivity increasing of the samples, the amplitude of the notch frequency is increased. For this experiment, a shaved mice skin with

about 300 µm thickness wrapped inside a sealed plastic bag is used between the sensor and the liquid. Hence, the sample is located in further distance from the sensor. As illustrated in Fig. 3.31, the sensitivity of the sensor is decrease as the result of increasing the distance between ISF sample and the sensor. But, even though, the sensitivity is still within a very promising range far beyond the state-of-the-art works.

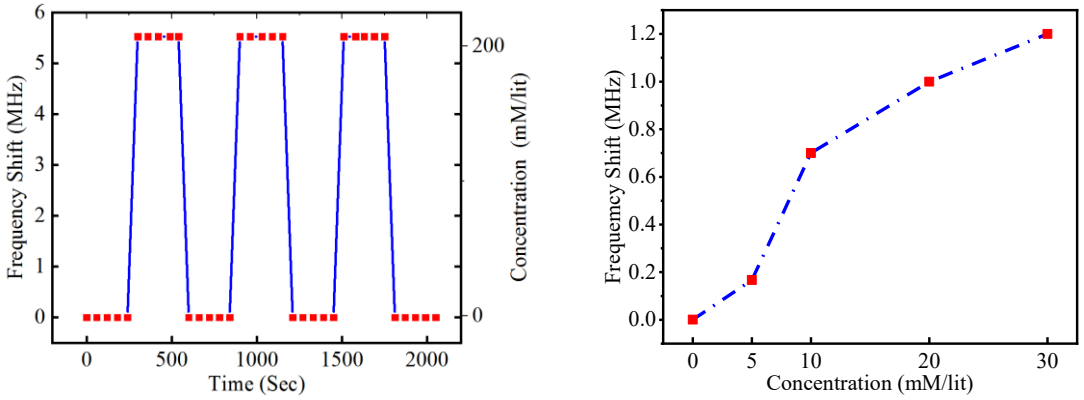

(a) (b)

Fig. 3.31. Experimental results of impact of glucose concentration variation in samples with DI water + serum + saline solution. (a) Frequency shift of the sensor as the response to alternatively changing the glucose concentration from zero to 200mM/lit. it could be seen that, the proposed sensor presents a stable and repeatable response over time. (b) Frequency shift of the sensor as the response of small variation of glucose concentration. It could be seen that, according to introducing of the skin between the sensor and the sample, the overall sensitivity is reduced to 38 kHz/1mM/lit of glucose concentration variation.

Although microwave resonators possess impressive characteristics, there is still a very challenging issue remained. Since any variation in the permittivity of MUT is reflected in frequency shift of the resonator, there is a concern about the uncertainty of the actual source of frequency shift. For addressing this issue, an extensive discussion part including some experiments is provided.

The presented sensor aims to measure glucose concentration in ISF which is a fluid contains around 40% of human body's water surrounding the cells acting as the nutrient transporting from blood capillaries and waste collecting medium for the cells. Beside water and plasma, ISF contains glucose, fatty acids and minerals. So far, glucose variation effects

have been tested. Here, we provide some experiments for studying the effects of mineral variations on the frequency shift of the sensor. the main minerals in ISF are, Sodium, Potassium, Calcium, Chloride, Bicarbonate and Phosphate. Since Sodium and Chloride have one or more orders of magnitude higher variation range in comparison with the other minerals, for the sake of simplicity, they considered as the only varying minerals in the experiments. It could be seen from Fig. 3.32 that since minerals mostly affect the conductivity of the MUT, it won't change the frequency of the sensor. Hence, since frequency change is considered as the main output of the sensor, mineral concentration variations is not interfering with results from glucose related frequency shift. In addition, fatty acid concentration variation inside ISF is in the range of µM/lit which its effect is negligible on frequency shift in comparison with effect of glucose variation.

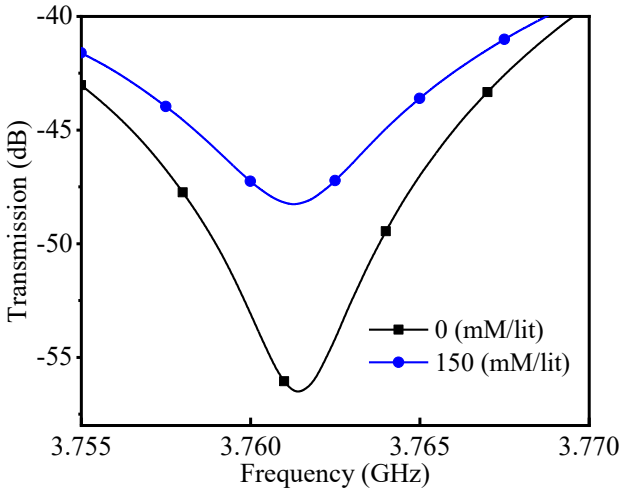

Fig. 3.32. Effect of saline variations on the response of the sensor; here only Na and Cl concentrations have been changed as the major electrolytes in ISF from 0 to 150mM/lit. Although the maximum variation happens in human body is limited from 136-150 mM/lit, an exaggerate variation is tested here to presents the proof of concept. It could be seen that saline concentration has in important impact on the amplitude of the response but its resulting frequency shift is less than 20KHz which is completely negligible. The case would be even more negligible in real life case, because of less variations in the electrolytes.

The most important parameter which needs a special attention is dehydration. Dehydration happens as the results of loss of more water than we take. It could mostly

happen because of diarrhea and vomiting or bladder or lung infections for old adults. It also could be simply occurred due to not taking enough water in a hot summer. Dehydration directly affects the water content in ISF and therefore could change its permittivity and consequently affects the performance and precision of the sensor. Sample preparation method is presented in the next section. Fig. 3.33 presents the frequency shift versus dehydration percentage with all the other ingredients remained constant. It could be seen that, low to moderate dehydration has a minor effect on the frequency shift even less than the effect of 1 mM/lit variation in glucose concentration. But severe dehydration could overtake the frequency shift as the result of glucose variation and produce a completely wrong response. By taking the possible users of this system into account, whom are diabetes patients, their lifestyle supposed to be under control and they are very unlikely to be

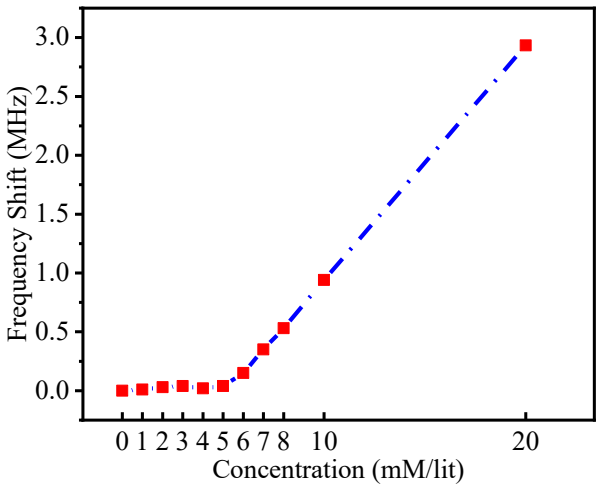

Fig. 3.33. Frequency shift as the results of dehydration. It could be seen that, low to moderate dehydration (up to 5%), have very small interference with the response of the sensor. But, severe dehydration could have the same impact on the frequency shift as about 50mM/lit variation in glucose concentration. Although it's results in huge error, severe dehydration is a deadly problem and patients should be hospitalized immediately accordingly. So, one could consider the effect of low to moderate dehydration as a minimal error which is less than the impact of 0.3mM/lit variation in glucose concentration.

subjected to severe dehydration. Moreover, severe dehydration is very dangerous itself and could be fatal and required emergency care, so this false response, if occurred, could be

taken into account as an alarm for taking the patient to hospital immediately. By considering all the mentioned discussions, it seems that the proposed structure, with its remarkable features, could be considered as a reliable sensor for real-time glucose monitoring non-invasively.

Chapter 4 Distant Sensing Enhancement Using Locally Strong Coupled Microwave Resonator

In Chapter 3, a noncontact reader-tag microwave sensor has been introduced where the tag is the main sensing element energized through its EM coupling with the reader. Comparing to the conventional planar microwave sensors, the introduced concept significantly enhances sensitivity while the sample under test is placed in further distances. The introduced chipless tag is a great candidate for harsh environment sensing and wearable non-invasive biomedical sensors. The sensor has been applied to real-time Volatile Organic Compound (VOC) concentration detection (as low as 10 ppm) for air quality monitoring applications. Furthermore, the simultaneous detection of multiple gases and vapors (i.e., VOC and humidity) compounds in a gas stream is another application of the proposed system. The proposed methodology has the potential to be applied for sensing multi-component gas mixture in harsh environment sensing applications. The impressive performance of the reader-tag based sensor, which removes many barriers against utilization of microwave resonator sensors for biomedical applications and especially wearable electronic, provided the possibility of distant glucose sensing with an accuracy of ~1mM/lit with 38 kHz of the resonance frequency shift. Besides all these advantages, there is a need for a constant coupling strength over longer distances in some applications such as non-contact wireless microwave sensors for oil and gas industry and biomedical applicators.

In this chapter, new coupled structures have been investigated to achieve longer distances in planar microwave sensors. It is shown that there is a positive correlation between the gap

size in a pair of gap-coupled transmission lines (GCTLs) and the effective distance of reader and sensing resonators in a planar microwave sensor. On the other hand, the coupling strength in a pair of GCTLs is negatively correlated to the gap size between the two lines where the larger gap sizes result in weaker coupling strength or vice versa. Strong electromagnetic coupling is locally demonstrated between a pair of GCTLs using a new artificial perfect electromagnetic conductor (PEMC) boundary. A practical and easy-to-fabricate combination of perfect electric and magnetic boundaries is demonstrated which does not allow electromagnetic power reflected to the source over larger gap sizes in GCTLs. In Section 4.1, the gap coupled transmission lines will be studied and in Section 4.2, the theory behind localized EM region is illustrated. Section 4.3 is focused on application of the introduced design in sensing. In Section 4.4, the proposed structure with strong localization of EM coupling is employed to design flexible distant microwave gap-coupled resonator for humidity, Bitumen, and glycerol level sensing applications.

4.1 Study of Distant Gap Coupled Transmission Lines

GCTLs are used as the main discontinuity in planar microwave structures to selectively couple EM waves form I/O ports to a resonator [115]–[121]. The coupling between the coupled transmission lines is directly proportional to the closeness of the lines. Fig. 4.1 shows the EM simulated results of the coupling between the conventional GCTLs for different values of the gap size. Inspecting the results, the coupling is significantly dropped by increasing the gap size. On the other hand, larger gap sizes between GCTLs are required to design a non-contact microwave sensor for longer distances between the reader and tag. Fig. 4.2 shows the schematic diagram of a typical microwave sensor including a reader and a sensing tag. For longer distance monitoring, the gap size between the GCTLs (ℓc) must

be increased to realize proportional wavelength variation for EM waves between the two GCTLs (ℓc) on one hand and GCTLs and the tag (ℓct1 and ℓct2) on the other hand.

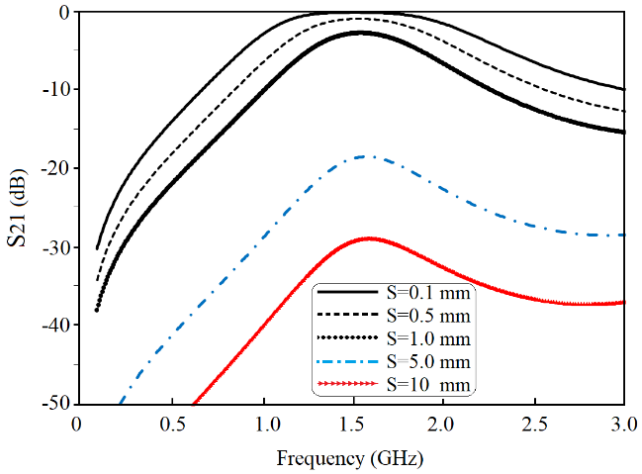

Fig. 4.1. EM simulated coupling between the conventional GCTLs for different distances with maximum coupling level: S=0.1 mm (S_{21}=0.2 dB), S=0.5 mm (S_{21}=0.9 dB), S=1.0 mm (S_{21}=2.75 dB), S=5 mm (S_{21}=18.5 dB), S=10 mm (S_{21}=28.9 dB).

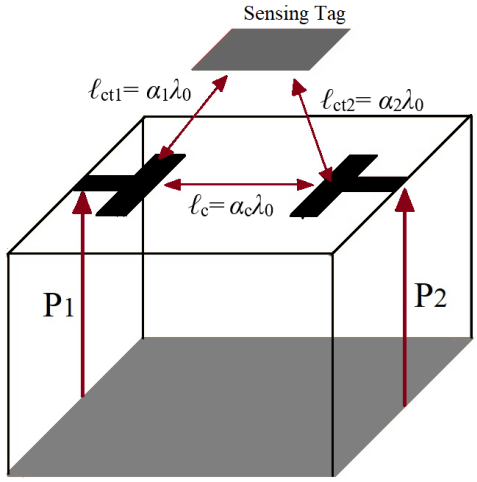

Fig. 4.2. Schematic diagram of a typical noncontact microwave sensor including a reader and a sensing tag.

The primary requirement for the realization of a typical sensing structure in Fig. 4.2 is to reduce the dependence of coupling strength on the closeness of the lines (ℓc) in a pair of CGTLs. EM waves are more reflected to the source by increasing the gap size, ℓc, through coupling to the ground of the structure. Artificial perfect electromagnetic conductor (PEMC)

boundary is employed to decrease the coupling between the GCTLs and the ground and subsequently block the reflected EM waves to the source. There are some techniques to block the reflected EM waves using PEMC boundary including high-permeability posts and metal wires both perpendicular to ground, Tellegen particle or photonic bandgaps [122]–[124]. These techniques are reported to be effective for EM waves blocking in some certain areas; however, they add complexity to the structure. Here, a simple technique is developed with the least complexity realized on a single-layer substrate.

As shown in the proposed artificial PEMC boundary (See Fig. 4.3(a)), the area with the strongly localized coupled EM waves under the CGTLs is enclosed using PMC boundary [28]. The PMC boundary isolate the area with the strong coupled EM from the rest of the ground with weakly coupled EM waves. On the other hand, the isolated metallic conductor under the GCTLs behaves as an artificial PEC boundary which increases the coupled EM waves between the GCTLs. It is shown that the artificial PEMC boundary makes the coupling strength independent of the coupled transmission lines' closeness.

Lumped element equivalent circuit is employed to explain the mechanism of strong coupled fields in the distributed-element transmission lines (See Fig. 4. 3 (b)). The lumped element equivalent circuit of each TL can be considered as a *Π C-L-C* circuit coupled through air and the material inside the substrate [44], [125], [126]. As studied in [44], the series *L-C* part of the circuit behaves as a short circuit at the frequency corresponding to λ/4. At this frequency the EM waves are maximally coupled to the ground and reflected to the other TL.

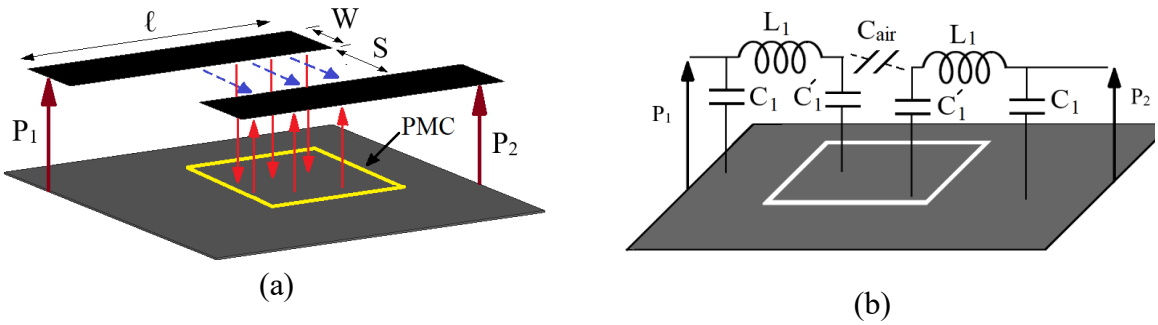

Fig. 4.3. (a) GCTLs with locally strong coupling (b) Lumped element equivalent circuit with ℓ=37 mm and W= 1 mm.

Fig. 4.4(a) shows the lumped element equivalent circuit of the structure in which the detached PEC boundary under the GCTLs is modeled with an inductor, e.g., L′p. The coupled lines and the PEC boundary are modeled with lumped element components while the ground plane is distributed element structure. Inspecting the circuit, there are two paths for the EM waves to be coupled from port 1 to port 2. The two paths include L1-Cair-L1 and L_1-C' -L_p- C'- L_1 circuits. The values of lumped element components are calculated using the following equations [44]:

$$\omega L = 2Z_0 \tan\left(\frac{\theta_0}{2}\right) \qquad (4\text{-}1)$$

$$\omega C = \frac{\tan\left(\frac{\theta_0}{2}\right)}{2Z_0} \qquad (4\text{-}2)$$

The values of *L*-*C* components in the circuit are calculated using equations (4-1) and (4-2) at f_0=1.6 GHz corresponding to the electrical length of λ/4 with the characteristic impedance of 113 Ω. This characteristic impedance is calculated for a transmission line with a width of 1 mm on a 1.52-mm-substrate with a dielectric constant of 2.2. The calculated values of the lumped element components in Fig. 4. 4(a) are optimized to match the EM and *LC* simulated results. Table 4.1 gives the optimized values of the components.

Fig. 4. 4(b) compares the simulated results for the lumped and distributed element structures. A good agreement is observed over the pass-band of the structure except a spurious resonance frequency at 2.9 GHz. This spurious resonance frequency is due to capacitive coupling between PEC boundary and the ground which has not been incorporated in the lumped element equivalent circuit.

Table 4.1 Optimized Values For Lumped Element Components In Fig.3

Component	C1 (pF)	C1′ (pF)	Cair (pF)	L1 (nH)	Lp′ (nH)
Opt. Value	0.47	1	0.1	5.1	11

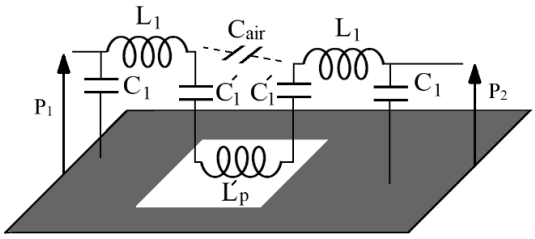

(a)

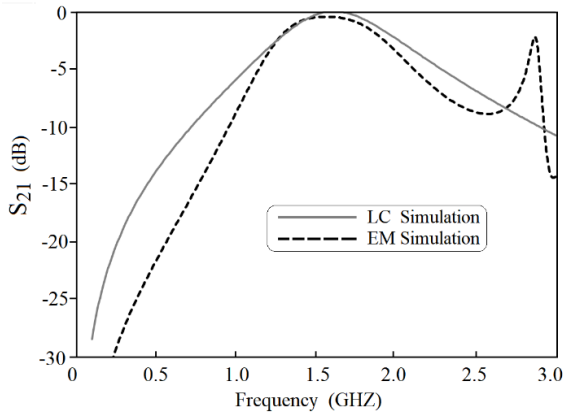

(b)

Fig. 4.4. (a) Lumped element equivalent circuit of the detached locally strong-coupled EM waves (b) LC and EM simulated results.

The increase in the gap size of the GCTLs mostly affects the C_{air} in the circuit. To validate the concept, the structure is simulated for the different values of the gap size between the GCTLs. Fig. 4.5 shows the EM simulated and measured results of the coupling strength

between the GCTLs for different values of the gap size compared to the conventional ones. The results show that the coupling strength is gradually dropped by increasing the gap size of GCTLs in the developed structure in contrast to the conventional ones .

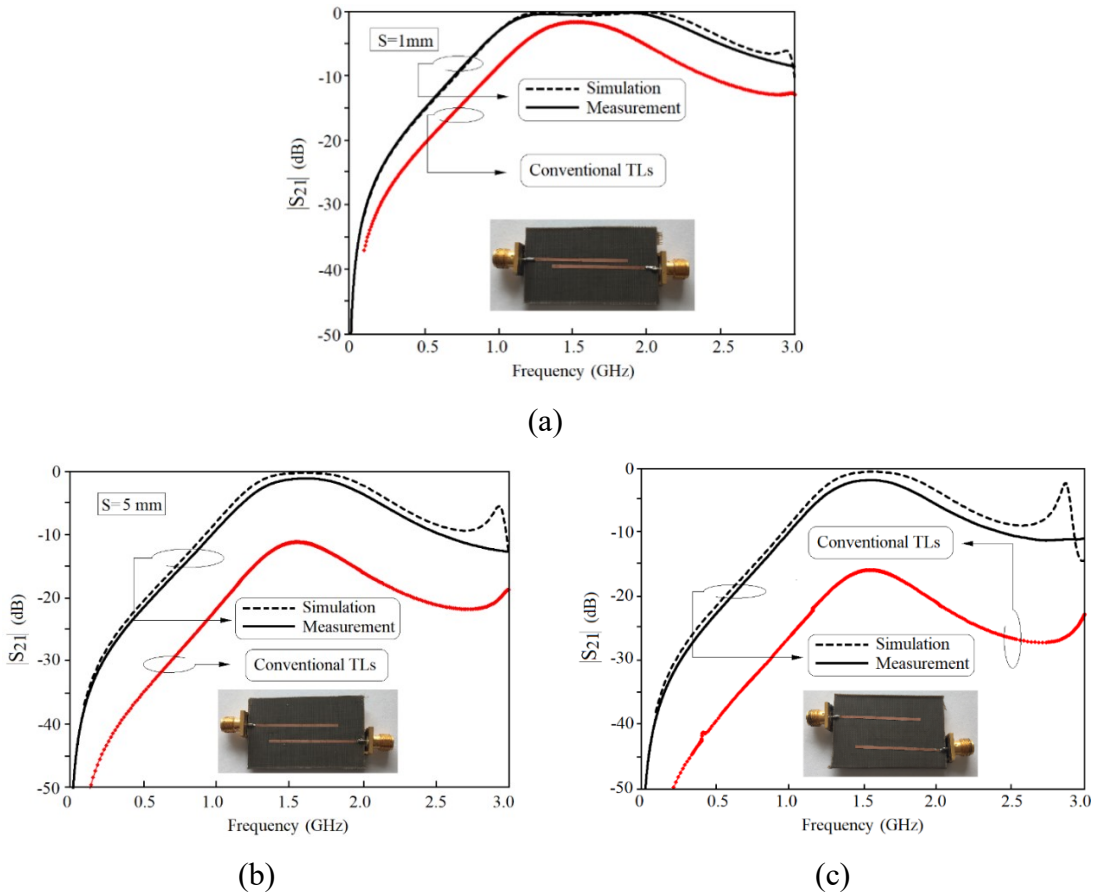

Fig. 4.5. EM simulated and measured results of the coupling strength between the GCTLs for different values of gap size compared to the conventional ones (a) S=1 mm (b) S=5 mm (c) S=10 mm.

Table 4.2 compares the coupling strength in the conventional and developed GCTLs for three different gap sizes of S=1 mm, 5 mm and 10 mm. The simulated results in Table II confirm that the coupling strength between the GCTLs in the developed structure is significantly independent of the gap size. A strong over-coupling is observed for the gap size of 1mm which imposes an extra insertion loss by separating the different modes of the structure [19]. This results in a coupling with wider bandwidth (Fig. 4.5(a)). In another effort, the coupling strength between the GCTLs and the detached PEC boundary is studied

for distance variations. Later is shown that the detached PEC boundary can be used as a sensing tag (strongly coupled to the main resonator as a reader) for distant sensing applications.

Table 4.2 Measured And Simulated Coupling Level Of The Modified And Conventional Coupled TLs

Distance (mm)	Conventional TLs	Modified TLs (Sim/Meas)
S=1.0	-2.52 dB	-0.82/-0.9 dB
S=5.0	-11.1 dB	-0.23/-1.0 dB
S=10	-15.9 dB	-0.47/-1.8 dB

4.2 Study of Distant Localized EM Waves Region

4.2.1 Patch-Based Sensor

It has been shown that the coupling strength variation versus the gap size in a pair of GCTLs can be controlled by detaching the localized area with strongly coupled EM waves from the non-localized area with weakly coupled EM waves in the structure. In this section the GCTLs and the detached PEC boundary with strongly coupled EM waves are used as the reader and sensing tag to design a noncontact distant sensor.

Fig. 4.6 shows the structure of the noncontact sensor in which the detached PEC boundary is placed away from the GCTLs with the distance of S1. The lumped element equivalent circuit of the entire structure is derived in which the detached PEC boundary is modelled with an inductor, e.g., L''_p, coupled to the rest of the circuit via C_1''. The circuit in Fig. 4. 6(b) is similar to the one in Fig. 4. 4(a) with different values for the lumped element components. The difference between the values originates from the unequal dielectric constants of the substrate and air.

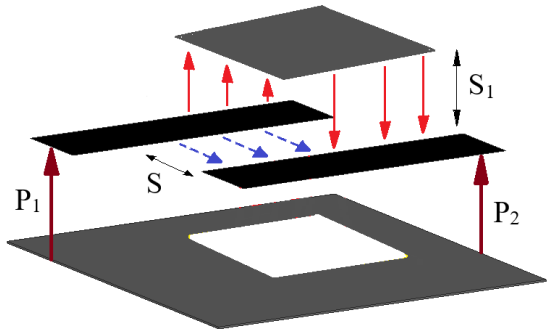

(a)

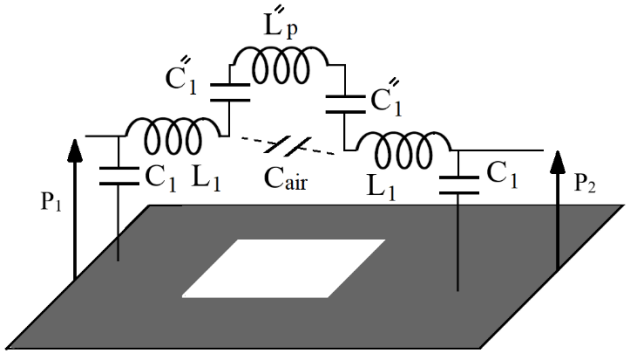

(b)

Fig. 4.6. (a) Detached PEC coupled to GCTLs (b) Lumped element equivalent circuit.

Fig. 4.7 shows the EM simulated results of the structure with a fixed gap size of S=5mm in the GCTLs and different distances between the detached PEC and GCTLs, e.g., S1=1 mm and S_1=5 mm (See Fig. 4.7(a)). The structure is redesigned for S=10mm, S_1=1 mm and S1=10 mm (Fig. 4.7 (b)). Inspecting the results for S=5 mm, the structure demonstrates two wide-band band-pass couplings at f_{01}=1.72 GHz and f_{02}=1.68 GHz with the fractional bandwidths (FBWs) of around 58% and 50% for S1=1mm and 5mm, respectively. The results for S=10mm are reported to be two wide-band band-pass couplings at f_{01}=1.72 GHz and f_{02}=1.71 GHz with the FBWs of around 42% and 34% for S_1=1mm and 10mm, respectively.

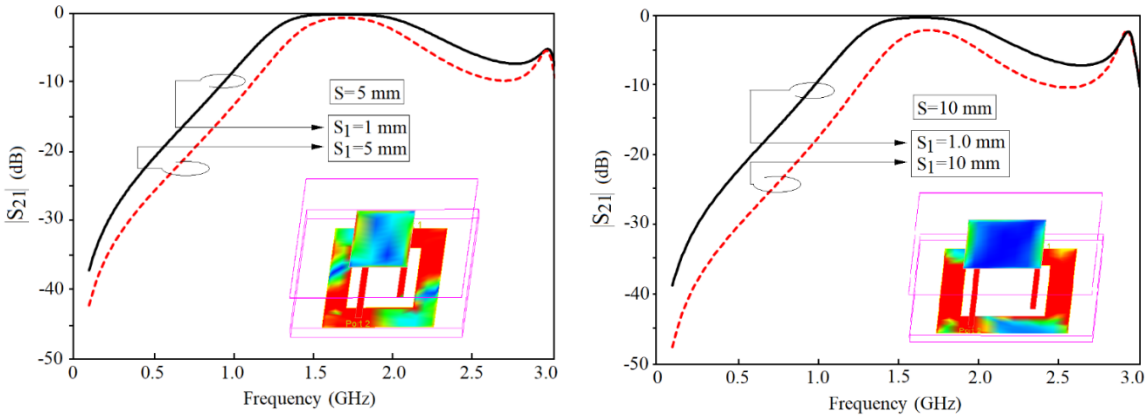

Fig. 4.7. EM simulated results for distant patch (PEC) (a) S=5mm, S1=1 mm (solid lines) and S1=5 mm (dashed lines) (b) S=10mm, S1=1 mm (solid lines) and S1=10 mm (dashed lines).

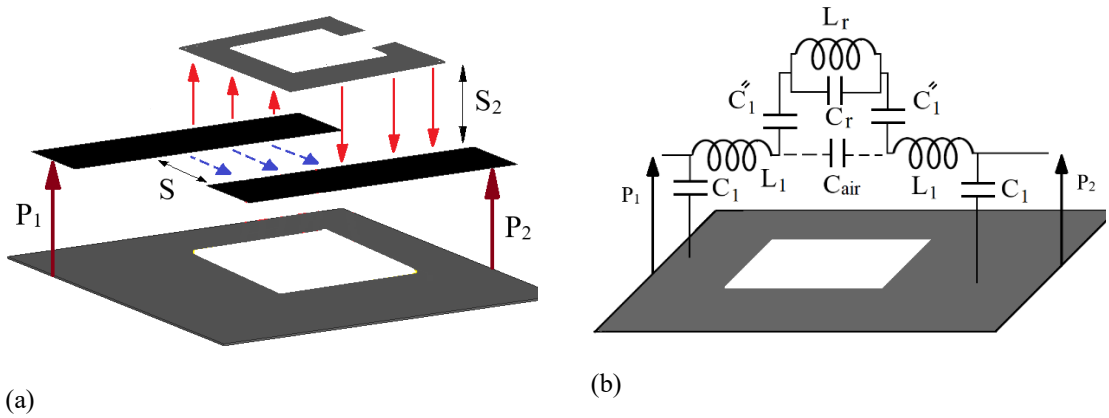

Fig. 4.8. (a) Distant open-loop ring resonator coupled to GCTLs (b) Lumped element equivalent circuit.

4.2.2 Resonator-Based Sensor

As shown in Fig. 4.7, the structure with the uniform PEC (detached patch) demonstrates a wide-band (low quality factor) coupling between I/O ports. As studied in [19], open loop ring resonators are capable of high-quality pass-band realization. To increase the quality factor of the structure in Fig. 4.7, consisting of the distant PEC patch coupled to GCTLs, the uniform patch is replaced with a microstrip open-loop ring resonator (See Fig. 4.8(a)). Fig. 4.8(b) shows the lumped element equivalent circuit of the structure in which the tag resonator is modelled with a parallel Lr-Cr circuit [29]. The structure is simulated on a 1.52-mm-thickness substrate with a dielectric constant of 2.2.

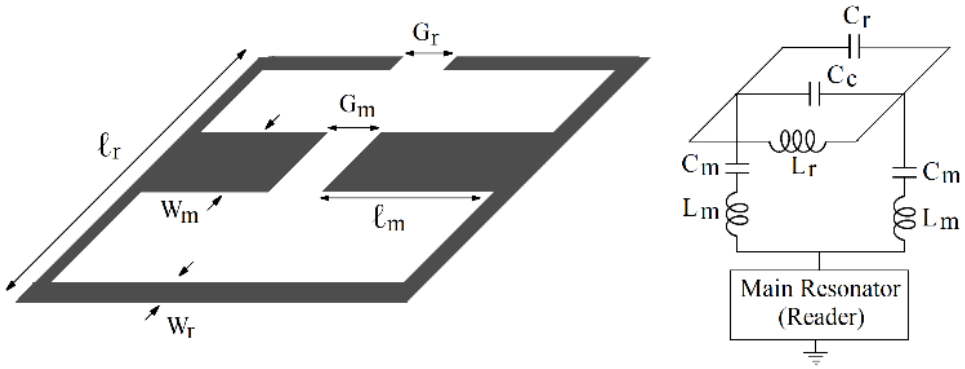

(a) (b)

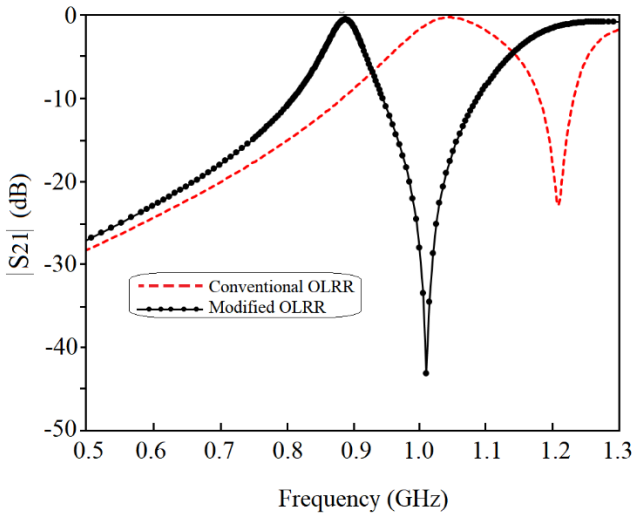

(c)

Fig. 4.9. Open-loop ring resonator (OLRR) integrated with two low-impedance end-coupled stubs (b) Lumped element equivalent circuit (c) EM simulated performance compared to the conventional one without stubs with optimized values of ℓr=21.5mm, ℓm=21mm, Wr=1mm, Wm=9.2mm, Gr=1.54mm and Gm=1.27mm.

To further increase the quality factor of the conventional open-loop ring resonator, two low-impedance end-coupled stubs are incorporated in the resonator (See Fig. 4.9(a)). The two coupled stubs realize a coupling capacitor, Cc, as well as two series Lm-Cm circuits between the tag and the reader (See Fig. 4.9(b)) [30]. The coupling capacitor Cc improves the quality factor of the resonator (See equation (4-3) [17]), while the two series Lm-Cm circuits increase the suppression level of the resonator's transmission zero [126].

$$Q = \omega_0(C_r + C_c)R \qquad (4\text{-}3)$$

where ω0 and R are the resonance frequency and the loss of the resonator, respectively [118].

Fig. 4.9(c) compares the EM performances of the modified open-loop ring resonator in Fig. 4.9(a) with and without low-impedance end-coupled stubs as the conventional structure. The two open-loop ring resonators demonstrate two pass-band filters with fractional bandwidths of 5% and 13.3% at the resonance frequencies of f_{01}= 0.89 GHz and f_{02}=1.05 GHz, respectively. The suppression level for the transmission zeros of the two resonators are reported to be -43.1 dB and -22.8 dB at f_{tz1}= 1.09 GHz and f_{tz2}=1.21 GHz, respectively.

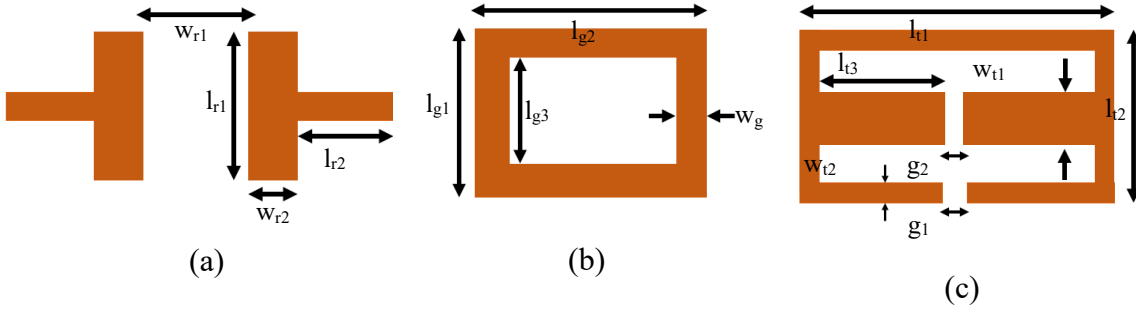

Fig. 4.10. Schematic of the proposed microwave sensor including (a) reader top side, (b) reader bottom side and (c) flexible tag.

4.3 Sensor Design and Simulation

The detailed schematic for the proposed sensor is presented in Fig. 4.10. The core of this sensing platform consists of a flexible sensing tag placed vertically at a distance from a microwave reader circuit. The design procedure starts with determining the critical dimensions of the reader circuit. The front side of the reader circuit (Fig. 4.10(a)) consists of two coupled transmission lines.

The coupling between the transmission lines directly depends on the distance of the lines. On the other hand, larger gap sizes between the two transmission lines at the front side of

the reader are required to provide the capability of locating the reader and tag. For longer distance monitoring, the gap size between the coupled transmission lines (w_{r1}) must be increased. Reducing the dependence of coupling strength on the closeness of the lines (w_{r1}) is the primary requirement for the realization of an optimum sensing platform.

EM waves are more reflected at the source by increasing the gap size, w_{r1}, through coupling to the ground of the structure. In order to decrease the coupling between the transmission lines and the ground, which results in increasing the distance between tag and the reader, the area with the strongly localized coupled EM waves under the gap-coupled transmission lines has been detached to isolate the localized area with strongly coupled EM waves from the non-localized area with weakly coupled EM waves in the structure. The dimensions of the defect of the ground plane have been optimized in order to minimize the coupling to the ground as well as keeping the coupling high enough for maximizing the distance between the tag and the reader.

The overall length of the tag determines the resonance frequency, which is designed based on the material used as the sample under test. Since the dielectric constant of bitumen is much less than water for a wide range of frequencies, the determining factor for selection of the resonance frequency of the sensor is the conductivity. According to literature, bitumen electromagnetic conductivity is a high value in frequencies between 1 MHz to 500 MHz [127]. Obviously, frequencies less than 1MHz will result in unrealistically large dimensions for the sensor and therefore slightly higher frequency than 500 MHz has been selected for this application. Additionally, the $l_{t3} * w_{t1}$ elements are added to the sensing tag in order to maximize the capacitive coupling between the tag and the reader. This improvement in optimizing the resonance frequency and the coupling enables the tag to perform sensing at

a higher vertical distance from the reader. The design details and critical dimensions of the proposed microwave sensor are demonstrated in Fig. 4. 10 for both sides of the reader and the tag. The quantity for the dimensions is shown in Table 4.3.

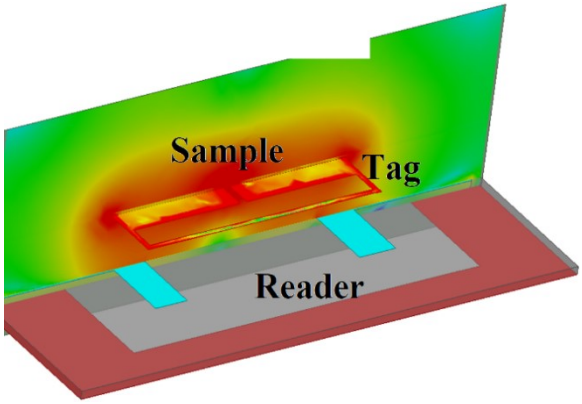

Fig. 4.11.Electromagnetic field distribution between the reader, tag and sample.

Table 4.3 Design parameters for the proposed sensor (dimensions are in mm)

Parameter		Parameter	
wr1	33.3	wg	14
lr1	25.4	lt1	45
wr2	7	lt2	21.4
lr2	24.6	lt3	20.5
lg1	57.27	wt1	9
lg2	95.8	wt2	1
lg3	40	g2, g1	1.4

To achieve better insight into the designed sensor, Fig. 4.11 presents the electromagnetic field distribution of both reader and tag. As illustrated in Fig. 4.11, field concentration around the tag at the sample position is strong. Fig. 4.12 compares EM simulated results of the structure for different vertical distances between the tag and the reader (d) increasing

from 10 mm to 60 mm. Inspecting the simulated and measured results, both the resonance frequency and quality factor increase with increasing distance, satisfying expectations.

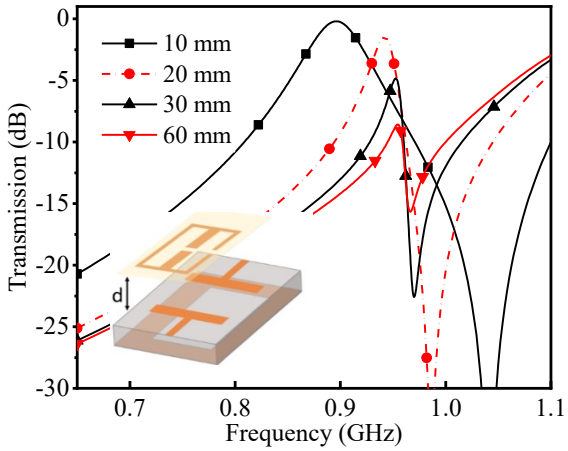

Fig. 4.12. EM simulated and results of the resonator coupled with the reader for different distance d = 10 mm, 20 mm, 30 mm, and 60 mm.

The response of the resonance profile of a microwave sensor is dependent on the variation of the complex permittivity in the ambient area of the tag resonator. The complex permittivity is described by:

$$\varepsilon = \varepsilon' - j\varepsilon'' \qquad (4\text{-}4)$$

where ε' is the real part of the permittivity, indicating the polarity of the substance. The imaginary part ε" is called loss factor, and is a measure of dissipation or loss of a material in the presence of an external electric field. Variation in ε' will affect the resonance frequency ($f_r \propto \frac{1}{\sqrt{\varepsilon'}}$); f_r is the resonance frequency (Hz)). Variation of ε" will primarily be reflected in changes in amplitude and quality factor.

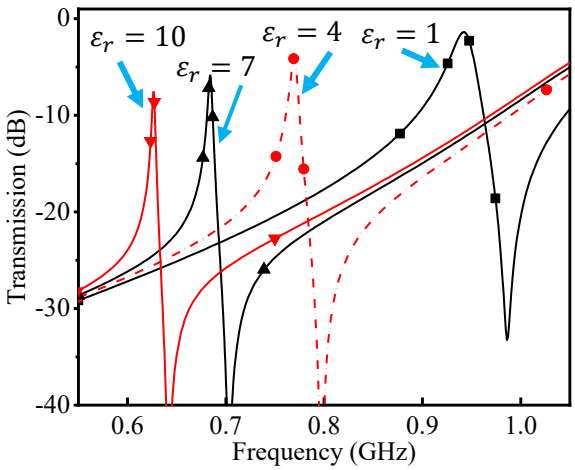

(a)

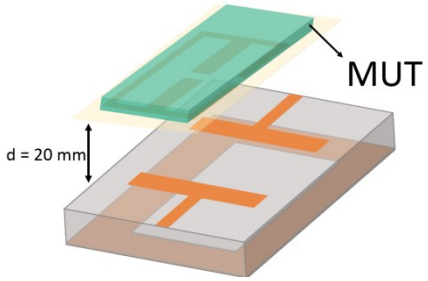

(b)

Fig. 4.13. (a) Resonant frequency variation for 4 different effective permittivities (ε_r) of the MUT, (b) the schematic to clarify MUT location.

The sensing capability (sensitivity) of the structure was verified in simulation by maintaining a vertical distance of 20 mm between the tag and reader while placing a 1mm-thick MUT above the tag. The relative permittivity ($\varepsilon_r = \frac{\varepsilon'}{\varepsilon_0}$) of the MUT was varied from 1 to 10 to observe the change in resonance frequency. Fig. 4.13 (a) and (b) present the resulting transmission response of the simulation.

Another noteworthy simulation is the stability of the sensor while misalignment or rotation is impacting the placement of the tag and the reader. Fig. 4.14(a) shows the

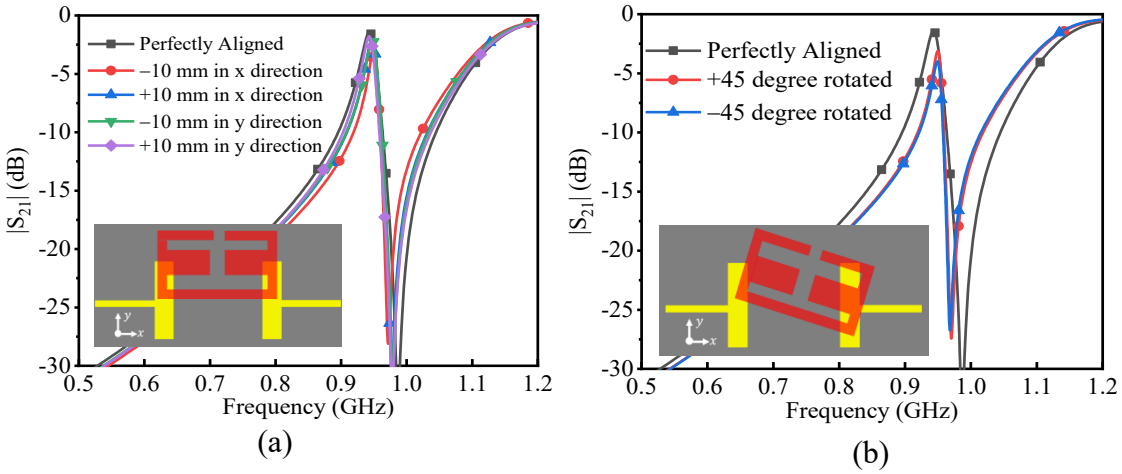

Fig. 4.14. EM simulated results of the noncontact sensor (a) different distances, S2= 10 mm, 20 mm, 30mm and 40 mm the tag and the reader distance changes from d = 5 mm to 12mm, (b) Tag with misalignments (c) Tag with ± 45 degrees rotation (the top view of the tag-reader pair is included).

resonance profile variation of the sensor in which the tag and the reader are placed away in the vertical distance of 20 mm (S_2 = 20 mm) with tag misalignment in x or y direction. The results in Fig. 4.14(a) show that the tag misalignment has negligible impacts on the performance of the sensor in comparison to the case with no misalignment. Fig. 4.14(b) shows the EM simulated results for the case in which the tag is tilted and placed in a vertical distance of S_2 = 20 mm from the reader. The results confirm sustainable performance of the sensor with the different positions of the tag and reader.

4.4 Applications of the Proposed Defected Ground Structure in Distant Sensing

In this section, some of the most important application enabled by the proposed sensor are introduced. Due to the demonstrated sensing potential up to 60 mm, the sensor is great candidate for harsh environment and high temperature sensing.

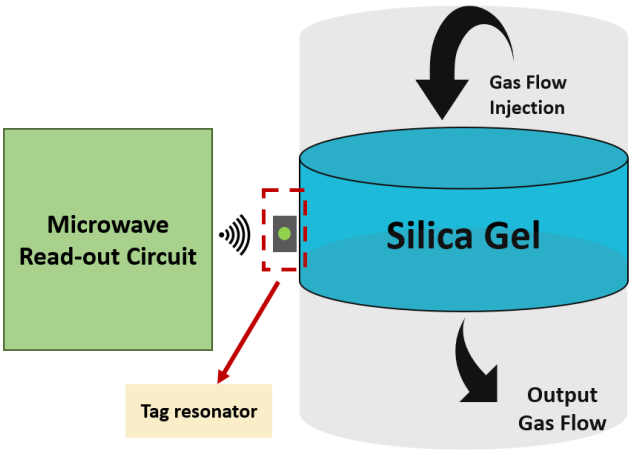

Fig. 4.15. Schematic of a noncontact gas sensor based on open-loop ring resonator coupled to GCTLs.

Porous-structure absorbents are sensitive to specific vapor and/or humidity. As they are exposed to humidity, the moisture is absorbed and settled down into their pores and subsequently the overall effective permittivity observed by the sensor will be increased. The permittivity of adsorbent will be changed due to its interaction (i.e. adsorption) with target compound (e.g. humidity). The permittivity changes, however, depend on the concentration of the compound in the gas stream. The compound (i.e. adsorbate) concentration in the gas, therefore, can be measured using the sensor by correlating the variations in permittivity and compound concentration.

4.4.1 Adsorbent Assisted Humidity Sensing

In the applications where the sensing environment must be isolated from the electronics, the proposed reader and tag structure offers a great solution for real-time monitoring. The proposed coupled structure in this chapter is employed to design a noncontact sensor conducting Relative Humidity (RH%) sensing in longer distances between the reader and the sensing tag.

Adsorbent material near the resonator is employed to improve the selectivity as well as the sensitivity of the microwave sensor [13], [14]. Fig. 4.15 schematically shows the proposed humidity sensing structure. Industrial Silica Gel is used as the adsorbent to increase the sensitivity of RH% detection. The chipless passive tag, open-loop ring resonator, enables the sensor to operate with zero DC power in harsh and inaccessible environments.

The proposed structure is experimentally tested for humidity sensing. Fig. 4.16 (a) and (b) show the fabricated humidity sensor and measured transmission response for different distances between the tag and read-out resonators. As shown in Fig. 4.16 (b), the transmission response is measured while the distance between the tag and reader resonators is increased from 2 mm to 60 mm.

Fig. 4.17 shows the schematic and experimental setup of the humidity sensor. The gas detection set-up consists of mass flow controllers (MFC), a Vector Network Analyzer (VNA), and a data acquisition system which is performed using LabVIEW software recording the signals every 10 seconds. The output of the MFCs is humidified to be saturated (100% relative humidity). 4g of Industrial Silica gel adsorbent is used for the experiments. Prior to testing, the samples are heated in an oven at 120ºC overnight to remove impurities such as moisture. Resonance frequencies of the sensor will be changed in the consequence of the changes in the effective permittivity of the environment (Silica Gel). The chipless tag represents exclusive behavior with respect to near-by ambient variation. The tag is placed at 35 mm distance from the readout resonator.

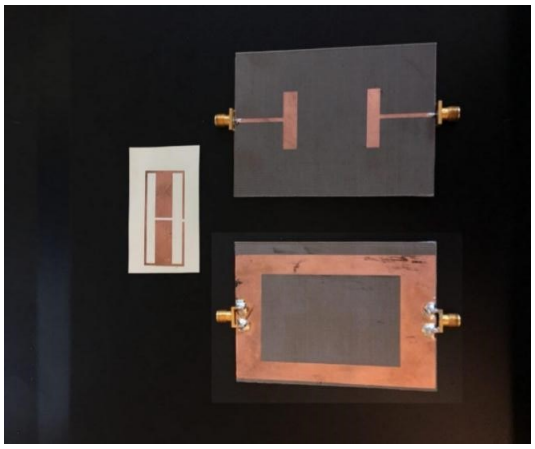

(a)

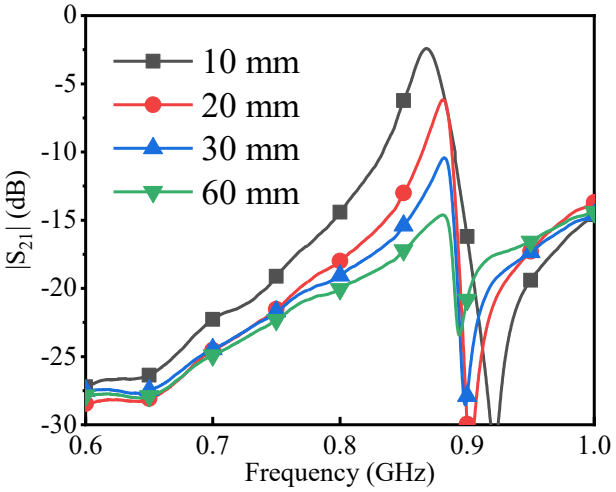

(b)

Fig. 4.16. (a) Fabricated humidity sensor: tag, top and bottom views of the reader with coupled lines 25mm×5.6 mm, gap size of 33.6 mm, two μ-strip lines of 24.5mm×1.8 mm for port connections (b) Measured S21 response for different distances between tag and the reader from 10 mm to 60 mm.

The sensor monitors the permittivity variations due to the adsorption of water vapor in the beads. Moreover, Blue Silica Gel beads start to change their color to pink after 2 minutes of being purged by humid air which is an additional indication of absorbed humidity. Fig. 14(a) shows the transmission response of the sensor at the start time, after 500 seconds, and after 1400 seconds of flowing the humid air with RH% of 50 through the quartz tube. Fig. 4.18(b) shows the measured results of humidity sensing for different RH% (RH=30% to 100%) versus the sensor resonance frequency shift.

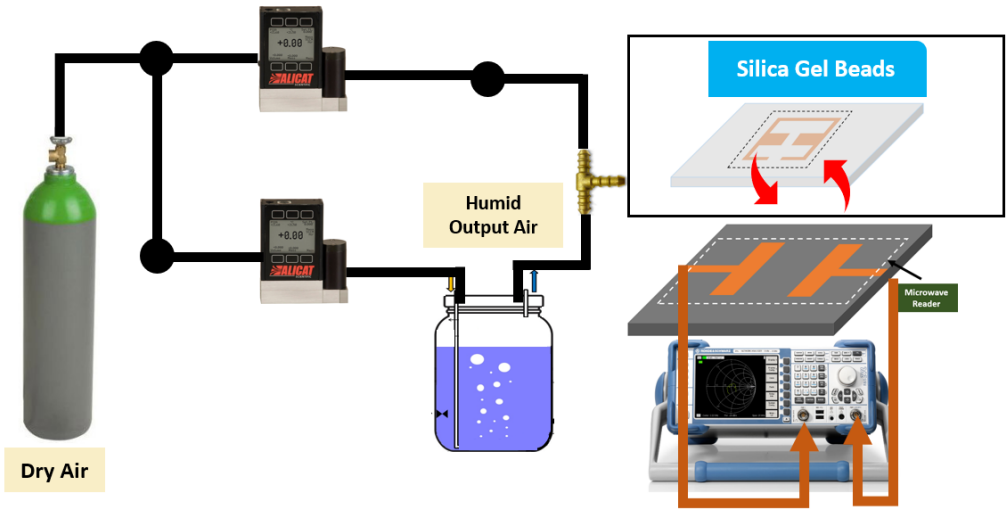

(a)

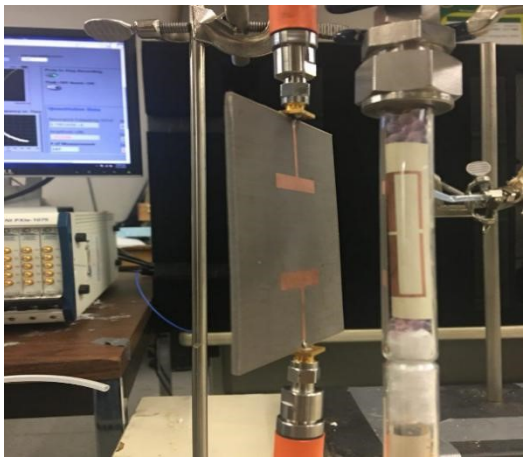

(b)

Fig. 4.17. Humidity sensing (a) schematic and (b) In lab set-up containing the implemented reader, chipless tag, and silica gel as the humidity adsorbent.

Table 4.4 Measured RH% for Different Time Constants

RH%	A_1	t_1	y_0
30	33.81	-850.1	-34.26
50	56.97	-730.12	-56.93
70	107.57	-649.57	-107.52
100	154.88	-520.32	-154.80

Fig. 4.18(b) shows the measured results of humidity sensing for different RH% with the sensor resonance frequency shift from RH=30% to 100%. The time-based measurement

graphs in Fig. 4.18 (b)has been approximated with an exponential function to extract the time constant for each of them. The parametric exponential approximation function is $y = A_1 e^{\frac{x}{t_1}} + y_0$ and the parameters for each RH% is presented in Table 4.4. The time constant can be used for any measurements result to be related to the RH%.

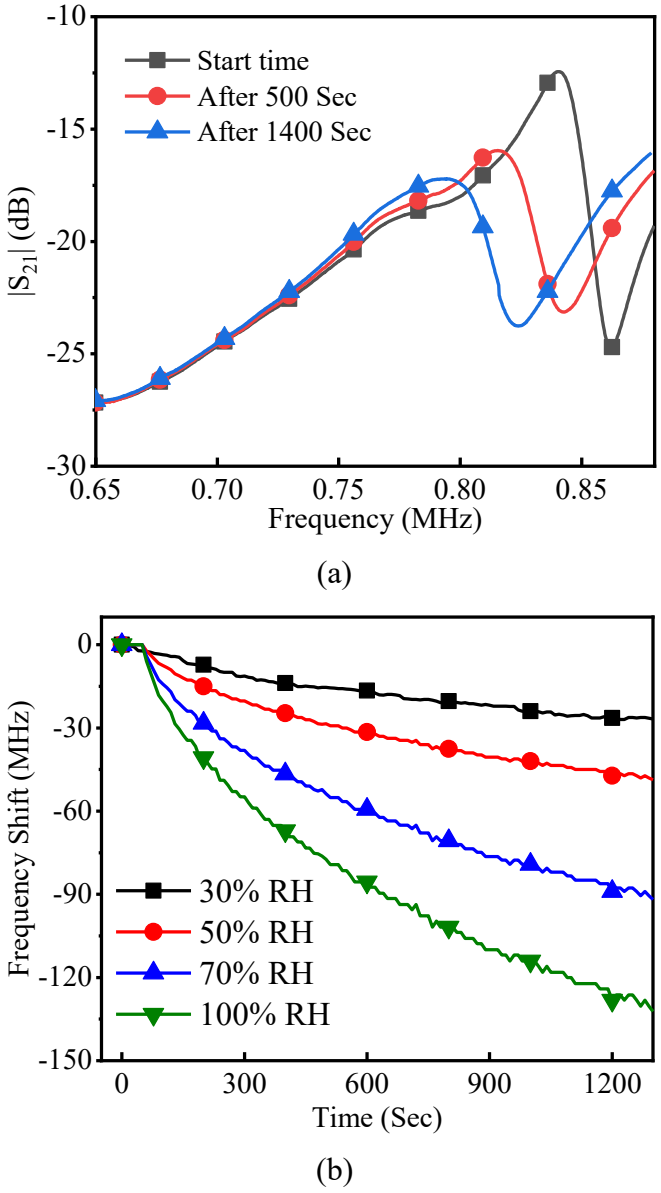

Fig. 4.18. (a) Transmission response of the sensor at the start time, after 500 seconds, and after 1400 seconds (b) Frequency shift of the sensor for RH=30% to 100%.

Table 4.5 Comparison Of Conventional And Developed Noncontact Sensors

Ref.	Structure	freq. (GHz)	Size (λg2)	Contact	Distance (mm)
[128]	Planar microwave	0.51	0.6×0.3	No	1
[129]	Active+ Coil	0.12	Not Given	No	4
[6]	3D Cavity	2.5	0.5×0.5	No	3
[5]	Active + Microwave	2.5	0.7×0.5	No	3
[130] (the proposed design)	Planar Microwave	0.85	0.4×0.2	No	36

Table 4.5 summarizes the performance of the developed noncontact microwave sensor compared to the conventional ones in terms of structure, operation frequency, size and sensing distance. Inspecting the results, the developed noncontact sensor, not only realizes a miniaturized planar microwave sensor, it but also significantly increases the effective sensing distance between the reader and sample under test.

4.4.2 Design and Implementation of Microwave Resonator for Bitumen Concentration Measurement at High Temperatures

Bitumen is an extremely viscous form of petroleum available naturally in many countries with 28.11 Gm3 (70.8%) of the worldwide bitumen deposited in the form of oil-sand in Alberta, Canada [131]. Bitumen production is generally associated with massive water consumption. In the SAGD process, about 20% of the produced mixture, after 90% of recycling, is water [132]. Therefore, real-time water content monitoring is essential for

energy and water management through the production process [133]. In addition, since bitumen refining and purification is a highly exhaustive and intensive process, continuous monitoring of water content could reduce the consumed energy by process optimization especially in SAGD.

The front-end of the bitumen refining process is gravity separation, usually with aeriation assistance. The output of this process is called bitumen froth, which contains about 50-60% of bitumen, a near-constant percentage of solids around 8-9% and 30-40% of water [133]. Cell performance is gauged by the fraction of the recovered bitumen where aeration, temperature and time are all important. Hence, real-time monitoring of the process output is essential in this stage. Froth requires further treatment to obtain the product quality for downstream reactor either by paraffinic or naphthenic processes. These processes remove water and solids to achieve a higher quality bitumen called dilbit. Unfortunately, dilbit still contains 2-5% of the water in the form of small trapped droplets [134], [135]. Water concentration monitoring in this step is crucial, and the water content available in the mixture of the final product should be less than 0.2%.

Bitumen content measurement in oil-sand is conventionally carried out by the Dean-Stark method [136]; however, this method is toxic, costly and time-consuming. Another method which has been widely used recently is employing Nuclear Magnetic Resonance (NMR) [137]. Although this technique is much faster than the Dean-Stark method, it is off-line and requires a sophisticated, expensive NMR apparatus. For the optimization of process control and minimization of energy consumption and costs, real-time monitoring of water content is crucial.

The main benefits of these sensors are that they are noncontact and low cost, which has provided a strong solution for many industrial measurement problems [5], [57], [138], [139]. Despite the mentioned benefits, conventional microwave SRR-based offer limited field distribution requires that the MUT be placed very close to the hotspot of the sensor [140]–[142]. A chipless RF tag sensor associated with a defected ground gap-coupled transmission line reader would address difficult challenges, such as real-time, highly sensitive water content measurement in bitumen at high temperatures (harsh environments). According to these promising capabilities, this sensor is able to measure water content in bitumen for both steady-state (batch) and turbulent (continuous) processes in high temperatures.

- *Material preparation:*

The samples were prepared for both low-temperature batch and high temperature turbulent continuous experiments. For the low-temperature measurements, refined bitumen from Cold Lake, Alberta, Canada with the viscosity of 32,800 cp at room temperature was preheated to 100°C to reduce its viscosity to around 170 cp [143] and then mixed with deionized hot water (with a resistivity of 18 MΩ) with different volumetric fractions. Prepared samples were kept in 5 mL plastic vials with sealed lids and cooled down to room temperature. The plastic vials had a relative permittivity of approximately 2.25. Fig. 4.19 shows the prepared samples, and Fig. 4.20 presents the experimental setup for this test.

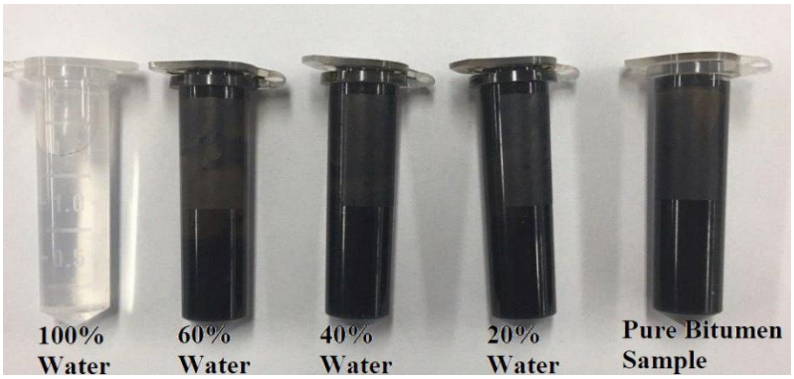

Fig. 4.19. Prepared samples for low-temperature batch experiment.

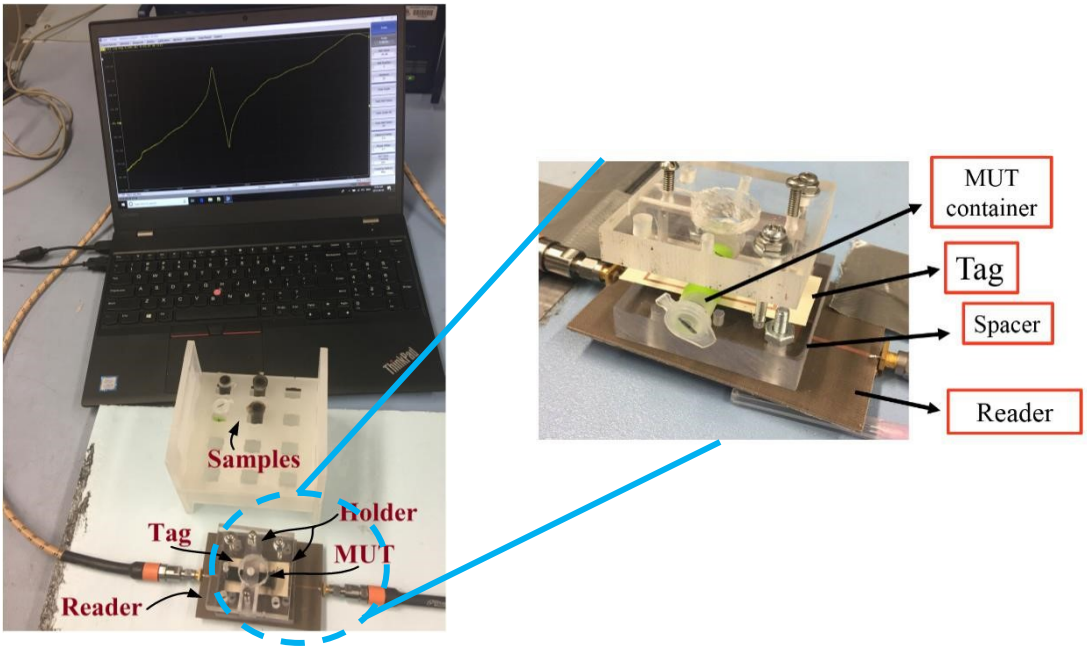

Fig. 4.20. Experimental setup for the low-temperature batch test.

Conditions for experiments at high temperatures require the samples to be measured right after preparation and are discussed in more detail in section 3. The aforementioned bitumen samples were heated up to 250°C and then mixed with boiling deionized water in a heated Borosilicate glass beaker ($\varepsilon_r = 4.3$) with the tag sensor attached to its bottom. The overall mixture temperature was around 210°C during the measurement. The setup for this experiment is presented in Fig. 4.21.

- *Measurement tools and signal processing:*

For measuring the scattering parameters of the sensor, a high-resolution model C2420 Vector Network Analyzer (VNA) from Copper Mountain technologies were employed. For the first experiment (batch), the VNA was calibrated from 600 MHz to 750 MHz with 8001 points to attain a very high-resolution measurement. For the second set of experiments (turbulent), the calibration range was from 500 MHz to 700 MHz with 8001 points to cover significant frequency variation. The transmission parameter (S21) of the tag was used for resonance frequency and amplitude extraction. Room temperature was monitored during the experiments to prevent the effect of environmental temperature variations over the measurements. Attained data from the VNA is further processed using MATLAB.

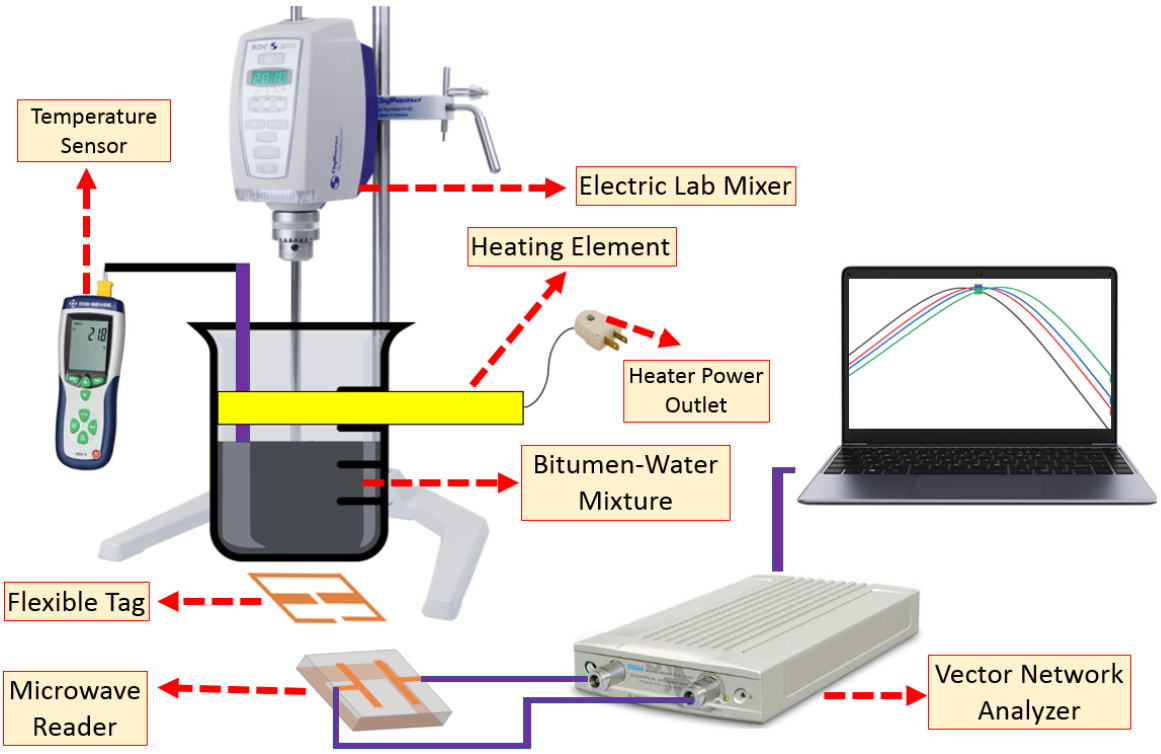

Fig. 4.21. Experimental setup for turbulent online measurement of water concentration measurement in bitumen at high temperatures.

- *Experimental results and analysis*

Low-Temperature Steady-State Measurements: This section addresses measurements in the steady-state room temperature situation (i.e. 25°C), similar to the atmospheric distillation column and batch measurements. Low-to-mid temperature processes, from extraction to final refining, could benefit from the achievements observed in this experiment. It is especially important to characterize froth to identify the efficiency of the system and determine the required amount of solvent to break the emulsion [144].

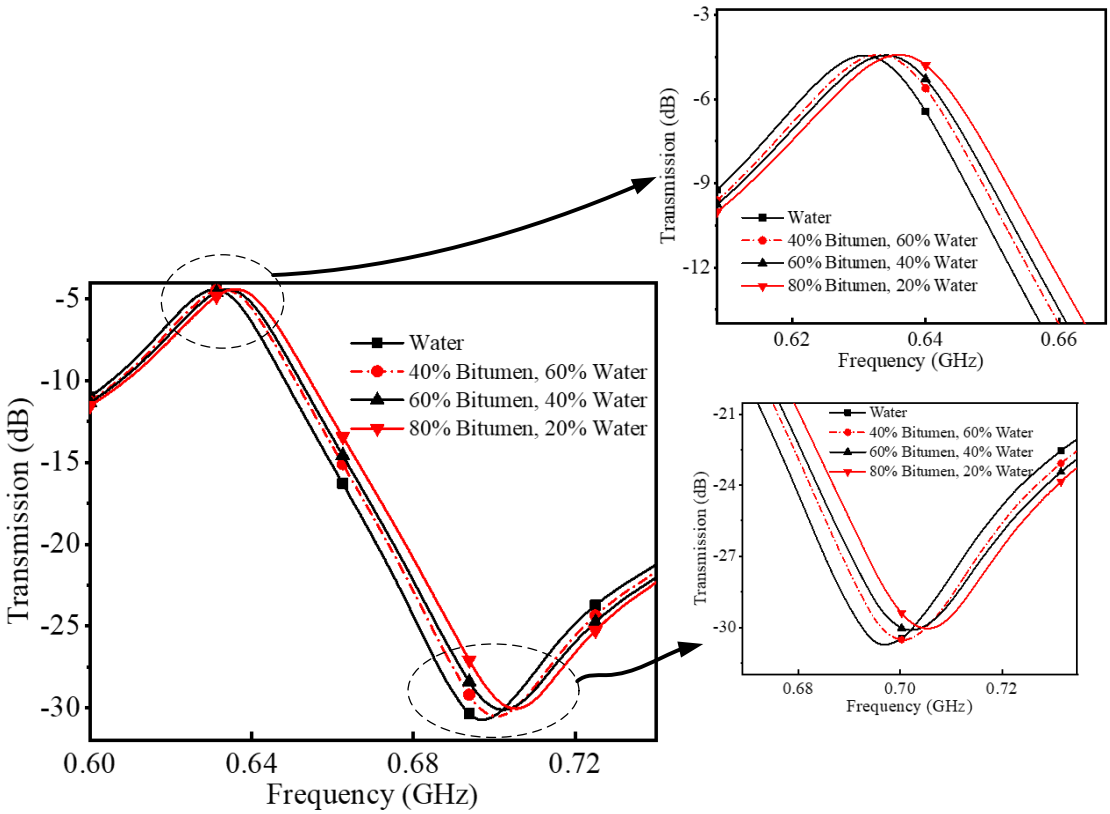

Fig. 4.22. Transmission response of the sensor to the steady-state experiment at room temperature for 5 mL samples with different concentrations of bitumen.

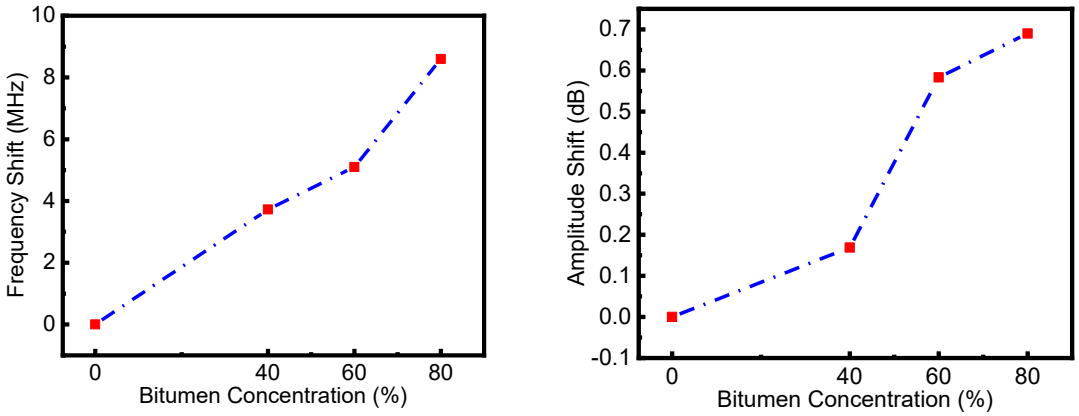

(a) (b)

Fig. 4.23. (a) Frequency and (b) amplitude variations of the sensor versus bitumen concentration in steady-state low-temperature 5 mL samples.

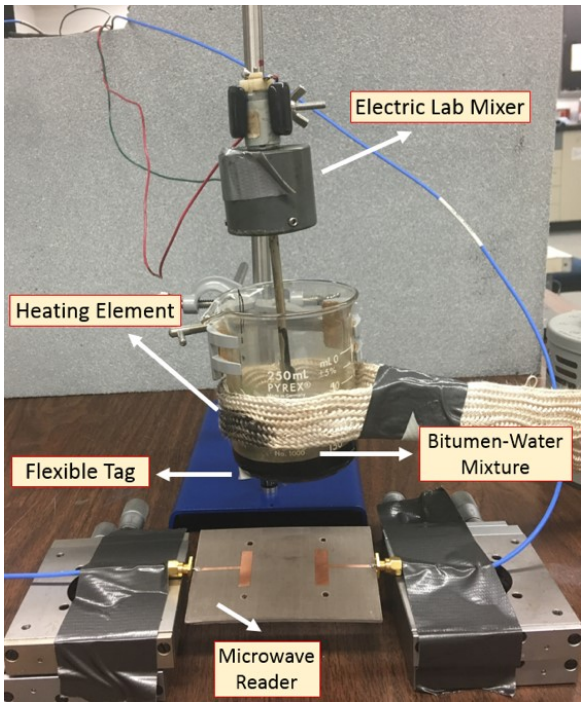

Fig. 4.24. Experimental setup for high-temperature turbulent measurement.

As previously shown in Fig. 2, for this test, deionized water and bitumen were separately preheated to 100°C, mixed, and then cooled to room temperature. Fig. 4.22 illustrates S_{21} (transmission) of the sensor due to the introduction of samples with different bitumen concentration in 5 mL beakers. The tag, when taking the beaker wall into account, is located 2 mm far from the sample. The actual distance between the reader and the MUT is 30 mm.

Fig. 4.23 presents the frequency and amplitude variations of the sensor versus bitumen concentration, respectively. The results present a considerable sensitivity of 100 kHz (1% of bitumen concentration), which is impressive for such a large distance between the sensor and the material. Additionally, over 0.7dB of amplitude variation has been achieved. It is important to mention that the sensitivity to 1% variation in the material is not resolving the sensor detection limit. This value is essential to compare it with the related research available in the literature.

High-temperature turbulent measurement: Another experiment was performed with a different setup to create an in-lab modeling platform for the flow of liquids inside the SAGD extraction process pipes, including the effect of the turbulent materials in high-temperature conditions. The average temperature of this experiment was about 210°C, achieved by using a filament heater wrapped around the beaker. The materials were combined and continually stirred in a 50 mL beaker using a small electric mixer. This helps the bitumen mixture to be kept in a uniform and homogeneous state and avoid any water-bitumen clumps in the solution. The tag is placed directly underneath the beaker, thus experiences very high temperatures during the measurements, while the reader and connected equipment are kept safe at room temperature owing to the gap between the tag and the reader. Fig. 4.24 depicts the experimental setup.

Transmission characteristics of the tag are presented in Fig. 4.25 for different concentrations of bitumen. The resonance frequency and amplitude variations versus bitumen concentration are presented in Fig. 4.26. Interestingly, the sensor exhibits a remarkably large value of 500 kHz (1% of bitumen concentration) for sensitivity, with an overall resonance frequency change of 50MHz for full-scale variation of bitumen. This huge

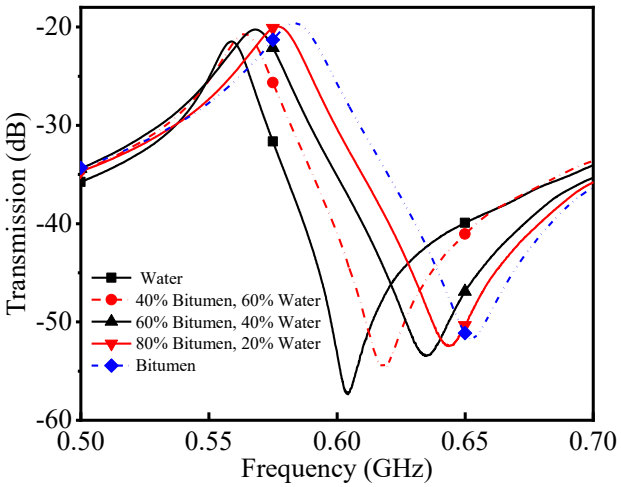

Fig. 4.25. Transmission response of the sensor to the turbulent high-temperature experiment for 50mL samples with different concentrations of bitumen.

improvement in sensitivity in comparison with the previous test is due to a much higher volume of samples (10X), and reduced distance between tag and sample. The latter means, the material was introduced to higher concentrations of electromagnetic fields of the tag, and therefore it will affect the total permittivity around the tag and consequently the resonance frequency.

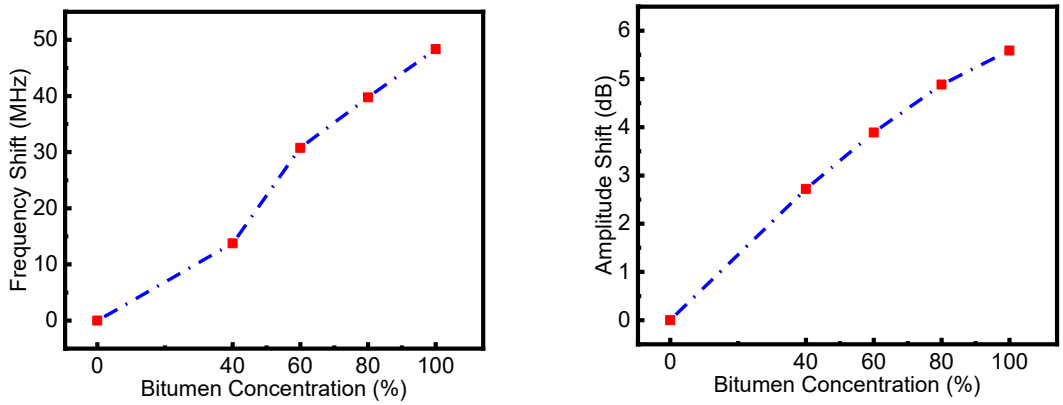

Fig. 4.26. (a) Frequency and (b) amplitude variations of the sensor versus bitumen concentration in the turbulent high-temperature experiment for 50mL samples.

Although, water content in bitumen is brackish water with impurities, all the experiments accomplished in this paper utilized DI water instead for the sake of simplicity. However,

brackish water available in real-life bitumen samples as impurities has a similar dielectric permittivity as DI water but with much higher conductivity. Since the measuring parameter of the sensor is the resonance frequency shift, those impurities will not change the frequency shift response of the sensor but they have a significant impact on the amplitude response. An extra experiment is accomplished, verifying our justification (see Fig. 4.27). In this experiment, the response of the sensor at its resonance frequency to samples with DI water and brackish water with 5g/lit of dissolved NaCl is measured. It could be seen that, although the amplitude responses of the sensor to the samples are different, the resonance frequencies due to the introduction of both samples are exactly the same.

According to the proposed design and structure, the presented sensor is capable of measuring water concentration in bitumen in both steady-state and turbulent conditions at high temperature.

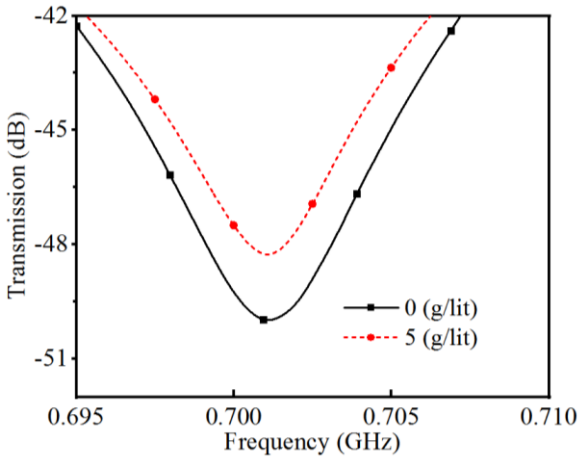

Fig. 4.27. response of the sensor to DI water and water with 5g/lit of dissolved salt; it could be seen that addition of the salt only changes the amplitude response with the resonance frequency remained the same.

4.4.3 Real-Time Non-Contact Integrated Chipless RF Sensor for Disposable Microfluidic Applications

Health care impacted enormously by recent progressive enhancements of Internet-of-Things (IoT) technology. IoT is a paradigm-shifting technology for biomedical applications toward individual specified diagnosis and therapy [145]. The front-end of biomedical IoT is wearable sensors that achieved great deals of interests in recent years [146]–[148]. Due to wearable technology, real-time simultaneously monitoring of multiple human biomarkers is possible, which is crucial for assisting physicians in deciding the best therapies for their patients. Ultimately, in conjunction with artificial intelligence and data processing techniques, wearable sensors technology could result in self-diagnosis self-therapeutic complex systems such as artificial pancreas [149]. These technologies altogether could reduce the diagnosis and therapeutic costs with higher efficiency and precision and help the patients to go back to their normal lives with minimum inconvenience. Liquid sensing is among the most important and useful devices in biomedical applications. However, they use have limitations such as power source requirement, incapability of noncontact sensing, or lacking a cost-effective and user-friendly sensing platform [150], [151].

One of the crucial monitoring parameters in human blood is glycerol level. Glycerol is considered as a very important precursor of intramuscular triglyceride synthesis [152]. Glycerol level in blood is also an indicator of hyperglyceridemia, which is a very serious genetic disorder. According to the national institute of health, this disease affects 200,000 people only in USA [153]. Temporary treatment is usually carried out using amphipathic carboxylic acids in combination with statin to lower the blood LDL cholesterol and triglyceride and to increase blood HDL level [153]. Delayed treatment of this disease could

be perilous and even fatal. Blood glycerol concentration is usually measured by sampling blood from the patients and in addition to being painful to consume a great deal of time. Different methods have been suggested in the literature for determination of the glycerol concentration in human serum including spectrophotometric, gas and liquid chromatography and enzymic methods [154]–[157]. However, these liquid/chemical detection and measurement methods require very sophisticated expensive facilities and are complex, costly and usually consume great deal of time to measure.

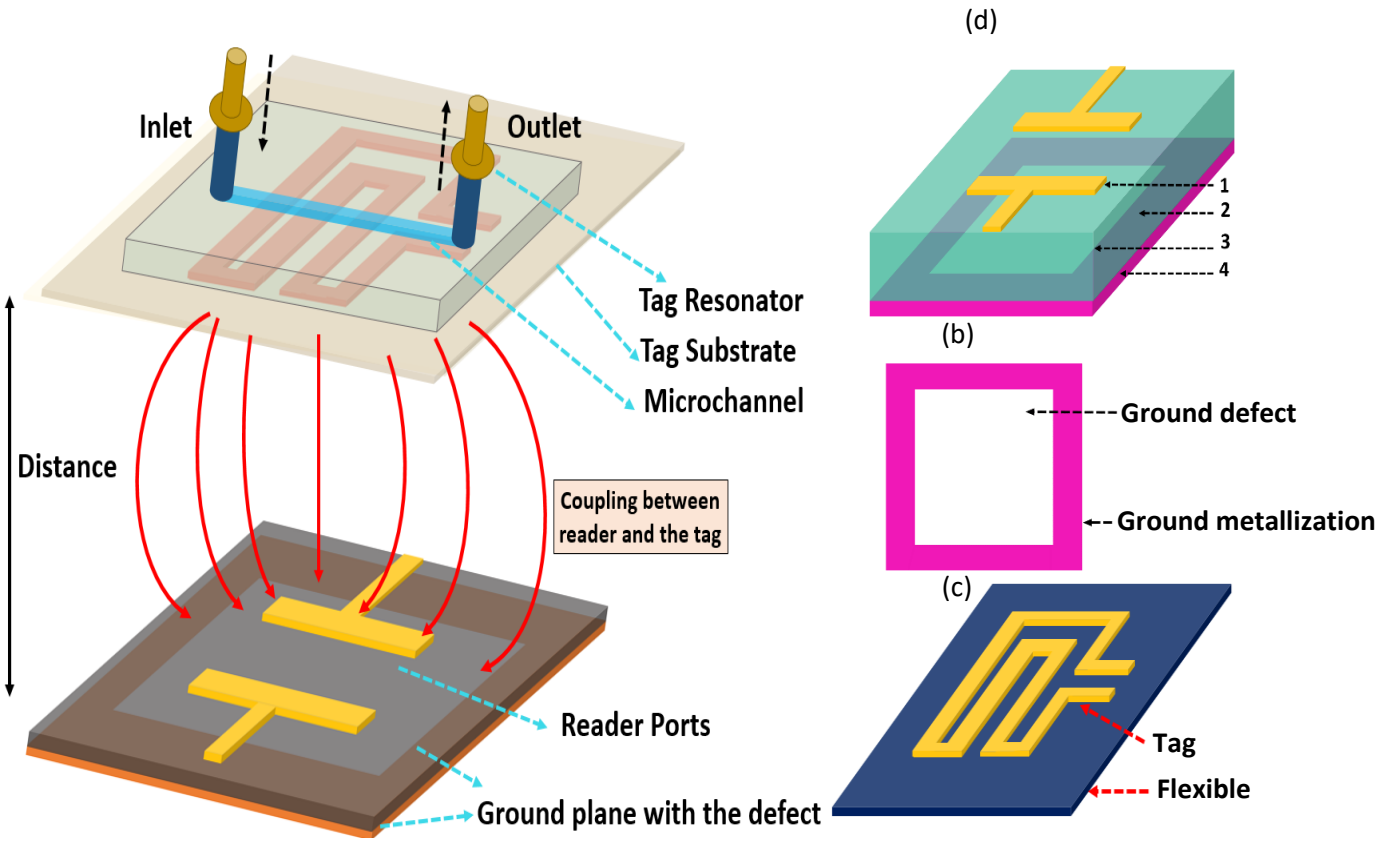

Fig. 4.28. (a) Big picture of the proposed sensing system including RF reader, flexible tag, and microfluidic chip. (b) schematic design of the reader: 1) coupled line ports, 2) substrate, 3) defect in the ground, 4) ground plane metallization, (c) top view of the ground plane including the defect and metallization, (d) flexible tag schematic presenting the tag resonator and its flexible ultra-thin substrate.

Additionally, due to the recent advancements in IoT and E-health care system, there is a great demand for low cost disposable microfluidic chips that can be monitored. Non-

invasive measurement of blood glycerol is, therefore, could be crucial. According to our research, there are no commercialized non-invasive blood glycerol measurement systems available in the market. Therefore, achieving such a promising technology could be brilliant and captivating.

The reader-tag sensor introduced in this chapter provides a new solution for developing a disposable microfluidic chip with sensing capability. This technique enables the sample to be placed further from the readout circuit and only add a chipless tag on the microfluidic channel. Microfluidic channel is employed here to mimic the blood vessels in terms of having a very small volume and also a reliable test structure.

To clarify the proposed design, a big picture of the sensing platform and all the available elements in the sensor are presented in Fig. 4.28. As shown in Fig. 4.28(a), the passive tag is placed under the microchannel, which is filled with samples with different concentrations of glycerol. Due to the strong coupling between the reader and the tag, the readout circuit could be placed with an arbitrary but defined and limited vertical distance from the tag and the sample, which highlights the capability of the structure in non-invasive sensing. As shown in Fig. 4.28(b), the structure of the reader circuit demonstrates gap coupled transmission lines with the special design of the ground plane. The tag resonator (Fig. 4.28(c)) has been designed on a flexible and thin substrate which makes it easier to be mounted on different containers without adding limitations.

- *Sensor Design and Simulations:*

The sensor structure and the schematic of the sensor including the reader, the coupled tag, and the microfluidic chip with the channel filled with the liquid are shown in Fig. 4.29(a).

To increase the quality factor of the reader in Fig. 4.29(a), a microstrip open-loop ring resonator has been used as the tag.

The tag has been designed in order to offer maximum quality factor in the pass-band of the reader. Twisting the microstrip line in the tag design provides lower resonance frequency with a miniaturized structure. Additionally, the sample inside the microfluidic channel will have significantly more interaction with the field distribution around the twisted structure comparing to its conventional ring counterpart.

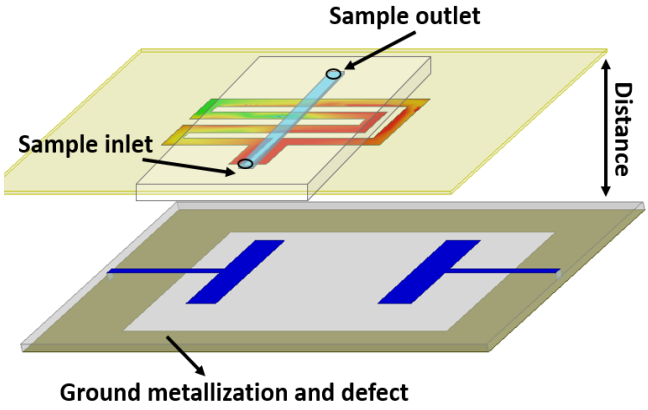

Fig. 4.29. Schematic of the proposed sensing system, including field concentration on the tag.

The sensing capability of the structure is verified in simulations with a constant vertical distance of 25 mm between the tag and the reader at the presence of the SUT and the resulting transmission response is observed. Fig. 4.30 presents the simulated structure while a layer of SUT with 1 mm thickness is placed at 1 mm away above the tag and with different values for the relative permittivity ($\varepsilon_r = \frac{\varepsilon'}{\varepsilon_0}$) of the SUT 1 to 10.

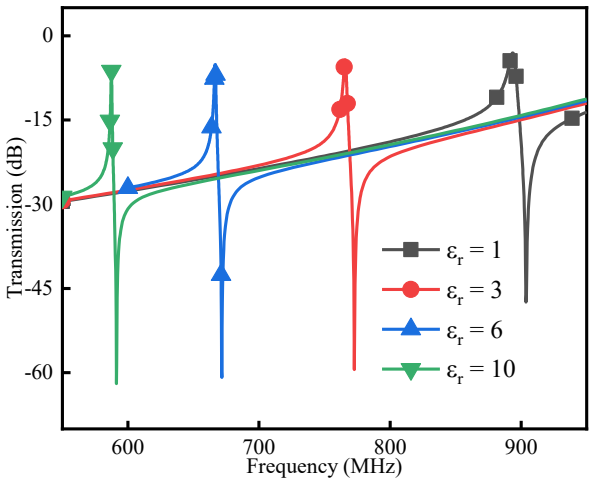

Fig. 4.30. Resonant frequency variation for 4 different effective permittivity (ε_r) of SUT.

As the simulation results illustrated in Fig. 4.30, the range of frequency shift when the permittivity of the SUT layer above the tag changes from $\varepsilon_r = 1$ to $\varepsilon_r = 10$ is 306 MHz. If we define the sensitivity of the sensing system as Δf/Δεr, the presented sensitivity is 34 MHz/(unit ε_r) which makes it capable of detecting small variation of permittivity or loss in the medium around. This considerable amount of sensitivity while using a layer over the tag as the sample emphasizes the potential of the proposed sensor in measuring permittivity variation in small volume scale applications. In Fig. 4.31, $\tan\delta$ (which is $\frac{\varepsilon''}{\varepsilon'}$) is the representation of the effect of increasing in ε'' or conductivity loss. As $\tan\delta$ increases, the amplitude of the transmission response decreases illustrating the sensitivity of the introduced sensing platform to conductivity as well as permittivity. Fig. 4.31(a), presents the results for much smaller variation in permittivity and conductivity of the sample under test where 3.2 MHz shift for $\Delta\varepsilon_r = 0.15$ indicate the capability of the structure for high sensitivity required applications. Additionally, the significant effect of ε''or conductivity loss on the transmission profile is shown in Fig. 4.31(b).

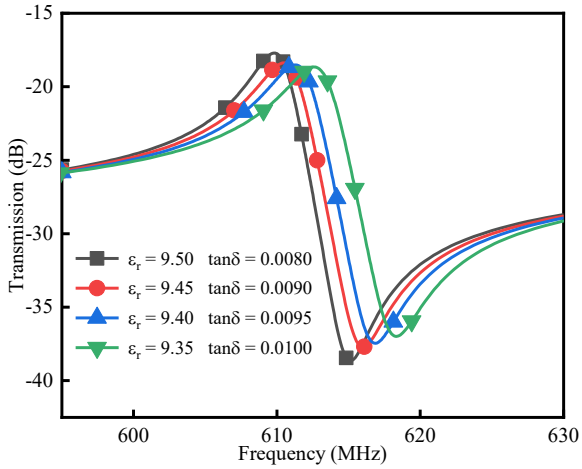

(a)

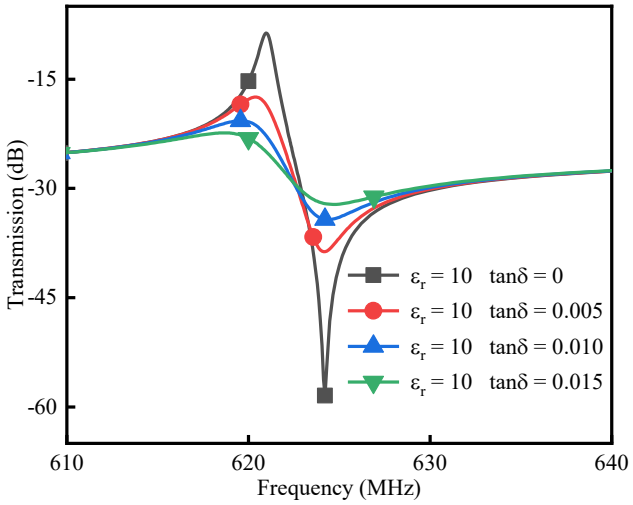

(b)

Fig. 4.31. (b) High-resolution resonance profile monitoring for ultra-small variation in permittivity (εr) and loss factor. (b) effect of conductivity loss of the amplitude and Q-factor of the transmission response.

- *Measurement Results and Discussions:*

After illustrating the sensor performance, the proposed design is integrated with a microfluidic channel to perform liquid sensing in nanolitre scale. The implemented resonators are shown in Fig. 4.32. The reader part is implemented on a substrate from Rogers Corporation (Rogers RT/duroid5880) with the relative permittivity of 2.2, a loss factor of 0.0003, and a thickness of 0.79 mm. The sensing tag is designed on a flexible substrate from Rogers Corporation (Rogers Ultralam 3850) with the relative permittivity of 3, the loss

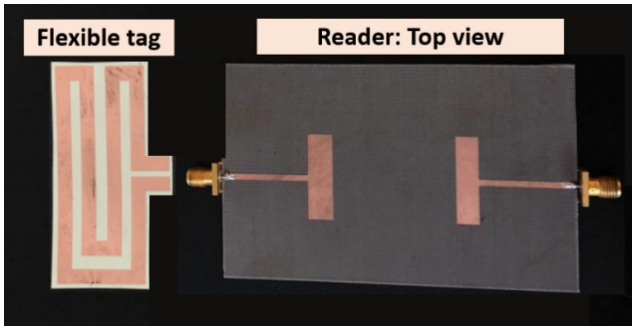

Fig. 4.32. Fabricated tag resonator and the reader circuit.

factor of 0.003, and thickness of 100 μm. The flexibility in the tag substrate enables it to be mounted on the container with any shape and makes it a user-friendly product. The experimental setup of the sensor is presented in Fig. 4.33(a). The chemical detecting setup includes a microfluidic chip with the channel dimensions of 30mm*1.6mm*20μm, a split ring resonator as a tag that is placed at the bottom of the microfluid channel, a reader microwave circuit, liquid injection pump, a Vector Network Analyzer (VNA), and a data acquisition system which is performed using LabVIEW software to record the samples every 10 seconds. The post-processing analysis was performed in MATLAB. As shown in Fig. 4.33(a), different samples have been prepared for the experiment from mixing different concentrations of deionized (DI) water, serum, and glycerol with 70% concentration.Fig. 4.33(b) presents the core of the sensing setup with more details. Flexible tag is placed at the bottom of the microfluidic chip in a way to have the channel over the gap area of the tag where the field concentration is maximum. The tag is placed in a 25 mm distance from the readout circuitry and the channel in Fig. 6(b) is shown while the second sample, is going inside the channel filled with DI water. Three different sets of measurements have been performed in order to demonstrate the sensitivity and resolution of the microwave sensor:

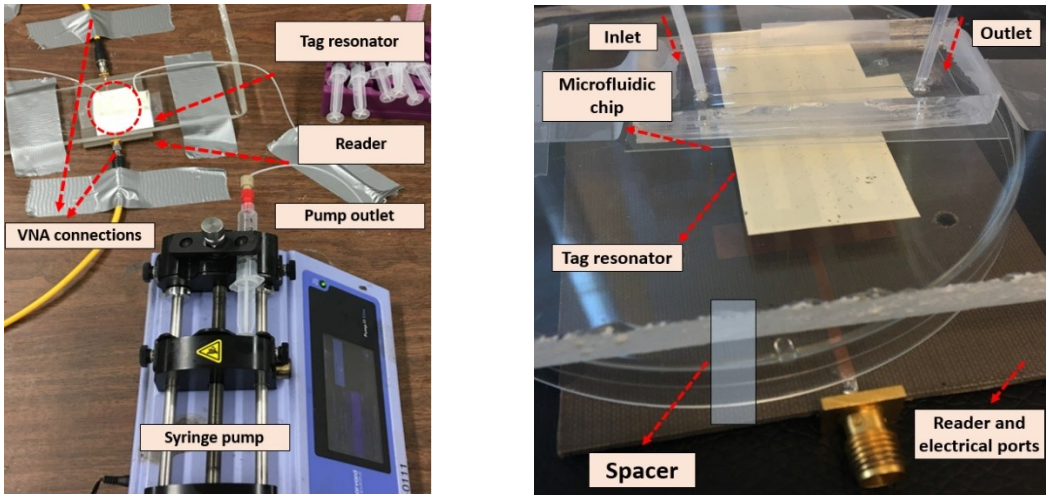

(a) (b)

Fig. 4.33. (a) Actual test setup for glycerol concentration measurement (b) detailed view of the sensor including microfluidic chip, tag resonator, and the reader.

- *Glycerol in DI Water Sensing:*

Five different samples have been prepared to test the sensing capability of the sensor while the concentration of glycerol in the solution changes. As it is shown in Fig. 4.34 (a), when the concentration of the glycerol liquid inside the microchannel changes, the resonance profile of the sensor shifts. As a reference, here we used the notch frequency to monitor the sensing capability of the sensor since it demonstrates more frequency shift and higher quality factor (Fig. 4.34(b)). The notch demonstrates 5.3 MHz of frequency up-shift as the SUT changes from DI Water to glycerol with 70% concentration.

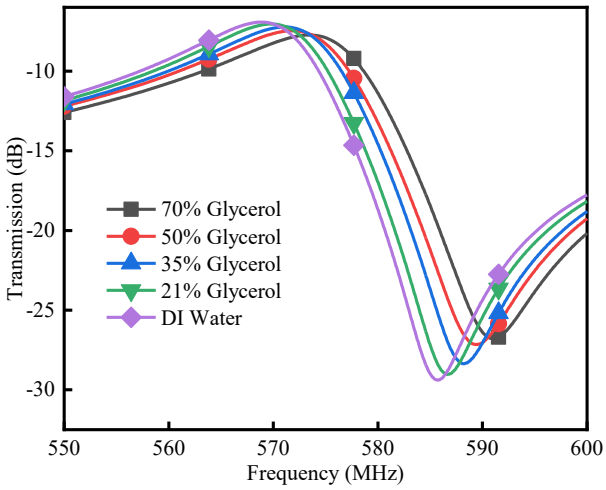

(a)

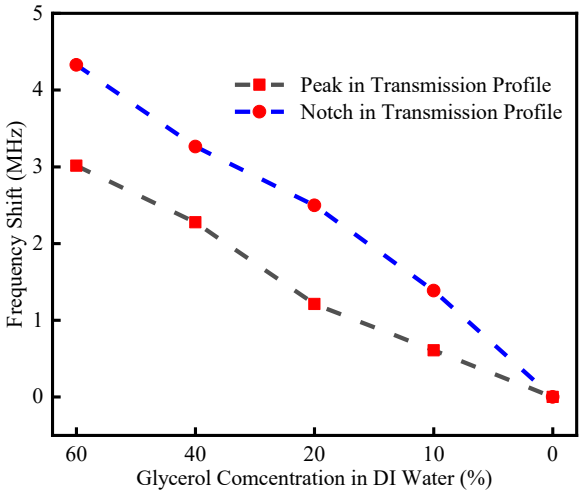

(b)

Fig. 4.34. (a) Resonance profile monitoring with more sensitive notch comparing to peak while the liquid inside the tube changes in concentration of glycerol (0% to 70%). (b) frequency shift monitoring for the peak and notch in the resonance profile when DI water is chosen as the comparison constant.

Time-based measurements have been done while the channel is initially filled with 70% glycerol (loaded Q-factor of 127), the concentration is reduced to the point that there is 100% DI water (loaded Q-factor of 60) at the last step. During all the measurements, the frequency and amplitude of the notch have been monitored as shown in Fig. 4.34(a) and (b). When a new sample with a lower concentration of glycerol fills the channel, the sudden variation in the permittivity and conductivity of the material creates the frequency shift. The steps in

these figures are referring to the time that the material injected from the syringe pump; then the injected sample stays the same for stable measurement. This process is

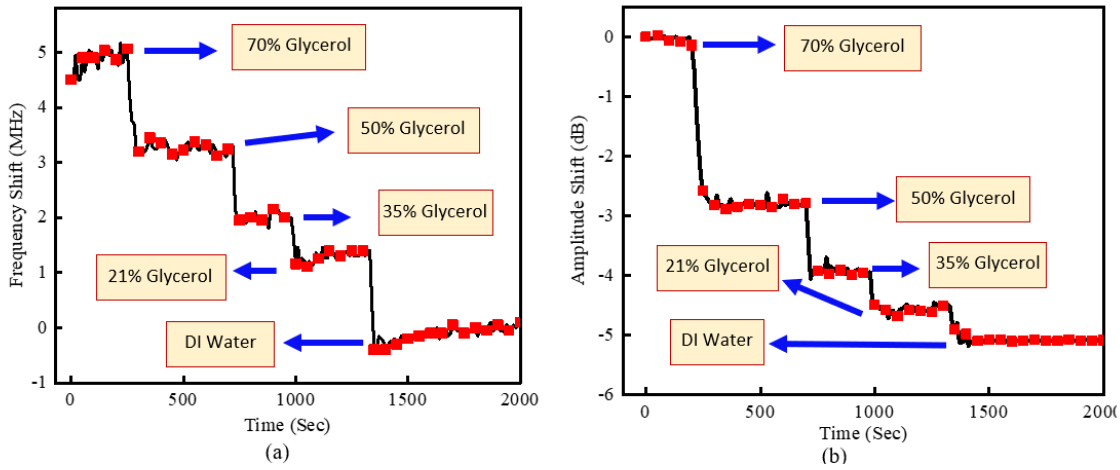

Fig. 4.35. Notch (a) frequency and (b) amplitude variation monitoring during the time while the sample changes from 70% glycerol to DI water.

repeated, and the results are illustrated in the step profile of Fig. 4.35. Since permittivity of the glycerol is less than DI water [158]–[160] in the frequency range this sensor has been designed, increasing the concentration of glycerol in water reduces the effective permittivity of the solution; thus an upshift in the frequency is expected. Additionally, theory verifies the amplitude variation in Fig. 4.35(b) demonstrating the fact that the conductivity of the glycerol is more than DI water ($\varepsilon''_{glycerol} \approx 12$ and $\varepsilon''_{DI\ Water} \approx 5$) in the operating frequency of the designed sensor [158], [161], [162]. In Fig. 4.36, the mean value of the shift in each concentration has been calculated, and the maximum value of the deviation from mean value has been reported as error

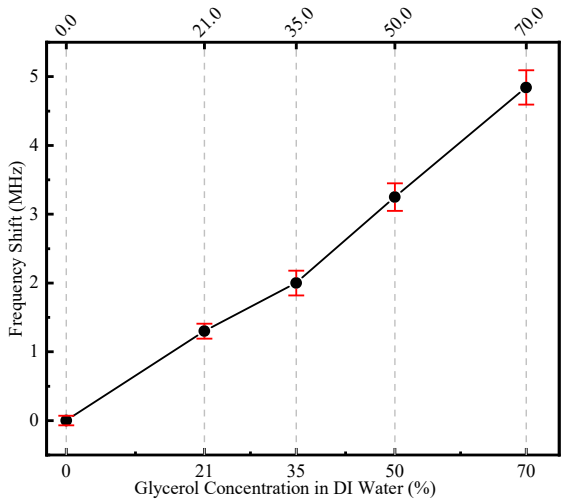

Fig. 4.36. The maximum value of error from the mean value of the frequency shift while the sample changes from 70% glycerol to DI water.

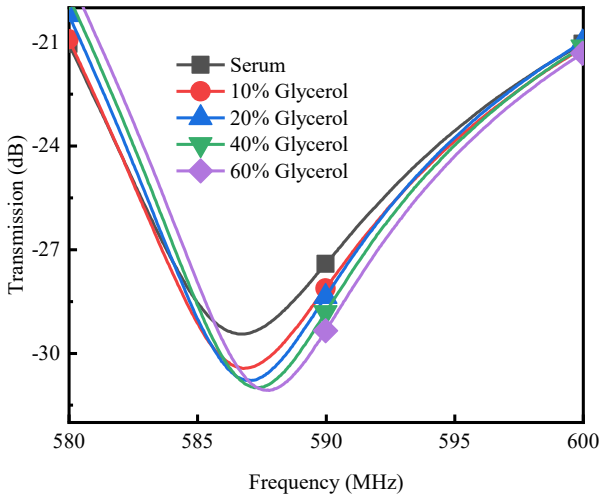

Fig. 4.37. Resonance profile monitoring with a sensitive notch while the liquid inside the tube changes in concentration of glycerol.

- *Glycerol in Serum Sensing:*

In order to determine the capability of the sensor for more realistic disposable applications, the concentration of glycerol in serum solution has been measured. Here horse serum with 10% concentration has been used to simulate the human body fluids. Samples with different concentration of Glycerol in serum has been prepared, from 60 percent glycerol concentration to 10%. As shown in Fig. 4.37, the notch in the transmission response

demonstrates 3.5 MHz of up-shift as the solution filling the channel changes from serum to 60% glycerol.

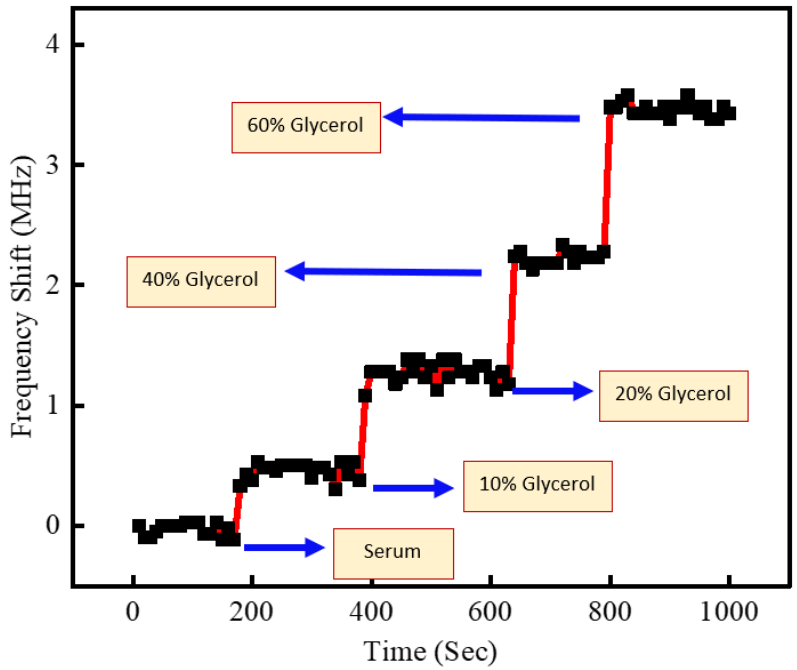

Fig. 4.38. Notch frequency variation monitoring during the time while the sample changes from serum solution to 60% of glycerol.

Time-based measurements of the resonance frequency have been done while the channel is initially filled with serum solution and the concentration of glycerol inside the channel increases gradually up to 60% (Fig. 4.37). As the concentration of glycerol in the liquid under test inside the microchannel increases, the variation in the permittivity and conductivity of the material creates the frequency shift. The steps in these figures determine the time that the liquid filling the channels changes. This process is repeated, and the results are illustrated in the step profile of Fig. 4.38. Since permittivity of the serum is less than DI water, increasing the concentration of glycerol in serum reduces the effective permittivity of the solution; thus an upshift in the frequency is expected. Fig. 4.39 presents the absolute

value of the maximum error from the mean value of the frequency shift as the concentration of glycerol in serum changes from 0% to 60%.

One of the most important parameters to be addressed for microwave sensors is their sensitivity. Since the output of the sensor is considered as frequency shift and the input as the glycerol concentration, in this paper, sensitivity defined as the achieved frequency shift for 1 percent variation in the concentration of the glycerol for the experimental verifications. According to this definition, the average sensitivity of the presented sensor is more than 85 kHz/(1%) which is a significant value according to very small volume of the exposed material under the test and the distance between the sensor and the sample.

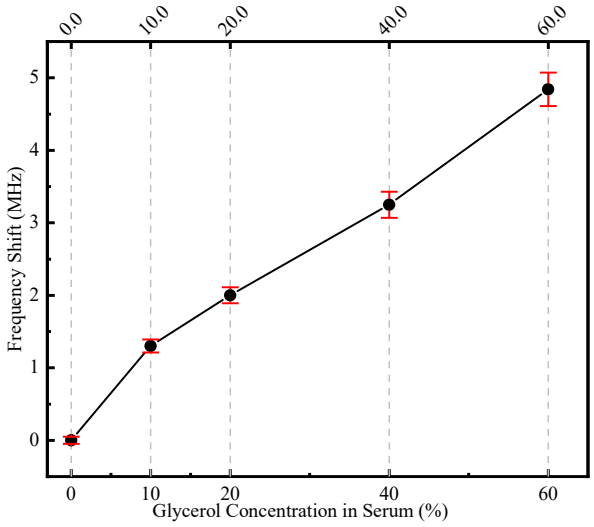

Fig. 4.39. The maximum value of error from the mean value of the frequency shift while the sample changes from 60% glycerol to Serum.

- *Small Variation Test:*

To determine the operation of the sensor over small variations in the concentration of glycerol in serum, sample with 2% of glycerol in 10% horse serum in DI water solution has been prepared. 2% glycerol concentration presents 2.5mg/ml and according to the entire volume of the exposed material to the sensor, the overall volume of glycerol varied from

3.2 nl (~ 4 µg) for 2% concentration to 112 nl (~141 µg) for 70% of glycerol concentration. As shown in Fig. 4.40, the notch resonance changes from 585.077 MHz to 585.2165 MHZ while the sample inside the microchannel changes from serum to 2% glycerol and 139.5 kHz of upshift is the result. Additionally, the amplitude of the transmission profile is different for the two samples since adding glycerol affects the conductivity of the serum solution. It could be seen from Fig. 4.40 that the amplitude difference between a serum-water sample and the same sample but with 2% of glycerol is about 0.2dB. Since nowadays power detectors with Tuned RF Level accuracies range of 0.005 dB are available commercially, one can claim detection of much smaller concentrations of glycerol in serum samples even in the range of 0.1% with the same sensor due to its extreme sensitivity. These values present the capabilities of the sensor for the detection of very small amounts of material change.

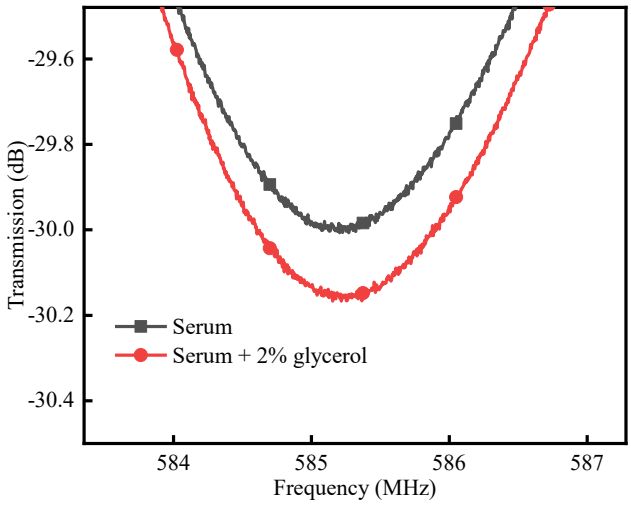

Fig. 4.40. Resonance profile variation as the liquid under test changes from serum to 2% glycerol concentration.

Chapter 5 High resolution Active sensor design for pH level sensing Applications

In Chapter 3 and Chapter 4 the development of distant microwave sensing by combing a flexible chipless tag energized through the electromagnetic coupling between the tag and the reader was presented, increasing the distance between the sample under test and the readout circuitry up to 60 mm. The proposed reader-tag pair sensor were then investigated for a variety of applications that require real-time noncontact sensing, including air quality monitoring, glycerol, and glucose concentration measurements, and high-temperature bitumen concentration monitoring, each exhibiting significant enhancement compared to their counter parts in the literature.

Since one of the main goals of this thesis is increasing sensing resolution, in this Chapter, we proposed utilization of microwave resonator armed with an active feedback loop to compensate for the sample loss and enable high-resolution microwave sensing. A passive microwave planar resonator is utilized and combined with an active feedback loop to enhance the quality factor for orders of magnitude and enable high-resolution measurements. Therefore, the sensor enables measuring very small complex permittivity variation of the sample under test [1], [42].

In Section 5.1, the correlation between the ε' and ε'' to pH values is presented based on equations. Section 5.2 focuses on the circuit theory behind active microwave design for high-resolution sensing. The expectation about the response variation trend as the sample changes is set, and measurements verify simulations and theoretical results. The introduced

pH sensor-enabled non-invasive pH sensing using microwave sensors for the first time and by modification in design, it has been applied for early-stage pH variation monitoring to prevent steel pipeline corrosion.

5.1 Correlation of pH level and Dielectric properties

As mentioned in the previous chapters, microwave sensors are sensitive to complex permittivity variation of the sensing media, which alters the electric field distribution around the sensor and enables sensing operation. The complex permittivity (ε) is a constitutive parameter that describes the interaction of the medium with an external electric field. In other words, permittivity is a measure of how an electric field affects and is affected by a medium. A material's permittivity is usually normalized to the permittivity of vacuum (ε_0), known as relative permittivity (ε_r). The real part of the relative permittivity (ε'_r) is a measure of how much energy from an external electric field is stored in a material. The imaginary part ε''_r is called loss factor and is a measure of how dissipative or lossy a material is exposed to an external electric field.

Calculation of each of the ε'_r or ε''_r become more complicated when it comes to liquids, and specifically highly conductive aqueous solutions like acidic or alkaline solutions. These solutions could be prepared by dissolving different concentrations of acidic or alkaline salts. Generally, two different phenomena occur during this dissolving chemical interaction:

1) The salts consist of ions, and after being dissolved in the solvent, ions will be separated, and the conductivity of the solution will be increased, which is responsible for the loss in the microwave system.

2) Since two different materials with different levels of relative permittivity are mixed in order to make as a specific acidic or alkaline solution, the effective permittivity of the final solution would be different from the solvent or the salt. The complex relative permittivity of polar liquids is well described by Debye model using [6], [163], [164]:

$$\varepsilon_r(\omega) = \varepsilon_\infty + \frac{\varepsilon_s - \varepsilon_\infty}{1+\mathrm{j}(\omega\tau)} \qquad (5\text{-}1)$$

where $\omega = 2\pi f$, f is the frequency, ε_s is the permittivity in the static limit, $\omega\tau \ll 1$, ε_∞ is the high-frequency limit of dielectric permittivity, and τ is the relaxation time. Referring to the fact that $\varepsilon_r(\omega)$ could be separated into a real part and an imaginary part as studied in [165], [166]:

$$\varepsilon_r{}' = \varepsilon_\infty + (\varepsilon_s - \varepsilon_\infty)\frac{1+(\omega\tau)^{1-\alpha}\sin\frac{\pi\alpha}{2}}{1+2(\omega\tau)^{1-\alpha}\sin\frac{\pi\alpha}{2}+(\omega\tau)^{2(1-\alpha)}} \qquad (5\text{-}2)$$

$$\varepsilon_r{}'' = (\varepsilon_s - \varepsilon_\infty)\frac{(\omega\tau)^{1-\alpha}\cos\frac{\pi\alpha}{2}}{1+2(\omega\tau)^{1-\alpha}\sin\frac{\pi\alpha}{2}+(\omega\tau)^{2(1-\alpha)}} \qquad (5\text{-}3)$$

where ε_s is the static dielectric permittivity, ε_∞ is the high-frequency limit of dielectric permittivity, ω is the circular frequency, τ is the relaxation time, and α is a distribution parameter of the relaxation time. The value of ε_∞ for solutions was taken equal to 5 regardless of temperature and concentration. Dielectric permittivity and losses in equation 5-2 and 5-3 are calculated based on the parameters which are defined specifically for different concentrations (molarity or mole per liter) of salt in solutions. The pH is also a number which can be simply calculated from molarity (M) of the solution:

$$pH = -\log[M] \qquad (5\text{-}4)$$

For instance, comparing the measured ε'_r and ε''_r presented in the table for NaOH and HCl with different pH level, it will be found that both ε''_r and ε'_r are considerably changed for the solutions having different pH levels. The calculated values correlating pH values to the permittivity and conductivity are shown in Table 5.1 based on equations. As shown in Table 5.1, by going from neutral pH to stronger acid or alkaline solution, significant decreasing/increasing in $\varepsilon'_r/\varepsilon''_r$ occur and this fact verifies the theory behind.

Table 5.1 Dielectric Permittivity and Loss for Different Solutions

pH of the solution	ε'_r	ε''_r	$\tan\delta$
pH=1	25.19	3.4	0.18647
pH=7	79.68	13.42	0.13706
pH=14	42.18	7.3	0.17294

5.2 Circuit Theory and Analysis

The core of the microwave sensor is a planar passive SRR, which initially has low quality-factor that requires enhancement. This goal could be achieved by assisting a transistor amplifier in the feedback loop and coupled to the microwave resonator as shown in Fig. 5.1.

The passive resonator structure is coupled to a positive feedback loop to compensate for all sources of loss (dielectric loss, conductor loss, radiation, etc.). A comparison between the sensor's transmission response in both passive and active mode (Fig. 5.2(b)) in full wave simulation with HFSS shows a remarkable enhancement in quality factor which enables the sensor for highly accurate measurements with capability of monitoring small variations. The transition from the passive sensor to high quality active sensor has been shown in Fig. 5.2(c) while bias voltage of the amplifier changes.

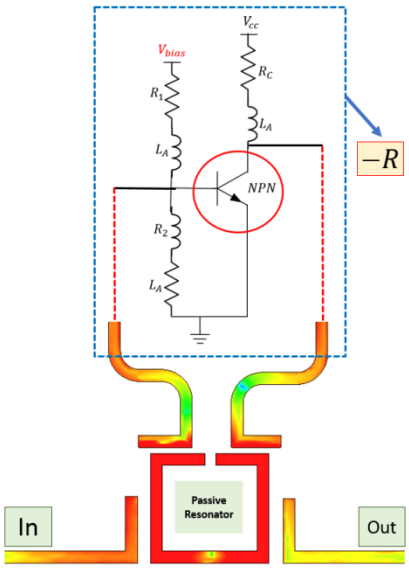

Fig. 5.1. Conceptual active resonator with the transistor amplifier in the feedback as the loss compensation circuit.

Fig. 5.3(a) presents a comparison of the resonant profiles for a high-quality resonator and a passive resonator sensor. The response of the proposed sensor with and without the loss compensation feedback loop has been simulated while the permittivity of the sample under test changes from $\varepsilon_r = 2$ to $\varepsilon_r = 2.05$. In the passive sensor, the peak in the transmission response is wide and lacks capability of detecting small changes. This sensor does not offer small limit of detection and is not an option for highly accurate sensing applications. Loss compensation and quality-factor improvement not only enhances the resolution of the sensor, but also increases stored electric field in the sensor medium, resulting in non-contact sensing and sharp resonance profile. The resolution is a quantitative description for quality factor and sharpness of the transmission response. High resolution response enhances the minimum limit of detection enabling the sensor to distinguish smaller variation. In this simulations, the metallic traces are chosen as perfect conductor, the sample under test has variable permittivity to demonstrate the sensing capability of the design, and the coating is PTFE layer ($\varepsilon_r = 2$ and $tanD = 0.0002$).

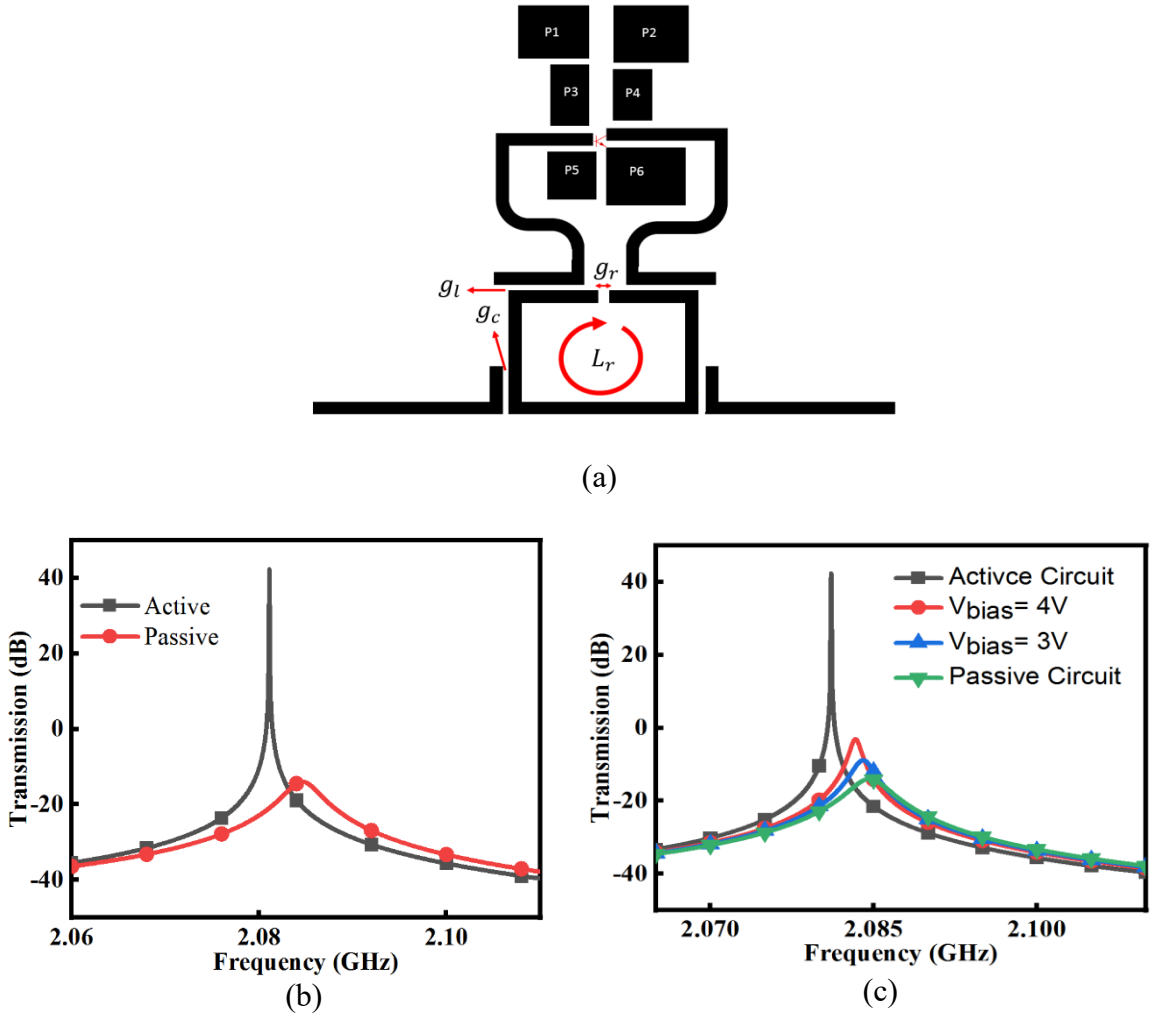

Fig. 5.2. (a) the designed circuit including the important design dimensions (g_l = 0,6 mm, g_c = 0.6 mm, g_r = 1.1 mm , and L_r = 56 mm) (b)Quality-factor improvement in active resonator (c) Quality-factor monitoring while the bias voltage is compensating for loss in the system (V_{bias} in the active circuit is 4.86 V).

The field distribution around the sensitive gap of the resonator is demonstrated in Fig. 5.3 (b). The strong electric field in front of the active resonator allows for the detection of permittivity variations in the medium located at a larger distance from the sensor. The permittivity variation of the solution trapped inside the coating (Fig. 5.3(c)) affects the resonance profile as shown in Fig. 5.3(a) comparing resonance frequency shift for the active and passive resonator's response. Due to the ultra-high quality factor provided by the active

resonator, the sensor is capable of detecting a 2.5% variation in the permittivity of the trapped solution (Fig. 5.3 (c)).

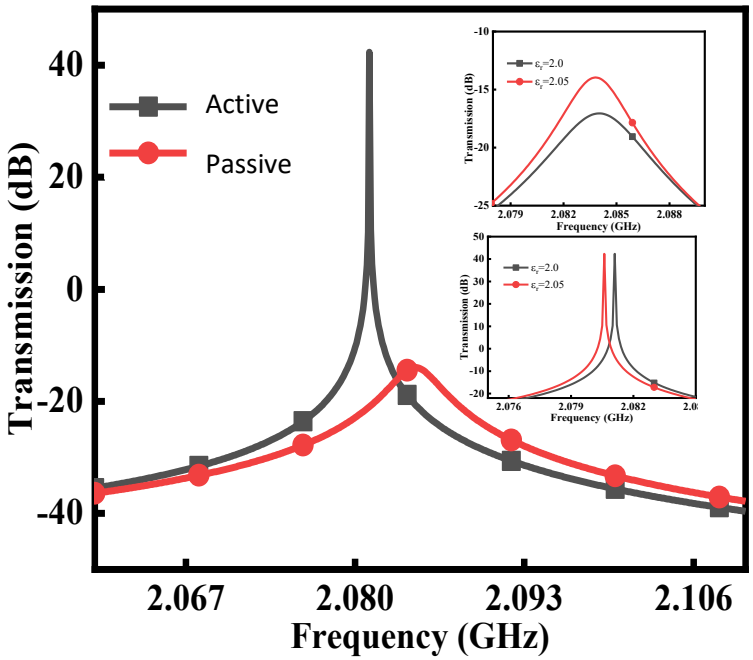

Fig. 5.3. (a) Simulated resonant profile for active (Q = 105800) and passive resonator (Q = 475) including the effect of 2.5% variation in permittivity of the trapped solution on the resonance profiles of active and passive resonator sensors is presented in simulation. (b) electric field distribution around the resonator for active resonator.

5.3 pH Level Detection Using High-resolution Microwave Sensor

After analyzing high-resolution microwave non-invasive pH sensor from both material and circuit design aspects, in this section the proposed concept has been applied to biomedical pH sensing and, with some design modifications, it enabled noncontact pH sensing around a steel pipeline to detect early stage possibility of corrosion.

5.3.1 Biomedical pH Sensing

The pH value is among the few chemical parameters that are ubiquitously of high importance and it is also one of the most fundamental parameters that dictates the outcome of a wide range of chemical and biological reactions from governing a normal function of a human body to ensuring proper industrial process. Monitoring pH variances has been of long-standing interest and deviation from an specific pH range is an indicator of altered cellular metabolism in diseases including stroke and cancer [167], [168]. Wound bed healing could be also tracked by monitoring pH as a key indicative for progress assessment. Unlike the healthy skin that have a slightly acidic pH (5.5-6.5), infected wounds often exhibit pH values higher than 7.4 due to the alkaline by-products of the infecting bacterial colonies [169]. Due to the irregular vascular structure of the chronic wound, diverse distribution of infection in the wound bed can be caused, resulting in extreme pH variation throughout the affected area [170]. The core of the microwave sensor is a planar passive SRR, which initially has low quality-factor.

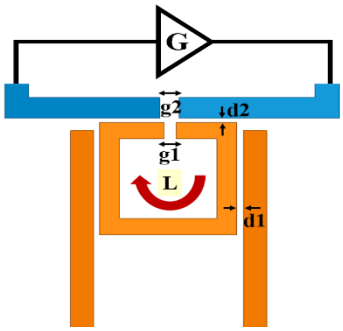

Fig. 5.4. Conceptual schematic of the proposed passive resonator beside its critical dimensions designed in HFSS (g1=1.2mm, g2=1.4mm, d1=0.8mm, d2=0.6mm, L=54.78mm).

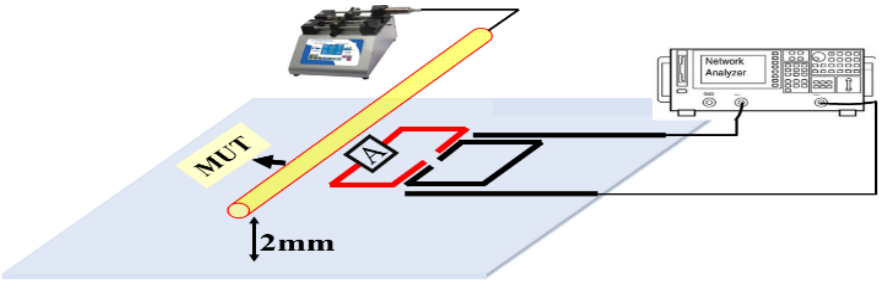

(a)

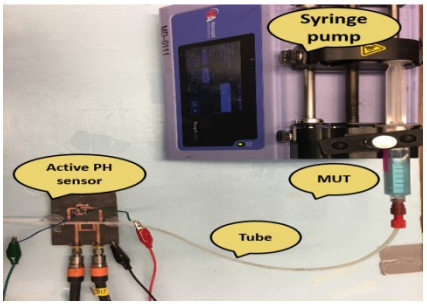

(b)

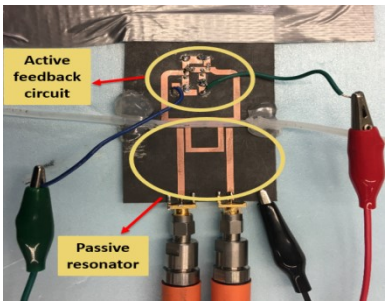

(c)

Fig. 5.5. pH sensing set-up: (a) schematic, (b) actual test set-up with details of liquid injection, (c) the implemented high-resolution pH sensor.

The passive sensor structure and important dimensions are shown in Fig. 5.4. The resonator is designed at $f_r = 2.534\ GHz$ and implemented (Fig. 1(b)) on Rogers 5880 substrate with the permittivity of 2.2, loss factor of 0.0003, and a thickness of 0.79mm.

The schematic (Fig. 5.5(a)) and experimental (Fig. 5.5(b)) setup up includes a $1/8''$ PTFE tube with 2 mm distance over the sensor's sensitive region, a split ring resonator with active feedback loop, syringe pump for injecting liquid with constant flow rate, and a Vector Network Analyzer (VNA).

In overall, ten different solutions with the pH levels from 1 to 10, obtained by mixing the appropriate amount of standard buffer solutions from Cole-Parmer, have been examined. pH=7 has been injected in between each test, and frequency response is recorded as the reference point. Then, each pH solution is injected, and the sensor frequency response is obtained in order to confirm the stability of the sensor during the measurements. This test

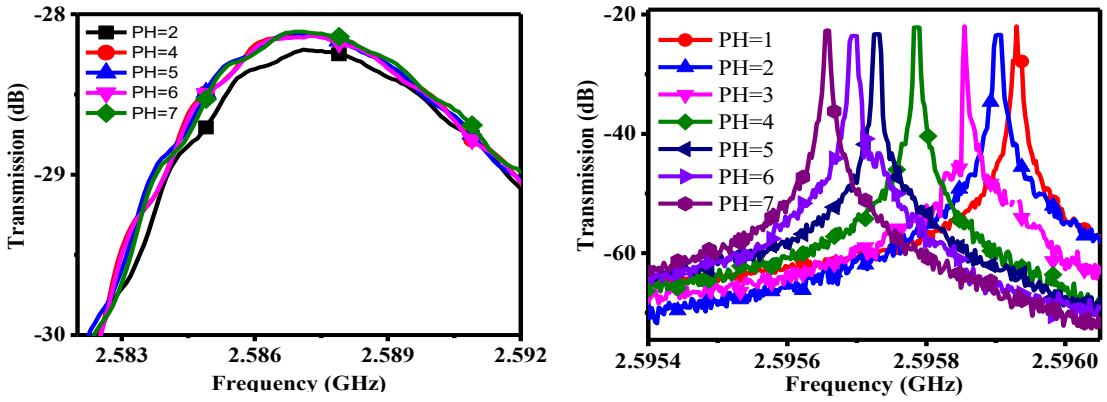

(a) (b)

Fig. 5.6. Measured results for various buffered solutions with different pH levels: (a) passive sensor, (b) active sensor.

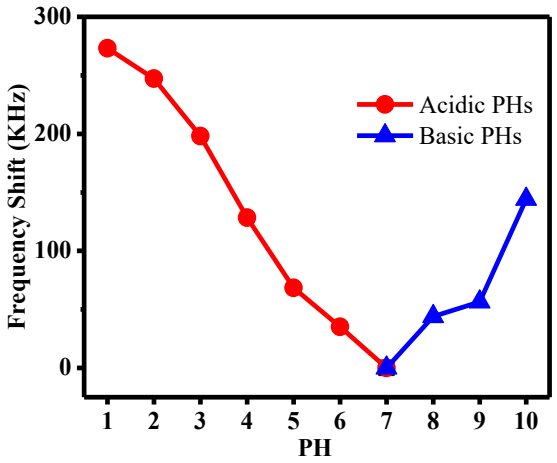

Fig. 5.7. Resonant frequency-shift versus different pH levels of the solution under test.

has been repeated for both passive and active sensors to illustrate the superiority of the proposed solution for pH sensing. As it is shown in Fig. 5.6(a), the frequency shift is not distinguishable when the pH measurement has been performed by the passive sensor; however, resonant frequency for the active sensor is completely separated, and the active sensor has high level of selectivity (Fig. 5.6(b)). The frequency shifts which are reported in Fig. 5.7 is the difference between the resonant frequency of each pH and pH=7. As the pH goes further from the neutral point, the upshift in the frequency response increases. This result confirms the theory which is explained in section II describing the fact that the

complex dielectric permittivity decreases as the concentration on the ions in the solution increases translating to either more acidic or alkaline pH levels.

5.3.2 pH level Sensing for Pipeline Integrity

This section includes the first feasibility study report that employs non-contact microwave sensors to inspect both near-neutral pH and high pH Stress Corrosion Cracking (SCC) threats to pipeline integrity. SCC as a type of Environmentally Assisted Cracking (EAC), happens where the combination of a potent environment, susceptible materials and tensile stress are present [171]–[174]. SCC manifests itself through formation of colonies of longitudinally or circumferentially oriented shallow cracks on the external surface of the pipe where the pipeline's coating is disbonded. These cracks could propagate either intergranular or transgranular and coalesce to form longer and deeper cracks, which lead to leakage or sudden fracture of the pipe [175]–[179].

It is well known that the environmental condition determines the mode of the fracture as well as the crack propagation mechanism. Table 5.2 summarized the required environmental conditions, fracture mode, crack propagation mechanisms. On the one hand, transgranular cracks propagate in the near-neutral pH environment through a hydrogen-enhanced corrosion fatigue mechanism. Hence, fluctuation in internal pressure of the pipeline (that caused hydrogen diffusion to the crack tip and fatigue) is the most detrimental factor that should be avoided to mitigate Near-Neutral pH Stress Corrosion Cracking (NNpHSCC) or controls crack growth rate. On the other hand, intergranular cracks initiate in the high concentration carbonate-bicarbonate environment at relatively low stresses and propagate via anodic dissolution mechanism. Ergo, the best available platform to stop High pH Stress

Corrosion Cracking (HpHSCC) is to prevent formation of high pH environment or remove the aforementioned environment [184].

Table 5.2 Comparison between high pH SCC and Near Neutral pH SCC [180]–[183].

Type of failure	High pH SCC	Near-Neutral pH SCC
Crack morphology	Intergranular Crack propagates along the grain boundaries	Transgranular Crack propagates through the grains
Environmental Condition	Coal tar, asphalt, tape coatings Concentrated carbonate-bicarbonate solution Sensitive to temperature Narrow potential range (-600 to -750 mV_{CSE}) pH between 9 to 12	High resistivity tape coatings Dilute ground water containing dissolved CO_2 Not affected by temperature in the range of 5to 45° C Wide potential range pH ≈6.5
Crack growth mechanism	Anodic dissolution Cracks propagates under either static loading or load fluctuation	Hydrogen-enhanced corrosion fatigue Crack growth depends on pressure fluctuation in particular large pressure fluctuation
Remedy to mitigate or control crack propagation	Avoiding the formation of environmental conditions	Avoiding internal pressure fluctuation slows down crack growth and mitigate SCC

The non-destructive testing (NDT) methods such as using pulsed eddy current could be employed to determine corrosion as well as cracks beneath the coating successfully and take required actions to maintain safe operation of the pipeline. There is an increasing tendency to apply such methods to detect defects and corrosion in different engineering applications [185]–[187]. However, finding suspicious spots before the onset of cracking has great advantage over conventional NDT methods. In particular, initiation and

propagation of intergranular cracks could be prevented through detecting the environmental condition, as noted earlier [188]–[190].

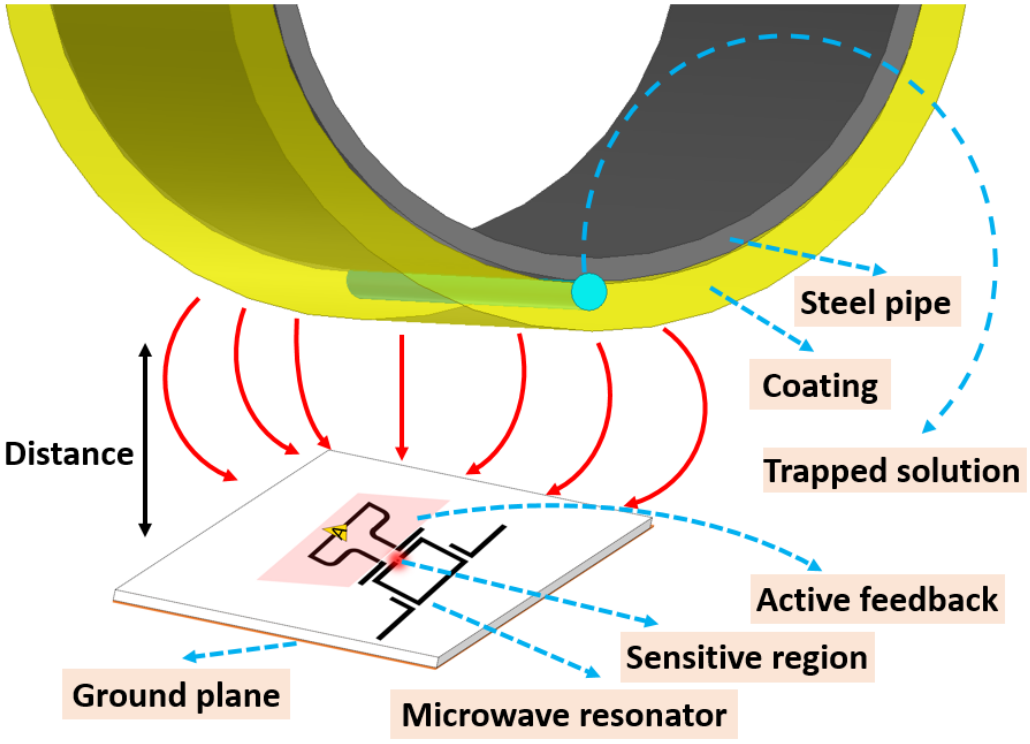

Fig. 5.8. Schematic of a non-invasive, non-contact pH sensor based on microwave ring resonator.

As illustrated in Fig. 5.8, the pH level values of the solutions trapped beneath the coatings in a non-contact manner can be monitored without the need to remove the coating. This method could be employed in SSCDA, direct examination step, to determine whether breeding ground for HpHSCC is created or not.

- *Theory of High pH environment Formation:*

In order to protect buried pipelines against external corrosion, coating and cathodic protection are two strategies that are employed simultaneously. However, failure in coatings like disbonded area and holidays is inevitable during deposition of the coating,

transportation, installation and pipeline performance. When such defects are formed on the coatings, the ground water with the pH of 6 to 7 penetrates beneath the coating and touchesthe steel pipeline. Then, the pH value of the water increases due to the following cathodic reactions:

$$2H_2O + 2e \rightarrow H_2 + 2OH^- \quad (5\text{-}5)$$

$$O_2 + 2H_2O + 4e \rightarrow 4\ OH^- \quad (5\text{-}6)$$

Increase in the pH value through increase in hydroxyl ion content is accompanied by absorption of carbon dioxide originated from either geological reactions or decayed organic. Under these circumstances, carbonate and bicarbonate ions are [191] :

$$CO_2 + OH^- \rightarrow HCO_3^- \quad (5\text{-}7)$$

$$HCO_3^- + OH^- \rightarrow CO_3^{2-} + H_2O \quad (5\text{-}8)$$

Eventually, the equilibrium between carbonate and bicarbonate ions determines the pH value based on the following equations

$$HCO_3^- \rightarrow CO_3^{2-} + H^+ \quad (5\text{-}9)$$

$$\text{Log}\frac{[CO_3^{2-}]}{[HCO_3^-]} = -10.34 + \text{pH} \quad (5\text{-}10)$$

On the condition that formation of such high pH solutions is accompanied by improper cathodic protection, intergranular could forms on the external surface of the pipelines during their operation Therefore, detection and monitoring high pH could be strong indication of the pipe corrosion and its detection would be of significant value.

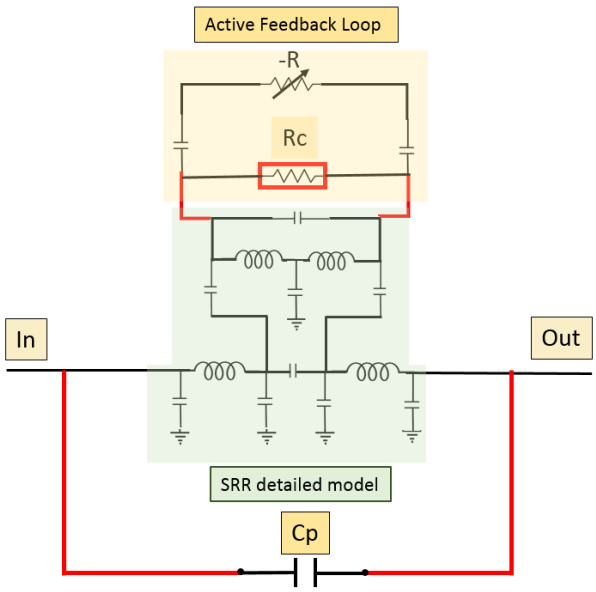

Fig. 5.9. Detailed circuit model of the active microwave pH sensor including the steel pipe (C_p) which has considerable impact.

5.3.1 Microwave Sensor Design with the Impact of Steel Pipeline

It is very important to take the effect of the steel pipeline availability around the sensor into account in every stage of designing the sensor. For better understanding, the circuit model for the active sensor, including the steel pipe is shown in Fig. 5.9. The general form of the circuit model for passive SRR-based sensor has been presented [7], [44]. The

material is modeled with R_C and it is supposed to be placed at the hotspot of the sensor which is the gap area. The active feedback amplifier could be modeled with a negative resistance, -R, in its active region and compensates for the loss applied to the sensor from material. When the steel pipe is placed in the vicinity of the microwave sensor, a huge capacitance will appear and change the performance of the design (C_p). Here, in order to keep the resolution and sensitivity high while the steel pipe is available, the sizes of every gap in the design has been increased. As a result, all the coupling capacitances caused by

the gaps would be smaller, and this lack of strong coupling is compensated by the parallel capacitance added by the pipe.

Unlike the passive microwave sensor in which effect of conductivity variation is more significant on amplitude and quality factor of transmission response, the story is different for active circuits. The circuit model for passive SRR including the active feedback loop which has been coupled to it using the coupling capacitors is presented in Fig. 5.9. The active feedback loop has been modeled with a negative resistance which compensate for the loss in the system and presence of a lossy sample in the gap area of an SRR is modeled with R_c resistor. When analyzing the impact of the solution change from neutral to strong acidic, two impact is considered which are the real and imaginary part of the complex permittivity. Based on the information in Table 4.1, by going further from the neutral pH (pH=7) to strong acidic or alkaline solution, decreasing in real part of the complex permittivity is expected and as a result, frequency downshift would occur in transmission response. On the other hand, the effect of sample's loss has been simulated as shown in Fig. 5.10. As the loss (conductivity of the sample) increases, there will be an upshift in the resonance frequency profile of the response in Fig. 5.10. As the result, the effect of permittivity decreasing and conductivity increasing signifies frequency shift in the same direction.

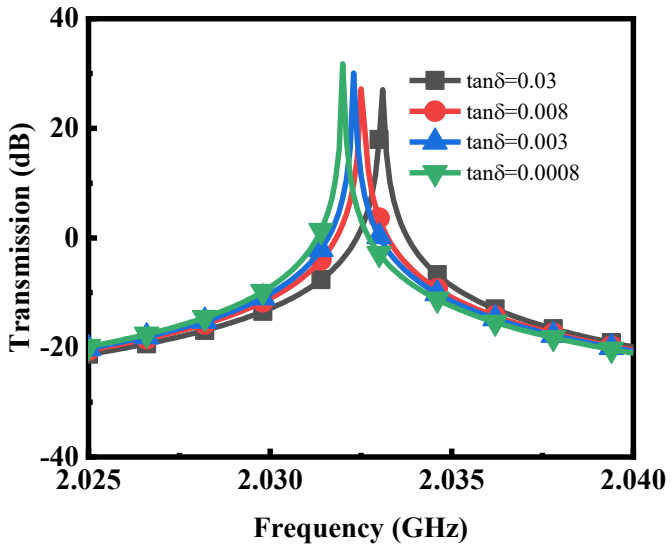

Fig. 5.10. Effect of conductivity variation of sample under test on active sensor in circuit model simulations.

Table 5.3 Chemical composition of the high pH solution

Solution	$NaHCO_3$ (g L^{-1})	Na_2CO_3 (g L^{-1})	pH
1M $NaHCO_3$	84.01	-	8.6
1M $NaHCO_3$ + 0.17M Na_2CO_3	84.01	25.66	9
1M $NaHCO_3$ + 0.75M Na_2CO_3	84.01	79.49	9.6
0.75M $NHCO_3$ + 1M Na_2CO_3	63	105.99	10
0.35M $NaHCO_3$ + 1M Na_2CO_3	29.40	105.99	10.4
0.1M $NaHCO_3$ + 1M Na_2CO_3	8.40	105.99	11
1M $NaHCO_3$ + 1M Na_2CO_3	84.01	59.99	9.3

Samples within the range of 8.6 to 11 have been prepared by dissolution of a different portion of sodium carbonate and sodium bicarbonate salts in deionized water in a room temperature. The details of the prepared solutions are summarized in Table 5.3. These solutions represent the high concentration carbonate/bicarbonate solution that is found under the coating.

- *Sample Preparation and Measurement Results:*

Seven aqueous solutions with the pH, in addition to the high pH solution, and an aqueous solution, namely C2, was prepared to represent near-neutral pH environment with the pH of 6.29. The chemical composition of this solution is reported in Table 5.4. A gas mixture of 5% carbon dioxide balanced with nitrogen was purged through C2 solution before the test to achieve a pH value of 6.29.

Table 5.4 Chemical composition of C2 solution

Chemical Composition	**Concentration (mg L-1)**
$MgSO_4$	274
$CaCl_2$	255
$CaCO_3$	606
$NaHCO_3$	195
KCl	35

In order to verify the proposed pH sensor for the low-pH and acidic range as well, 6 different solutions with the pH levels from 1 to 7, obtained by mixing appropriate amount of standard buffer solutions from Cole-Parmer, has been examined. recorded as the reference point. The schematic for the microwave pH sensor is presented in Fig. 5.11(a). The prepared pH-variable samples are injected into the liquid container tube buried in the coating, simulating the trapped liquid sample, using syringe pump with a constant flow rate. The sensor is placed in 3 mm vertical distance from the sample under test on the steel pipe layer. The test structure models water ingress underneath the coating with different pH levels. A vector network analyzer (VNA) has been used as the readout circuitry connected to the sensor which records the sensing data for the post processing using MATLAB.

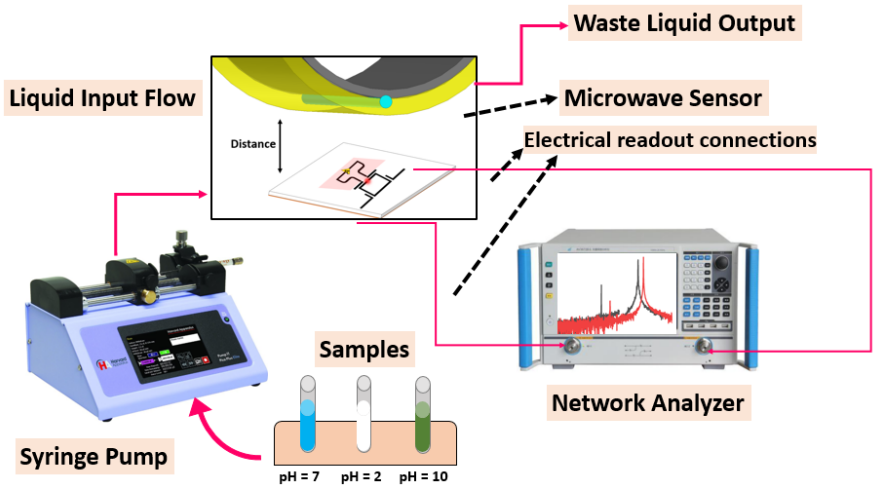

(a)

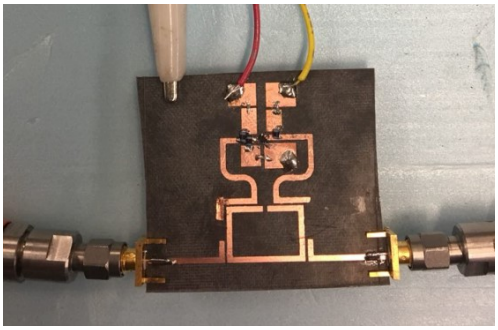

(b)

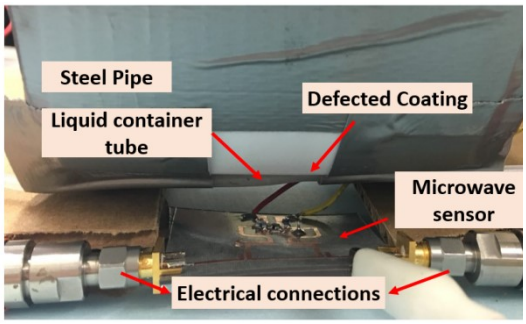

(c)

Fig. 5.11. (a) detailed schematic for pH level measurement (b) detailed view of the sensor, including the active feedback loop (c) Actual test setup for microwave HpHSCC monitoring.

The active sensor is designed at $f_r = 2.08\,GHz$ and implemented (Fig. 5.11(b)) on Rogers 5880 substrate with the permittivity of 2.2, loss factor of 0.0003, and a thickness of 0.79mm. The actual test setup in Fig. 5.11(c) up includes a 1/8" PTFE tube with 3 mm distance over the sensor's sensitive region. In order to simulate the defected pipe when the HpHSCC is formed, the PTFE tube has been used acting as the defect in the coating with an underlying trapped pH-variable solution between the coating and the pipe.

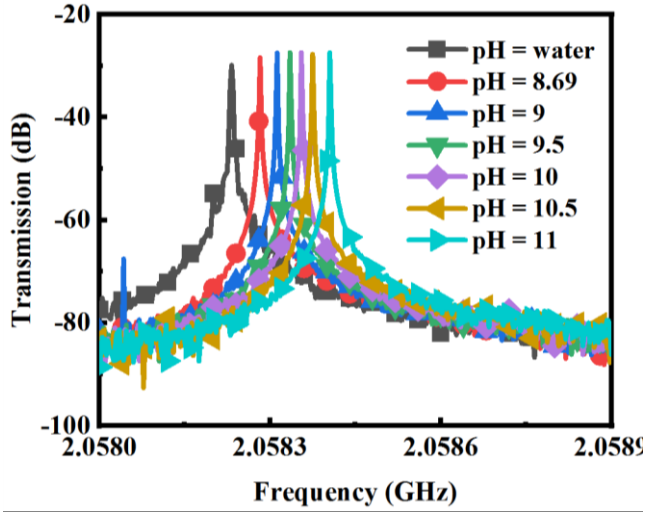

Fig. 5.12. Measured results for HpHSCC formation: pH level changes from 7 to 11.

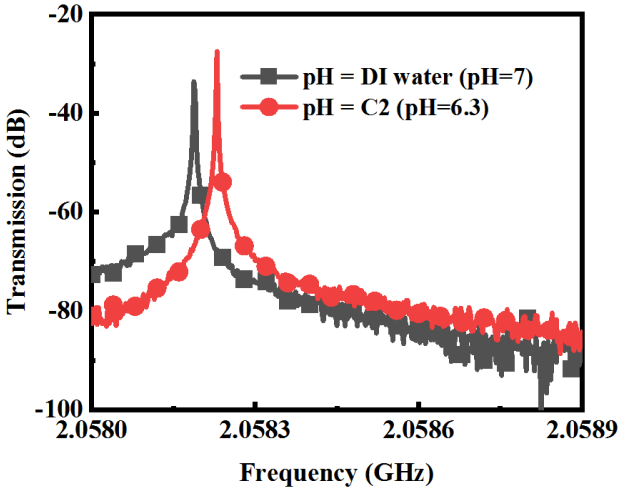

Fig. 5.13. Measured results for C2 sample to represent near-neutral pH environment with the pH of 6.3.

The measurement results for the prepared samples to form the HpHSCC in the lab are presented in Fig 5.12. The measurement verifies the trend for the resonance profile predicted by the theory and simulations. As the pH level of the solution increases from neutral pH (DI water, pH=7), permittivity reduction occurs as well as the conductivity increasing. Both of these phenomena lead the measurements result to upshift in frequency as the pH increases. The results demonstrate significantly distinct frequency shift of 174 kHz as the pH increases from 7 to 11. Another important parameter to measure is detecting the near-neutral pH

environment formation. As presented in Fig. 5.13, representing 40.22 kHz frequency upshift as the pH level of the sample under test changes from 7 to 6.3.

To demonstrate the sensor's capability in full-range pH measurements, the implemented sensor and setup have been used for pH measurement in acidic range (Fig. 5.14) where the samples are prepared using Cole-Parmer solutions. As the pH level changes from 7 to 1, the sensor demonstrates a 228 kHz frequency upshift.

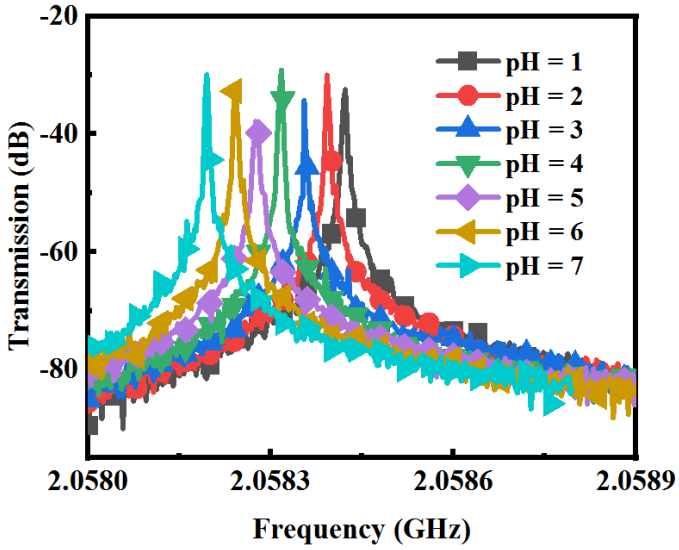

Fig. 5.14. Measured results for pH level of 1 to 7 to cover acidic solution range.

Since the electrical properties (conductivity and permittivity) of the solution changes in the same trend as the sample changes from neutral pH to strong acid and alkaline solution, the sensor is expected to demonstrate the same trend of variation for high-pH and low-pH solutions as shown in Fig. 5.12 and Fig. 5.14. The confirmation of the same trend is presented in Fig. 5.15 where the difference between the resonant frequency of testing solutions with different pH levels and pH=7 is demonstrated. Additionally, Fig. 5.15 presents the frequency shift result of three sets of measurements from the neutral pH for

different samples. The maximum error is less than 12 % at its highest and this level of error does not cause misinterpretation of the measurement data. Beside all the advantages that the proposed sensing platforms offers, there are some challenges that limits the performance of the design. One of the major challenges is the effect of environmental variation such as changes in the level of the moisture in the ambient around the senor.

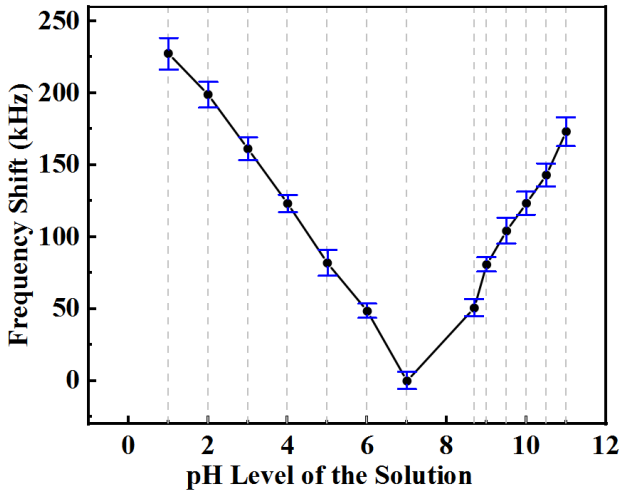

Fig. 5.15. Resonant frequency shift versus different pH levels of the solution under test including the error values as the result of different measurements.

Table 5.5 Comparison of the Proposed Sensor and some Related Works

Ref	Technology	Non-contact Sensing	Measuring Parameter
[192]	Microwave	No	Frequency
[9]	Microwave	No	frequency
	Optics	Yes	Fluorescence intensity
[193]	Material assisted	No	Voltage level
[194]	Laser	No	Raman intensity ratio
[6]	Microwave	Yes	Quality factor
[195]This work	Microwave	Yes	Frequency

To have a better idea and comparison, some of the previously proposed pH sensor have been brought up in Table 5.5. The fact that make the proposed design, [6], and [196] shine

among the other available pH sensors is their capability of performing non-contact sensing. However, the design and sensing platform proposed in [6] lacks performance in some aspects comparing to this work such as the resolution and limit of detection which is considerably higher in this work. Also, the material should be placed at the surface of the sensor while in this work the sensor is capable of performing measurement while there is an arbitrary distance between the sample and the sensor. The proposed optical sensor in [196] is another non-contact sensing platforms and due to being expensive and complicated, it is not the best option for large scale integration.

Chapter 6 High-Resolution Chipless Tag RF Sensor

As highlighted in Chapter 2, planar microwave resonators have recently shown to be great candidates for sensing and monitoring applications due to their multiple advantages [197]. However, the conventional microwave sensors suffer from two major deficiencies: 1) limited sensitivity and resolution, and 2) distance-limited sensing performance. Different approaches have been investigated to enhance the resolution of these sensors [198]. Assisting an active feedback loop using an active microwave device integrated and coupled to a passive split-ring resonator (SRR) has enhanced the quality factor (Q- factor) and, therefore, the resolution of the sensor could be improved [5]. This method has enabled different applications that were assumed impossible; however, their dc adjustment and calibration requirement are important issues that need to be solved. Another problem associated with the active microwave sensor is the limited operating temperature range. On the other hand, in both conventional and active feedback assisted microwave sensors, the material under the test needs to be placed very close to the sensitive hotspot of the of the sensor, which limits the sensors utilization for wearable and inaccessible environment applications. As mentioned in Chapter 3 and Chapter 4, using a second passive chipless SRR, "the tag," coupled to a conventional SRR with ports and cables, "the reader," proved [7] to perform sensing. The tag is the main sensing part demonstrated high sensitivity while there is up to 6 mm distance between the reader and the material around the tag [7], [199]. This distance has been improved to up to 60 mm in the defected ground structure [102], [104], [200].

In this Chapter, we propose to combine the benefit of the high-resolution sensing using active feedback loop and distant sensing enabled by EM coupling between the reader and the tag. The reason that makes this combination distinguishable among all the chipless tags, is the fact that the proposed sensor is capable of high-resolution distant sensing initiated by the coupling between resonators enabling sensing in the extremely lossy environment.

6.1 Introduction

The wireless monitoring of chemical, biological, and physical quantities and variations is one of the most essential steps in any industrial plant and wearable medical device. Wireless sensing offers a distant monitoring/sensing platform, which is the most compatible approach in expanding the Internet of Thing (IoT) ecosystem [201]–[203]. Massive sensor deployment and real-time data acquisition for control, optimization, and data-driven predictions in various applications are current and near future IoT demands [204], [205].

Moreover, remote sensing is the best solution for harsh environments and inaccessible real-time monitoring [206], [207], bio-implants inside the human body [203], [208], telesurgery [209], Lab-on-a-chip systems [210], drug delivery [211], [212], air-quality monitoring [199], and pipeline integrity (high temperature and pressure media) [213] are all among the most important applications that have been looking for non-contact real-time sensing solutions.

Advances in technologies leveraging Radio Frequency (RF) have introduced different solutions and enabled a variety of wireless sensing applications [202]. Radio-frequency identification (RFID) is one of the most viable ways to achieve contactless and real-time measurement for the above-mentioned applications [214]. Among all different designs of

RFID tags, passive RFID tags are the most prominent RF-based wireless technology, without any internal power source but a shorter range of communication compared to their active counterpart. They demonstrate sensing tags, including a microchip, with the required power provided by an embedded energy harvester. On the other hand, their level of sensitivity is not enough for highly sensitive applications [215], and using the microchip in the designs adds a limitation to the sensor's application in harsh environments. Other RF solutions have also been introduced for non-contact sensing applications in a low-frequency range [214], [216].

Using the passive flexible tag in the distance from the active reader empowers the sensing device to stands harsh environmental conditions, i.e., high temperature, high pressure, and hazardous material sensing. Other important advantages of the proposed structure, i.e., being simple to fabricate, low-cost, and flexible, making it a great choice for biomedical applications since it could be taped or even tattooed over the patient's skin. The tag sensor is energized through the established EM coupling between the tag and the reader and its spectrum is reflected in the spectrum of the reader in the same manner. Therefore, the EM coupling can replace the need for any readout or communication circuitry on the sensor side, and since the sensor consumes zero power, the sensing system is battery-less. The high-resolution sensing performance is achieved when the distance between the tag and the reader increases to 2.5 mm, making the system capable of being embedded inside smart watch/phone for wearable sensing applications. Fig. 6.1 schematically describes the reader, the RF tag, and the coupling between them. In order to verify the sensor's capability in detecting ultra-small permittivity variation around the tag, a microfluidic channel is used as

the Material Under Test (MUT) container. A lumped element equivalent circuit is employed to rigorously model the EM behavior of the structure.

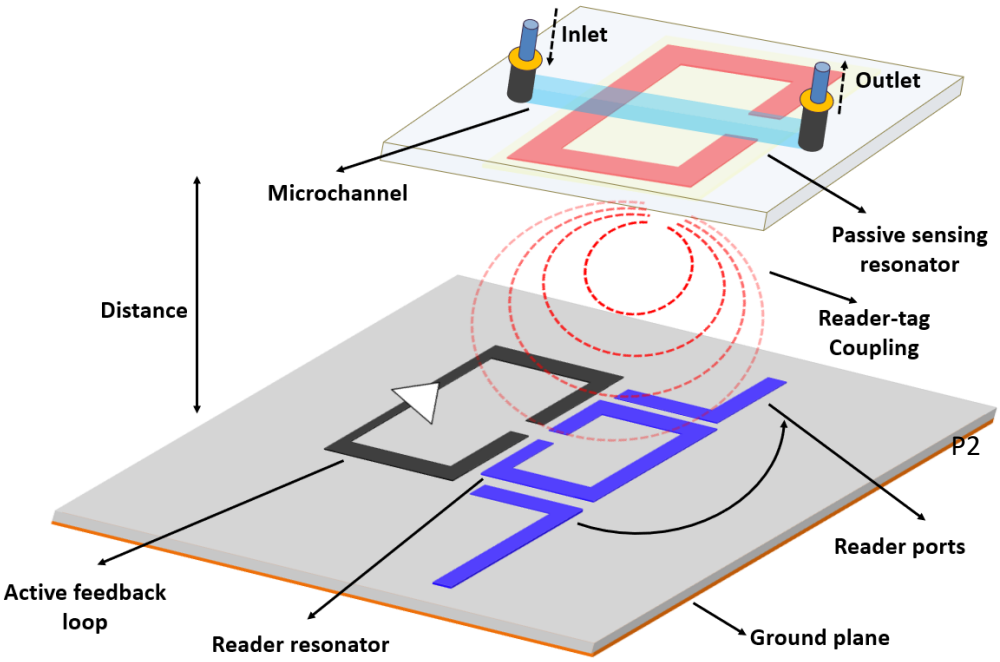

Fig. 6.1. Schematic of the high-resolution sensing setup including Reader resonator, active feedback loop, EM coupling, and flexible chipless tag resonator.

6.2 Sensor Design and theory of Operation

The schematic of the proposed microwave sensor is presented in Fig. 1 including the reader and the tag as main parts that require very accurate design procedure. Design procedure starts with the design of the reader part, which is a split ring resonator with a resonance frequency of 2.6 GHz. The resonance frequencies have been designed to have the maximum permittivity difference for the desired sensitivity tests in this paper and make the detection between the materials we are interested, more distinguishable [217]. At the second stage, the flexible tag resonator has been designed at 1.6 GHz, which is a copper trace in the form of SRR. The frequency gap between the resonance frequencies of the reader and the

tag is considered such that the design of the feedback amplifier and the bandwidth limiting capacitor (to be described) is relaxed. It also allows us to isolate the peaks from each other, even in the most extreme frequency shifts while sensing. The two resonance frequencies of the reader and the tag are shown in the transmission response presented in Fig. 6.2.

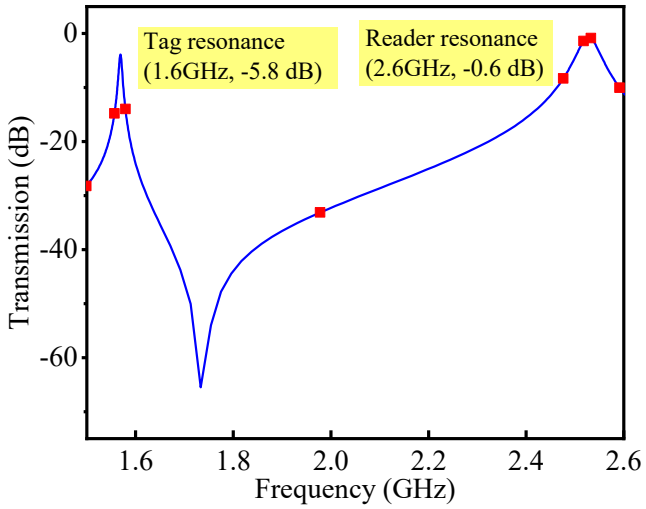

Fig. 6.2. Transmission response of the passive reader and the tag.

After designing the tag-reader passive sensor, the active feedback needs to be optimally designed to create high resolution frequency response for tag-related resonance. The basic design of the active feedback loop consists of a common-emitter amplifier, as shown in Fig. 6.3(a). This regenerative feedback loop creates a 180-degree phase shift on its output, and another 180-degree phase shift is introduced by the passive resonator; therefore, constructive feedback is created around the passive resonator, which compensates the power loss and increases the quality factor. The proposed active feedback loop will be coupled to the reader resonator while the tag is placed in distance performing as the main sensing element of the platform. At the starting point, the active feedback loop mainly consists of a BFP405 RF bipolar NPN transistor from Infineon Technologies and resistors.

However, since the resonance of the reader always has a higher transmission amplitude than that of the tag (due to the distance between the tag and the reader which reduces the strength of the electro-magnetic field provided by the tag), as shown in Fig. 6.2, the feedback loop oscillator starts compensating for the loss of the reader resonator and regenerates the reader's resonance frequency. In order to solve this problem and customize the amplifier in order to activate the tag resonance frequency at 1.6 GHz, a capacitance has been connected between collector and emitter of the NPN transistor. For calculation of the open loop gain (A_v) the simplified small signal model of the transistor (Fig. 6.3(a)) is used. Assuming the input impedance as (Z_{in}):

$$Z_{in} = r_\pi || R_B \qquad (6\text{-}1)$$

where $R_B = R_2 || R_1$ and by adding the effect of the connected capacitor between emitter and collector of the transistor C_f, the output impedance (Z_{out}) will be:

$$Z_{out} = r_o || C_f = \frac{r_o}{1+j\omega C_f r_o} \qquad (6\text{-}2)$$

The open-loop gain then could be calculated as in the following equation where R_S is the source impedance which is zero for an ideal source:

$$A_v = \frac{1}{(1+R_S Y_{in})} \frac{-g_m}{(1+R_c Y_{out})} \qquad (6\text{-}3)$$

Fig. 6.3(b) demonstrates the effect of adding C_f on the open loop gain. The effect of having C_f in the emitter-collector feedback significantly affects the flat profile of the basic amplifier. In the initial common-emitter amplifier, $A_v@f_{tag} = 23.14\ (dB)$ and $A_v@f_{reader} = 23\ (dB)$ (where Av@ftag and Av@freader are the open-loop amplifier gains at the tag and the reader's frequencies respectively), also as Fig. 6.2 illustrates, the

resonance peak of the reader has 5dB higher amplitude than the tag. Combining the passive sensor with the amplifier creates a higher level of loss compensation in the reader resonance which causes regeneration at the reader's resonance frequency instead of the tag (as we desired) as shown in Fig. 3(c). However, by adding C_f to the circuit, the profile of A_v would be different with higher slope ($A_v@f_{tag} = 9.5\ (dB)$ and $A_{v-reader} = 3\ (dB)$).

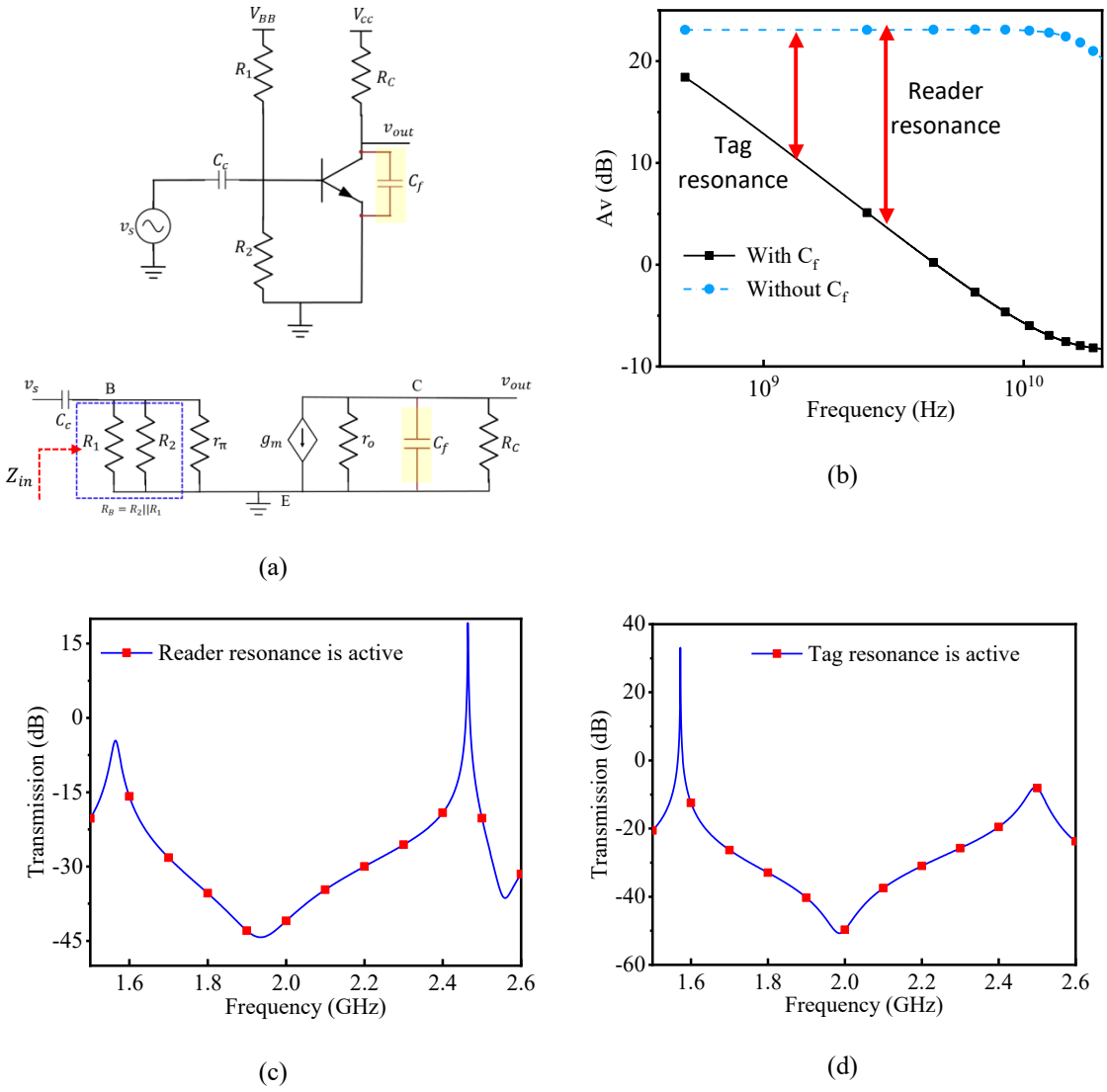

Fig. 6.3. (a) Simple form and circuit model of the proposed amplifier with the added capacitor C_f (b) AV versus the frequency for both cases of the amplifier (with and without Cf) (c) the transmission response while there is no feedback capacitor and the reader resonance is active (d)) the transmission response while there is a feedback capacitor and the tag resonance is active.

As a result, the tag resonance amplification would compensate for being 5dB lower in amplitude empowers it to have higher peak after the compensation. Hence, the oscillation starts-up at the tag's resonance frequency which makes the tag capable of high-resolution sensing, as shown in Fig. 6.3(d).

In this case, the overall microwave sensor system operates as a two-tank system with positive feedback for loss compensation at the tag's resonance frequency constructing an oscillator. Although the open-loop gain of the compensating amplifier could be higher than the loss of both resonances, after the transition phase of the oscillation start-up of the resonance with less loss, the gain of the amplifier reduces because of non-linearity in the transistor according to large-signal effects in steady-state oscillation. This non-linear effect is the preventing parameter against oscillation at both frequencies concurrently. Simultaneous oscillation could not happen unless the gain of the amplifier at the steady-state oscillation of the lower loss resonance frequency becomes equal to or higher than the loss of higher loss resonance, which is not possible unless the extreme case of having resonances with exactly equal losses. Therefore, locking the oscillator at one of the resonances, causes desensitization of the amplifier's gain to the other mode as the results of the mentioned non-linearity. In the case of the presented work, according to Fig. 6.2, the resonance related to the reader has less loss and as shown in Fig. 6.3(b), since the open-loop gain of the feedback amplifying system is flat for both resonance frequencies, the whole system will oscillate in the resonance frequency related to the reader. Since the considered sensing element in this work is tag, having high resolution sensing demanding for manipulating the spectrum of the open-loop gain of the amplifier such that the amplifier's gain difference at the resonance frequency of the tag covers the loss difference between the

tag and reader's related resonance frequencies. As illustrated in Fig. 6.3(a), this is accomplished by connecting a capacitor between collector and emitter of the amplifying transistor which results in a change in open-loop spectrum from a flat line to a decaying line compensating the loss difference (see Fig. 6.2 and Fig. 6.3(b)). This difference and its comparison with the loss difference between resonances guarantees the oscillation at the resonance frequency of the tag as illustrated in Fig. 6.3(c) and (d).

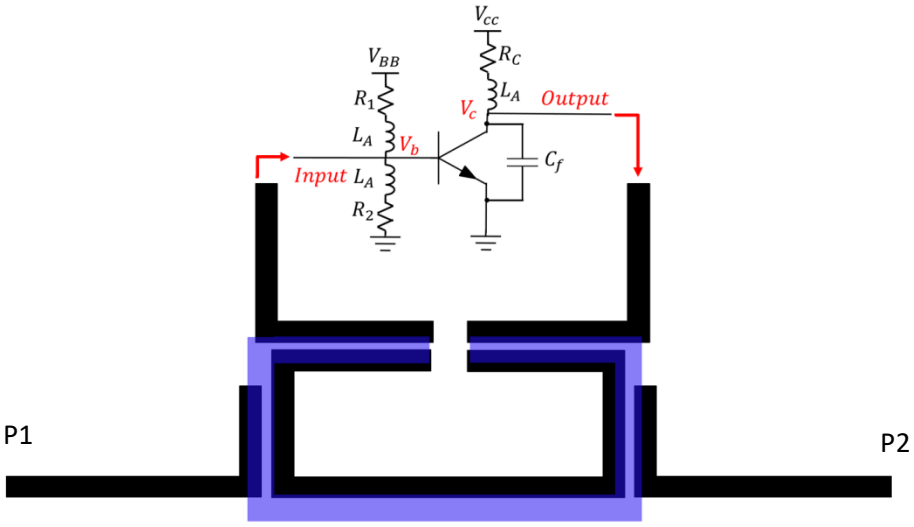

Fig. 6.4. layout of the proposed sensor with all the important dimensions.

6.3 Distant Sensor Analysis and Simulations

As shown in Fig. 6.1, the sensor consists of two split ring resonators and an active feedback loop. To understand the entire system operation, we have focused on both EM analysis and circuit model of the coupled resonators. We will consider the active reader structure as the basic part of the sensor. After that, the coupled reader–tag system will be described in detail.

Fig. 6.4(a) demonstrate a schematic view of the passive reader resonator, active feedback, and the passive tag resonator. Comparing to the basic amplifier in Fig. 6.3(a), three inductors

are added to minimize the effect of unwanted DC voltage of the transistor. On the other hand, the tag resonator is arranged in such a way to realize a mixed EM coupling between the two resonators. The amplifier is coupled to the passive resonator of the reader, compensating for the loss in the system. As mentioned in section 6.2, the design parameters of the amplifier and resonators are chosen for compensating for the loss of the system at the tag resonance frequency.

The main part of the reader is an SRR integrated with two gap-coupled micro-strip lines. The LC circuit modeling is found to be very useful in analyzing and control the behavior of the EM structure for the final sensing system. The reader circuit is integrated with another passive SRR (tag) through EM coupling which is the sensor part of the proposed platform. The tag resonator is arranged in such a way to realize a mixed EM coupling between the two resonators. The EM waves through the inductors of tag resonator are coupled to the capacitors of the reader resonator.

The top view of the designed microwave planar, including the RF tag, the reader, and the feedback circuit, is presented in Fig. 6.4. The HFSS EM simulations for the circuit while the active feedback loop is on (active) and off (passive) is presented in Fig. 6.5(a). The active feedback loop in the circuit would compensate for the loss of the tag and not the reader, as mentioned with details in section II. The more detailed simulations around the tag resonance (Fig. 6.5(b)) could clarify the significant loss compensation in the active sensor. While in the passive sensor the tag resonance has low Q-factor (~ 43) resulting in a wide peak, the loss compensation caused by the active circuit will result in ultra-high Q-factor and sharp peak providing a high level of sensitivity to the proposed sensor.

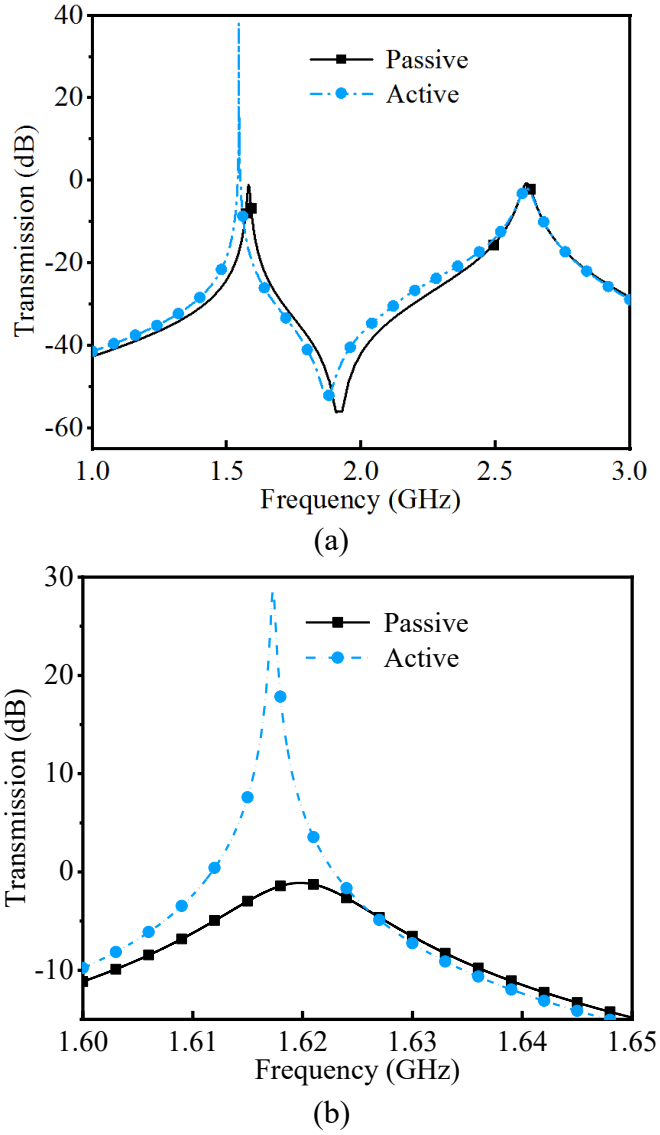

Fig. 6.5. (a) active and passive simulation result (b) zoomed version of the tag resonance in both active and passive simulations.

Since all the parameters are fixed after the final design and tuning for the fabrication step, the only variable parameter is the bias voltage of the amplifier, which changes base voltage, V_b, and is tuned by a precisely controlled voltage source. Changing the gain of this amplifier

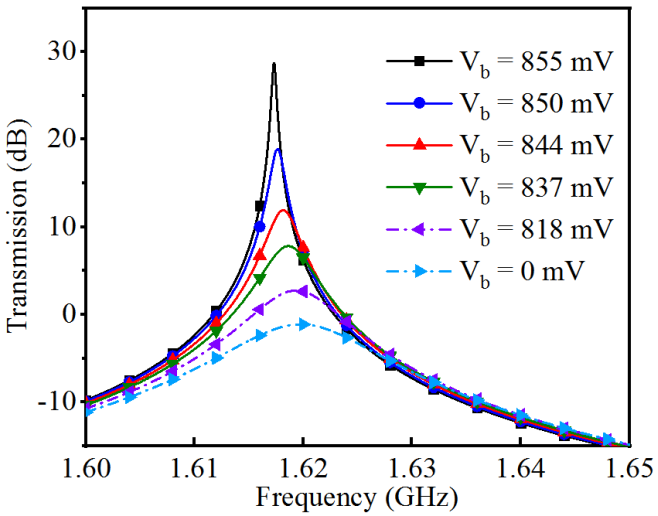

(a)

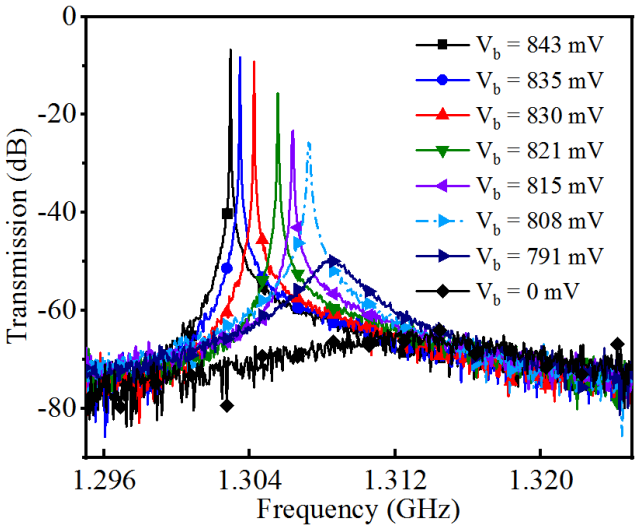

(b)

Fig. 6.6. The quality factor variation for different V_b values in (a) EM simulations and (b) measurements of the actual fabricated sensor.

affects the quality factor as well as the resonance frequency of the tag resonance. Fig. 6.6 (a) and (b) show the quality factor variation for different V_b values in EM simulations and the fabricated sensor measurements. At the zero V_b, the feedback loop has the lowest impact on the main resonator and the sensor response is the same as the low-Q passive coupled tag-reader. Increasing V_b to 800 mV results in huge increment in the quality factor. After this breaking point, the transistor starts to work in its linear region and as a result, a very high

gain and compensation will be applied to the sensor results in exponential increasing of Q-factor. As it is shown in the measured results of Fig. 6.6(b), by increasing the bias voltage, the resonance frequency of the tag resonator demonstrates 10 MHz of downshift and the Q-factor of up to 75000. This is mainly because of increasing the output miller capacitance of the amplifier as the result of gain increasing due to increasing the base voltage of the transistor. It is worthy to mention that the difference in the resonance frequency of Fig. 6.6(a) and (b) is the result of placing low-loss holders and fixing pins to avoid any movements of the tag and the reader. Also, Due to the limitation of the power level in the measurement setup, a microwave attenuator has been added to limit the power level which create a difference in the output level between the simulated and measured results. The attenuator only adjusts the signal level without affecting the sensitivity and performance of the design.

This extremely high Q-factor creates a very sharp peak, which empowers the sensor to perform high-resolution measurements for ultra-small variation of permittivity around it. Fig. 6.7 shows the measured quality factor of the tag resonance frequency as V_b increases from 0 to 914 mV. The loss compensating of this negative resistance value is determined by the amplifier's gain depends to bias current I_C (collector current) of the transistor, and since there is an exponential relation between V_b and I_C:

$$I_C = I_S(e^{\frac{qV_{BE}}{KT}} - 1) \qquad (6\text{-}4)$$

the value of the negative resistance will change exponentially, making the Q-factor following the same trend (see Fig. 6.7).

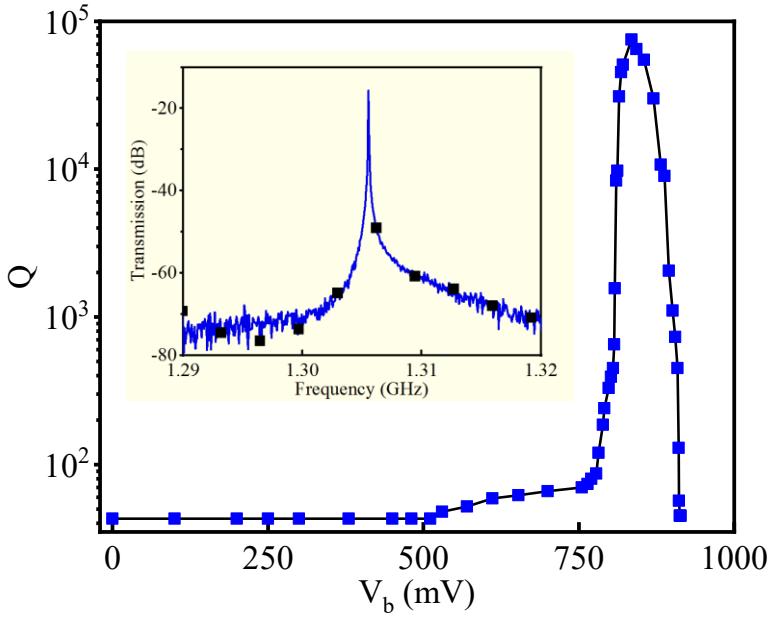

Fig. 6.7. The measured quality factor of the tag resonance frequency as V_b increases from 0 to 914 mV.

As shown in Fig. 6.7, the quality factor starts decaying after manually increasing the bias voltage to the certain value since the transistor starts to enter its non-linear region (saturation) at higher bias voltages. The measured results for the effect of the distance between the reader and the tag resonators are presented in Fig. 6.8. As it is shown, by increasing the distance between the tag and the reader from 2 mm to 10 mm, the peak Q-factor drops and the coupling between the tag and the reader is decayed which resulting in the tag resonance disappearing at 7 mm distance. In this case, the reader resonance amplitude would be significantly higher than the tag resonance amplitude, and the designed active feedback loop may start locking in the reader's resonance frequency instead. Overall, the resonant frequency is still sharp and detectable even up to 5 mm distance, which is completely enough for many applications such as biomedical and wearable electronics.

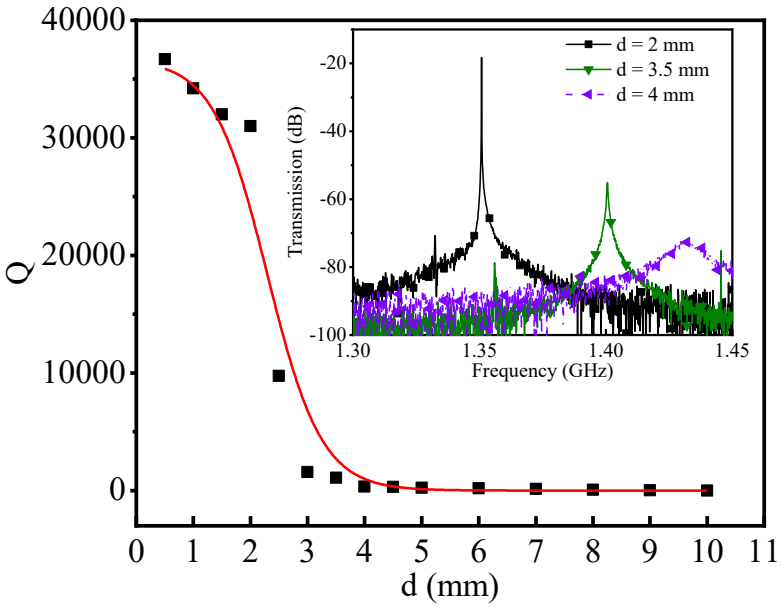

Fig. 6.8. Measured results for the effect of the distance between the reader and the tag resonators on the Q-factor.

Aside from the high quality factor achieved from oscillator based sensing, sensor's reliability is another very important parameter to discuss. Since the output signal of the presented sensor is the oscillation frequency, reliability could be translated to frequency stability for stable conditions (i.e., when MUT is not changing, the output frequency of the structure is fixed). The most acceptable parameter to measure the frequency stability of the oscillators is phase noise. Phase noise measures the random fluctuations in the phase of the output signal [218]. The experimental phase noise of the presented oscillatory sensor is illustrated in Fig. 6.9. It could be seen that the phase noise of the presented sensor is in an acceptable range. Although far from carrier phase noise floor is about -120dBc/Hz at 1MHz offset frequency, for very high precision sensing, close-to carrier phase noise is of more importance because it determines the reliability level of the sensor and the highest achievable resolution. Measured close to the carrier phase noise of the sensing system is

about -40dBc/Hz at 1 kHz offset frequency, which according to high sensitivity of the tag structure, it could detect extremely small variations in the permittivity of MUT.

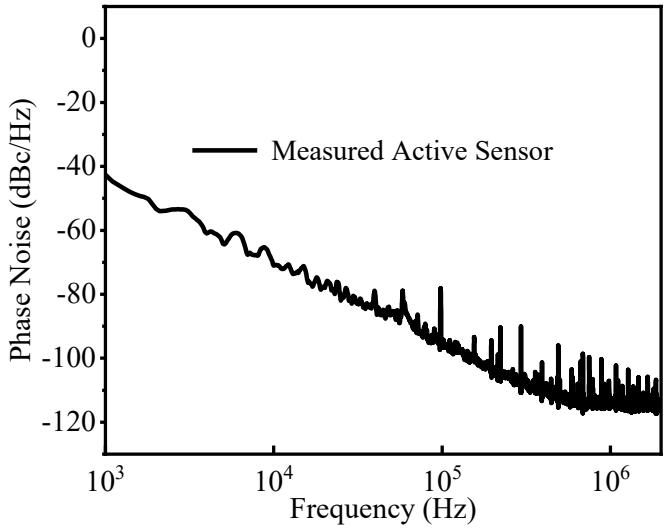

Fig. 6.9. Measured phase noise of the presented sensing system.

6.4 Fabricated Prototype and Measured Results

To experimentally verify the high-resolution sensing capability of the proposed sensor, a small volume of distant non-contact liquid sensing is accomplished. The implemented resonators, including the reader and the tag, are shown in Fig. 6.10 (a) and (b). The reader part is implemented on a substrate from Rogers Corporation (Rogers RT/duroid5880) with the relative permittivity of 2.2, a loss factor of 0.0003, and a thickness of 1.52 mm. The sensing tag is designed on a flexible substrate from Rogers Corporation (Rogers Ultralam 3850) with the relative permittivity of 3, the loss factor of 0.003, and a thickness of 100 μm. BFP405, a low noise, high gain, and low-cost transistor with a typical cut-off frequency of 25 and low current characteristics from Infinion Technologies is used as the main element of the active amplifier in the feedback loop. DC bias couplers to provide bias for the transistor are high frequency high quality inductors (560 nH). The flexibility in the tag

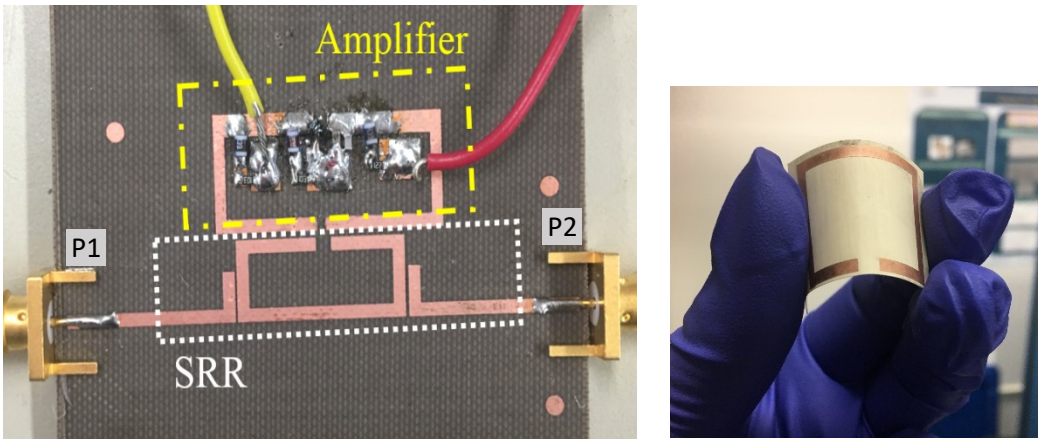

(a) (b)

Fig. 6.10. (a) the fabricated reader including the active feedback and passive SRR-based resonator, (b) fabricated flexible passive tag.

substrate provides an important extra degree of freedom for the user since there is no limitation on its installation process. Fig. 6.11(a) presents the schematic of the microfluidic chip and the sensor while performing liquid sensing. The microchannel full of the liquid is placed over the tag gap, which is the EM hotspot with the highest sensitivity.

The chemical detecting setup includes a microfluidic chip with the channel dimensions of 30mm*1.6mm*20µm, a flexible tag that is placed at the bottom of the microfluidic channel, a reader with integrated active microwave circuit, liquid injection pump, a Vector Network Analyzer (VNA), and a data acquisition system which is performed using LabVIEW software to record the measurement samples. The post-processing analysis was performed in MATLAB. As shown in Fig. 6.11(b), the tag has been fixed in its location at a 2 mm vertical distance from the reader over a low-loss spacer. The location of the microfluidic chip is fixed over the tag to avoid any possible movement that could cause an error in the measurement results. The microfluidic channel has been placed over the tag's EM hotspot for maximum sensitivity purposes. A thin glass layer (250 µm) at the bottom of

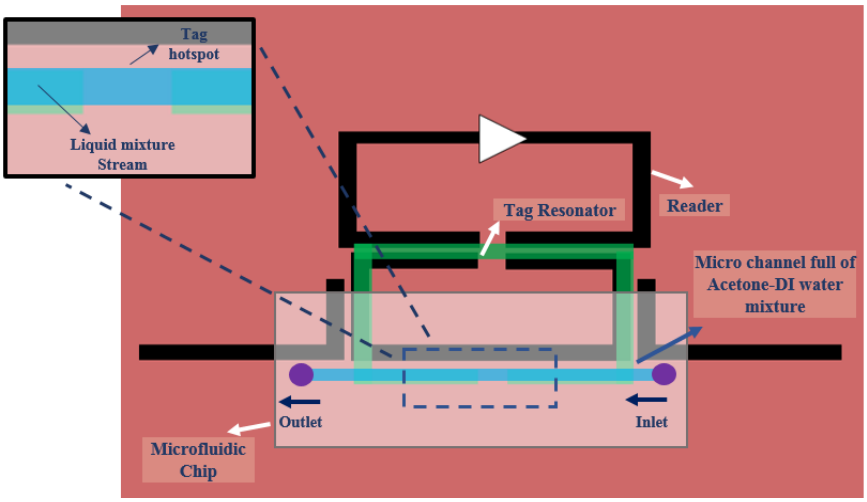

(a)

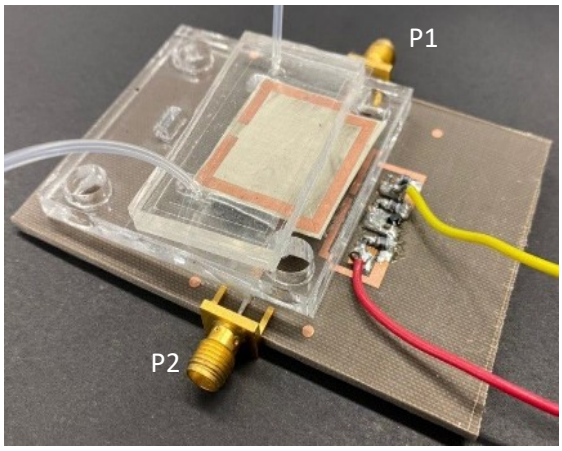

(b)

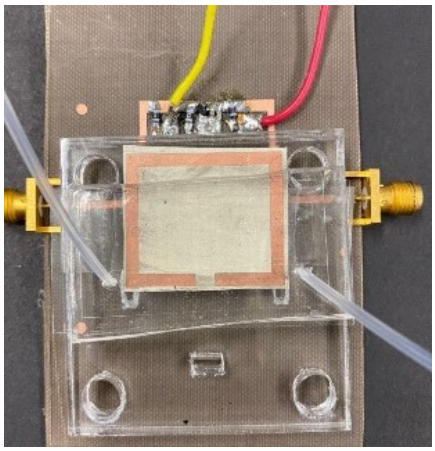

(c)

Fig. 6.11. (a) the schematic of the microfluidic chip and the sensor, (b) side view of the setup showing the distance between tag and the reader, (c) top-view of the sensing setup.

the channel separation is the only material between the tag and the liquid inside the channel in order to have minimal impact on the sensitivity. The under-the test liquid sample is a mixture of acetone and deionized (DI) water with different percentages of acetone (0% to 100%). As the liquid inside the microchannel changes from pure acetone ($\varepsilon_{r-Acetone} = 21.3$) to the samples with more DI water ($\varepsilon_{r-DI\ water} = 80$) content, the effective permittivity of the ambient around the tag increases. Also, the thin and low permittivity substrate of the tag resonator makes the effective permittivity of the ambient around the tag

highly dependent to the liquid inside the channel. Increasing the effective permittivity of the material inside the channel makes the resonance frequency of the tag to change relatively.

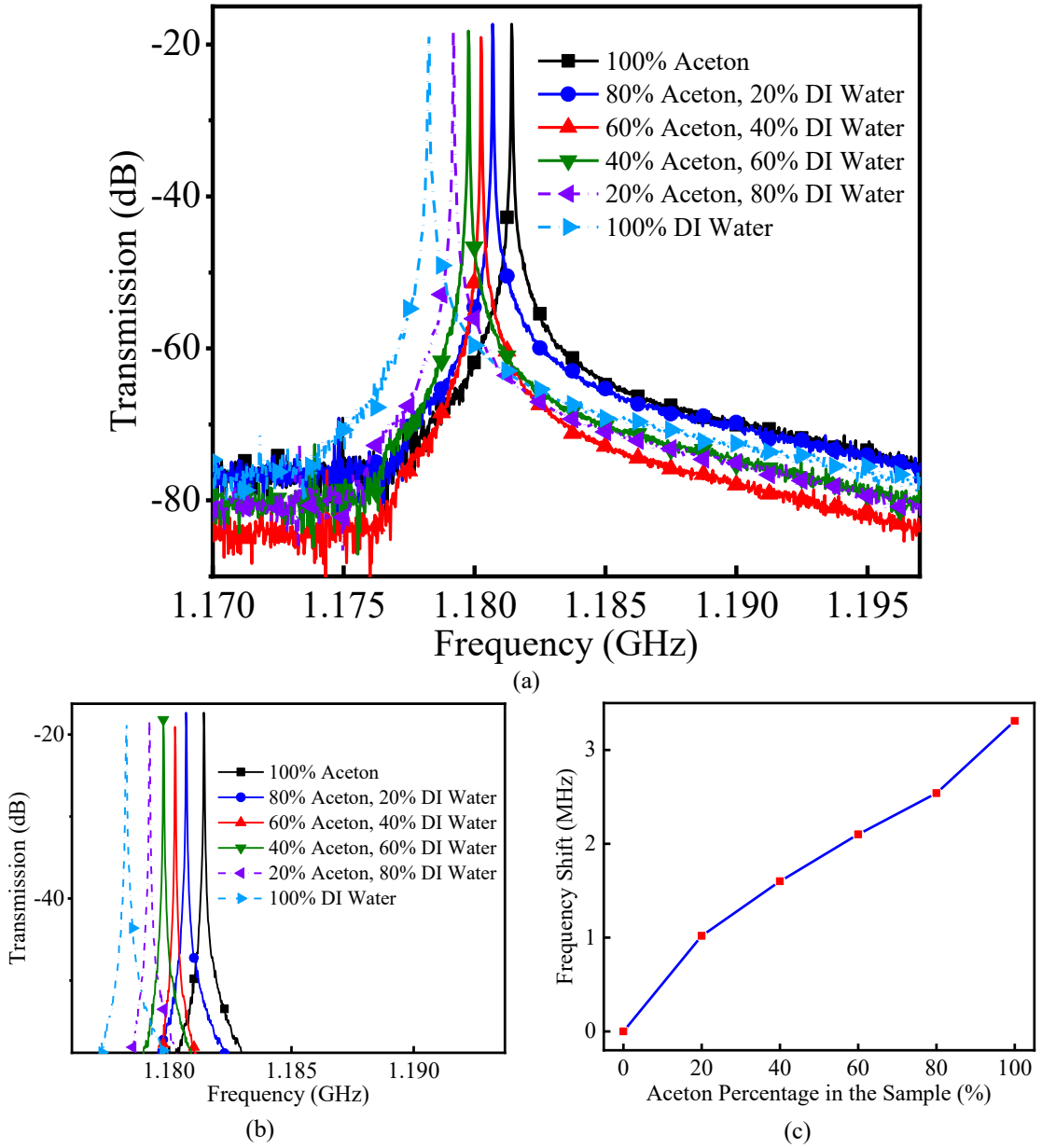

Fig. 6.12. (a) the measurement results while the sample inside the channel changes from pure acetone to DI water, (b) zoomed view of the resonance peak while sensing, (c) resonance frequency shift of the tag resonance as the sample increases in acetone percentage.

Fig. 6. 12(a) shows the measurement results, while the sample inside the channel changes from pure acetone to DI water. Since the permittivity of the mixture increases as the DI water content percentage of the mixture goes higher, the downshift in the resonance

frequency of the tag (f_{r_tag}) is expected. The sensor demonstrates a 3.3 MHz downshift in frequency when the liquid filling the channel changes from acetone to DI water. In this paper, sensitivity is defined as the achieved frequency shift for 1 percent variation in the concentration of acetone for the experimental verifications. According to this definition, the average sensitivity of the presented sensor is more than 35 kHz/(1%), which is a significant value according to a very small volume of the exposed material under the test (the volume of the whole channel is 960 nlit, but the volume of the introduced volume to the hotspot of the sensor is about 32nlit) and the distance between the sensor and the sample. It is worth to mention that the mentioned sensitivity means the sensor presents 35 kHz of frequency shift for variation of as extremely small volume of acetone as 320 plit. The ultra-high Q peak presented in Fig. 6.12(b) demonstrates the capability of the sensor in performing extremely high resolution and ultra-highly sensitive performance of the sensor. Fig. 6.12(c) presents a real-time resonance frequency shift of the tag resonator as the sample increases in acetone percentage and the reference point is pure DI water filling the channel. Based on the reference material and as expected, by increasing the acetone percentage, the effective permittivity will be reduced and frequency upshift is expected. The achieved promising results verify the performance of the proposed structure. Our research on performance improvement of microwave sensors is ongoing.

The sensor has been realized using a chipless tag as the main sensing element and a split ring resonator integrated with a transistor and its biasing circuitry as the reader. The structure is an oscillator locked in the tag resonance frequency, which is usually associated with a smaller amplitude rather than the reader because its located in the distance from the circuitry. The frequency locking mechanism at the tag frequency with lower amplitude has been

carried out by bandwidth reduction of the feedback amplifier through a parallel capacitor in order to decrease its gain for the higher frequency reader to compensate the mentioned resonance amplitude difference. In addition to achieving to as high Q as 75,000 and high-frequency stability, the oscillatory nature of this system relaxed the readout circuitry and reduced it to a simple frequency counter. Experimental results have presented exceptional capability of the overall structure in distinguishing between samples in a microfluidic channel with a very small volume.

Chapter 7 Conclusions and Future Considerations

In this chapter, the main findings of the thesis are summarized and the possible future work expanding the introduced concept are presented.

7.1 Summary

This thesis's main goal was to develop and propose new techniques and sensor platforms for non-invasive/non-contact distant high-resolution microwave sensing with the minimum complexity based on the EM couplings. New types of coupled resonator-based sensors and some of their many potential applications were introduced to fulfill this goal.

In Chapters 3, an initial study was proposed to increase the sensing distance between the material under the test and the read-out circuitry using a chipless flexible passive SRR. The sensors demonstrated great sensing potential in air-quality monitoring applications and non-invasive glucose sensing. However, the distance offered by the sensor is limited.

The enhancement in the distance has been achieved in Chapter 4 using a locally strong coupled microwave resonator system, which is a combination of a split ring resonator as the sensing tag and a ground-engineered coupled line reader to make the sensing significantly less dependent to the distance. Monitoring and detection in harsh environment by the introduced platform, such as real-time high-temperature bitumen concentration monitoring, disposable microfluidic glycerol sensing, and humidity sensing. The chipless tag structure is inexpensive and easy to integrate with different material containers making it a great candidate for large-scale production.

To overcome the sensitivity limitations of the reader-tag structure presented in Chapter 3 and Chapter 4, we introduced a high-resolution sensing concept in Chapter 5 to enhance sensing resolution and minimize limit of detection. The design enables non-invasive non-contact pH level sensing for the first time.

Finally, the benefits of high-resolution and distant sensing are combined, creating a passive chipless RF tag which is capable of high-resolution sensing. The design was tested for disposable microfluidic applications and presented an inexpensive sensor for sensing in nano liter volume scale.

7.2 Thesis Contributions

The main contributions described in this thesis can be summarized as follows:

- A new method has been introduced to address the limited-to-surface sensitivity drawback in the conventional planar SRR-based structures. The sensor consists of two parts: (1) the “tag,” which is the main sensing element fabricated on an ultra-thin flexible substrate in the shape of SRR electromagnetically coupled to (2) the “reader” SRR designed at a different frequency, placed and in an arbitrary, but limited to 15 mm, distance from each other. Due to the sensing tag's unique design, the sensitivity level offered by this design is far beyond the reported values for various applications. The tag sensor is energized through the established electromagnetic coupling between the tag and the reader, and its spectrum is reflected in the spectrum of the reader in the same manner. Therefore, there is no requirement for any readout or communication circuitry on the sensor side, and since the sensor consumes zero power, the sensing system is battery-less. The design,

analysis, and fabrication of coupled passive microwave resonators for sensing applications are presented. The full theoretical analysis and circuit modeling are described. Compared to conventional SRR-based microwave sensors, the proposed sensing tag allows for significantly higher sensitivity and increases the distance between the reader and the material under the test. The stability of the proposed design in distance sensing has been verified in different simulation tests.

- The proposed reader-tag pair concept has offered a simple and highly accurate solution for real-time air-quality monitoring applications to detect VOCs' concentration, which is serious health threats even in very low concentration. The flexibility of the tag and its capability of being located far from the reader enabled the user to place the tag in the gas container and detect as low concentrations of VOC as 10 ppm while keeping the reader and readout circuitry at a certain distance. This concept has been improved for non-contact real-time humidity sensing for agricultural applications as well. The advanced version of this work is a dual tag structure that has demonstrated the capability of real-time analysis of a bi-component gas.

- The capability of non-invasive real-time sensing of the tag with zero power consumption makes it a great candidate for medical sensing and measurements. The design and shown great results for glucose and lactate level monitoring. The reader could be embedded in a smartwatch, and a tag sensor could be taped over the patient’s skin. The impressive sensitivity of the design is attained as the results of the reduction of field concentration between the tag and the ground plane by removing the substrate of the tag. The impacts of some of the possible interferences

on the response of the sensor is also investigated, and promising results verifying the robustness of the sensor are achieved. As a result, electrolyte variations are tested to have a negligible effect on the of the sensor.

- Sensing distance microwave resonator using PEMC boundary is enhanced. We designed and presented a new tag-reader structure capable of distant sensing up to 60 mm. The reader includes a gap coupled transmission lines, and the relation between the coupling strength and the closeness of the lines has been significantly reduced using the engineered defect in the ground plane. The ring resonator of the passive tag, which is placed in distance from the reader, creates a high quality factor response.

- The significant harsh environment sensing potential of the ground-engineered structure is demonstrated. The design has shown a great potential for real-time high temperature measurement of water content in Bitumen sample, which introduces a cost-effective solution for a more efficient refinery and has been very well received by oil and gas industries in Alberta. The integration of the tag with microfluidic chip enable non-invasive real-time glycerol level measurement and droplet sensing for medical and drug delivery purposes.

- The design, fabrication, and sensing characterization of a high-resolution active sensor is presented. The level of sensitivity offered by passive reader-tag sensing does not offer the Limit of Detection (LoD) required for non-contact monitoring very small variations. Improving the quality factor, which is another representation for the sharpness, of the response empowers microwave sensors to offer high resolution sensing performance with minimum LoD. This goal could be achieved by

assisting a transistor amplifier in the feedback loop coupled to the microwave resonator where the positive feedback loop acts as a negative resistor compensating for all sources of loss (dielectric loss, conductor loss, radiation, etc.) and creates a high-Q response (from 450 in passive sensor to 75000 in active sensor).

- The level of sensitivity offered by the active microwave sensor is what non-invasive medical applications is demanding for where a very small variation of a specific component needs to be detected. This work has been offered a novel solution for non-invasive real-time pH level sensing and monitoring for the first time. Additionally, the proposed active sensor has been used to detect early-stage detection and mitigation of High pH Stress Corrosion Cracking (HpHSCC) through monitoring the pH range beneath the disbonded coating in buried steel pipeline[195].
- High-resolution Chipless Tag RF Sensor are presented to simultaneously improve the sensitivity and Q-factor of the microwave sensor and increased the distance between the sample under test and the readout circuitry. A reader-tag pair as the main parts of the sensing platform are designed where the reader is capable of high-resolution sensing using an active feedback loop, and the chipless flexible tag is a passive resonator. The tag sensor is energized through the established EM coupling between the tag and the reader; therefore, the EM coupling can replace the need for any readout or communication circuitry on the sensor side. The reason that makes this combination distinguishable among all the other tag-reader based sensing devices is the fact that the proposed sensor is capable of high-resolution distant sensing using a miniaturized passive tag with zero power consumption. This design enables sensing in an extremely lossy environment by standing harsh environmental

conditions. i.e., high temperature, high pressure, and hazardous material sensing. Other significant advantages of the proposed structure, i.e., being simple to fabricate, low-cost, and flexible, making it an excellent choice for biomedical applications since it could be taped or even tattooed over the patient's skin.

All in all, this thesis work offers solutions to increase the distance between the MUT and the planar microwave sensor while significantly enhancing the resolution and sensitivity. The introduced tag-reader structures initiates an entirely new generation of low-power microwave sensors, which enhances the sensitivity, resolution and enables harsh environment sensing capability. It is worthy to mention that highly important topics related to the introduced concept in this thesis are still open for investigation and development.

7.3 Future Considerations

In this thesis, new sensing platforms have been investigated to enhance sensing resolution and distance. Some of the many applications of these techniques haven been studied in Chapter 3 to 6; however, these techniques can be further studied to enhance the performance of the structure and expand the applications the designs could be applied to. Some of the recommended future works are listed below:

- Selectivity enhancement of microwave sensing is a solution for many critical real-world sensing applications, but it has not been deeply investigated. Providing a simple and low-cost design-based solution is not applicable when there are multiple variables in the system where each of them needs to be detected and monitored independently. Involving artificial intelligence and signal processing techniques in the post-processing stages of sensing data is a promising start point

for selective sensing without a complicated power-consuming structure that should be explored.

- Due to the requirement of future technology and to provide an IoT compatible healthcare-related products, designing and developing of non-invasive wearable sensing platforms and ultra-low-power sensors is a direction that this research can be continued to. The wearable RF sensing research aims to develop highly sensitive biomedical sensors based on planar microwave resonators enabling non-invasive real-time monitoring of different biomedical parameters. For biomedical applications, we are detecting small variations mostly in the millimolar (mM) range, and variations in other parameters may mask the measurement of the desired parameter. Interlinking between microwave sensors and biomedical science opens tremendous new applications for this kind of sensors.

- To have a user-friendly sensing device, the high level of sensitivity and other unique benefits of microwave sensors need to be combined with reliability of the results in different measurement conditions. Novel design techniques are required to make the sensor and the coupling between the reader and the tag more robust against rotation and misalignment.

- The sensor needs aggressive engineering to be protected from variation in environmental conditions. Physical stresses, contamination, and humidity are some examples of real-use environmental conditions that need to be mitigated. This enhancement may allow detection of extremely low variations and

empowers the sensor to be a great candidate for integration on a smartwatch, smartphone, or other portable convenient gadgets.

- The high level of sensitivity offered by microwave sensing has the potential to be used in lab-on-a-chip applications. A combination of distant RF chipless tag with microfluidics offers a low-cost disposable setup to handle the small volume samples. A promising start point is developing a real-time concentration measurement method to replace the chemical in-contact sensing. Using high-resolution RF chipless tag to detect an extremely small variation of dielectric properties of the material under test for early-stage detection of disease and drug delivery monitoring is another direction that that need to be studied.
- Wireless data communication for sensing and monitoring applications in harsh and out-of-access environments is another important direction for future expansion of this work where the near-field communication using EM coupling would not be an effective solution. This part of the research will be focused on 1) designing antennas and 2) designing sensor arrays, and each of these parts needs to be addressed based on the application. One of the very interesting applications of harsh environment sensing, which requires a wireless solution, is pipeline integrity monitoring. Canadian pipeline companies have been looking for a solution for real-time monitoring of the pipelines in order to prevent any possible failures resulting in major environmental and financial problems. This proposed solution highly increases the reliability of pipeline and helps to solve the possible environmental issues preventing the pipeline expansion in Canada. Designing a

communication platform that is able to continues data communication in long-distance and lossy channels like buried pipe under the ground can be explored.

Thesis Publication List (as of November 2020)

This section lists the academic contribution made during the course of this doctoral thesis, including journal and conference publications.

Journals

1. Abbasi, Zahra, Masoud Baghelani, and Mojgan Daneshmand. "High-Resolution Chipless Tag RF Sensor " Accepted in IEEE Transactions on Microwave Theory and Techniques (2020).
2. Abbasi, Zahra, Hamid Niazi, Mohammad Abdolrazzaghi, Weixing Chen, and Mojgan Daneshmand. "Monitoring pH Level Using High-Resolution Microwave Sensor for Mitigation of Stress Corrosion in Steel Pipelines." IEEE Sensors Journal (2020).
3. Baghelani, Masoud, Zahra Abbasi, and Mojgan Daneshmand. "Noncontact high sensitivity chipless tag microwave resonator for bitumen concentration measurement at high temperatures." Fuel 265 (2020): 116916.
4. Abbasi, Zahra, Masoud Baghelani, Mehdi Nosrati, Amir Sanati-Nezhad, and Mojgan Daneshmand. "Real-Time Non-Contact Integrated Chipless RF Sensor for Disposable Microfluidic Applications." IEEE Journal of Electromagnetics, RF and Microwaves in Medicine and Biology (2019).

5. Abbasi, Zahra, Pooya Shariaty, Mehdi Nosrati, Zaher Hashisho, and Mojgan Daneshmand. "Dual-Band Microwave Circuits for Selective Binary Gas Sensing System." IEEE Transactions on Microwave Theory and Techniques 67.10 (2019): 4206-4219.

6. Nosrati, Mehdi, Zahra Abbasi, Masoud Baghelani, Sharmistha Bhadra, and Mojgan Daneshmand. "Locally Strong-Coupled Microwave Resonator Using PEMC Boundary for Distant Sensing Applications." IEEE Transactions on Microwave Theory and Techniques 67.10 (2019): 4130-4139.

7. Nosrati, Mehdi, Zahra Abbasi, and Mojgan Daneshmand. "Single-layer substrate-integrated waveguide evanescent-mode filter." IEEE Microwave and Wireless Components Letters 28, no. 12 (2018): 1107-1109.

8. Abbasi, Zahra, Masoud Baghelani, and Mojgan Daneshmand. " Highly Reliable Real-time Microwave Tire Tread Monitoring Sensor" Under Review in IEEE Access (2020).

9. Baghelani, Masoud, Zahra Abbasi, Peter Light, and Mojgan Daneshmand. "Non-Invasive Chipless Printable Passive Tattoo Sensor with Zero-Power Consumption for Blood Glucose Measurement Based on Microwave Split Ring Resonators " Accepted in Nature Scientific Reports (2020).

10. Baghelani, Masoud, Zahra Abbasi, Peter Light, and Mojgan Daneshmand. " Non-Invasive Real-Time Lactate Monitoring System Using Wearable Chipless Microwave Resonator Based Sensors with Enhanced Sensitivity and Zero Power Consumption" Under Review in Nature Electronics (2020).

11. Amir Nosrati, Mehdi Nosrati, Zahra Abbasi, Thomas Robert Jones, Mahmoud Mohammad-Taheri, Ramin Sayadi, Mojgan Daneshmand" Bandpass Filters Based on Integrated Aperture- and Gap-Coupled Discontinuities " Under Review in IET Microwaves, Antennas & Propagation (2020).

Conferences

1. Abbasi, Zahra, Masoud Baghelani, and Mojgan Daneshmand. “Disposable Microwave Sensor for Real-time Monitoring and Content Sensing of Droplets in Microfluidic Devices," Accepted for presentation in APS 2020.
2. Abbasi, Zahra, Masoud Baghelani, and Mojgan Daneshmand. “High-resolution Non-contact RF Sensor for Glycerol Concentration Monitoring," Submitted to IEEE Sensors 2020.
3. Abbasi, Zahra, Masoud Baghelani, and Mojgan Daneshmand. "Zero Power Consumption Chipless Distant Microwave Moisture Sensor for Smart Home Applications." In 2019 IEEE SENSORS, pp. 1-4. IEEE, 2019.
4. Abbasi, Zahra and Mojgan Daneshmand. " Microwave-Microfluidic Integrated Noncontact Sensor for Noninvasive In-Situ Chemical Monitoring Applications," Presented in International Conference on Electromagnetics in Advanced Applications (ICEAA), Granada, Spain, September 2019.
5. Abbasi, Zahra, Pooya Shariaty, Zaher Hashisho, and Mojgan Daneshmand. "SilicaGel-Integrated Chipless RF Tag for Humidity Sensing," 2018 18th International Symposium

on Antenna Technology and Applied Electromagnetics (ANTEM), Waterloo, ON, 2018, pp.1-2.

6. Abbasi, Zahra and Mojgan Daneshmand. "Contactless pH Measurement Based on High Resolution Enhanced Q Microwave Resonator." 2018 IEEE/MTT-S International Microwave Symposium-IMS. IEEE, 2018. Abbasi, Zahra, Mohammad Hossein Zarifi, Pooya Shariati, Zaher Hashisho, and Mojgan Daneshmand. "Flexible coupled microwave ring resonators for contactless microbead assisted volatile organic compound detection." In 2017 IEEE MTT-S International Microwave Symposium (IMS), pp. 1228-1231. IEEE, 2017.

References

[1] M. H. Zarifi and M. Daneshmand, "Monitoring Solid Particle Deposition in Lossy Medium Using Planar Resonator Sensor," *IEEE Sens. J.*, 2017.

[2] A. Ebrahimi, J. Scott, and K. Ghorbani, "Differential Sensors Using Microstrip Lines Loaded with Two Split Ring Resonators," *IEEE Sens. J.*, 2018.

[3] A. Ebrahimi, W. Withayachumnankul, S. F. Al-Sarawi, and D. Abbott, "Microwave microfluidic sensor for determination of glucose concentration in water," in *Microwave Symposium (MMS), 2015 IEEE 15th Mediterranean*, 2015, pp. 1–3.

[4] P. Vélez, J. Muñoz-Enano, K. Grenier, J. Mata-Contreras, D. Dubuc, and F. Martín, "Split ring resonator-based microwave fluidic sensors for electrolyte concentration measurements," *IEEE Sens. J.*, vol. 19, no. 7, pp. 2562–2569, 2018.

[5] Z. Abbasi and M. Daneshmand, "Contactless pH Measurement Based on High Resolution Enhanced Q Microwave Resonator," in *2018 IEEE/MTT-S International Microwave Symposium-IMS*, 2018, pp. 1156–1159.

[6] H. Hamzah, J. Lees, and A. Porch, "Split ring resonator with optimised sensitivity for microfluidic sensing," *Sensors Actuators A Phys.*, vol. 276, pp. 1–10, 2018.

[7] Z. Abbasi, P. Shariaty, M. Nosrati, Z. Hashisho, and M. Daneshmand, "Dual-Band Microwave Circuits for Selective Binary Gas Sensing System," *IEEE Trans. Microw. Theory Tech.*, 2019.

[8] H. Choi *et al.*, "Design and in vitro interference test of microwave noninvasive blood glucose monitoring sensor," *IEEE Trans. Microw. Theory Tech.*, vol. 63, no. 10, pp. 3016–3025, 2015.

[9] S. Bhadra, D. J. Thomson, and G. E. Bridges, "Monitoring acidic and basic volatile concentration using a pH-electrode based wireless passive sensor," *Sensors Actuators B Chem.*, vol. 209, pp. 803–810, 2015.

[10] A. Sohrabi, P. M. Shaibani, M. H. Zarifi, M. Daneshmand, and T. Thundat, "A novel

technique for rapid vapor detection using swelling polymer covered microstrip ring resonator," in *2014 IEEE MTT-S International Microwave Symposium (IMS2014)*, 2014, pp. 1–4.

[11] M. H. Zarifi, P. Shariaty, M. Abdolrazzaghi, Z. Hashisho, and M. Daneshmand, "Particle size characterization using a high resolution planar resonator sensor in a lossy medium," *Sensors Actuators B Chem.*, vol. 234, pp. 332–337, 2016.

[12] J. Naqui, L. Su, J. Mata, and F. Martín, "Analysis of transmission lines loaded with pairs of coupled resonant elements and application to sensors," *J. Magn. Magn. Mater.*, vol. 383, pp. 144–151, 2015.

[13] Y. Zhao *et al.*, "RF evanescent-mode cavity resonator for passive wireless sensor applications," *Sensors Actuators A Phys.*, vol. 161, no. 1–2, pp. 322–328, 2010.

[14] K. Venugopalan and N. Agrawal, "Applications of Microwave Sensors in Medicines," in *World Congress on Medical Physics and Biomedical Engineering, September 7-12, 2009, Munich, Germany*, 2009, pp. 6–8.

[15] S. Murai, "Remote sensing note," *Japan Assoc. Remote Sensing, 284pp*, 1993.

[16] J. Naqui, C. Damm, A. Wiens, R. Jakoby, L. Su, and F. Martin, "Transmission lines loaded with pairs of magnetically coupled stepped impedance resonators (SIRs): Modeling and application to microwave sensors," in *Microwave Symposium (IMS), 2014 IEEE MTT-S International*, 2014, pp. 1–4.

[17] M. H. Zarifi, S. Farsinezhad, M. Abdolrazzaghi, M. Daneshmand, and K. Shankar, "Selective microwave sensors exploiting the interaction of analytes with trap states in TiO 2 nanotube arrays," *Nanoscale*, vol. 8, no. 14, pp. 7466–7473, 2016.

[18] T. Adame, A. Bel, A. Carreras, J. Melià-Seguí, M. Oliver, and R. Pous, "CUIDATS: An RFID–WSN hybrid monitoring system for smart health care environments," *Futur. Gener. Comput. Syst.*, vol. 78, pp. 602–615, 2018.

[19] M. H. Zarifi *et al.*, "Time-resolved microwave photoconductivity (TRMC) using planar microwave resonators: Application to the study of long-lived charge pairs in photoexcited titania nanotube arrays," *J. Phys. Chem. C*, vol. 119, no. 25, pp. 14358–14365, 2015.

[20] M. Abdolrazzaghi, M. Daneshmand, and A. K. Iyer, "Strongly enhanced sensitivity in planar microwave sensors based on metamaterial coupling," *IEEE Trans. Microw. Theory Tech.*, vol. 66, no. 4, pp. 1843–1855, 2018.

[21] M. H. Zarifi *et al.*, "Effect of phosphonate monolayer adsorbate on the microwave photoresponse of TiO2 nanotube membranes mounted on a planar double ring resonator," *Nanotechnology*, vol. 27, no. 37, p. 375201, 2016.

[22] M. H. Zarifi and M. Daneshmand, "Wide dynamic range microwave planar coupled ring resonator for sensing applications," *Appl. Phys. Lett.*, vol. 108, no. 23, p. 232906, 2016.

[23] R. Huang, B. Zhang, D. Qiu, and Y. Zhang, "Frequency splitting phenomena of

magnetic resonant coupling wireless power transfer," *IEEE Trans. Magn.*, vol. 50, no. 11, pp. 1–4, 2014.

[24] C. G. Caro and J. A. Bloice, "Contactless apnoea detector based on radar," *Lancet*, vol. 298, no. 7731, pp. 959–961, 1971.

[25] M. Pieraccini, G. Luzi, D. Dei, L. Pieri, and C. Atzeni, "Detection of breathing and heartbeat through snow using a microwave transceiver," *IEEE Geosci. Remote Sens. Lett.*, vol. 5, no. 1, pp. 57–59, 2008.

[26] A. D. Droitcour *et al.*, "Non-contact respiratory rate measurement validation for hospitalized patients," in *Engineering in Medicine and Biology Society, 2009. EMBC 2009. Annual International Conference of the IEEE*, 2009, pp. 4812–4815.

[27] A. Alemaryeen, S. Noghanian, and R. Fazel-Rezai, "Respiratory rate measurements via doppler radar for health monitoring applications," in *Engineering in Medicine and Biology Society (EMBC), 2017 39th Annual International Conference of the IEEE*, 2017, pp. 829–832.

[28] A. Alemaryeen, S. Noghanian, and R. Fazel-Rezai, "Antenna Effects on Respiratory Rate Measurement Using a UWB Radar System," *IEEE J. Electromagn. RF Microwaves Med. Biol.*, vol. 2, no. 2, pp. 87–93, 2018.

[29] P. Escobedo, M. A. Carvajal, L. F. Capitán-Vallvey, J. Fernández-Salmerón, A. Martínez-Olmos, and A. J. Palma, "Passive UHF RFID tag for multispectral assessment," *Sensors*, vol. 16, no. 7, p. 1085, 2016.

[30] E. Perret, *Radio Frequency Identification and Sensors: From RFID to Chipless RFID*. John Wiley & Sons, 2014.

[31] S. Preradovic and N. C. Karmakar, "Design of chipless RFID tag for operation on flexible laminates," *IEEE Antennas Wirel. Propag. Lett.*, vol. 9, pp. 207–210, 2010.

[32] S. Preradovic and N. Karmakar, "Fully printable chipless RFID tag," in *Advanced Radio Frequency Identification Design and Applications*, InTech, 2011.

[33] A. Vena, E. Perret, and S. Tedjni, "A depolarizing chipless RFID tag for robust detection and its FCC compliant UWB reading system," *IEEE Trans. Microw. Theory Tech.*, vol. 61, no. 8, pp. 2982–2994, 2013.

[34] B. Kubina, M. Schusler, C. Mandel, A. Mehmood, and R. Jakoby, "Wireless high-temperature sensing with a chipless tag based on a dielectric resonator antenna," in *SENSORS, 2013 IEEE*, 2013, pp. 1–4.

[35] S. Deif, L. Harron, and M. Daneshmand, "Out-of-Sight Salt-Water Concentration Sensing Using Chipless-RFID for Pipeline Coating Integrity," in *2018 IEEE/MTT-S International Microwave Symposium-IMS*, 2018, pp. 367–370.

[36] M. H. Zarifi, P. Shariaty, Z. Hashisho, and M. Daneshmand, "A non-contact microwave sensor for monitoring the interaction of zeolite 13X with CO2 and CH4 in gaseous streams," *Sensors Actuators B Chem.*, pp. 2–9, 2016.

[37] M. Abdolrazzaghi and M. Daneshmand, “Enhanced Q double resonant active sensor for humidity and moisture effect elimination,” in *Microwave Symposium (IMS), 2016 IEEE MTT-S International*, 2016, pp. 1–3.

[38] M. H. Zarifi and M. Daneshmand, “Non-contact liquid sensing using high resolution microwave microstrip resonator,” in *2015 IEEE MTT-S International Microwave Symposium*, 2015, pp. 1–4.

[39] M. Daneshmand and M. H. Zarifi, “APPARATUS AND METHOD FOR HIGH RESOLUTION COMPLEX PERMITTIVITY SENSING USING HIGH Q MICROWAVE SENSORS FOR LOSSY OR NON-LOSSY MEDIUMS AND SAMPLES.” US Patent 20,160,091,544, 31-Mar-2016.

[40] R. Boudot and E. Rubiola, “Phase noise in RF and microwave amplifiers,” *IEEE Trans. Ultrason. Ferroelectr. Freq. Control*, vol. 59, no. 12, pp. 2613–2624, 2012.

[41] M. Nick and A. Mortazawi, “Low phase-noise planar oscillators based on low-noise active resonators,” *IEEE Trans. Microw. Theory Tech.*, vol. 58, no. 5, pp. 1133–1139, 2010.

[42] M. Abdolrazzaghi and M. Daneshmand, “Dual Active Resonator for Dispersion Coefficient Measurement of Asphaltene Nano-Particles,” *IEEE Sens. J.*, vol. 17, no. 22, pp. 7248–7256, 2017.

[43] P. Vélez, L. Su, K. Grenier, J. Mata-Contreras, D. Dubuc, and F. Martín, “Microwave microfluidic sensor based on a microstrip splitter/combiner configuration and split ring Resonators (SRRs) for dielectric characterization of liquids,” *IEEE Sens. J.*, vol. 17, no. 20, pp. 6589–6598, 2017.

[44] M. Nosrati and M. Daneshmand, “Substrate Integrated Waveguide L-Shaped Iris for Realization of Transmission Zero and Evanescent-Mode Pole,” *IEEE Trans. Microw. Theory Tech.*, vol. 65, no. 7, pp. 2310–2320, 2017.

[45] M. Kampa and E. Castanas, “Human health effects of air pollution,” *Environ. Pollut.*, vol. 151, no. 2, pp. 362–367, 2008.

[46] G. B. Leslie, “Health risks from indoor air pollutants: Public alarm and toxicological reality,” *Indoor Built Environ.*, vol. 9, no. 1, pp. 5–16, 2000.

[47] “No Title,” *Agency, U.S. Environmental Protection*, 2013. [Online]. Available: http://www.epa.gov.

[48] F. Pariselli, M. G. Sacco, J. Ponti, and D. Rembges, “Effects of toluene and benzene air mixtures on human lung cells (A549),” *Exp. Toxicol. Pathol.*, vol. 61, no. 4, pp. 381–386, 2009.

[49] R. Atkinson, “Atmospheric chemistry of VOCs and NOx,” *Atmos. Environ.*, vol. 34, no. 12–14, pp. 2063–2101, 2000.

[50] M. A. Lillo-Ródenas, D. Cazorla-Amorós, and A. Linares-Solano, “Behaviour of activated carbons with different pore size distributions and surface oxygen groups for benzene and toluene adsorption at low concentrations,” *Carbon N. Y.*, vol. 43,

no. 8, pp. 1758–1767, 2005.

[51] F. M. Bowman, C. Pilinis, and J. H. Seinfeld, “Ozone and aerosol productivity of reactive organics,” *Atmos. Environ.*, vol. 29, no. 5, pp. 579–589, 1995.

[52] S. G. Ramalingam *et al.*, “Different families of volatile organic compounds pollution control by microporous carbons in temperature swing adsorption processes,” *J. Hazard. Mater.*, vol. 221, pp. 242–247, 2012.

[53] M. Tancrede, R. Wilson, L. Zeise, and E. A. C. Crouch, “The carcinogenic risk of some organic vapors indoors: a theoretical survey,” *Atmos. Environ.*, vol. 21, no. 10, pp. 2187–2205, 1987.

[54] B. R. Kim, D. H. Podsiadlik, D. H. Yeh, I. T. Salmeen, and L. M. Briggs, “Evaluating the conversion of an automotive paint spray-booth scrubber to an activated-sludge system for removing paint volatile organic compounds from air,” *Water Environ. Res.*, vol. 69, no. 7, pp. 1211–1221, 1997.

[55] R. Potyrailo and R. R. Naik, “Bionanomaterials and bioinspired nanostructures for selective vapor sensing,” *Annu. Rev. Mater. Res.*, vol. 43, pp. 307–334, 2013.

[56] M. H. Zarifi, A. Sohrabi, P. M. Shaibani, M. Daneshmand, and T. Thundat, “Detection of volatile organic compounds using microwave sensors,” *IEEE Sens. J.*, vol. 15, no. 1, pp. 248–254, 2015.

[57] Z. Abbasi, M. H. Zarifi, P. Shariati, Z. Hashisho, and M. Daneshmand, “Flexible coupled microwave ring resonators for contactless microbead assisted volatile organic compound detection,” in *Microwave Symposium (IMS), 2017 IEEE MTT-S International*, 2017, pp. 1228–1231.

[58] M. Fayaz, M. H. Zarifi, M. Abdolrazzaghi, P. Shariaty, Z. Hashisho, and M. Daneshmand, “A novel technique for determining the adsorption capacity and breakthrough time of adsorbents using a noncontact high-resolution microwave resonator sensor,” *Environ. Sci. Technol.*, vol. 51, no. 1, pp. 427–435, 2016.

[59] P. Shariaty, M. J. Lashaki, Z. Hashisho, J. Sawada, S. Kuznicki, and R. Hutcheon, “Effect of ETS-10 ion exchange on its dielectric properties and adsorption/microwave regeneration,” *Sep. Purif. Technol.*, vol. 179, pp. 420–427, 2017.

[60] M. H. Zarifi, P. Shariaty, Z. Hashisho, and M. Daneshmand, “A non-contact microwave sensor for monitoring the interaction of zeolite 13X with CO 2 and CH 4 in gaseous streams,” *Sensors Actuators B Chem.*, vol. 238, pp. 1240–1247, 2017.

[61] H. El Matbouly, N. Boubekeur, and F. Domingue, “Passive microwave substrate integrated cavity resonator for humidity sensing,” *IEEE Trans. Microw. Theory Tech.*, vol. 63, no. 12, pp. 4150–4156, 2015.

[62] J.-K. Park, T.-G. Kang, B.-H. Kim, H.-J. Lee, H. H. Choi, and J.-G. Yook, “Real-time Humidity Sensor Based on Microwave Resonator Coupled with PEDOT: PSS Conducting Polymer Film,” *Sci. Rep.*, vol. 8, no. 1, p. 439, 2018.

[63] G. A. Eyebe, B. Bideau, N. Boubekeur, É. Loranger, and F. Domingue, "Environmentally-friendly cellulose nanofibre sheets for humidity sensing in microwave frequencies," *Sensors Actuators B Chem.*, vol. 245, pp. 484–492, 2017.

[64] Y. Zhang, J. Zhao, T. Du, Z. Zhu, J. Zhang, and Q. Liu, "A gas sensor array for the simultaneous detection of multiple VOCs," *Sci. Rep.*, vol. 7, no. 1, p. 1960, 2017.

[65] C. Di Natale, E. Martinelli, and A. D'Amico, "Counteraction of environmental disturbances of electronic nose data by independent component analysis," *Sensors Actuators B Chem.*, vol. 82, no. 2–3, pp. 158–165, 2002.

[66] L. Zhang and F. Tian, "Performance study of multilayer perceptrons in a low-cost electronic nose," *IEEE Trans. Instrum. Meas.*, vol. 63, no. 7, pp. 1670–1679, 2014.

[67] F. Tian, Z. Liang, L. Zhang, Y. Liu, and Z. Zhao, "A novel pattern mismatch based interference elimination technique in E-nose," *Sensors Actuators B Chem.*, vol. 234, pp. 703–712, 2016.

[68] R. Gras, J. Luong, and R. A. Shellie, "Miniaturized micromachined gas chromatography with universal and selective detectors for targeted volatile compounds analysis," *J. Chromatogr. A*, vol. 1573, pp. 151–155, 2018.

[69] V. K. Tomer and S. Duhan, "Ordered mesoporous Ag-doped TiO 2/SnO 2 nanocomposite based highly sensitive and selective VOC sensors," *J. Mater. Chem. A*, vol. 4, no. 3, pp. 1033–1043, 2016.

[70] J. Jun *et al.*, "Wireless, room temperature volatile organic compound sensor based on polypyrrole nanoparticle immobilized ultrahigh frequency radio frequency identification tag," *ACS Appl. Mater. Interfaces*, vol. 8, no. 48, pp. 33139–33147, 2016.

[71] A. K. Nayak, R. Ghosh, S. Santra, P. K. Guha, and D. Pradhan, "Hierarchical nanostructured WO 3–SnO 2 for selective sensing of volatile organic compounds," *Nanoscale*, vol. 7, no. 29, pp. 12460–12473, 2015.

[72] W. T. Chen, K. M. E. Stewart, R. R. Mansour, and A. Penlidis, "Polymeric sensing material-based selectivity-enhanced RF resonant cavity sensor for volatile organic compound (VOC) detection," in *2015 IEEE MTT-S International Microwave Symposium*, 2015, pp. 1–3.

[73] M. H. Zarifi, M. Fayaz, J. Goldthorp, M. Abdolrazzaghi, Z. Hashisho, and M. Daneshmand, "Microbead-assisted high resolution microwave planar ring resonator for organic-vapor sensing," *Appl. Phys. Lett.*, vol. 106, no. 6, p. 62903, 2015.

[74] A. M. Gómez *et al.*, "Continuous glucose monitoring versus capillary point-of-care testing for inpatient glycemic control in type 2 diabetes patients hospitalized in the general ward and treated with a basal bolus insulin regimen," *J. Diabetes Sci. Technol.*, vol. 10, no. 2, pp. 325–329, 2016.

[75] T. Lin, Y. Mayzel, and K. Bahartan, "The accuracy of a non-invasive glucose monitoring device does not depend on clinical characteristics of people with type 2 diabetes mellitus," *J. drug Assess.*, vol. 7, no. 1, pp. 1–7, 2018.

[76] I. F. GODSLAND and C. WALTON, “Maximizing the success rate of minimal model insulin sensitivity measurement in humans: the importance of basal glucose levels,” *Clin. Sci.*, vol. 101, no. 1, pp. 1–9, 2001.

[77] T. Scully, “Diabetes in numbers,” *Nature*, vol. 485, no. 7398, pp. S2–S3, 2012.

[78] G. Wang and M. P. Mintchev, “Development of wearable semi-invasive blood sampling devices for continuous glucose monitoring: A survey,” *Engineering*, vol. 5, no. 5B, pp. 42–46, 2013.

[79] M. J. Tierney, J. A. Tamada, R. O. Potts, L. Jovanovic, S. Garg, and C. R. Team, “Clinical evaluation of the GlucoWatch® biographer: a continual, non-invasive glucose monitor for patients with diabetes,” *Biosens. Bioelectron.*, vol. 16, no. 9–12, pp. 621–629, 2001.

[80] K. McLACHLAN, A. Jenkins, and D. O’NEAL, “The role of continuous glucose monitoring in clinical decision-making in diabetes in pregnancy,” *Aust. New Zeal. J. Obstet. Gynaecol.*, vol. 47, no. 3, pp. 186–190, 2007.

[81] R. Boyd, B. Leigh, and P. Stuart, “Capillary versus venous bedside blood glucose estimations,” *Emerg. Med. J.*, vol. 22, no. 3, pp. 177–179, 2005.

[82] M. Phillip *et al.*, “Nocturnal glucose control with an artificial pancreas at a diabetes camp,” *N Engl J Med*, vol. 368, 2013.

[83] C. Cobelli, E. Renard, and B. P. Kovatchev, “Artificial pancreas: past, present, future,” *Diabetes*, vol. 60, 2011.

[84] F. H. El-Khatib, S. J. Russell, D. M. Nathan, R. G. Sutherlin, and E. R. Damiano, “A bihormonal closed-loop artificial pancreas for Type 1 Diabetes,” *Sci. Transl. Med*, vol. 2, 2010.

[85] V. Gingras *et al.*, “Impact of erroneous meal insulin bolus with dual-hormone artificial pancreas using a simplified bolus strategy-A randomized controlled trial,” *Sci. Rep.*, vol. 8, no. 1, pp. 1–9, 2018.

[86] A. M. Albisser *et al.*, “Clinical control of diabetes by the artificial pancreas,” *Diabetes*, vol. 23, no. 5, pp. 397–404, 1974.

[87] W. J. Tze, F. C. Wong, L. M. Chen, and S. O’YOUNG, “Implantable artificial endocrine pancreas unit used to restore normoglycaemia in the diabetic rat,” *Nature*, vol. 264, no. 5585, pp. 466–467, 1976.

[88] L. Bernardi, “Wearable artificial pancreas.” Google Patents, 05-Jan-1993.

[89] J. Yadav, A. Rani, V. Singh, and B. M. Murari, “Prospects and limitations of non-invasive blood glucose monitoring using near-infrared spectroscopy,” *Biomed. Signal Process. Control*, vol. 18, pp. 214–227, 2015.

[90] M. Goodarzi and W. Saeys, “Selection of the most informative near infrared spectroscopy wavebands for continuous glucose monitoring in human serum,” *Talanta*, vol. 146, pp. 155–165, 2016.

[91] N. Spegazzini *et al.*, "Spectroscopic approach for dynamic bioanalyte tracking with minimal concentration information," *Sci. Rep.*, vol. 4, p. 7013, 2014.

[92] M. Kuroda *et al.*, "Effects of daily glucose fluctuations on the healing response to everolimus-eluting stent implantation as assessed using continuous glucose monitoring and optical coherence tomography," *Cardiovasc. Diabetol.*, vol. 15, no. 1, p. 79, 2016.

[93] J. Y. Sim, C.-G. Ahn, E.-J. Jeong, and B. K. Kim, "In vivo microscopic photoacoustic spectroscopy for non-invasive glucose monitoring invulnerable to skin secretion products," *Sci. Rep.*, vol. 8, no. 1, pp. 1–11, 2018.

[94] L. Lipani *et al.*, "Non-invasive, transdermal, path-selective and specific glucose monitoring via a graphene-based platform," *Nat. Nanotechnol.*, vol. 13, no. 6, pp. 504–511, 2018.

[95] J. Kim, A. S. Campbell, and J. Wang, "Wearable non-invasive epidermal glucose sensors: A review," *Talanta*, vol. 177, pp. 163–170, 2018.

[96] C. D. Malchoff, K. Shoukri, J. I. Landau, and J. M. Buchert, "A novel noninvasive blood glucose monitor," *Diabetes Care*, vol. 25, no. 12, pp. 2268–2275, 2002.

[97] E. V Karpova, E. V Shcherbacheva, A. A. Galushin, D. V Vokhmyanina, E. E. Karyakina, and A. A. Karyakin, "Noninvasive diabetes monitoring through continuous analysis of sweat using flow-through glucose biosensor," *Anal. Chem.*, vol. 91, no. 6, pp. 3778–3783, 2019.

[98] A. A. Karyakin, S. V Nikulina, D. V Vokhmyanina, E. E. Karyakina, E. K. H. Anaev, and A. G. Chuchalin, "Non-invasive monitoring of diabetes through analysis of the exhaled breath condensate (aerosol)," *Electrochem. commun.*, vol. 83, pp. 81–84, 2017.

[99] J. R. Sempionatto *et al.*, "Eyeglasses-based tear biosensing system: Non-invasive detection of alcohol, vitamins and glucose," *Biosens. Bioelectron.*, vol. 137, pp. 161–170, 2019.

[100] M. Bariya, H. Y. Y. Nyein, and A. Javey, "Wearable sweat sensors," *Nat. Electron.*, vol. 1, no. 3, pp. 160–171, 2018.

[101] A. Bhide, S. Muthukumar, A. Saini, and S. Prasad, "Simultaneous lancet-free monitoring of alcohol and glucose from low-volumes of perspired human sweat," *Sci. Rep.*, vol. 8, no. 1, pp. 1–11, 2018.

[102] M. Nosrati, Z. Abbasi, M. Baghelani, S. Bhadra, and M. Daneshmand, "Locally Strong-Coupled Microwave Resonator Using PEMC Boundary for Distant Sensing Applications," *IEEE Trans. Microw. Theory Tech.*, 2019.

[103] M. H. Zarifi, H. Sadabadi, S. H. Hejazi, M. Daneshmand, and A. Sanati-Nezhad, "Noncontact and nonintrusive microwave-microfluidic flow sensor for energy and biomedical engineering," *Sci. Rep.*, vol. 8, no. 1, p. 139, 2018.

[104] M. Baghelani, Z. Abbasi, and M. Daneshmand, "Noncontact high sensitivity

chipless tag microwave resonator for bitumen concentration measurement at high temperatures," *Fuel*, vol. 265, p. 116916, 2020.

[105] A. K. Jha, N. Delmonte, A. Lamecki, M. Mrozowski, and M. Bozzi, "Design of microwave-based angular displacement sensor," *IEEE Microw. Wirel. Components Lett.*, vol. 29, no. 4, pp. 306–308, 2019.

[106] W. Liu, X. Yang, Y. Niu, and H. Sun, "Improve planar multiple split-ring sensor for microwave detection applications," *Sensors Actuators A Phys.*, vol. 297, p. 111542, 2019.

[107] T.-T. Tsai *et al.*, "High throughput and label-free particle sensor based on microwave resonators," *Sensors Actuators A Phys.*, vol. 285, pp. 652–658, 2019.

[108] B. Camli, E. Kusakci, B. Lafci, S. Salman, H. Torun, and A. Yalcinkaya, "A microwave ring resonator based glucose sensor," *Procedia Eng*, vol. 168, pp. 465–468, 2016.

[109] N.-Y. Kim, K. K. Adhikari, R. Dhakal, Z. Chuluunbaatar, C. Wang, and E.-S. Kim, "Rapid, sensitive and reusable detection of glucose by a robust radiofrequency integrated passive device biosensor chip," *Sci. Rep.*, vol. 5, no. 1, pp. 1–9, 2015.

[110] N. Sharafadinzadeh, M. Abdolrazzaghi, and M. Daneshmand, "Investigation on planar microwave sensors with enhanced sensitivity from microfluidic integration," *Sensors Actuators A Phys.*, vol. 301, p. 111752, 2020.

[111] B. Kapilevich and B. Litvak, "Optimized microwave sensor for online concentration measurements of binary liquid mixtures," *IEEE Sens. J.*, vol. 11, no. 10, pp. 2611–2616, 2011.

[112] C. G. Juan, E. Bronchalo, B. Potelon, C. Quendo, E. Ávila-Navarro, and J. M. Sabater-Navarro, "Concentration Measurement of Microliter-Volume Water–Glucose Solutions Using $ Q $ Factor of Microwave Sensors," *IEEE Trans. Instrum. Meas.*, vol. 68, no. 7, pp. 2621–2634, 2018.

[113] T. Chretiennot, D. Dubuc, and K. Grenier, "Microwave-based microfluidic sensor for non-destructive and quantitative glucose monitoring in aqueous solution," *Sensors*, vol. 16, no. 10, p. 1733, 2016.

[114] A. A. M. Bahar, Z. Zakaria, M. K. M. Arshad, A. A. M. Isa, Y. Dasril, and R. A. Alahnomi, "Real Time Microwave Biochemical Sensor Based on Circular SIW Approach for Aqueous Dielectric Detection," *Sci. Rep.*, vol. 9, no. 1, pp. 1–12, 2019.

[115] J.-S. G. Hong and M. J. Lancaster, *Microstrip filters for RF/microwave applications*, vol. 167. John Wiley & Sons, 2004.

[116] M. Nosrati, M. Daneshmand, and B. S. Virdee, "Novel compact dual-narrow/wideband branch-line couplers using T-Shaped stepped-impedance-stub lines," *Int. J. RF Microw. Comput. Eng.*, vol. 21, no. 6, pp. 642–649, 2011.

[117] G. L. Matthaei, L. Young, and E. M. T. Jones, *Microwave filters, impedance-matching networks, and coupling structures*. Artech house, 1980.

[118] D. M. Pozar, *Microwave engineering*. John wiley & sons, 2009.

[119] M. Nosrati, N. Vahabisani, and M. Daneshmand, "A novel ultra wideband (UWB) filter with double tunable notch-bands using MEMS capacitors," in *2013 IEEE MTT-S International Microwave Symposium Digest (MTT)*, 2013, pp. 1–3.

[120] A. Anand and X. Liu, "Reconfigurable planar capacitive coupling in substrate-integrated coaxial-cavity filters," *IEEE Trans. Microw. Theory Tech.*, vol. 64, no. 8, pp. 2548–2560, 2016.

[121] M. Nosrati, T. Faraji, and Z. Atlasbaf, "A compact composite broad stop-band elliptic-function low-pass filter for ultra wide-band applications using interdigital capacitors," *Prog. Electromagn. Res.*, vol. 7, pp. 87–95, 2009.

[122] I. V Lindell and A. H. Sihvola, "Perfect electromagnetic conductor," *J. Electromagn. Waves Appl.*, vol. 19, no. 7, pp. 861–869, 2005.

[123] I. V Lindell and A. H. Sihvola, "Transformation method for problems involving perfect electromagnetic conductor (PEMC) structures," *IEEE Trans. Antennas Propag.*, vol. 53, no. 9, pp. 3005–3011, 2005.

[124] I. V Lindell and A. H. Sihvola, "Realization of the PEMC boundary," *IEEE Trans. Antennas Propag.*, vol. 53, no. 9, pp. 3012–3018, 2005.

[125] M. Nosrati and M. Daneshmand, "Gap-coupled excitation for evanescent-mode substrate integrated waveguide filters," *IEEE Trans. Microw. Theory Tech.*, vol. 66, no. 6, pp. 3028–3035, 2018.

[126] M. Nosrati, Z. Abbasi, and M. Daneshmand, "Single-layer substrate-integrated waveguide evanescent-mode filter," *IEEE Microw. Wirel. Components Lett.*, vol. 28, no. 12, pp. 1107–1109, 2018.

[127] J. M. Sowa, P. Sheng, M. Y. Zhou, T. Chen, A. J. Serres, and M. C. Sieben, "Electrical properties of bitumen emulsions," *Fuel*, vol. 74, no. 8, pp. 1176–1179, 1995.

[128] M. Abdolrazzaghi, S. Khan, and M. Daneshmand, "A Dual-Mode Split-Ring Resonator to Eliminate Relative Humidity Impact," *IEEE Microw. Wirel. Components Lett.*, no. 99, pp. 1–3, 2018.

[129] M. H. Zarifi and M. Daneshmand, "High-resolution RFID liquid sensing using a chipless tag," *IEEE Microw. Wirel. Components Lett.*, vol. 27, no. 3, pp. 311–313, 2017.

[130] S. B. and M. D. M. Nosrati, Z. Abbasi, M. Baghelani, "Locally Strong-Coupled Microwave Resonator Using PEMC Boundary for Distant Sensing Applications," *IEEE Trans. Microw. Theory Tech.*, 2019.

[131] P.-R. Bauquis, "What future for extra heavy oil and bitumen: The Orinoco case," in *Paper presented by TOTAL at the World Energy Congress*, 1998, pp. 13–18.

[132] L. Rosa, K. F. Davis, M. C. Rulli, and P. D'Odorico, "Environmental consequences

of oil production from oil sands," *Earth's Futur.*, vol. 5, no. 2, pp. 158–170, 2017.

[133] J. D. Miller and J. E. Sepulveda, "Separation of bitumen from dry tar sands." Google Patents, 17-Oct-1978.

[134] Y. Long, T. Dabros, and H. Hamza, "Stability and settling characteristics of solvent-diluted bitumen emulsions," *Fuel*, vol. 81, no. 15, pp. 1945–1952, 2002.

[135] S. Goel, S. Ng, E. Acosta, and A. Ramachandran, "The roles of contact time and contact pressure on the coalescence of water droplets suspended in concentrated bitumen solutions," *Fuel*, vol. 223, pp. 486–495, 2018.

[136] J. T. Bulmer and J. Starr, "Syncrude analytical methods for oil sand and bitumen processing," *AOSTRA, Edmont.*, 1979.

[137] M. Jones and S. E. Taylor, "NMR relaxometry and diffusometry in characterizing structural, interfacial and colloidal properties of heavy oils and oil sands," *Adv. Colloid Interface Sci.*, vol. 224, pp. 33–45, 2015.

[138] G. Galindo-Romera, F. J. Herraiz-Martínez, M. Gil, and J. Juan, "Submersible Printed Split-Ring Resonator-Based Sensor for Thin-Film Detection and Permittivity Characterization," *Sensors*, vol. 14169, p. 1, 2016.

[139] M. Abdolrazzaghi, M. H. Zarifi, C. F. A. Floquet, and M. Daneshmand, "Contactless Asphaltene Detection Using an Active Planar Microwave Resonator Sensor," *Energy & Fuels*, vol. 31, no. 8, pp. 8784–8791, 2017.

[140] P. Vélez, J. Muñoz-Enano, K. Grenier, J. Mata-Contreras, D. Dubuc, and F. Martín, "Split Ring Resonator (SRR) based Microwave Fluidic Sensors for Electrolyte Concentration Measurements," *IEEE Sens. J.*, 2018.

[141] M. H. Zarifi, S. Farsinezhad, K. Shankar, and M. Daneshmand, "Liquid sensing using active feedback assisted planar microwave resonator," *IEEE Microw. Wirel. Components Lett.*, vol. 25, no. 9, pp. 621–623, 2015.

[142] J. Naqui, M. Durán-Sindreu, and F. Martín, "Novel sensors based on the symmetry properties of split ring resonators (SRRs)," *Sensors*, vol. 11, no. 8, pp. 7545–7553, 2011.

[143] J. Y. Yuan, D. H. S. Law, and T. N. Nasr, "Benefit of wettability change near the production well in SAGD," in *Canadian international petroleum conference*, 2002.

[144] A. de Klerk, M. R. Gray, and N. Zerpa, "Unconventional oil and gas: Oilsands," in *Future energy*, Elsevier, 2014, pp. 95–116.

[145] P. Gope and T. Hwang, "BSN-Care: A Secure IoT-Based Modern Healthcare System Using Body Sensor Network," *IEEE Sens. J.*, vol. 16, no. 5, pp. 1368–1376, 2016.

[146] Y. Lu, M. C. Biswas, Z. Guo, J.-W. Jeon, and E. K. Wujcik, "Recent developments in bio-monitoring via advanced polymer nanocomposite-based wearable strain sensors," *Biosens. Bioelectron.*, vol. 123, pp. 167–177, 2019.

[147] X. Xuan, H. S. Yoon, and J. Y. Park, “A wearable electrochemical glucose sensor based on simple and low-cost fabrication supported micro-patterned reduced graphene oxide nanocomposite electrode on flexible substrate,” *Biosens. Bioelectron.*, vol. 109, pp. 75–82, 2018.

[148] W. Gao *et al.*, “Fully integrated wearable sensor arrays for multiplexed in situ perspiration analysis,” *Nature*, vol. 529, p. 509, Jan. 2016.

[149] B. Kovatchev, “Automated closed-loop control of diabetes: the artificial pancreas,” *Bioelectron. Med.*, vol. 4, no. 1, p. 14, 2018.

[150] J. C. Yeo and C. T. Lim, “Emerging flexible and wearable physical sensing platforms for healthcare and biomedical applications,” *Microsystems Nanoeng.*, vol. 2, p. 16043, 2016.

[151] G. Matzeu, L. Florea, and D. Diamond, “Advances in wearable chemical sensor design for monitoring biological fluids,” *Sensors Actuators B Chem.*, vol. 211, pp. 403–418, 2015.

[152] H. Li *et al.*, “Measurement of serum total glycerides and free glycerol by high-performance liquid chromatography,” *J. Lipid Res.*, vol. 47, no. 9, pp. 2089–2096, 2006.

[153] U. S. D. of H. & H. Services and Health, “Hyperglycerolemia,” 2013. [Online]. Available: https://rarediseases.info.nih.gov/diseases/2807/hyperglycerolemia.

[154] V. Narwal and C. S. Pundir, “Development of glycerol biosensor based on co-immobilization of enzyme nanoparticles onto graphene oxide nanoparticles decorated pencil graphite electrode,” *Int. J. Biol. Macromol.*, vol. 127, pp. 57–65, 2019.

[155] K. Kurahashi, K. Hisada, M. Kashiwagi, S. Yoshihara, T. Nomura, and H. Tokumoto, “Analysis of the Continuous Bioconversion of Glycerol by Promotion of Highly Glycerol-Resistant Glycerol-Degrading Bacteria,” *Waste and Biomass Valorization*, pp. 1–10, 2018.

[156] M. S. Ribeiro and F. R. P. Rocha, “A single-phase spectrophotometric procedure for in situ analysis of free glycerol in biodiesel,” *Microchem. J.*, vol. 106, pp. 23–26, 2013.

[157] K. Sandra, A. dos Santos Pereira, G. Vanhoenacker, F. David, and P. Sandra, “Comprehensive blood plasma lipidomics by liquid chromatography/quadrupole time-of-flight mass spectrometry,” *J. Chromatogr. A*, vol. 1217, no. 25, pp. 4087–4099, 2010.

[158] P. M. Meaney, C. J. Fox, S. D. Geimer, and K. D. Paulsen, “Electrical characterization of glycerin: Water mixtures: Implications for use as a coupling medium in microwave tomography,” *IEEE Trans. Microw. Theory Tech.*, vol. 65, no. 5, pp. 1471–1478, 2017.

[159] U. Schneider, P. Lunkenheimer, R. Brand, and A. Loidl, “Dielectric and far-infrared spectroscopy of glycerol,” *J. Non. Cryst. Solids*, vol. 235, pp. 173–179, 1998.

[160] D. W. Davidson and R. H. Cole, “Dielectric relaxation in glycerol, propylene glycol, and n-propanol,” *J. Chem. Phys.*, vol. 19, no. 12, pp. 1484–1490, 1951.

[161] D. C. Campos, E. L. Dall’Oglio, P. T. de Sousa Jr, L. G. Vasconcelos, and C. A. Kuhnen, “Investigation of dielectric properties of the reaction mixture during the acid-catalyzed transesterification of Brazil nut oil for biodiesel production,” *Fuel*, vol. 117, pp. 957–965, 2014.

[162] S. Asif, B. Braaten, and A. Iftikhar, “Effectiveness of a dielectric probe calibration using deionized, distilled and tap water,” in *2017 IEEE International Symposium on Antennas and Propagation & USNC/URSI National Radio Science Meeting*, 2017, pp. 893–894.

[163] R. Buchner, G. Hefter, P. M. May, and P. Sipos, “Dielectric relaxation of dilute aqueous NaOH, NaAl (OH) 4, and NaB (OH) 4,” *J. Phys. Chem. B*, vol. 103, no. 50, pp. 11186–11190, 1999.

[164] A. K. Lyashchenko and A. Y. Zasetsky, “Complex dielectric permittivity and relaxation parameters of concentrated aqueous electrolyte solutions in millimeter and centimeter wavelength ranges,” *J. Mol. Liq.*, vol. 77, no. 1–3, pp. 61–75, 1998.

[165] A. S. Lileev, V. L. Dar’ya, and A. K. Lyashchenko, “Dielectric properties of aqueous hydrochloric acid solutions,” *Mendeleev Commun.*, vol. 17, no. 6, pp. 364–365, 2007.

[166] A. S. Lileev, D. V Loginova, and A. K. Lyashchenko, “Microwave dielectric properties of potassium hydroxide aqueous solutions,” *Russ. J. Inorg. Chem.*, vol. 56, no. 6, pp. 961–967, 2011.

[167] N. McVicar *et al.*, “Quantitative tissue pH measurement during cerebral ischemia using amine and amide concentration-independent detection (AACID) with MRI,” *J. Cereb. Blood Flow Metab.*, vol. 34, no. 4, pp. 690–698, 2014.

[168] R. V Shchepin *et al.*, “15N Hyperpolarization of Imidazole-15N2 for magnetic resonance pH sensing via SABRE-SHEATH,” *ACS sensors*, vol. 1, no. 6, pp. 640–644, 2016.

[169] S. Schreml, R. J. Meier, O. S. Wolfbeis, M. Landthaler, R.-M. Szeimies, and P. Babilas, “2D luminescence imaging of pH in vivo,” *Proc. Natl. Acad. Sci.*, vol. 108, no. 6, pp. 2432–2437, 2011.

[170] R. Rahimi *et al.*, “A low-cost flexible pH sensor array for wound assessment,” *Sensors Actuators B Chem.*, vol. 229, pp. 609–617, 2016.

[171] J. L. Alamilla, E. Sosa, C. A. Sánchez-Magaña, R. Andrade-Valencia, and A. Contreras, “Failure analysis and mechanical performance of an oil pipeline,” *Mater. Des.*, vol. 50, pp. 766–773, 2013.

[172] H. reza Hajibagheri, A. Heidari, and R. Amini, “An experimental investigation of the nature of longitudinal cracks in oil and gas transmission pipelines,” *J. Alloys Compd.*, vol. 741, pp. 1121–1129, 2018.

[173] W. Chen, "30 - Modeling and prediction of stress corrosion cracking of pipeline steels A2 - El-Sherik, A.M. BT - Trends in Oil and Gas Corrosion Research and Technologies," in *Woodhead Publishing Series in Energy*, Boston: Woodhead Publishing, 2017, pp. 707–748.

[174] T. R. Jack, K. Krist, B. Erno, and R. R. Fessler, "Generation of Near Neutral pH and High pH SCC Environments on Buried Pipelines." NACE International.

[175] N. E. Board, "Stress corrosion cracking on Canadian oil and gas pipelines," *Natl. Energy Board, Calgary, Alberta*, 1996.

[176] J. A. Beavers and R. G. Worthingham, "The Influence of Soil Chemistry on SCC of Underground Pipelines," no. 36207. pp. 1671–1678, 2002.

[177] R. N. Parkins and P. M. Singh, "Stress Corrosion Crack Coalescence," *CORROSION*, vol. 46, no. 6, pp. 485–499, Jun. 1990.

[178] a W. Peabody and R. L. Bianchetti, *Control of Pipeline Corrosion Second Edition*. 2000.

[179] I. Thompson and J. R. Saithala, "Review of pipeline coating systems from an operator's perspective," *Corros. Eng. Sci. Technol.*, vol. 51, no. 2, pp. 118–135, Feb. 2016.

[180] M. J. Wilmott, T. R. Jack, G. Van Boven, and R. Sutherby, "Pipeline Stress Corrosion Cracking: Crack Growth Sensitivity Studies Under Simulated Field Conditions," in *Corrosion 96. NACE International*, 1996.

[181] J. a. Beavers and B. a. Harle, "Mechanisms of High-pH and Near-Neutral-pH SCC of Underground Pipelines," *J. Offshore Mech. Arct. Eng.*, vol. 123, no. 3, p. 147, 2001.

[182] M. Yu, W. Chen, K. Chevil, G. Van Boven, and J. Been, "Retarding Crack Growth by Static Pressure Hold for Pipeline Steel Exposed to a Near-Neutral pH Environment," no. 50251. p. V001T03A091, 2016.

[183] H. Niazi, H. Zhang, K. Korol, and W. Chen, "High pH Crack Growth Sensitivity to Underload-Type of Pressure Fluctuations," no. 51869. p. V001T03A064, 2018.

[184] J. A. Beavers, "Integrity management of natural gas and petroleum pipelines subject to stress corrosion cracking," *Corrosion*, vol. 70, no. 1, pp. 3–18, 2014.

[185] C. A. Tokognon, B. Gao, G. Y. Tian, and Y. Yan, "Structural health monitoring framework based on Internet of Things: A survey," *IEEE Internet Things J.*, vol. 4, no. 3, pp. 619–635, 2017.

[186] B. Gao, W. L. Woo, G. Y. Tian, and H. Zhang, "Unsupervised diagnostic and monitoring of defects using waveguide imaging with adaptive sparse representation," *IEEE Trans. Ind. Informatics*, vol. 12, no. 1, pp. 405–416, 2015.

[187] R. Yang, Y. He, H. Zhang, and S. Huang, "Through coating imaging and nondestructive visualization evaluation of early marine corrosion using

electromagnetic induction thermography," *Ocean Eng.*, vol. 147, pp. 277–288, 2018.

[188] H. R. Vanaei, A. Eslami, and A. Egbewande, "A review on pipeline corrosion, in-line inspection (ILI), and corrosion growth rate models," *Int. J. Press. Vessel. Pip.*, vol. 149, pp. 43–54, 2017.

[189] S. Kharkovsky and R. Zoughi, "Microwave and millimeter wave nondestructive testing and evaluation-Overview and recent advances," *IEEE Instrum. Meas. Mag.*, vol. 10, no. 2, pp. 26–38, 2007.

[190] Y. He, G. Tian, H. Zhang, M. Alamin, A. Simm, and P. Jackson, "Steel corrosion characterization using pulsed eddy current systems," *IEEE Sens. J.*, vol. 12, no. 6, pp. 2113–2120, 2012.

[191] H. Hikita, S. Asai, and T. Takatsuka, "Absorption of carbon dioxide into aqueous sodium hydroxide and sodium carbonate-bicarbonate solutions," *Chem. Eng. J.*, vol. 11, no. 2, pp. 131–141, 1976.

[192] S. Bhadra, D. S. Y. Tan, D. J. Thomson, M. S. Freund, and G. E. Bridges, "A wireless passive sensor for temperature compensated remote pH monitoring," *IEEE Sens. J.*, vol. 13, no. 6, pp. 2428–2436, 2013.

[193] S. Y. Oh *et al.*, "Skin-attachable, stretchable electrochemical sweat sensor for glucose and pH detection," *ACS Appl. Mater. Interfaces*, vol. 10, no. 16, pp. 13729–13740, 2018.

[194] M. Lin, B. Xu, H. Yao, A. Shen, and J. Hu, "An in vivo quantitative Raman-pH sensor of arterial blood based on laser trapping of erythrocytes," *Analyst*, vol. 141, no. 10, pp. 3027–3032, 2016.

[195] Z. Abbasi, H. Niazi, M. Abdolrazzaghi, W. Chen, and M. Daneshmand, "Monitoring pH Level Using High-Resolution Microwave Sensor for Mitigation of Stress Corrosion in Steel Pipelines," *IEEE Sens. J.*, 2020.

[196] W. Shi, S. He, M. Wei, D. G. Evans, and X. Duan, "Optical pH sensor with rapid response based on a fluorescein-intercalated layered double hydroxide," *Adv. Funct. Mater.*, vol. 20, no. 22, pp. 3856–3863, 2010.

[197] J. Muñoz-Enano, P. Vélez, M. Gil, and F. Martín, "Planar Microwave Resonant Sensors: A Review and Recent Developments," *Appl. Sci.*, vol. 10, no. 7, p. 2615, 2020.

[198] W. Su, B. S. Cook, and M. M. Tentzeris, "Additively manufactured microfluidics-based 'peel-and-replace' RF sensors for wearable applications," *IEEE Trans. Microw. Theory Tech.*, vol. 64, no. 6, pp. 1928–1936, 2016.

[199] Z. Abbasi, P. Shariaty, Z. Hashisho, and M. Daneshmand, "SilicaGel-Integrated Chipless RF Tag for Humidity Sensing," in *2018 18th International Symposium on Antenna Technology and Applied Electromagnetics (ANTEM)*, 2018, pp. 1–2.

[200] Z. Abbasi, M. Baghelani, M. Nosrati, A. Sanati-Nezhad, and M. Daneshmand,

"Real-Time Non-Contact Integrated Chipless RF Sensor for Disposable Microfluidic Applications," *IEEE J. Electromagn. RF Microwaves Med. Biol.*, 2019.

[201] S. N. R. Kantareddy, I. Mathews, R. Bhattacharyya, I. M. Peters, T. Buonassisi, and S. E. Sarma, "Long Range Battery-Less PV-Powered RFID Tag Sensors," *IEEE Internet Things J.*, 2019.

[202] J. Kimionis *et al.*, "Zero-power sensors for smart objects: Novel zero-power additively manufactured wireless sensor modules for IoT applications," *IEEE Microw. Mag.*, vol. 19, no. 6, pp. 32–47, 2018.

[203] R. Das, F. Moradi, and H. Heidari, "Biointegrated and Wirelessly Powered Implantable Brain Devices: A Review," *IEEE Trans. Biomed. Circuits Syst.*, vol. 14, no. 2, pp. 343–358, 2020.

[204] S. N. R. Kantareddy *et al.*, "Perovskite PV-powered RFID: enabling lowcost self-powered IoT sensors," *IEEE Sens. J.*, 2019.

[205] L. Da Xu, W. He, and S. Li, "Internet of things in industries: A survey," *IEEE Trans. Ind. informatics*, vol. 10, no. 4, pp. 2233–2243, 2014.

[206] H.-P. Phan *et al.*, "Wireless Battery-Free SiC Sensors Operating in Harsh Environments Using Resonant Inductive Coupling," *IEEE Electron Device Lett.*, vol. 40, no. 4, pp. 609–612, 2019.

[207] D. G. Senesky, B. Jamshidi, K. B. Cheng, and A. P. Pisano, "Harsh environment silicon carbide sensors for health and performance monitoring of aerospace systems: A review," *IEEE Sens. J.*, vol. 9, no. 11, pp. 1472–1478, 2009.

[208] A. Aldaoud, C. Laurenson, F. Rivet, M. R. Yuce, and J.-M. Redouté, "Design of a miniaturized wireless blood pressure sensing interface using capacitive coupling," *IEEE/ASME Trans. Mechatronics*, vol. 20, no. 1, pp. 487–491, 2014.

[209] T. Haidegger, J. Sándor, and Z. Benyó, "Surgery in space: the future of robotic telesurgery," *Surg. Endosc.*, vol. 25, no. 3, pp. 681–690, 2011.

[210] B. S. Cook, J. R. Cooper, and M. M. Tentzeris, "An inkjet-printed microfluidic RFID-enabled platform for wireless lab-on-chip applications," *IEEE Trans. Microw. Theory Tech.*, vol. 61, no. 12, pp. 4714–4723, 2013.

[211] S. H. Sung *et al.*, "Flexible wireless powered drug delivery system for targeted administration on cerebral cortex," *Nano Energy*, vol. 51, pp. 102–112, 2018.

[212] L. Y. Chen *et al.*, "Continuous wireless pressure monitoring and mapping with ultra-small passive sensors for health monitoring and critical care," *Nat. Commun.*, vol. 5, p. 5028, 2014.

[213] S. Deif and M. Daneshmand, "Multi-Resonant Chipless RFID Array System for Coating Defect Detection and Corrosion Prediction," *IEEE Trans. Ind. Electron.*, 2019.

[214] M. Sakhdari, M. Hajizadegan, Y. Li, M. M.-C. Cheng, J. C. H. Hung, and P.-Y. Chen, "Ultrasensitive, Parity–Time-Symmetric Wireless Reactive and Resistive Sensors," *IEEE Sens. J.*, vol. 18, no. 23, pp. 9548–9555, 2018.

[215] M. Hajizadegan, M. Sakhdari, S. Liao, and P.-Y. Chen, "High-Sensitivity Wireless Displacement Sensing Enabled by PT-Symmetric Telemetry," *IEEE Trans. Antennas Propag.*, vol. 67, no. 5, pp. 3445–3449, 2019.

[216] P.-Y. Chen *et al.*, "Generalized parity–time symmetry condition for enhanced sensor telemetry," *Nat. Electron.*, vol. 1, no. 5, p. 297, 2018.

[217] Y. Divin, M. Lyatti, U. Poppe, and K. Urban, "Liquid identifier based on Hilbert spectroscopy: Concept and proof of principle," in *SENSORS, 2008 IEEE*, 2008, pp. 126–129.

[218] A. Goel and H. Hashemi, "Concurrent dual-frequency oscillators and phase-locked loops," *IEEE Trans. Microw. Theory Tech.*, vol. 56, no. 8, pp. 1846–1860, 2008.